Flexible Microelectrode Probes for Scanning Electrochemical Microscopy – From Concept to High-Throughput Applications

Von der Fakultät für Mathematik und Naturwissenschaften
der Carl von Ossietzky Universität Oldenburg
zur Erlangung des Grades und Titels eines

Doktors der Naturwissenschaften (Dr. rer. nat.)

angenommene Dissertation

von Herrn

Dipl.-Chem. Andreas Lesch
geboren am 24.08.1983 in Oldenburg

Oldenburg, September 2012

Diese Arbeit entstand von Juni 2009 bis August 2012 unter der Betreuung von Herrn Prof. Dr. Gunther Wittstock an der Carl von Ossietzky Universität Oldenburg im Institut für Reine und Angewandte Chemie und dem Center of Interface Science.

Es bestand im Rahmen eines Gemeinschaftsprojektes eine Kooperation mit dem Labor der Physikalischen und Analytischen Elektrochemie (Laboratoire d'Electrochimie Physique et Analytique; LEPA) an der Eidgenössischen Hochschule Lausanne (École Polytechnique Fédérale de Lausanne, EPFL) unter der Leitung von Professor Hubert H. Girault. Das Projekt wurde gemeinschaftlich gefördert von der Deutschen Forschungsgemeinschaft (DFG, Wi 1617/10) und dem Fonds National Suisse pour la Recherche Scientifique (grant no. 20PA21_121570/1) mit dem Titel "High throughput SECM imaging". Die Kooperation beinhaltete eine Arbeitszeit von 7 Wochen in Lausanne.

Teile der Arbeit wurden publiziert und sind mit [A#] gekennzeichnet. Eine Auflistung befindet sich unter 13.1.

Gutachter:	Prof. Dr. Gunther Wittstock
Zweitgutachter:	Prof. Dr. Christoph Lienau
Tag der Disputation:	03.12.2012

Abstract

Linear arrays of eight individually addressable microelectrodes were developed as new scanning electrochemical microscopy (SECM) probes in order to perform high-throughput scanning and modification. These arrays were made on thin polymeric supports like polyethylene terephthalate or polyimide sheets that provide a certain flexibility and stability to scan surfaces in contact mode in a brushing-like way. Several automated fabrication techniques, such as UV photoablation, Aerosol Jet®, and inkjet printing were applied which are suitable for batch production. Carbon, gold and silver microelectrodes were obtained which were coated with a thin insulation layer of Parylene C. High-throughput imaging of flat, tilted and curved surfaces was performed using the soft microelectrode arrays in contact regime. The soft probes follow the topography of the sample and provide an almost constant working distance. Differences in the lateral position and in the electrochemical response of the individual microelectrodes are corrected by calibration measurements. Typical difficulties in SECM imaging of large areas approaching square centimeter, such as a sample tilt, electrode fouling, sample aging and electrolyte evaporation, can be overcome. The imaging time is drastically reduced, while keeping the resolution of SECM. Mechanically sensitive surface structures like oligo(ethylene glycol)-terminated self-assembled monolayers (SAMs) on gold were modified by electrogeneration of bromine at the carbon microelectrodes followed by SECM imaging in contact mode without damaging the SAM. This is due to a very weak pressure exerted by the probe on the sample which is about three orders of magnitude less than that of conventional SFM tips. An automated routine was integrated in SECMx to pattern complex structures from patterning files. The array probes are applicable to the screening of combinatorial material libraries consisting of electrocatalysts, such as catalytically active compounds for hydrogen peroxide decomposition, an undesired intermediate and product in many technical applications based on the oxygen reduction reaction.

Zusammenfassung

Flexible, lineare Arrays aus acht individuell adressierbaren Mikroelektroden wurden als neuartige Sonden für die elektrochemische Rastersondenmikroskopie (SECM, scanning electrochemical microscopy) für Abbildungs- und Modifizierungsexperimente in Hochdurchsatz-Verfahren entwickelt. Die Arrays wurden in dünnen Polymerfolien aus Polyethylenterephthalat oder Polyimid hergestellt. Dadurch wird eine gewisse Flexibilität und Stabilität gewährleistet, um zu untersuchende Proben mit den Sonden zu “bürsten”. Verschiedene automatisierte Fabrikationstechniken wie die UV Photoablation, das Aerosol Jet®-Drucken und das Inkjet-Drucken wurden verwendet, die auch für Serienfertigungen benutzt werden können. Kohlenstoff-, Gold- und Silber-Mikroelektroden wurden erhalten, welche mit einer isolierenden Schicht aus Parylen C abgedeckt wurden. Hochdurchsatz-Abbildungen von flachen, gekippten und gekrümmten Oberflächen wurden mit den weichen Mikroelektrodenarrays im Kontaktmodus aufgenommen. Die weichen Sensoren folgen der Topographie der Probe und sorgen für einen nahezu konstanten Arbeitsabstand. Abweichungen der lateralen Positionen und der elektrochemischen Signale der einzelnen Mikroelektroden werden mit Hilfe von Kalibriermessungen korrigiert. Typische Schwierigkeiten beim Erstellen von SECM-Abbildungen großer Flächen im Quadratzentimeterbereich entstehen durch gekippte Proben, Verunreinigungen der aktiven Elektrodenflächen oder durch Lösungsmittelverdunstung. Diese Limitierungen werden mit den weichen Array-Sonden überwunden. Die Dauer einer SECM-Messung unter Beibehaltung der mit dem SECM zu erreichenden Auflösung wurde drastisch reduziert. Mechanisch empfindliche Oberflächenstrukturen wie Oligo(ethylenglycol)-terminierte selbst-assemblierte Monoschichten (OEG SAM) auf Gold wurden mit Brom modifiziert, welches elektrochemisch an den Kohlenstoff-Mikroelektroden erzeugt wurde. Die Array-Sonden konnten dann von den modifizierten Stellen SECM-Abbildungen im Kontaktmodus erstellen ohne die SAMs mechanisch zu beschädigen. Die mechanischen Drücke, die die weichen Sonden auf die Probe ausüben, sind um drei Größenordnungen kleiner als die von konventionellen Rasterkraftmikroskopie-Spitzen. Eine automatisierte Routine wurde in die SECMx-Software intergiert um komplexe Muster mit Hilfe sogenannter „Patterning“-Files zu erzeugen. Die Array-Sonden sind anwendbar für die Vorauswahl innerhalb von kombinatorischen Materialbibliotheken, die zum Beispiel Elektrokatalysatoren für die Zersetzung von Wasserstoffperoxid enthalten, einem

Reaktionsintermediat in vielen wichtigen technischen Anwendungen, die auf der Sauerstoffreduktion basieren.

Acknowledgements

This thesis was prepared between June 2009 and August 2012 within the framework of a joint project “High throughput SECM imaging: Development and applications” supported by Deutsche Forschungsgemeinschaft (Wi 1617/10, PI G. Wittstock) and the Fonds National Suisse pour la Recherche Scientifique (grant no. 20PA21_121570/1, H. H. Girault).

First of all, I would like to thank my adviser Prof. Dr. Gunther Wittstock for his dedication and support, namely the personal discussions from which I not only advanced scientifically, but also benefited for my personal and professional development. I am thankful for Mr. Wittstock’s great support in the further development of the in-house made SECMx software, and his quickly performed extensions in the software MIRA for treating array experiments. I also enjoyed the many ideas raised from the group seminars. I really appreciate the possibilities to present the results of this thesis in international conferences and to publish in very important chemistry journals. I owe thanks to the Arbeitsgemeinschaft Elektrochemischer Forschungsinstitutionen e.V. (AGEF), and the Electrochemical Society for travel grants

I also would like to thank Prof. Dr. Christoph Lienau who kindly agreed to provide the second referee report for this thesis.

Many thanks go to our cooperation partners at the Laboratoire d’Electrochimie Physique et Analytique (LEPA) at the École Polytechnique Fédérale de Lausanne (EPFL, Lausanne, Switzerland) under Prof. Dr. Hubert H. Girault. I am very thankful in particular for the collaboration with Dr. Fernando Cortés-Salazar und Dmitry Momotenko. The success of the project was strongly related to the excellent common experimental work, discussions and exchange of ideas. During my stays in Lausanne the complete preparation of carbon microelectrode arrays and the Parylene C coating of all used probes was performed in collaboration with Fernando and Dmitry. Furthermore, some of the results presented in this thesis were obtained during my stays in LEPA. I also would like to thank Dmitry for the support in the development of the geometric considerations in Section 6.5.5.

I would like to thank Britta Vaske for introducing me in the preparation and modification of the oligo(ethylene glycol)(OEG)-terminated self-assembled monolayers including the investigation of adsorbed proteins by confocal laser scanning microscopy.

Many thanks also go to Frank Meiners whose expertise in scanning force microscopy (SFM) increased the value of some figures included in this thesis. Figures 35b, 36, and 72a-c were made in cooperation with him.

I also want to thank Dr. Ushula Mengesha Tefashe for his collaboration in the shear force measurement (Figure 37). I guided the students Daniel Witte and Julian Behnken during the preparations of their MEd. or BSc. theses. I would like to thank both for their productive collaboration. Daniel prepared silver lines by inkjet printing which I used for the fabrication of silver microelectrode arrays (Section 6.3.3). Julian searched for appropriate parameters for the deposition of a mesoporous platinum film on soft carbon microelectrodes. This procedure was adopted in this thesis (Section 5.3). Furthermore, I would like to thank Dr. Guy Denuault (University of Southampton, UK) and Heinz Bülter for the discussions about the deposition of the mesoporous platinum film. Guy also provided the combinatorial material library used in Chapter 8.

I also would like to thank Jan Ross and Prof. Dr. Jens Christoffers (Carl von Ossietzky University of Oldenburg, Oldenburg, Germany) for providing the thiol for the preparation of the OEG SAM.

Many thanks go to Folkert Roelfs (workshop of the Carl von Ossietzky University of Oldenburg) who designed many components enabling many of the reported experiments and from whom I learned a lot during productive discussions.

Furthermore, I would like to thank Renate Kort and Dr. Erhard Riehl for the instruction and support in the usage of the scanning electron microscope, Dr. Robert Pomraenke for the assistance during the measurements of the resonance frequency of the soft probes (Section 7.1.1), and apl. Prof. Dr. Achim Kittel for the opportunity to measure the resistance of the gold tracks in his laboratory.

A fruitful collaboration with Dr. Ingo Wirth (Fraunhofer Institute for Manufacturing Technology and Applied Materials Research, IFAM, Bremen, Germany) lead to the manufacturing of the gold microelectrode arrays by Aerosol Jet® printing (Section 6.3.2).

Finally, I would like to thank all former and current group members of the Wittstock group for the scientific discussions, collaborations and the delightful atmosphere.

Table of Contents

1 Introduction

The localized characterization and patterning of surfaces on micro- and nanoscale received great attention and still experience a rising attraction in many different fields of science. This includes the investigation of microchips, sensor arrays, molecular electronic devices, single living cells, and new materials for energy conversion and storage. Scanning probe microscopies (SPMs) record a distance-dependent interaction between a micrometric or nanometric scanning probe and the substrate. Alternatively, such probes can exploit such interaction for a local surface modification. Exemplary SPMs are scanning tunneling microscopy (STM),[1] scanning force microscopy (SFM) also known as atomic force microscopy (AFM),[2] electrochemical scanning tunneling microscopy (ECSTM),[3] scanning near-field optical microscopy (SNOM),[4] and scanning electrochemical microscopy (SECM).[5-8] Depending on the interaction exploited, SPM images provide information about the physical properties of the sample such as topography, stiffness, adhesion, reactivity, etc. The mentioned techniques have in common that the probe is translated laterally in space (*i.e.* the x,y plane) with respect to the sample under study and that a map of the specific probe-sample interaction is recorded. The resolution depends on the probe size, the probe-to-substrate distance and the probe-sample interaction.

SECM uses an amperometric disk-shaped ultramicroelectrode (UME, diameter < 25 µm) embedded in an insulating glass sheath as probe. The UME is held or moved in close proximity to the substrate while the gap between microelectrode and sample is filled with electrolyte solution. Faradaic currents are measured at the UME which can be perturbed by the local properties of the substrate. This perturbation provides information about the nature of the substrate under study. SECM can be applied to a variety of interfaces such as solid-liquid,[9, 10] liquid-liquid[11, 12] or liquid-gas.[13, 14] In general, SECM is capable to image spatially resolved variations in the electrochemical reactivity. Furthermore, it allows to induce local electrochemical surface modifications,[15-19] to perform electrochemistry in small volumes,[20, 21] and to investigate heterogeneous[12, 22] as well as homogeneous kinetics.[23]

SECM applications such as screening of combinatorial catalyst libraries,[24-28] assessing the integrity of technical coatings,[29-31] imaging of latent human fingerprints,[32, 33] reading-out electropherograms[34] or protein arrays,[35, 36] and parallelizing surface modification protocols require abilities for working with large areas approaching square centimeter. With standard SECM instrumentation, two considerable limitations arise for these kinds of samples (details in Section 4.1).

i) In conventional SECM, the UME is scanned in constant height mode and the sample tilt must be minimized. In fact, the SECM signals depend strongly on the probe-sample working distance *d*. An experimentally experienced operator might eliminate the tilt by aligning the sample to the horizontal scanning plane of the UME. However, this procedure is time consuming and becomes obsolete when studying curved, corrugated or terraced surfaces, or surfaces with very different reactivity.

ii) As in other SPM techniques, the probe is moved line by line in the image plane and the probe interrogates all points of a sample sequentially. This leads to long imaging times which can result in artifacts caused by electrode fouling, sample aging and solvent evaporation.

Several approaches have been demonstrated to overcome both problems independently. For instance, a constant *d* can be achieved by combining SECM with other techniques, such as SFM,[37-53] ECSTM[54] or shear force sensors[55-61] which can be operated in constant distance mode (overview in Section 4.2). However, these hybrid configurations require additional instrumentation and in most cases the setups are limited to single nanoelectrodes applicable to small areas in the square micrometer scale.

Three strategies are followed to decrease the imaging time: increasing the probe translation rate and step size,[25, 62] renewal of electrolyte solution and electrochemical reactivation of the UME inbetween individual image frames,[25] and multiplexing individual probes.[63-66] However, as discussed in Section 4.3, these approaches did not reach a level of technical readiness suitable for routine experimentation.

The scope of the research project presented in this thesis was the development and application of new SECM probes for high-throughput imaging and surface modification. The conceptual ideas will be introduced in Section 6.1. Briefly, soft probes based on flexible polymeric materials can touch the sample, bend and scan tilted, curved and corrugated large surfaces in a brushing-like way. As a consequence, the probe can follow the topography of the sample providing an almost constant *d*. Moreover, the extension of the probe design to linear arrays of eight microelectrodes for parallel imaging and modification reduces the experimental time significantly. The operation of such arrays was enabled by new features in the in-house made SECMx software connected to new hardware components (Section 6.2). For scanning in contact regime, a new lift-off mode was integrated in the SECM imaging experiment in order to reposition the bent array and to scan adjacent image frames in an automated routine (Sections 6.2.4 and 6.5.1).

Several fabrication techniques were used to prepare various kinds of new soft probe types as summarized in Table 1.

Table 1. Types of soft linear arrays of microelectrodes presented in this thesis.

Electrode material	Fabrication technique	Section	Reference
Carbon	UV laser ablation	6.3.1	[**A2**],[**A3**],[**A8**]
Gold	Aerosol Jet® printing	6.3.2	[**A6**]
Silver	Inkjet printing	6.3.3	

The arrays were optically and electrochemically characterized and high-throughput SECM imaging was demonstrated with proof of concept experiments.[**A2**],[**A3**],[**A6**] Due to the fabrication protocols, the individual electrodes vary slightly in their exact positions, geometries and sizes. Calibration routines were developed in order to correct the current responses as discussed in Sections 6.5.3 and 6.5.4.[**A2**],[**A6**],[**A8**] Automated new software functions allow writing and reading of complex micrometer-sized patterns in millimeter-sized regions (Chapter 7).[**A8**] The established manipulation of cell repellent self-assembled monolayers (SAMs) by electrogeneration of bromine at the array microelectrodes and imaging the obtained modified regions in phosphate buffered solutions was used as a test case for the application of soft microelectrode arrays in such scenarios.[67][**A8**] Along with this experiment, it was tested if the soft probe arrays can brush delicate samples such as SAMs without damaging them (Section 7.1.1).[**A8**] In Chapter 8, a combinatorial material library of a C/Pt electrocatalyst for hydrogen peroxide decomposition was investigated by modified carbon microelectrode arrays. For this purpose, a mesoporous platinum film was deposited onto the carbon electrodes by a procedure adopted from literature.[68]

In Chapter 9, new features in the SECMx software are described that came up by the implementation of digital bipotentiostats. These represent new specialized experiments that are started via SECMx, but which are completely handled by the digital hardware. The data are read and stored afterwards like in standard experiments. This enables for example electrochemical impedance spectroscopy or fast cyclic voltammetry during SECM operations.

2 Theory and Principles of Scanning Electrochemical Microscopy (SECM)

First experiments that can be considered as SECM were reported by Engstrom *et al.*[6] in 1986. They employed an amperometric UME to measure the concentration profiles of a redox-active species generated at macroscopic electrodes. In an independent and contemporary work Bard and coworkers[7] developed an SECM on the basis of an ECSTM. Unusual large currents were recorded although the tip-sample separation exceeded the tunneling distance. After Kwak and Bard had formulated the feedback mode, SECM developed to a valuable technique for surface characterization and manipulation.[8, 69] They found out that contrary to ECSTM the UME response relied on diffusion-limited Faradaic currents as a function of the distance *d* between substrate and UME. The general setup was adopted from the ECSTM and is shown schematically in Figure 1.

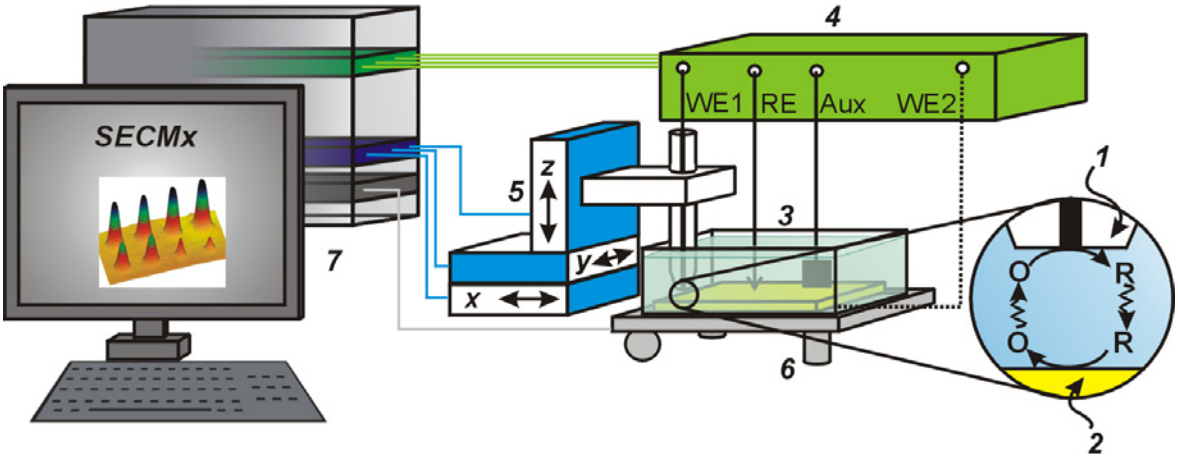

Figure 1. Scanning electrochemical microscope: 1, ultramicroelectrode (UME); 2, substrate; 3, electrochemical cell; 4, (bi)potentiostat; 5, positioning system; 6, tilt table; 7, personal computer.

A bipotentiostat is used to control the potential of the UME and optionally of the substrate. The UME can be moved by a three-axes positioning system. A personal computer controls the experiments and records the currents as a function of UME position. Nowadays, SECM represents a pivotal technique for many applications regarding electrochemistry at interfaces. The number of commercially available systems increases continuously, but custom-made setups still play an important role in the development and progression of SECM. Several reviews and books demonstrate the growing influence of SECM.[70-72] The current at the UME or the substrate can be recorded as a function of the UME-sample distance *d* (approach curve) or the *x*,*y*-position of the probe when it is moved laterally in both horizontal directions in space (imaging). Several operation modes of SECM were developed, such as the feedback mode (Section 2.2),[8] tip-generation/substrate-collection (TG/SC) mode (Sections 2.3),[73] sample-generation/tip-collection (SG/TC) mode (Section 2.3),[74] direct mode (Section 3.1),[75] and the redox competition mode (Section 2.4)[76] These modes were developed for various specific applications in order to detect signals with highest achievable resolution and are discussed in the denoted sections.

2.1 Properties of Ultramicroelectrodes

UMEs are defined as electrodes having at least one dimension smaller than the thickness of the diffusion layer δ in the critical time t_C of the experiment.[77, 78] δ is defined as the diffusion length of a species with diffusion coefficient D within the critical time t_C ($\delta = (2 \cdot D \cdot t_C)^{1/2}$). SECM relies strongly on the electrochemical properties of UMEs, which become apparent with diameters smaller than 25 µm.[79] Various types of UMEs were introduced over the past decades, that have recently been reviewed.[80] The UME is normally an amperometric disk-shaped electrode enclosed in an insulating sheath, typically made of glass or epoxy.[81] Metallic wires, including Pt and Au, or carbon fibers are most often used as electrode materials. But also mercury,[82] pyrolytic carbon[83] and boron-doped diamond[84] UMEs have been used successfully for SECM experiments. Other UME shapes such as sphere,[85] hemisphere,[86] and band[87] have been employed as well. Potentiometric probes such as pipette tips find also application,[88, 89] but are not described in this thesis.

A Pt-UME encapsulated in a borosilicate glass capillary was used as conventional UME in this thesis for comparative purposes. The radius of the active electrode area was $r_T = 25$ µm (Figure 2a). Following the general practice, all geometric properties of the conventional UMEs as well as applied potentials and measured currents are indexed with "T" (for "tip") in this thesis although the UMEs are flat disks. An RG value is defined for disk electrodes which is the radius of the glass r_{glass} divided by the radius of the disk r_T (Figure 2b). Figure 2c shows a typical sigmoidal-shaped cyclic voltammogram CV of a UME using a standard redox mediator like ferrocenyl methanol in an electrolyte solution. The reduced form R is oxidized at anodic potentials according to Eq. (1).

$$R \rightarrow O + ne^- \qquad (1)$$

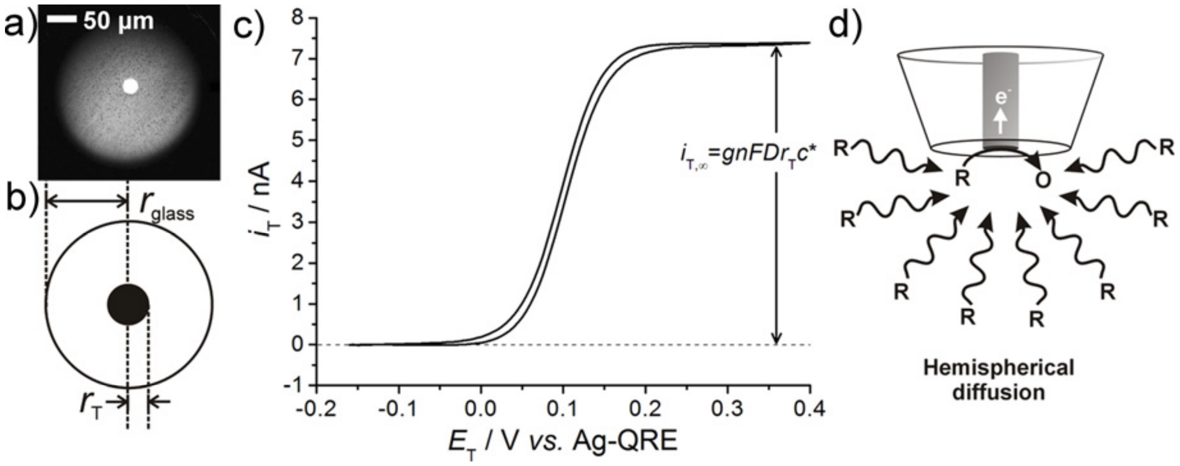

Figure 2. Properties of UMEs. a) Confocal laser scanning microscope reflexion image of a UME consisting of a 25 µm Pt wire enclosed in a glass sheath. b) Definition of the *RG* value; $RG = r_{glass}/r_T$. c) Cyclic voltammogramm in 2 mM ferrocenyl methanol (FcMeOH); oxidation leads to a diffusion-controlled steady-state current due to a hemispherical diffusion of the redox-active species (d).

Alternatively, a redox mediator can also be reduced from the oxidized form O to R. For simplicity, only the first case is described in the following. In order to perform SECM measurements, diffusion-controlled currents at the UMEs are important. Therefore, an excess of supporting electrolyte is added to exclude migration and slow probe movements are applied to keep stirring and convective perturbations insignificant. One advantage of UMEs is the formation of a hemispherical diffusion field due to a more efficient mass transfer than at macroscopic electrodes. In case the UME is positioned quasi infinitely far away from any kind of the substrate ($d > 20\ r_T$), a steady-state diffusion-limited current $i_{T,\infty}$ is rapidly established as demonstrated by the formation of a plateau in the CV at $E_T > 0.2$ V *vs.* Ag-QRE (Figure 2c). Eq. (2) describes $i_{T,\infty}$ for a disk-shaped electrode encapsulated in an insulating sheathing

$$i_{T,\infty} = g\, n\, F\, D\, c^*\, r_T \tag{2}$$

where g is a geometry-dependent factor related to the electrode shape, n is the number of transferred electrons, F is the Faraday constant, D is the diffusion coefficient and c^* the bulk concentration of the redox mediator. For infinite large insulators g equals 4, but represents in principle a good approximation for RG values ≥ 10.[90, 91] The diffusion of the redox-active species is $\sim D \cdot c \cdot r_T^{-1}$ and is quite large, thus the recorded currents are relatively stable against convection for probe translation rates of up to 10 µm s^{-1}.[92] A steady-state current is achieved within a relatively short time of approximately $r_T^2\, D^{-1}$. For a typical

UME of 10 µm diameter, this takes only 1.3 s.[93] UMEs stand also out due to other advantageous properties such as low capacitive currents and low ohmic drops.

2.2 Feedback Mode

As described in the previous section for a steady-state diffusion-controlled current, $i_{T,\infty}$ is measured at a UME in the bulk solution when an appropriate potential for the oxidation of the redox mediator R is applied. A different situation occurs when the probe is placed within a few r_T above a substrate. An electrically insulating surface (Figure 3a) blocks partially the diffusion of R to the UME.

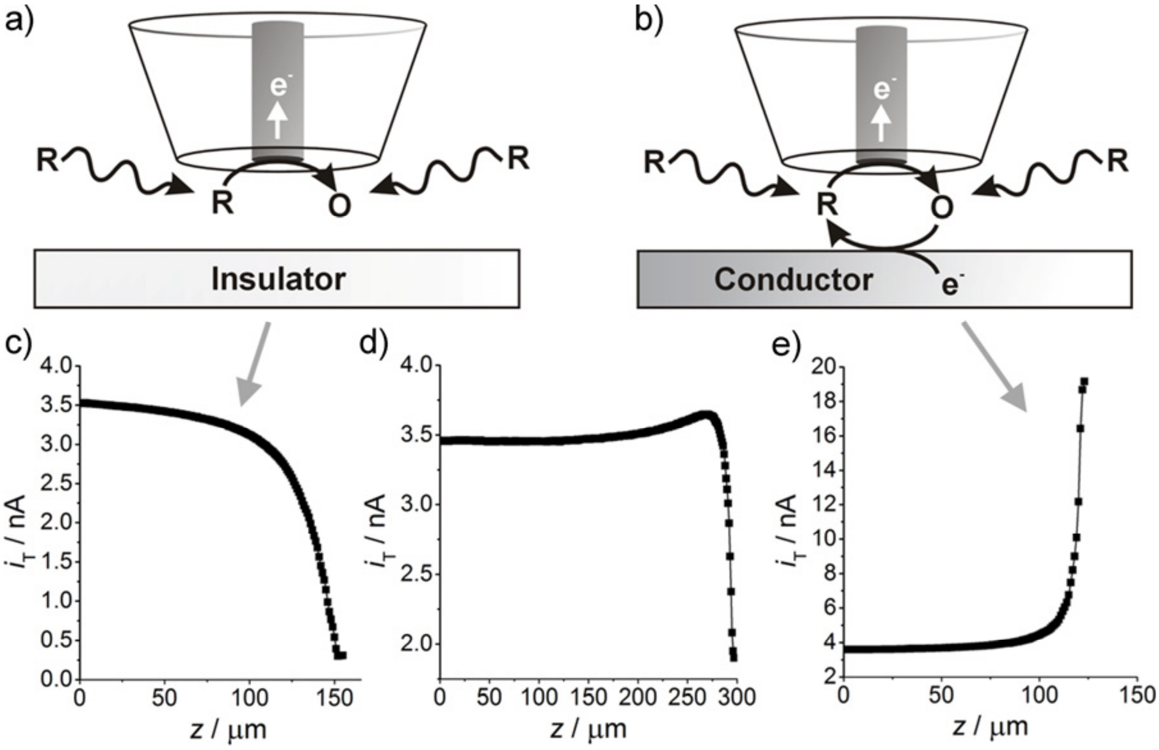

Figure 3. Basic principle of the SECM feedback mode with the probe in close proximity to a substrate. a) UME is near an insulating substrate with $i_T < i_{T,\infty}$ (left panel) and b) near a conductive surface with $i_T < i_{T,\infty}$ (right panel). Experimental approach curves over an insulator (c), a surface with finite kinetics (d) and a conductor (e).

This hindered diffusion reduces the flux of R at the UME causing a lower current than in the solution bulk ($i_T < i_{T,\infty}$). As the UME approaches the sample, i_T decreases and eventually becomes zero. This can be seen in a typical experimental approach curve towards an insulating surface in Figure 3c. In this thesis, the recorded experimental approach curves with original values start with $z = 0$ µm and the direction of the vertical translation towards the sample surface is defined as positive. The decreasing current with decreasing working distance is called “negative feedback”. The flat UME is orientated in parallel to the substrate which should result in a zero current for d = 0 µm due to a complete blocking of the redox mediator. Practically, the probe is often not absolutely aligned to the sample surface which leads to a small positional offset d_0 (distance between active electrode area and sample surface) when the probe touches the sample. The real working distance is then calculated by

$$d = z_{\max} - z + d_0 \tag{3}$$

where $z_{\max}$ is the vertical position for which the probe gets in mechanical contact with the sample relative to the start position of the approach curve (Figure 4).

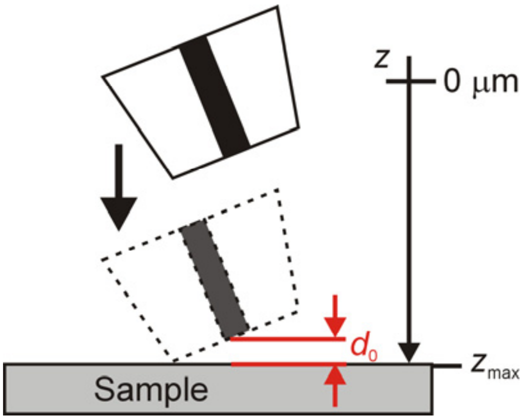

Figure 4. Scheme about the determination of *d*. The misalignment of the UME is exaggerated. Adopted and modified from Supporting Information (SI) of Ref. [94].

The contact between UME and the sample is realized when the decreasing current values start to stay constant. If the UME is brought close to an electrically conductive substrate like gold, the blocking effect of the sample surface is overcome by the electrochemical regeneration of R from O at the substrate (Figure 3b). For typical mediators, the electron transfer reaction at conducting substrates is very fast and thus diffusion-controlled. R diffuses to the UME and increases the flux of R compared to the situation in solution bulk. Therefore, i_T increases with decreasing d over conducting substrates ($i_T > i_{T,\infty}$). This is called “positive feedback”. In case d approaches zero, the UME may reach the regime of tunneling currents. The UME current becomes very large and follows another principle.[95]

An intermediate situation occurs where the regeneration of O at a substrate occurs with a finite rate. As the consequence, the approach curves lay inbetween the limiting cases of negative and positive feedback (Figure 3d). This situation is obtained for example on a gold substrate covered with a self-assembled monolayer (SAM) formed with mercaptoundecanoic acid and using ferrocenyl methanol as redox mediator. When the UME is approached to the substrate until the working distance is some few UME radii, the reaction of O back to R is fast enough to compete with the diffusional transport of O and R. Hence, i_T increases with decreasing d. When the UME gets closer to the substrate, the diffusion of O and R within the thin electrolyte layer between the UME and the substrate becomes faster. This increased transport rate is not matched by the regeneration reaction at the sample and, consequently, i_T decreases.

Approach curves are usually presented as normalized currents I_T (Eq. (4)) *vs.* normalized distances L (Eq. (5)) in order to make the data independent from experimental parameters like r_T, D, or c^*.

$$I_T = \frac{i_T}{i_{T,\mathrm{ref}}} \tag{4}$$

$$L = \frac{d}{r_T} \tag{5}$$

$i_{T,\mathrm{ref}}$ represents a reference current, which is mostly referred to the measured steady-state current $i_{T,\infty}$ in solution bulk. It does not always fit to the analytical expression $i_{T,\mathrm{ref}} = 4\,n\,F\,D\,c^*\,r_T$ (Eq. (2)) as it is often assumed for a disk-shaped UME enclosed in an infinitely large insulator. In particular for small RG and for slow reaction rates at the sample the difference has to be taken into consideration.[70]

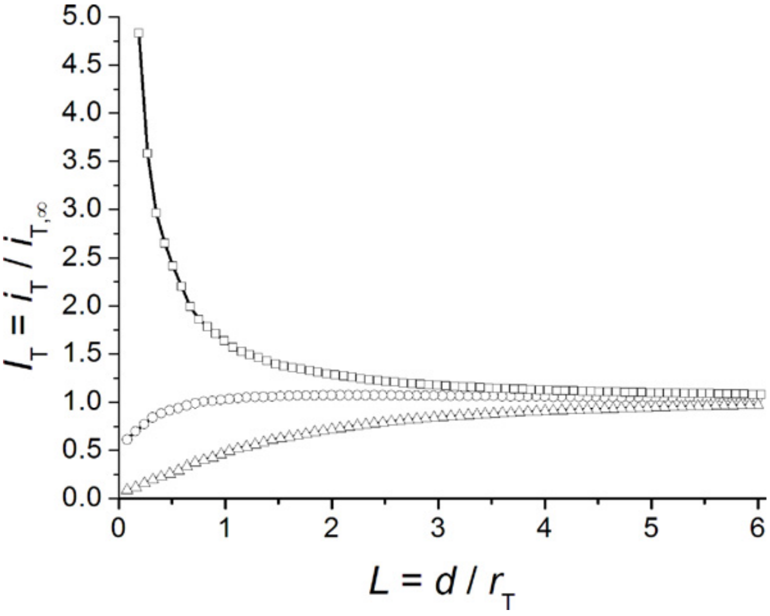

Figure 5. Normalized approach curves from Figure 3 towards an insulator (Δ), a surface with finite kinetics (○) and a conductor (□).

In Figure 5, the normalized currents from the measurements in Figure 3 are shown. Measured points after mechanical contact between probe and sample were cut. Approach curves are essential to determine the working distance. In this thesis, approach curves were used for several purposes. On the one hand they demonstrated the hindered diffusion and diffusion-controlled feedback mechanisms at the soft arrays of microelectrodes, and on the other hand they showed the point when the soft probes touched the surface and started to slide (Section 6.4).

Approach curves for feedback mode as shown in Figure 5 can also be simulated. A comparison of simulated and measured approach curves allows extraction of heterogeneous rate constants. Partial differential equations describe the diffusion of the mediator in the electrolyte solution between the UME and the sample and have to be solved numerically. For this purpose, different numerical methods are available.[96] For the simulations, assumptions have to be made concerning the electrochemical system under investigation. Because of this, the SECM system usually represents ideal geometries, *i.e.* a disk-shaped UME and an infinitely large flat substrate. Additionally, several boundary conditions have to be set. Over the past decade many attempts have been made to increase the accuracy and the application range of SECM simulations. However, these results are difficult to compare because the accuracy of the experimental SECM geometry, the accuracy of the numerical solutions and the accuracy of the analytical approximations of the discrete simulation results vary due to the degree of sophistication of the underlying simulation. In this thesis, no theoretical treatment of approach curves with the new soft linear arrays was performed and it is currently not recommended to apply them for the determination of rate constants for reasons that will be given in Section 6.4. A brief overview of the theory of feedback mode approach curves is given below because it represents an essential part of SECM understanding.

The two limiting cases of purely negative ($I_{\mathrm{T,ins}}$) and positive feedback ($I_{\mathrm{T,cond}}$) represent the most frequently simulated systems. The first approaches were calculated by Kwak and Bard.[69] Unfavorably, they used the steady-state current $i_{\mathrm{T},\infty} = 4\ n\ F\ D\ c^*\ r_{\mathrm{T}}$ for the current normalization, which is only valid for an imbedded disk, and they did not take into consideration the diffusion of the redox mediator from behind the UME insulation. More accurate are the simulations performed by Amphlett and Denuault who introduced the diffusion from the space behind the UME by expanding the simulation geometry to the region around the probe.[97] In reality, finite reaction rates are often obtained at the sample which results in approach curves that lie in-between the ones for positive and negative feedback. Eq. (6) was derived by Wei, Bard and Mirkin in order to describe this behavior with the boundary condition $0.1 \le L \le 1$.[98]

$$I_{\mathrm{T}}(L,\kappa) = I_{\mathrm{S,kin}}(L,\kappa)\left(1 - \frac{I_{\mathrm{T,ins}}(L)}{I_{\mathrm{T,cond}}(L)}\right) + I_{\mathrm{T,ins}}(L) \tag{6}$$

$I_{\mathrm{S,kin}}$ is the normalized current for finite substrate kinetics and the parameter κ represents a dimensionless heterogeneous rate constant for the redox mediator regeneration at the substrate (Eq. (7)).

$$\kappa = \frac{k_{\mathrm{eff}}\ r_{\mathrm{T}}}{D} \tag{7}$$

Data values from experimental approach curves can be fitted to the model and a value for κ can be extracted. With knowledge of D and r_{T} from independent experiments a first order heterogeneous rate constant k_{eff} can be calculated by using Eq. (7) [$k_{\mathrm{eff}} = \kappa\ D\ r_{\mathrm{T}}^{-1}$]. The kinetically controlled substrate current $I_{\mathrm{S,kin}}$ is normalized by dividing it by $i_{\mathrm{T},\infty}$. Eq. (6) is valid for $RG = 10$ and was originally developed for the investigation of electron kinetics and ion transfer at the liquid/liquid interface of two immiscible electrolyte solutions. The analytical approximations found by Amphlett and Denuault[97] can be used for $I_{\mathrm{T,ins}}$ and $I_{\mathrm{T,cond}}$. Analytical expressions were also found for $I_{\mathrm{S,kin}}$.[98]

The currently most popular model was presented by Cornut and Lefrou[96] and is more accurate. They developed an analytical approximate expression of feedback mode approach curves for a disk-shaped UME and finite irreversible kinetics at a sample.[96] Equation (8) describes the normalized current as a function of L, RG and the normalized heterogeneous rate constant κ.

$$I_{\mathrm{T}}(L,\kappa,RG) = I_{\mathrm{T,cond}}\left(L + \frac{1}{\kappa}, RG\right) + \frac{I_{\mathrm{T,ins}}(L,RG) - 1}{\left(1 + 2.47\ RG^{0.31}\ L\ \kappa\right)\left(1 + L^{0.006\ RG + 0.113}\ \kappa^{-0.0236\ RG + 0.91}\right)} \tag{8}$$

$I_{\mathrm{T,ins}}$ and $I_{\mathrm{T,\ cond}}$ are given by Eqs. (9)–(10).

$$I_{\mathrm{T,ins}}(L,RG) = \frac{\frac{2.08}{RG^{0.358}}\left(L - \frac{0.145}{RG}\right) + 1.585}{\frac{2.08}{RG^{0.358}}\left(L + 0.0023\ RG\right) + 1.57 + \frac{\ln RG}{L} + \frac{2}{\pi\ RG}\ln\left(1 + \frac{\pi\ RG}{2L}\right)} \tag{9}$$

$$I_{\mathrm{T,cond}}\left(L + \frac{1}{\kappa}, RG\right) = \alpha(RG) + \frac{\pi}{4\beta(RG)\arctan(L)} + \left(1 - \alpha(RG) - \frac{1}{2\beta(RG)}\right)\frac{2}{\pi}\arctan(L) \tag{10}$$

α and β stand for

$$\alpha(RG) = \ln 2 + \ln 2\left(1 - \frac{2}{\pi}\arccos\left(\frac{1}{RG}\right)\right) - \ln 2\left(1 - \left(\frac{2}{\pi}\arccos\left(\frac{1}{RG}\right)\right)^2\right) \tag{11}$$

$$\beta(RG) = 1 + 0.639\left(1 - \frac{2}{\pi}\arccos\left(\frac{1}{RG}\right)\right) - 0.186\left(1 - \left(\frac{2}{\pi}\arccos\left(\frac{1}{RG}\right)\right)^2\right) \tag{12}$$

Cornut and Lefrou proved that Eq. (8) can be used for all κ and for $L \geq 0.1$ with $RG \leq 20$ with an error below ±0.025. Eq. (8) is also valid for the limiting cases of purely insulating or conducting substrates when κ approximates 0 and ∞, respectively. Figure 6 shows calculated approach curves using Eqs. (8)-(12) for different κ. The plot includes different reaction rates as well as the theoretical data for diffusion-controlled feedback ($\kappa \rightarrow \infty$) and hindered diffusion ($\kappa = 0$).

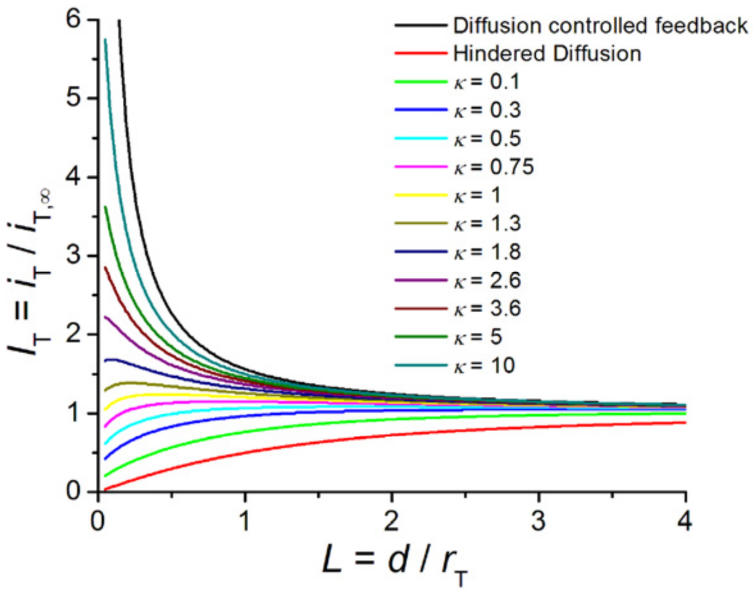

Figure 6. Calculated SECM feedback mode approach curves for diffusion-controlled feedback, hindered diffusion and kinetically controlled feedback reaction on a substrate for kinetically uncomplicated reaction with apparent first order rate law. The approach curves were calculated according to the approximations by Cornut and Lefrou.[96]

Simulations also allow determining the influence of parameters such as the RG value. The larger RG the smaller is the I_T at a given L (Figure 7). This dependence is much stronger for approach curves over insulators than over conductors. From theory, the current contrast between positive and negative feedback at a given *L* is much higher using large *RG* in order to distinguish insulating and conducting parts. Practically, the UME is hardly positionable in the UME holder in a way that it is perfectly aligned to the substrate. A minimum angle with respect to the surface normal leads to mechanical contact between the insulating sheath and the sample surface (Figure 4). This causes a positional offset which becomes larger with increasing *RG*. Hence, the theoretical advantage of a large *RG* turns into a practical disadvantage. In addition, the fabrication of UMEs with a defined size of active electrode area and glass sheath is challenging. Also the metal wire is often not centrically located in the glass sheath. Mechanical polishing can lead to a recess of the active electrode area.

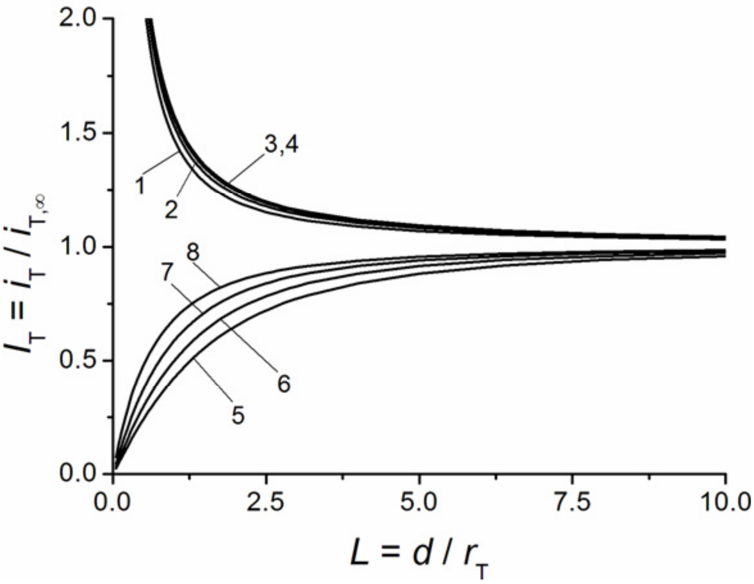

Figure 7. Simulated SECM feedback mode approach curves for diffusion-controlled feedback (curves 1-4) and hindered diffusion (5-8) for *RG* values of 20 (curves 1 and 5), 10 (2 and 6), 5 (3 and 7) and 2.5 (4 and 8). The approach curves were calculated according to the approximations by Cornut and Lefrou.[96]

As mentioned above, local reaction rates at the sample can be extracted by fitting experimental approach curves to simulated ones. These data are usually not accessible by other experimental techniques. On the other hand fitting can be used to extract important probe parameters as the *RG* value using Eq. (8). This can become important for small *RG* values and pipette-based probes. All these aspects make the approach curves an essential and important experiment for many SECM applications. In addition, it is required to select defined working distances for reactivity mapping. Nowadays, also experimental data for even more complicated situations can be simulated. For example, the conversion of an electrochemically detectable compound at an enzyme-modified substrate can be described by the Michaelis-Menten kinetics and corresponding approach curves have been calculated.[99-101]

2.3 Generation/Collection Mode

The generation/collection (G/C) mode using amperometric UME relies on the generation of a redox-active species at the UME or at an active site of the sample and the detection ("collection") of this compound at the opposing electrode.[6, 73] Therefore, both UME (i_T) and sample (i_S) measure a specific current. Two different modes of the G/C principle exist: the tip-generation/sample-collection (TG/SC, Figure 8a) mode and the sample-generation/tip-collection (SG/TC, Figure 8b) mode. Typical applications of the G/C mode are the screening of electrocatalysts for the oxygen reduction reaction using the TG/SC mode [102, 103] and SG/TC mode,[104, 105] but also the oxygen evolution reaction in SG/TC,[26] in the research of materials for fuel cells, biofuel cells and metal-air batteries.

In the TG/SC mode, the active area at the substrate is usually significantly larger than the UME. This ensures a collection efficiency $\Theta = i_S/i_T$ of 1 (= 100 %) for a stable species which has been formed at the UME. Alternatively, this UME-generated species can react in a homogeneous follow-up reaction. Depending on d, Θ becomes smaller and the rate constant of the homogeneous reaction can be determined.[106]

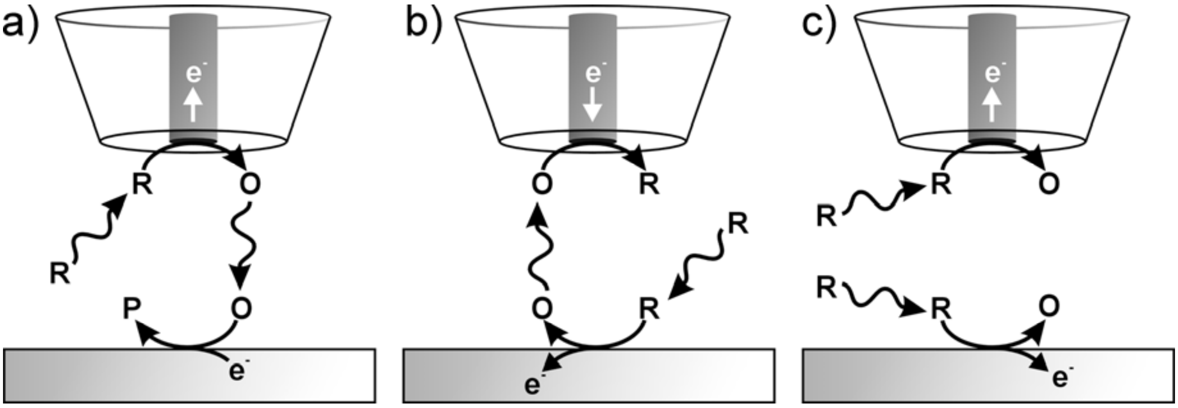

Figure 8. Schematic representation of the TG/SC mode (a), the SG/TC mode (b), and the RC mode.

In general, the G/C mode has a smaller resolution but higher sensitivity than the feedback mode. An alternative to the amperometric modes is the so-called potentiometric G/C mode where potentiometric probes are utilized.[88]

2.4 Redox Competition Mode

In the redox competition mode (RC, Figure 8c), both UME and sample compete for the same redox-active analyte in the solution. The RC mode was first introduced in a double potential step experiment by Eckhard *et al.*[76] in order to investigate electrocatalysts for the ORR. In an initial pulse, O_2 was generated at the UME and in a second pulse, the UME as well as the sample competed for this electrogenerated oxygen. The smaller the UME current, the more active is the substrate at this position for the ORR. Pulsing was required because a continuously applied potential would deplete the gap between UME and sample of O_2. A potential-pulse sequence mode was developed to distinguish between the two-electron and the four-electron pathway in the ORR.[107]

A so-called continuous RC mode (constant potential at tip and sample) was reported by Nogala *et al.*[108] They investigated the activity of the immobilized enzyme laccase. UME and enzyme competed for a quasi-reversible redox couple which was reduced at the enzyme in presence of O_2. A significantly lower noise was reported compared to the potential pulse RC modes.[108] In this thesis, the continuous RC mode was used in order to investigate the catalytic activity of electrocatalysts for hydrogen peroxide decomposition (Section 8.3).

2.5 Custom-Made SECM Instrumentation and Software

The SECM instrumentation developed by Wittstock and coworkers is based on the general idea of the utilization of in-house made generic software in order to control very flexibly a large number of various exchangeable hardware components to perform standard and specialized SECM experiments. Currently, the software runs on six fixed workstations and overall 27 hardware components can be operated. Several positioning systems with various resolutions as well as different (bi)potentiostats with sensitivities up to picoampere are used for specific experimental goals like the detection of biochemical functionalities. In order to investigate the local dye regeneration of a dye sensitized solar cell (DSSC) the illumination of the sample under study is controlled with a potentiostat-powered LED to control the light intensity with a small fixed wave length range.[109] An electronic tilt table allows the horizontal alignment of a sample after experimental determination of the tilt angles. An SECM can be built up very easily and fastly with a laptop, potentiostat, positioning system and electrochemical cell. Some SECM components can be mounted onto inverted optical and confocal laser scanning microscopes allowing time-resolved optical and fluorescence based inspections.

The SECM software concept reflects the connectivity of the hardware components. This is realized by a main application in order to control experimental parameters, data acquisition, data visualization and data storage, and by a so-called hardware abstraction layer (Figure 9).

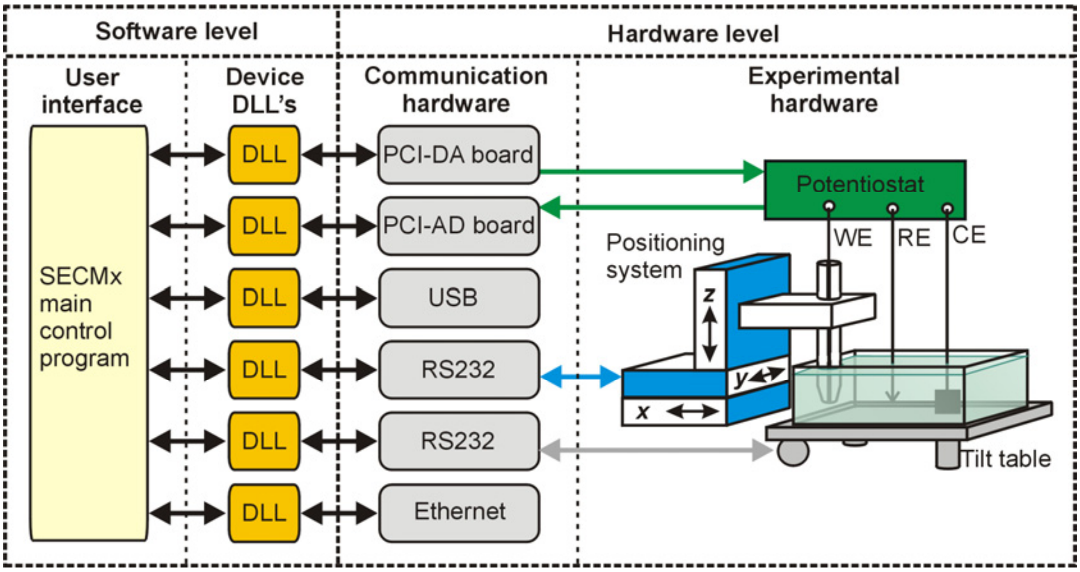

Figure 9. General block diagram of SECMx concept. The software is based on a experimental level (yellow) and a hardware abstraction layer (DLLs, orange). The main application controls the communication between the software and the devices via the DLLs.

A hardware abstraction layer is programmed individually for each device as dynamic link library (DLL, extension ".dll"). The DLLs are separated from the main program and can be individually installed, exchanged or deleted. For a certain SECM setup, the software will load only the DLLs for selected and physically present devices. By replacing one single hardware component and its associated DLL the system can easily be operated without changing the software. Analog, serial and digital communication ways between the main program and the operating hardware components are implemented. Some devices require loading of their own drivers during runtime. In SECMx, they are preferably transformed into static libraries (LIB, extension ".lib") which are included in the specific SECMx DLL's. Only in few exceptions dynamical loading of third party executable code is applied. Each kind of measurement device useful for SECM can be added by construction of a DLL and some minor changes in SECMx.

The development of the SECM operation software which is currently running under the fifth version was started and expedited by Prof. Wittstock. Former and current group members took part and take part in the further development of algorithms and program code. At present SECMx is written in C++ programming language using the C++ Builder Professional 6.0 from Borland Software Corporation (taken over from Micro Focus, Rockville, USA). C++ is an object-oriented programming language. This means that data objects are considered as the central point of the program development so that the functionality of the program is bound to the given data structure. The objects are defined as classes allowing the concept of inheritance and multiple inheritance which is the constitutively derivation of similar object classes from base classes. Due to a generic programming style, all devices can be used for existing experiments like cyclic voltammetry, chronoamperometry, line scans, approach curves or imaging. For each device, “channels” were defined in order to send “read”- and “write”-commands. These channels were classified depending on their communication way in analog (“AD”, ”DA”) and digital (“In”, “Out”). During the course of this thesis, the author took actively part in the development of the main application and in the integration of new hardware, such as potentiostats and positioning systems from different companies (Ivium, Gamry, Bio-Logic, Zahner, Physik Instrumente). Examples will be given in Sections 6.2, 6.5.1, and 7.1.4 and in Chapter 9.

3 Localized Structuring of Surfaces

The localized modification of surfaces in microscale finds versatile applications including the electronics industry, combinatorial catalyst research,[24, 110] and biotechnology.[111] Commonly utilized techniques to create well defined microstructures can be divided into static (photolithographic[112] or softlithographic techniques[113]) and dynamic tools (SPMs, inkjet[30, 114] and Aerosol Jet® printing[115, 116] or UV laser ablation[117, 118]). The former rely on pre-fabricated fixed masks or stamps with defined patterns whereas the latter take advantage of flexibly movable components. The modification of surface films can be of destructive (*e.g.* etching) or constructive nature (*e.g.* deposition of functional materials).

Photolithography is very important and most often used for the batch production of microchips in the electronic industry.[119] A substrate is coated with a light-sensitive surface (usually a photoresist) and locally transformed by illumination with UV light through a metallic mask (*e.g.* making the surface material soluble, insoluble or inducing a photochemical reaction). Afterwards, a suitable solvent is used to remove selectively the modified or unmodified organic films from the surface leaving the desired structure on the substrate. The technique has to be performed in a clean room and a problem can arise when surface films are intolerant against the illuminated UV light or the used solvents. An alternative approach to modify surfaces under milder conditions is softlithography including microcontact printing (µCP) where a polymeric stamp with a defined microstructure transfers a compound onto a substrate.[113] µCP was used in this thesis to create square-pattern of a SAM on a thin gold film (Section 7.1.2).**[A8]** The stamp is usually prepared by casting the polymer precursor on a photolitographically prefabricated master. Photolithographic techniques are expensive in particular for small and medium quantities; due to their dependence on masks and clean room facilities. In photolithography as well as in µCP (for the preparation of the stamps), a new mask for each new desired pattern is required.

In scanning probe techniques, such as ECSTM,[120] SFM,[121-123] dip-pen nanolithography (DPN)[124] or SECM,[125] the probe acts as a “pen” that allows to “write” patterns with high spatial resolution by the controlled lateral translation of the probe over the surface.

However, ECSTM, SFM and DPN usually use nanometer sized tips and create nanopatterns whereas structures in microscale or larger are difficult to achieve due to extremely long processing times. Furthermore, they are suitable for removal or deposition of materials but not for chemical/electrochemical transformation of surfaces as achievable by SECM. The modification of surfaces induced by SECM is discussed in detail in the following section.

3.1 Surface Modification Induced by SECM

SECM has been used since its inception as a tool for local surface modification using different modes like the direct mode,[17] feedback mode,[15] tip-generation/sample-collection mode,[126] or the surface interrogation mode.[18] The range of applications increases continuously and includes the etching of semiconductors[127-130] and metals,[15] the deposition of polymers[131-133] and metals,[134, 135] the modification of self-assembled monolayers,[17, 18, 136] and the deactivation of immobilized enzymes.[16] The deposition of organic films is often also called local electrografting.[19, 130] One big advantage of SECM relies on the template-free performance and the *in situ* induced chemical modification. It can perform surface transformations that are often not accessible by alternative methods. In general, the performed modification is irreversible and, due to the changed surface reactivity, SECM can be used not only for surface structuring but also for subsequently monitoring the result. Etchants can be generated at the UME from precursors and can react directly with the substrate or they can locally disturb an established heterogeneous equilibrium.[137] Defined patterns can be created by moving the UME laterally close to the surface while generating the active compound. Due to the large number of applications in this field, only a brief overview of the UME-induced surface modification modes can be given herein. The direct mode and the feedback mode are mainly used and are shown schematically in Figure 10.

The local surface modification induced by SECM in direct mode was preliminary developed by Bard and coworkers and still finds applications.[130, 138] In a two electrode arrangement, the UME acts as the working electrode and the sample as the counter electrode (Figure 10a). This causes opposite but equally large currents at both electrodes. The deposition or dissolution is localized due to the confined distribution of the electric field between UME and substrate. For high resolution the working distance has to be kept significantly small. Examples for the localized modification by the direct mode are the photoetching of n-GaAs,[139] the deposition and etching of metals,[75, 138] the deposition of submicrometer structures of Ag[140] and Cu.[141] Remarkable are the experiments performed by Schuhmann, Kranz and coworkers[142, 143] who used pulse experiments to deposit conducting polymers. They applied pulses for the deposition instead of a continuous potential in order to periodically renew the concentration of monomers in the inter-electrode gap up to a sufficient level. Potentiostatic reduction (*i.e.* no pulses) of the monomer completely depleted this compound in the gap between UME and sample and consequently no deposition took place. Interesting efforts were also demonstrated to pattern surfaces with organic molecules and biomolecules.[144-146] Alkane thiolates forming a SAM on Au are desorbed from the surface at negative potentials whereas they are oxidatively decomposed at positive potentials. [147] If a second thiol or disulfide like cystamine is present in the electrolyte solution, a directed self-assembly of this compound on the just exposed bare Au surface is carried out.[17]

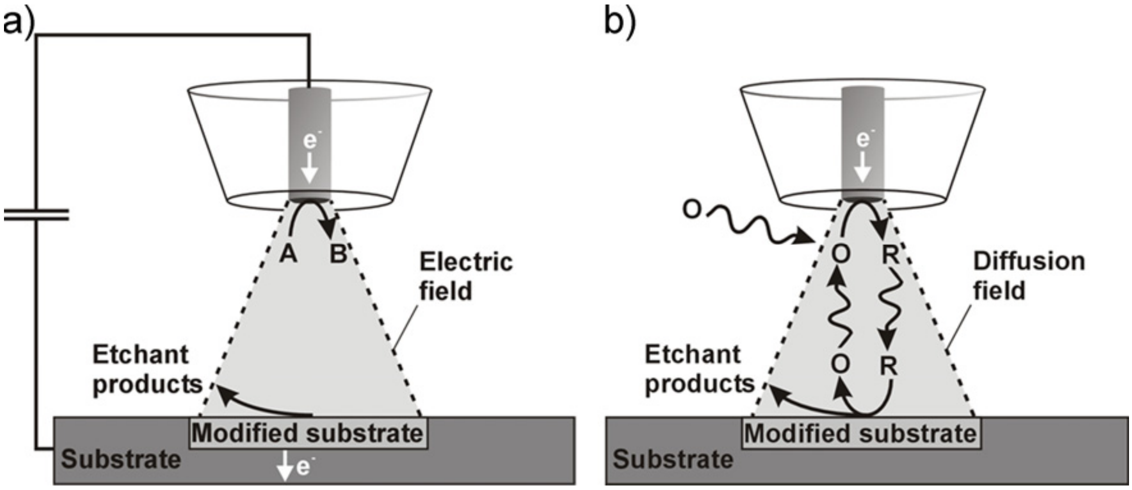

Figure 10. Schematic representation of local surface modification using SECM. The surface in the schemes is etched, but also deposition is possible. a) Direct mode: the modification relies on the electric field. b) Feedback mode: a chemically active compound is generated at the UME and diffuses to the substrate where it transforms the surface.

In the general feedback mode, a chemically active species is electrogenerated at the UME which diffuses to the substrate enabling well-defined surface transformations as shown schematically in Figure 10b. The rate of modification can be controlled quantitatively by the electrolysis current at the UME, the time of etchant generation and the working distance between sample and UME.[18, 125, 148, 149] In most cases the working distance is smaller than the radius r_T. The time of the potential pulse to generate the etchant influences the amount of produced active species and the size of the diffusion layer. The dimensions of modified regions are also given by the geometry of the active UME area. In case of arbitrary UMEs the modified surface areas will have the negative shapes of the UMEs.[128] The modification is more efficient as closer the active UME is positioned to the surface films. However, the thermodynamics and kinetics of the electrochemical process at the surface will influence the modification and can become a rate-limited step. The surface coverage of the unreacted (non-modified) surface molecules/atoms on the surface after performed modification may increase from the inside to the outside of the modified region.[18] The spreading and sharpness of the border between modified and unmodified regions can be regulated by adding a scavenger to the electrolyte solution.[133, 150, 151] This scavenger is a compound that cannot be consumed at the sample surface and UME but is chemically active to react homogeneously with the reactive etchant formed at the UME. In this way a so-called "chemical lens" is formed that limits the expansion of the diffusion layer and, as a consequence, it sharpens the transition from the modified to the unmodified region.[133, 150, 151] The working distance can be controlled simply by SECM approach curves using a redox mediator whose redox states are inactive for the sample surface. The electrogenerated compound and its stability during the diffusion from the UME to the substrate as well as its chemical reactivity play an important role in the modification of surfaces.

The first modifications in feedback mode were reported by Mandler *et al.*[15] for the deposition and etching of metals. They etched Cu by electrogenerating strong oxidants such as $Fe(phen)_3^{2+}$ and $Os(bpy)_3^{2+}$ (phen = 1,10-phenanthroline, bpy = 2,2'-bipyridine). In further developments, a flux of metal ions generated at the UME could be formed where the UME acts as sacrificial electrode. The UME was used like a pen for "microwriting" Ag,[134, 152] Au[153, 154] or Ni[155] microstructures on various substrates.

Among general etchants, Br_2 is particular versatile and often used for surface transformations. This reactive molecule can be electrochemically generated by the oxidation of bromide (Eq. (13)).

$$2\,\mathrm{Br}^- \rightarrow \mathrm{Br}_2 + 2\,\mathrm{e}^- \tag{13}$$

An overview about surface modifications using Br_2 as etchant is given in Table 2. First, Mandler and coworkers[148, 149] electrogenerated bromine at the UME and described the probable effect on the etching of GaAs and Si surfaces. However, the mechanism was not completely understood. Almost at the same time, Shiku *et al.*[16] reported hydrobromous acid HOBr as etchant, generated by the disproportionation of the probe-generated Br_2 in alkaline or neutral solutions into hydrobromic acid HBr and HOBr.

$$\mathrm{Br}_2 + \mathrm{H}_2\mathrm{O} \rightarrow \mathrm{HBr} + \mathrm{HOBr} \tag{14}$$

Both Br_2 and HOBr are strong oxidants and can be used for the transformation of various surface films such as the deactivation of enzyme molecules immobilized at a surface.[16] The reaction with a substrate is usually of destructive nature (etching, deactivation). Similar to the "chemical lens" reported by Borgwarth *et al.*,[133] Tian and coworkers[156-160] described a so-called confined etchant layer technique (CELT) in order to improve the etching resolution of Si and GaAs by Br_2. The expansion of the diffusion layer was limited by the introduction of arsenic acid H_3AsO_3 as scavenger (Sc) which reacted with the electrogenerated bromine. The difference between "chemical lens" and CELT is given by the fact that the scavenger in the latter system can also be consumed at the UME limiting the focusing effect. Tian and coworkers[156] developed an equation to calculate the thickness of the diffusion layer μ_D

$$\mu_\mathrm{D} = \left(\frac{D_{\mathrm{Br}_2}}{k_\mathrm{Sc}} \right)^{0.5} \tag{15}$$

where k_Sc is the pseudo first-order reaction rate constant of the reaction H_3AsO_3 with Br_2 and D_{Br2} the diffusion coefficient of Br_2.

Table 2. Overview about surface modifications induced by electrogenerated Br_2.

Application	**Ref.**
Etching of GaAs	[128, 161]
Deactivation of enzyme layers	[16]
Etching of Silicon	[149, 162]
Etching of Silicon with confined etchant layer technique (CELT)	[156-158]
Etching of GaAs with CELT	[156, 159, 160]
Deposition of conducting polymers	[133]
Oxidation of bovine serum albumin (BSA)-coated glass slides	[163]
Modification of oligo(ethylene glycol)(OEG)-terminated SAM	[67, 94, 164][**A8**]

Borgwarth *et al.*[133] created patterns of conducting polymers by SECM. Br_2 was electrogenerated at the UME and caused a transformation of various solid surface films. Briefly worded, polymers were transformed from its non-conductive into its conductive state or a polymer was locally deposited by the oxidation of its monomer. The group continued their work with other systems and reagents.[131, 165, 166] Kaji *et al.*[163] activated cell-repellent bovine serum albumin (BSA) layers with electrogenerated Br_2/HOBr to control living cell adhesion and migration. Wittstock and coworkers[67, 94, 164][**A8**] modified oligo(ethylene glycol)(OEG)-terminated SAMs by probe induced oxidation using the same reagent as Kaji *et al.*[163] The modification enabled the local etching of ethylene glycol groups allowing the spatially controlled adsorption of proteins, cells and bacteria.[67, 94, 164] In this thesis, the local modification of an OEG SAM by Br_2/HOBr is performed using soft array probes and is discussed in Section 7.1.3.

Also other attractive developments in the surface modification induced by SECM were made with alternative reagents. An important micropatterning application is the localized reduction of halogenated polymers such as poly(tetrafluoroethylene) (PTFE) into a carbon material as introduced by Combellas *et al.*[167-169] and Kanoufi *et al.*[170] Radical anions (*e.g.* from benzonitrile) were electrogenerated at the UME and carbonized the PTFE film. The modified regions showed for example a different wetting behavior.[170, 171] Electroless metal deposition[167] and graft copolymerization[169] were achieved as further modification steps.

Very interesting is also the localized patterning of fluorescence active molecules onto solid substrates by “click”-chemistry as introduced by Ku *et al.*[172] Cu(I) was generated at the UME by reduction of Cu(II) salen and catalyzed the formation of acetylene fluorophore derivates onto a glass substrate.

The patterning of organic mono- and multilayers on metal and carbon surfaces can be carried out by an aryldiazonium salt which is reduced at the substrate and covalently bonded to the substrate surface under the release of nitrogen in the SECM TG/SC mode as presented by Cougnon *et al.*[19, 151] In the presence of $NaNO_2$ and HCl, the aryldiazonium salt can formed *in situ* in a homogeneous reaction from an aryl amine which has been generated at the UME by the reduction of an aryl nitro precursor. Kongsfelt *et al.*[126] protonated aryltriazenes in order to form aryldiazonium salts. The acidic environment was created by oxidation of *N,N*’-diphenylhydrazine at the UME. SECM was also used to create patterns of reactive spots by local electrografting of poly-N-succinimidyl-acrylate onto conducting surfaces. These reactive spots may be post-functionalized with molecules having amines or other nucleophilic groups, such as proteins and enzymes.[173]

More recently, Hapiot and co-workers[174, 175] found that highly reactive oxygen species, mostly the very reactive hydroxyl radical $OH^{\bullet}$, can be formed easily by the reduction of oxygen at a Pt-UME and they can remove locally organic thin films.

3.2 Inkjet and Aerosol Jet® Printing

Other microfabrication techniques are for example inkjet[176] and Aerosol Jet®[115] printing which are based on the controlled maskless release of an ink or aerosol, respectively, through a printhead and find application in flexible electronics,[177] solar cell production[178] and the manufacturing of immunosensors.[179] Various special inks containing functional materials like nanoparticles[177, 180] or biomolecules[30, 180] can be printed onto substrates with comparable dimensions of the microstructures. 2D as well as 3D structures can be created. Both techniques are less expensive, less time consuming and allow high substrate flexibility compared to *e.g.* photolithography. This led to a noticeable increase in applications during the past decade. However, the basic principles of inkjet and Aerosol Jet® printing differ as shown schematically in Figure 11.

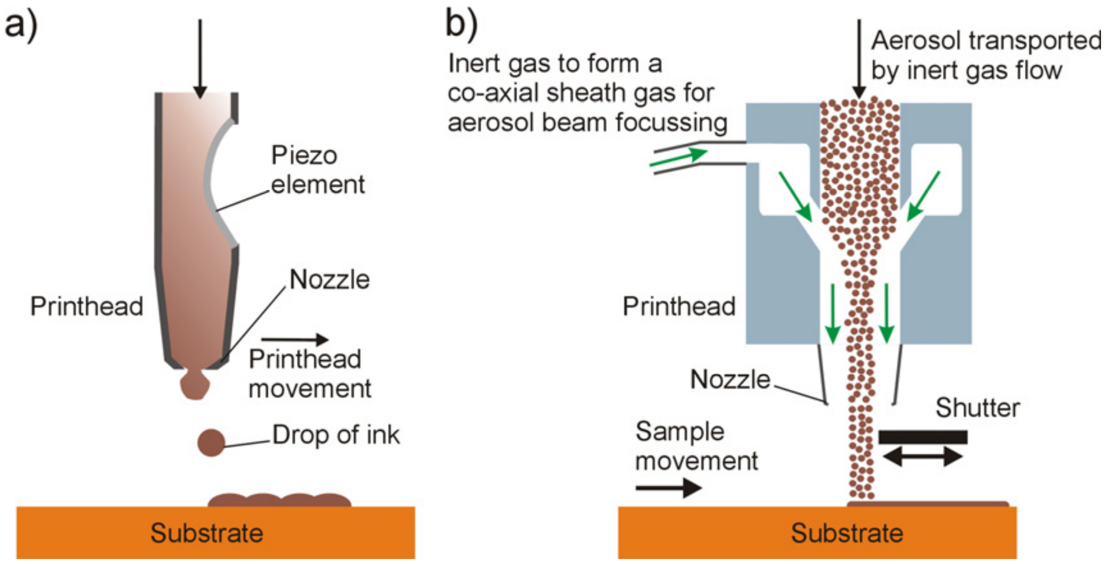

Figure 11. Schematic representation of drop-on-demand inkjet (a) and Aerosol Jet® printing. Figure 11a adopted from Ref. [176] and Figure 11b adopted from Ref. [180].

In inkjet printing, defined drops are released either by continuous inkjet (CIJ; continuous release of drops that has to be interrupted if desired) or drop-on-demand techniques (DOD; directed release of drops if desired, Figure 11a). For Aerosol Jet® printing, an aerosol is generated by an ultrasonic transducer or a pneumatic nebulizer depending on the viscosity of the ink. The volume of the drops in the aerosol is about three orders of magnitude smaller than for inkjet printing and a much broader range of viscosities and hence a larger variety of inks can be used (Table 3). The aerosol is carried by an inert gas stream into the printing module, where a co-axial flow of the aerosol stream forms an enclosing sheath gas stream to focus the aerosol beam. Because of the co-axial focusing, printing on planar and also on non-planar substrates is possible by a nozzle-substrate distance of up to 5 mm. A shutter is installed to interrupt the continuous aerosol flow.

Table 3. Comparison of parameters and ink properties for inkjet and Aerosol Jet® printing. Values adopted from Ref. [180].

Technique	Drop volume	Drop diameter	Viscosity
DOP inkjet	60 pL	50 µm	3-20 mPa·s
Aerosol Jet®	60 fL	1-5 µm	0.7 – 1000 mPa·s

In this thesis, inkjet and Aerosol Jet® printing were used to fabricate new types of soft microelectrode arrays (Sections 6.3.3 and 6.3.2, respectively).[181][**A6**]

3.3 Ultraviolet Laser Ablation

Ultraviolet (UV) photoablation can also be used for microstructuring surfaces. In this section, a brief overview about UV laser ablation of polymeric materials is given. For a detailed description, the reader is directed to Ref. [182]. UV photoablation involves the absorption of short-duration laser pulses in the UV region that can rapidly break chemical bonds (photochemical ablation) and/or melt the material (thermal ablation) within a restricted volume of a polymer, followed by an ejection of decomposed polymer fragments.[117, 183] UV laser ablation can be used to fabricate microholes and microchannels.[117, 183, 184] In this thesis, an excimer (abbr. for "excited dimer") laser was used to fabricate microchannels in PET films (Section 6.3.1). Excimer lasers use a mixture of a reactive gas, such as F_2, and an inert gas, such as Ar or Kr. By an electronic excitation a short-life dimer molecule is formed which emits UV radiation. The wavelength depends on the used compounds and pulse lengths are usually between 10 ns to 40 ns.[182]

The removal of material by UV photoablation starts with a single- or multiphoton excitation of the material.[182] In the thermal ablation model, the excitation energy is transformed into heat and causes vaporization of the material with or without melting of the surrounding material. Alternatively, the increase in temperature can induce stress to the material followed by an explosive ablation. Photochemical ablation is caused when the excitation energy is high enough to directly break chemical bonds of the polymer, followed then by desorption of the fragments. In an indirect path, the photochemically dissociated bonds can also induce stress to the materials which at the end results in a mechanical ablation. Both models can participate in the laser ablation process. This process is called photophysical ablation in which thermal and photochemical ablation can be considered as limiting cases.

Figure 12, left panel, shows the electronic energy scheme of an organic polymer.[182] S_0, S_1, … denote singlet states and T_1, T_2, … triplet states. D_1, D_2, … represent defect states including broken chemical bonds. Between these different energy states radiative and non-radiative translations can take place.

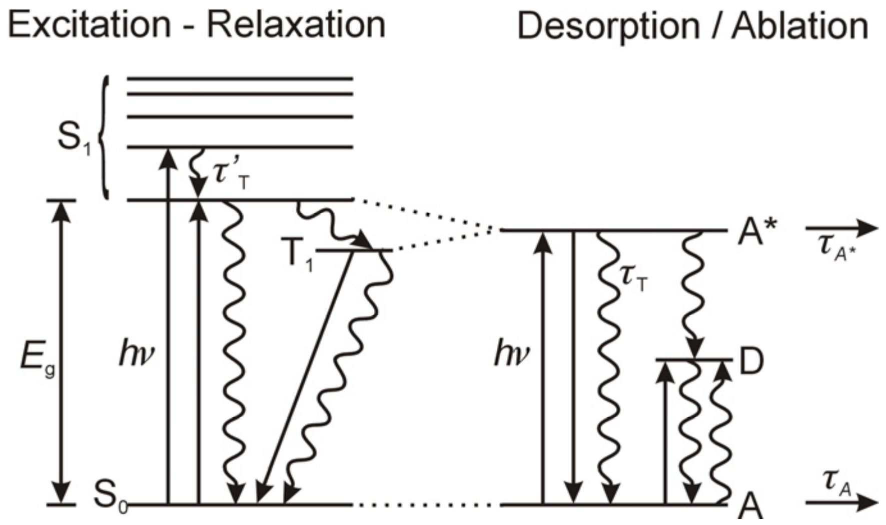

Figure 12. Schematic representation of the photophysical model describing the electronic states of the material (left panel) and by two states A and A* (right panel). Different types of excitation and energy relaxation of the material are shown. The absorption or emission of photons is indicated by straight lines and the non-radiative transitions are represented by oscillating lines. Adopted and modified from Ref. [182].

UV radiation can induce single- or multiphoton interband transitions ($S_0 \rightarrow S_1$, $S_0 \rightarrow S_2$) but also excite or generate defects. The latter become in particular important when the energy of the photons $h\nu$ is smaller than the band gap energy E_g of the material. Non-radiative transitions between different energy bands are characterized by a thermal relaxation time τ_T. The desorption of the organic polymer can be explained by a simplified ablation scheme demonstrating the photophysical model for a three-level system (Figure 12, right panel).[182] Considering this model, where A represents the ground state and A* the intrinsic electronically excited states, the photoablation depends on the relationship between τ_T and the relaxation times τ_A and τ_{A*} which represent the time for initiating a process such as a thermal or chemical reaction.[182] Excitation mechanisms become irrelevant and the energy is immediately transformed into heat (thermal process) when τ_T

$<< \tau_{A*}$ and $\tau_A << \tau_{A*}$. In contrast, the process is mainly photochemically affected when $\tau_T > \tau_{A*}$ and $\tau_{A*} << \tau_A$. If all three times are comparable or if $\tau_T << \tau_{A*} << \tau_A$, the photophysical process takes place.[182] Figure 12, right panel, shows a schematic representation of D describing defect states generated by the UV laser-light. Assuming a model in which the material removal is dominated by thermal "desorption" of the species related to the ground state, the total ablation velocity υ_{la} is described by Eq. (16):

$$\upsilon_{\mathrm{la}} \approx \upsilon_{\mathrm{A}} N_{\mathrm{A}}^{*}(0) + \upsilon_{\mathrm{A*}} N_{\mathrm{A*}}^{*}(0) + \upsilon_{\mathrm{D}} N_{\mathrm{D}}^{*}(0) \tag{16}$$

where υ_{i} represent rate constants for thermally activated desorption and N_{i}^{*} are the normalized number densities of the states i.

The change of layer thickness Δh can be expressed as

$$\Delta h = l_{\alpha} \ln\left(\frac{\phi}{\phi_{\mathrm{th}}}\right) \tag{17}$$

where l_{α} is the optical penetration depth, ϕ the laser fluence and ϕ_{th} the threshold fluence that is the minimum energy required for photoablation of a specific material. From Eq. (17) it can be concluded that the most effective laser ablation is achieved using materials with small ϕ_{th} and large l_{α}. The heat diffusion length l_{T} represents another intrinsic parameter influencing the ablation process. Materials with small values like PET ($l_{\mathrm{T}} = 90$ nm) concentrate the heat more easily as *e.g.* Al ($l_{\mathrm{T}} = 2.80$ µm) and are easier photoablated.[182]

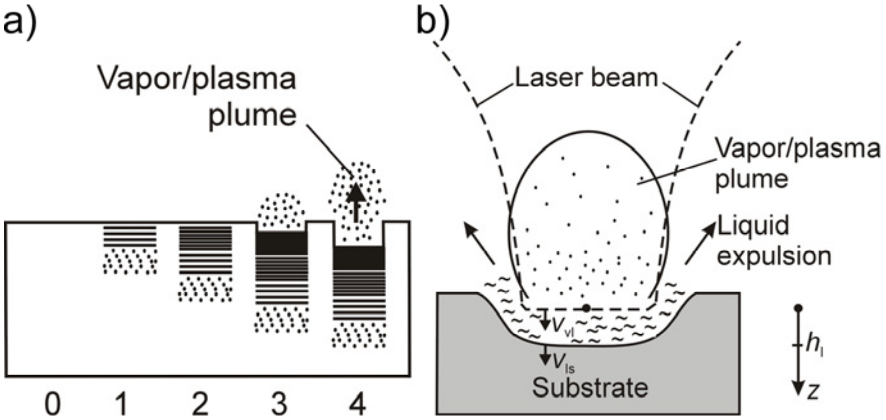

Figure 13. a) Scheme of the increase in absorption with successive laser pulses. a) Scheme of laser-induced surface melting, vaporization, and liquid-phase expulsion. (a) and (b) adopted and modified from Ref. [182].

Successive laser pulses increase the absorptivity within the irradiated volume as shown schematically in Figure 13a. This increase in energy absorption causes a decrease of ϕ_{th}. If ϕ is close to ϕ_{th}, the ablation starts after some pulses and a stationary condition can be achieved.[182] Plasma formation can take place as shown schematically in Figure 13b. Energy from the UV light can also be absorbed by the plasma followed by a possible transfer to the material.[182]

4 SECM Limitations, Developments and own New Concept for the Investigation of Extended Surfaces

SECM suffers some drawbacks when it is used for scanning big surface areas. In this chapter, a discussion about these problems is provided and several approaches to overcome them are reviewed.

4.1 Overview about SECM Limitations

Two major limitations arise for SECM imaging when investigating large samples approaching square centimeter. Firstly, possible solvent evaporation, sample aging,[185] and electrode fouling[25, 186] may occur if the experimental duration goes into a critical value. The measurement time in SECM can easily exceed some hours and it is related to the fact that the recorded current at the UME depends on the diffusional mass-transport associated with the time $t_{SS} \approx r_T^2 \cdot D^{-1}$ which is required until the steady state is reached.[187] Supported by digital simulations it was demonstrated that probe movements v_T faster than 10 µm s^{-1} (in dimensionless form $v_T \cdot r_T \cdot D^{-1} \geq 0.06$) can already perturb the current response due to convection.[92] Therefore, the probe is usually moved not faster than 25 µm s^{-1} in order to keep convectional disturbances negligible. Electrochemical signals have to be filtered, among other things to eliminate noise. This needs time and limits the frequency of data acquisition and thus translation rates. Scanning an area of 4 mm × 4 mm needed 35 h using conventional SECM parameters (v_T = 25 µm s^{-1} and step size 10 µm) for recording a squared grid of 160,801 data points in feedback mode (Figure 14a). The sample consisted of microcontact printed square-patterns of a SAM made of hexadecanethiol on gold. A current contrast in feedback mode imaging in aqueous solution was obtained due to a reduced permeability for the redox mediator ferrocenyl methanol (FcMeOH) through the SAM. This decreases the current compared to positive feedback over bare gold. During this experiment solvent evaporation became evident and it is indicated by a continuous increase of the current for positive feedback of approximately 100 % from the first line scan (y = 0 mm, i_T = 11.0 nA) to the last line scan (y = 4 mm, i_T = 21.2 nA). The effect is due to the increase of the electrolyte concentration and becomes worse when using rapidly evaporating organic solvents. As a consequence, dissolved compounds could precipitate on the sample as well as on the UME. Continuous refilling of the solution as an approach to overcome this problem is unpractical and it is almost impossible to keep the concentration of dissolved compounds constant. Also the probe translation rate for the modification of surfaces can be limited when the process is diffusion-controlled. Furthermore, limited reaction rate at the surface to be modified can require slow probe translation rates.

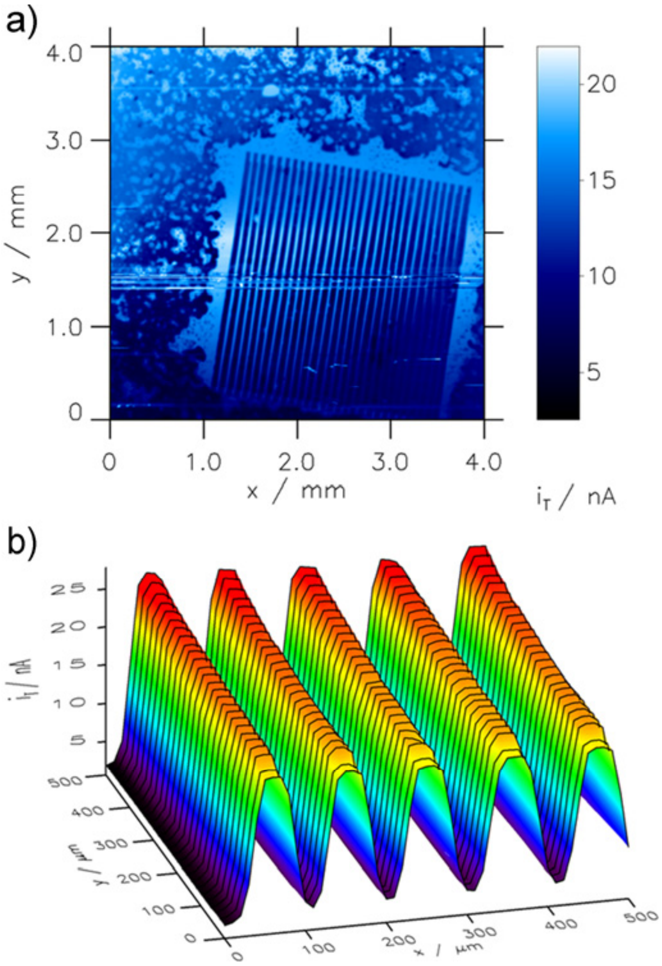

Figure 14. Limitations in SECM imaging using a conventional Pt UME (r_T = 12.5 µm, d = 3 µm). Feedback image of a 4 mm × 4 mm area covered with square-patterns of SAM on gold (a); UME translation rate v_T = 25 µm s^{-1} (rev 100 µm s^{-1}); step size in *x*- and *y*-direction 10 µm. b) Feedback image of a gold band structure on glass with a sample tilt in *y*-direction on a 500 µm scale. UME translation rate v_T = 20 µm s^{-1} (rev 20 µm s^{-1}); step size in *x*- direction 10 µm and in *y*-direction 20 µm. Electrolyte solution 2 mM FcMeOH in 0.1 M aqueous KNO_3.

The other problem is related to the strong dependence on the working distance *d* of the SECM signals (compare approach curves in Figure 6). In order to distinguish local variations in surface reactivity – *i.e.* changes in the dimensionless reaction rate κ at the sample – by laterally scanning the UME over the sample, *d* has to be chosen with care. Conventional SECM imaging is performed in constant height mode necessitating flat samples with negligible roughness with respect to the dimensions of *d* and r_T. However, a sample tilt with respect to the horizontal scanning plane of the positioning system associated with a change of d during the experiment is often obtained because of the manual fixing of the samples in electrochemical cells realized with the help of O-rings, Teflon covers and screws. Figure 14b shows a feedback image of a tilted gold band structure on glass recorded in feedback mode. The height of the gold bands was 100 nm and negligible for the SECM performance. The tilt in y-direction decreased d and the measured currents for positive feedback increased significantly. A varying working distance can become an issue especially for the interpretation of kinetically limited surface reactions. Assuming a tilted homogenous surface with $\kappa = 1$ (compare approach curve in Figure 6) a maximum of the measured current during lateral scanning will be measured (increasing or decreasing d). This peak pretends wrongly a reactivity maximum. Before starting an SECM image, a three point calibration by running three locally separated approach curves - forming a horizontal triangle on the sample - can be made in order to calculate the tilt angles in x- and y-direction. The obliqueness can then be corrected with a tilt table. However, the procedure requires experimental expertise and can be time consuming because it must be assured that the kinetics at the points of approach are equal. The result of surface modifications induced by an UME is also strongly affected by the working distance. Furthermore, for SECM imaging and modification of a tilted substrate, the possibility of a probe-sample contact has to be taking into consideration as shown schematically in Figure 15.

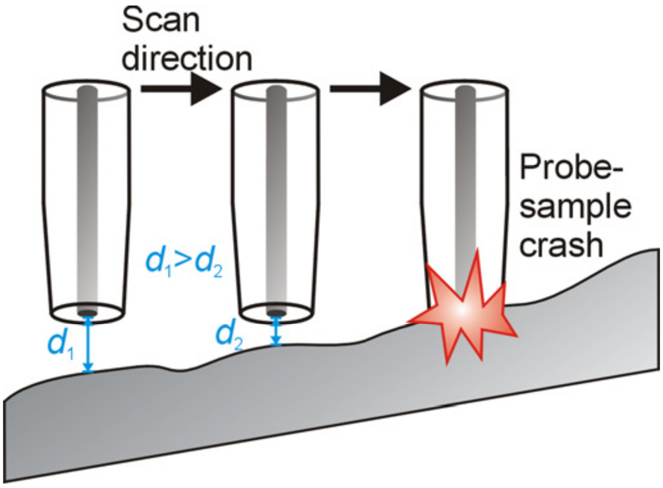

Figure 15. Schematic representation of experimental limitations when performing SECM conventionally in constant-height mode.

From the practical point of view, this problem is crucial since it can ruin the experiment. Figure 14a shows in the region of $y = 1.4$ µm horizontal stripes caused by short circuit currents. These were obtained due to a mechanical contact between the UME and the sample. This unintended effect can arise in particular when investigating big samples where the tilt calibration has to be performed with high accuracy. Unfortunately, this mechanical contact can cause the break of fragile glass UMEs and/or it can induce scratches and damages on delicate samples like organic thin films (Figure 14a) or living cells. In addition, a tilt correction becomes obsolete for curved, corrugated and protruding areas in case the surface features are large enough to affect d significantly. When investigating sample features with significant topography in SECM feedback mode, the situation can occur in which a current peak can be obtained by both a UME moving from and insulator over a conducting area (increasing κ, → positive feedback) or a UME moving over an hole of the surface (increasing d, → bulk current). In such a case, reactivity and topography cannot be distinguished. The situation is worst when both effects overlay. This limits in general the selection of samples for the conventional SECM to small and flat specimens.

In the following, an overview is given about important achievements in SECM to overcome the described limitations regarding working distance and imaging time. However, only minor efforts were made to solve both problems simultaneously. Our basic conceptual ideas will briefly be introduced at the end of both sections.

4.2 Approaching Constant Distance Imaging

The problem related to the working distance attracted much attention because it limits noticeably the SECM performance. A UME that follows the topography of the substrate in a constant distance mode was realized by several technical solutions. Most of them are based on the combination of SECM with other techniques relying on a distance control, such as SFM,[37-53] ECSTM,[54] impedance spectroscopy,[188-190] scanning ion conductance microscopy (SICM)[83, 191, 192] or shear force detection.[55-61] Recent developments are for example the intermittent contact (IC) SECM[193, 194] or the voltage-switching mode (VSM) SECM.[195] It is important to figure out that these combinations were mainly founded with the goal to increase the resolution of SECM by the implementation of nanoelectrodes. Smaller electrodes require a smaller d. This enhances the problems listed above. Those uses are sensible only in combination with additional instrumentation. In the following the various combinations are discussed.

Constant-current mode. When investigating electrically homogeneous surfaces, the distance depend current signal can be used to keep d constant.[196] A closed-feedback loop for vertical positioning regulates the vertical probe movement by adjusting the height related to the actual current signal (Figure 16a). More specialized is the utilization of a hydrophilic redox mediator for feedback mode imaging of living cells.[189, 195] The mediator is not regenerated at the cells and the cells' support which causes hindered diffusion at the substrate. Constant-current modes are only capable to detect topography and not reactivity and are therefore not suitable for most SECM applications.

ECSTM-SECM. Treutler and Wittstock[54] used an ECSTM instrument with an optimized tip to investigate a flame annealed gold substrate covered with an insulating self-assembled monolayer. The topography of the sample was recorded with the tip in tunneling distance to the sample as shown schematically in Figure 16b. Afterwards, the tip was retracted for SECM imaging and the tip followed the sample topography by the previously measured topographic information. However, the tip is small and ECSTM can only be applied for conducting substrates.

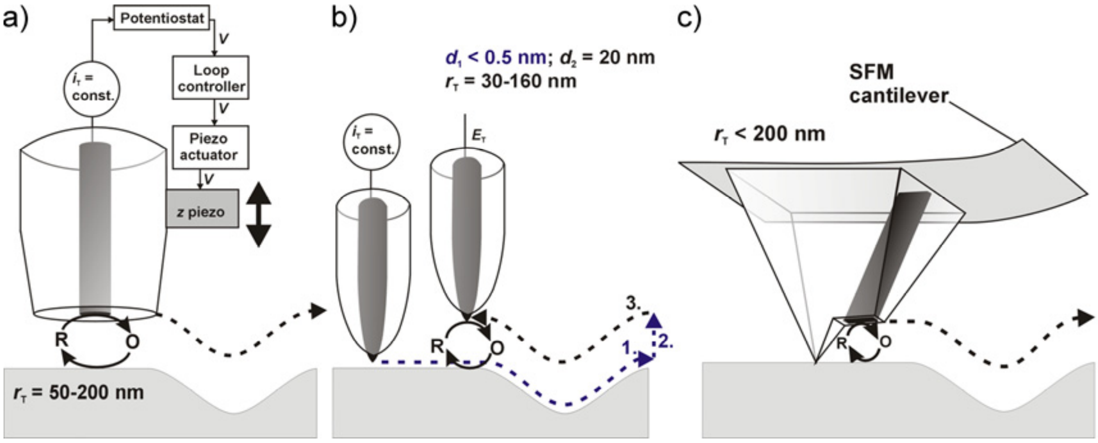

Figure 16. Schematic representation of constant current SECM (a), ECSTM-SECM (b) and SFM-SECM (c). Dimensions are not to scale and cannot be compared to each other. Figures made with information from references [54, 196, 197].

SFM-SECM. SFM-SECM is perhaps the most often applied combined SECM technique to provide a constant working distance for SECM measurements. Advantageous for this development were the large number of commercially available instruments, the automatic performance, the wide range of investigable samples and the feasibility to fabricate tips in batch production.[48, 198, 199] In general, SFM is based on the short-range forces between the scanning tip and the sample. The nanometer-sized tip is attached to a tiny cantilever. The SFM tip follows the topography of the sample in contact mode or tapping mode affecting the bending of the cantilever and the amplitude of the vibrating cantilever, respectively. A laser is continuously directed onto that cantilever and the reflected laser beam is detected. These signals are then converted into topographical information. SFM provides a resolution of sub-Å (z axis) and nanometer (x,y-axes). Modified SFM probes with integrated UME allow the simultaneous or successive detection of an amperometric current (SECM) and topography (SFM). Several approaches to produce these dual SFM-SECM probes exist that are mostly based on the modification of the apex of commercial SFM probes (see below). Surface structuring tools with high precision, such as focused ionic beam (FIB), low pressure and plasma enhanced chemical vapor deposition (LPCVD and PECVD) or electron beam lithography (EBL), are required to prepare the nanometer sized dual probes. Most progressive SFM probes consist of a sharp tip at the apex that works like in conventional SFM and a slightly recessed nanoelectrode for the electrochemical measurements (Figure 16c).

The first SFM-SECM tips were fabricated by Macpherson and coworkers[39] and consisted of a sharp metallic Pt tip that was used for both SFM scanning and current recording. Over the past decade the group developed further metallic (Pt and Au) tips of this type.[44, 52, 200] The sidewalls of the tips were insulated and only the very end of the tip was exposed. One limitation occurs with this kind of probes: the mechanical contact between tip and sample causes short circuit currents on conducting surface sites when a tip potential is applied. Therefore, simultaneous recording of topography and electrochemical activity can only be performed of insulating substrates.[39, 44] Alternatively, the tip can first measure the topographic information by using a conventional SFM mode, and subsequently perform a SECM line scan in liftmode™.[52, 200] The other problem that can arise with these tips is the abrasion or the possible contamination of the active electrode area with compounds from the surface in particular if thin organic films are investigated.

The most famous SFM-SECM concept so far was developed by Kranz *et al.*[42] who fabricated for the first time a UME which was recessed from the apex of the tip allowing simultaneous SFM and SECM imaging of many kinds of substrates. They sputtered a 100 nm gold layer on a standard commercial silicon nitride SFM tip and deposited a ≈700 nm thin insulation layer afterwards by chemical vapor deposition. Successive cutting by FIB formed a centered pillar providing the working distance in the submicrometer range.[42, 43, 201] At the same time, a UME with a squared-frame or a ring nanoelectrode is exposed that surrounds the pillar. The tip can also be used in tapping mode.[40] A large number of publications demonstrates the success of this SFM-SECM concept.[38, 40, 202-204] The tip was also successfully modified for the usage as an SFM-tip-integrated imaging biosensor.[41] More recently, the design was expanded to AFM-integrated boron-doped diamond electrodes.[49] Wittstock and coworkers[197, 205] deposited a layer of Au on a silicon dioxide pyramid followed by complete insulation. The electrode was then sliced off by FIB in the way that the active electrode area was exposed in the sidewall to give a thorn-shaped or angular SFM tip. This caused a lateral offset of the electrochemical signal and artifacts were obtained. Imaging in contact mode provided a constant working distance as shown schematically in Figure 16c. The system measures topography and amperometric signals simultaneously.

15 nm Pt_xSi_y tips were developed by Frederix and coworkers[45, 206, 207] using several fabrication steps including reactive ion etching (RIE) and chemical etching in buffered HF. Achieving a sharp tip is an issue. Due to the conductive material, topographical and electrochemical investigations had to be performed sequentially. Moreover, SECM detection was performed in constant height mode.

Davoodi *et al.*[47, 51] reported a different type of SFM-SECM probes with a centered, but recessed disk-shaped Pt-UME. A typical Pt-UME with a diameter of 1-5 µm with epoxy as insulating material was shaped by FIB to give a well defined L-shape where the Pt electrode was recessed and a sharp epoxy tip served as SFM tip. SECM scanning was performed with the retracted tip in constant distance mode after topographical detection.

The combination of SFM-SECM with SNOM was demonstrated by Suzuki and coworkers.[46, 208] It extended the topographical and chemical investigation by the optical detection of the membrane and cytoplasm of living cells. The optical fiber was centered and subsequently surrounded by a 200 nm thick gold ring electrode and a 100 nm thick insulating polymer. The cross-section was exposed by FIB under a defined angle of 60° allowing the polymeric part to act as SFM tip and to provide a constant working distance.

The combination of SECM with SFM demonstrates in principle how a constant working distance can be provided. However, in many cases topographical and electrochemical signals have to be recorded in two separated lateral scans which doubles the scanning time. SECM images can be recorded with very high resolution in nanoscale by taking advantage of the SFM instrumentation and nanometer-sized probes. But at the same time this limits the use to small sample regions. Piezo elements in commercial AFM devices are usually restricted to a translation range of 100 µm.

Shear force-based SECM. SECM based on the detection of shear forces found many applications since its inception.[55, 56, 209, 210] The scanning probe is brought closer than 1 µm to the surface and is laterally vibrated. Distance-dependent shear forces cause a damping of the amplitude and a phase shift which can be recorded with a dual lock-in amplifier. In the vibration spectra of the probe a frequency-dependent set point is determined representing a specific damping related to a defined working distance at a set frequency. During lateral scanning the probe is excited with one frequency and d is adjusted until the set point is reached by moving the probe up or down, respectively. In this way, the probe follows in a contactless mode the topography of the sample providing a constant working distance as demonstrated in Figure 17a. Simultaneous recording of the vertical probe position and of the current gives local topographical and electrochemical information of the sample under study. Nanoelectrodes are usually used as probes which consist of a Pt wire enclosed in an insulating quartz glass sheath. The small dimensions are achieved by the usage of a laser puller. A quartz capillary (outer diameter 0.9 mm and inner diameter 0.3 mm) including a Pt wire with a diameter of 25 µm is pulled under reduced pressure and various heating steps.[211] The achieved electrode radii are about one order of magnitude smaller than of conventional UMEs and increase the resolution of SECM for delicate samples with significant surface topography like living cells.[61, 212] Excitation and detection of the probe vibration are enabled either classically by two separated piezo plates or by a piezo tube (for excitation) and a split photodiode (for detection with a laser).[213] In principle, shear force based SECM can be used to scan areas exceeding square millimeter and centimeter. One recent approach to scan large complex shapes by shear force-based SECM was reported by Etienne *et al.*[214] They performed 9 line scans separated by 1cm with a Pt-UME (25 µm in diameter) to scan an area of 1 mm × 8 cm of a corrugated steel sample. This area is large, but the experiment demonstrated at the same time some drawbacks. The step sizes were set to large values (25 µm and 1 cm, respectively) compared to the size of the electrode. Surface features in-between steps are hardly detectable. However, despite the large steps the imaging time was still more than 4 hours due to translation rate limitations. Additionally, the probe was lifted off 100 µm for safety reasons in-between steps followed by a slow re-approach increasing the measurement time.

TPM-SECM. The vertical position of a UME can be modulated by applying a small sinusoidal amplitude ($0.1 \cdot r_T$) and the measured modulated current can be used for distance control as introduced by Wipf and Bard.[215] This mode is called tip-position modulation (TPM) SECM. A constant potential was applied to the UME providing a diffusion-limited current. However, the measured signal consisted of a normal dc component and of an ac current induced by the z motor motion. With a 15 Hz filter the dc component was filtered.

The ac signal was amplified by a lock-in amplifier and a phase resolved root mean square ac response was recorded. The ac current represented a much higher current contrast to distinguish between conducting and insulating surfaces because the phase is shifted by 180° comparing both situations. Furthermore, the ac signal could be used to maintain a constant current mode by taking advantage of a closed feedback loop (schematic representation in Figure 17b). The technique was not widely adopted. One reason could be that the mechanisms taking place were not easily understandable and the hardware periphery is much more advanced than standard SECM setups. Just recently, Edwards *et al.*[216] quantified the influence of convection on TPM SECM. Another limitation is that the TPM mode can only be used for the feedback mode and not for the G/C mode.

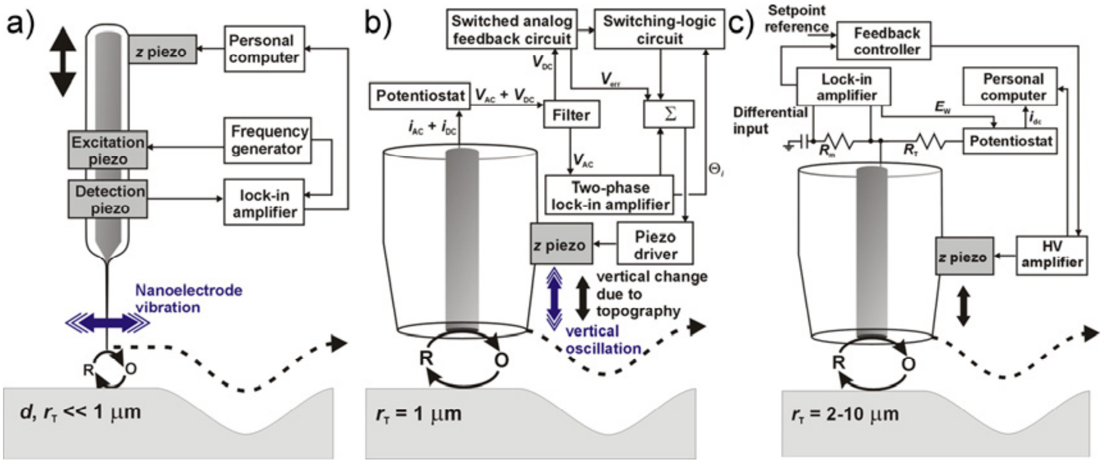

Figure 17. Schematic representation of shear force-based SECM (a), TPM-SECM (b) and impedance-based SECM (c). Dimensions are not to scale and cannot be compared to each other. Figures made with information from References [56, 188, 217].

AC-SECM. Although the TPM mode did not write a successful story, the principle of using ac signals and its dependence of the working distance found application in a different mode. One example is the measurement of the electrochemical impedance at the UME which depends on the working distance.[188] Vivier and coworkers applied a base potential to the UME to cause a diffusion-controlled current by conversion of a redox-active compound.[218] Additionally, between the UME and a counter electrode a high frequency ac voltage is applied which is too fast to influence the diffusion of the redox mediator. The low frequency amperometric current related to the Faradaic reaction at the UME and the high frequency current response related to the impedance were separated by an RC filter. A constant distance mode was achieved by integrating a closed feedback loop that kept the impedance signal constant by changing the working distance. In this way, the topography and reactivity of a Pt-electrode was detected using the sample-generation/tip-collection mode. AC-SECM can also be used without redox mediator since the local impedance of the UME-sample system is probed.[219] As can be seen in the schematic representation (Figure 17c), additional instrumentation is required. In addition, an advanced knowledge about impedance is needed in order to interpret the measured data.

SECM-SICM. SECM-SICM uses dual nanoelectrode-nanopipette tips as scanning probes. First probes were fabricated by depositing a 200-250 nm gold film by electron beam evaporation onto the outside of a borosilicate based nanopipette (100 nm diameter opening) followed by insulation with a thin Al_2O_3 film by atomic layer deposition.[191] The cross-section was exposed by FIB and a Au ring-electrode was obtained. More popular are the double barrel carbon nanoprobes (DBCNPs) as reported recently by Korchev and coworkers.[83] In SICM, the nanopipette is filled with electrolyte solution and a bias voltage is applied between two electrodes positioned inside and outside the nanopipette, respectively. Thus an ion current is generated which decreases the closer the tip is brought to the surface due to a blocking effect by the sample on the migration of ions. This effect can be used for determining the working distance as shown schematically in Figure 18a. At a defined distance (current value compared to a reference value) the approach stops, the current is measured at the nanoelectrode, the whole probe is retracted, moved to the next *x*,*y*-position and the next probe approach is started. This procedure is known as “hopping” mode. The SECM-SICM is a nice example to get highly resolved topographic and reactivity images of various substrates. However, the scanning procedure is time consuming due to limited translation speeds and the technique is not suitable for large samples.

IC-SECM. Vibrating a UME in a sinusoidal manner parallel to the surface normal with a frequency of 70 Hz and with an amplitude of 1-4 % of the active electrode radius comparable to the SFM tapping mode was used by McKelvey *et al.*[193, 194] to detect the intermittent contact (IC) of a UME with a sample while approaching the UME slowly to the sample surface. The contact was defined as the distance when the probe oscillation decreased to 15 % of the initial value. This mode is called IC-SECM (Figure 18b) and differs from the earlier reported TPM-SECM because a non electrochemical signal is used in order to detect the positioning signal. The vertical movements of the UME were controlled by a piezoelectric positioner which was operated in a closed feedback loop. For imaging, the IC signals were detected in forward line scans while the extracted topographical information was used to apply a constant working distance in the corresponding reverse scans. Due to the UME movement ac current signals were measured. The authors demonstrated that the ac signal enhances the lateral resolution compared to the recorded dc signal: This allowed visualization and quantification of the hydrodynamic flow of species through multiporous membranes.

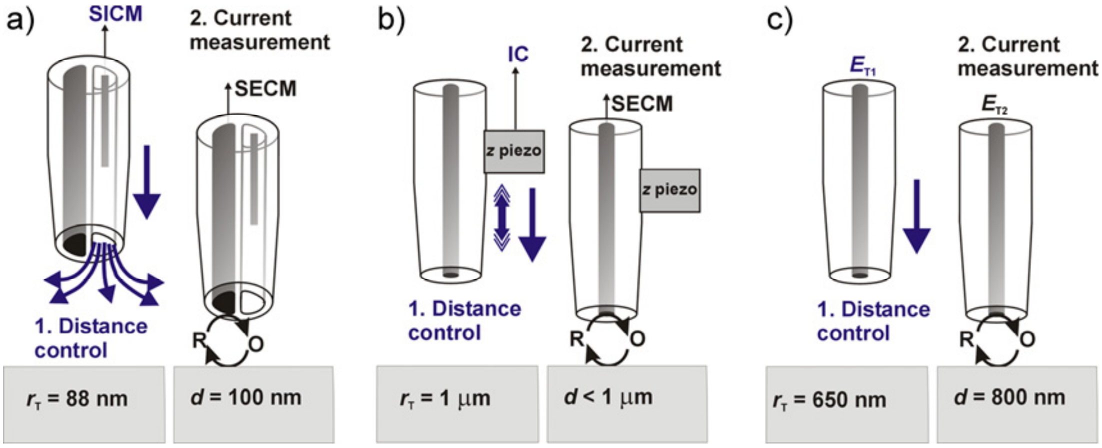

Figure 18. Schematic representation of SECM-SICM (a), IC-SECM (b) and VSM-SECM (c). Dimensions are not to scale and cannot be compared to each other. Figures made with information from References [83, 193, 195].

VSM-SECM. In order to image simultaneously the topography of living cells and the electrochemical detection of locally generated compounds at these cells Takahashi *et al.*[195] introduced a new so-called voltage-switching mode (VSM) SECM (Figure 18c). Nanometer resolution was achieved by using pyrolytic carbon nanoelectrodes with 6.5 nm and 100 nm radii and *RGs* of about 1.5 to 3.0. A hydrophilic redox mediator cannot cross a cell membrane and was used to determine the nanoelectrode-substrate distance. At each step of a lateral scan an approach curve was performed until a predefined current value (set point) was reached representing a defined d = 800 nm. During approaching a constant cathodic potential was applied to achieve a diffusion-controlled current at the nanoelectrode due to the reduction of the used redox mediator. When the set point was reached the probe was arrested, the z-position was monitored and the potential at the nanoelectrode was switched to an anodic potential in order to detect *p*-aminophenol which was generated by a catalytic reaction at specific cell regions. This switching could be performed in short time scales thanks to a steady state behavior after t < 20 ms.

Conclusion about the combined techniques. All briefly described techniques provide the possibility for distance-controlled SECM imaging, but are very specialized tools. Most of them require additional instrumentation, measurements and probe movements in order to provide a constant gap between the probe and the sample surface. The performance and the interpretation of data are often demanding compared to the conventional SECM modes and require advanced knowledge of SECM and other SPMs. Furthermore, except constant-current and impedance mode, the probe itself has to be modified which requires often very specialized techniques. The nature of several integrated techniques relies on tips and nanoelectrodes that are at least one order of magnitude smaller than the conventional UMEs. One advantage when using nanoelectrodes is their high spatial resolution. However, the working distance has to be decreased significantly to detect local differences of sample reactivity. This increases at the same time the potential for a tip-substrate contact.

Our new approach. Our approach is based on the utilization of soft probes that are based on flexible polymeric thin films. These probes can scan surfaces in contact regime similar to a giant SFM cantilever providing a constant working distance. Details about concept (Sections 6.1-6.2), fabrication and characterization (Section 6.3), and experiments (Chapters 6-8) will be discussed in this thesis.

4.3 Acceleration of Image Acquisition

Much less efforts were devoted to scan larger areas in appropriate time scales compared to the efforts in keeping a constant working distance. However, three strategies to overcome difficulties arising from long imaging times can be extracted from literature for SECM and other SPMs.

Strategy 1 – Increasing the probe translation rate or step size. The first strategy is based on the increment of the probe translation rate and the step size. Step sizes of 125 µm[25] and translation rates of 500 µm s^{-1}[62] were applied in imaging but compromises in the resolution have to be accepted. One reason is that a UME with $r_T = 12.5$ µm and d within some electrode radii cannot detect the regions in-between the 125 µm big steps. The other reason is the negative influence of convection on the resolution. At even higher translation rates exceeding 1000 µm s^{-1} SECM loses its ability to detect differences in surface reactivity.[92] Scanning of a large area with large steps (low resolution) in order to locate interesting surface features and subsequently rescanning of these interesting areas with adjusted resolution as reported for SICM could be an option.[220] An interesting approach was introduced by Kovács and coworkers[221] who developed an "automatic target location" for SECM. In order to locate a specific conductive target (largest current) on an insulating support material, the UME was translated several steps in x- and y-

direction in software-controlled “snail-like” movements instead of using the typical line by line performance.

Strategy 2 – Renewal of electrode surface and electrolyte solution. The second strategy is related to overcome negative influences caused by electrode fouling or electrolyte evaporation. Approaches were made in order to investigate the catalytic activity of a combinatorial library for fuel cell applications by successive scanning of five individual adjacent image frames and assembling them afterwards to a continuous image of 2.5 cm × 1.3 cm size.[25] Before each measurement the UME was electrochemically reactivated by cyclic voltammetry. Also the electrolyte solution can be exchanged. However, each image represents an individual experiment and does not contribute to decreasing the overall imaging time although problems like solution evaporation and electrode fouling have been addressed.

Strategy 3 – Multiplexing electrodes. The third strategy is based on the usage of multiple probes allowing parallel scanning and modification instead of a time consuming line by line performance (Figure 19). The time can be reduced by a factor related to the number of individually addressable electrodes.

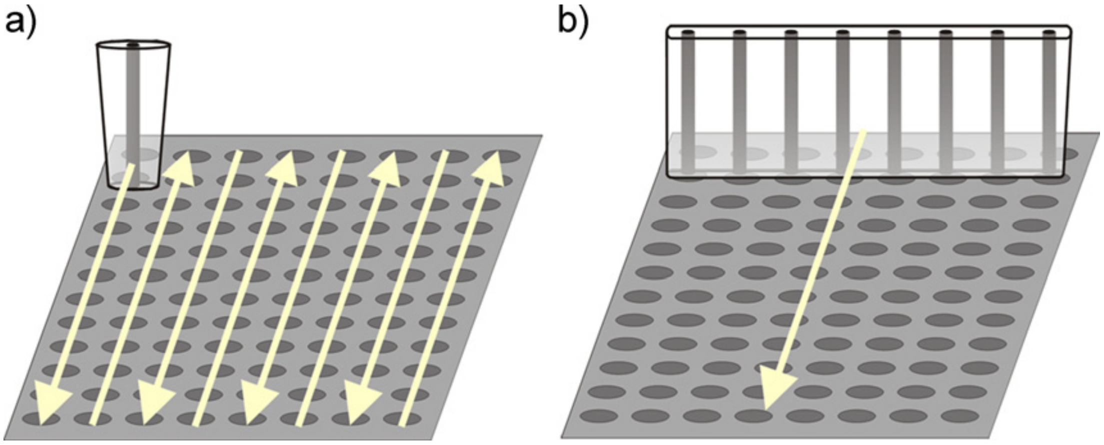

Figure 19. a) Conventional SECM for imaging and modification has to be performed line by line. b) A reduction of the processing time can be achieved by using an array of parallel electrodes. The decrease in time is related to the number of integrated electrodes.

Multi-tips to reduce the time required for an experiment were introduced in SFM[222-224] and DPN.[225-229] The approaches aim for parallel patterning of surfaces. A linear multi-SFM probe consisting of 50 individual cantilevers was fabricated by Minne *et al.*[222] and allowed high speed parallel imaging with a translation rate of 4 mm s^{-1}. Each of the cantilevers was constructed with its own piezoresistive sensor and ZnO actuator for *z*-

positioning. Vettiger *et al.*[223] introduced the "millipede" concept which is a two-dimensional SFM based data storage technique. Individually addressable SFM cantilevers in a 32 × 32 array arrangement were used for writing and reading. However, the vertical position of the individual cantilevers could not be controlled individually. Three sensors and actuators were integrated into the system for leveling the whole probe. More recently, multiple SFM lithography probes for high throughput nanopatterning were developed.[224] Up to five carbon tips were deposited linearly on one single cantilever to pattern structures on a silicon wafer by local oxidation. However, the tips are not individually addressable and imaging was not performed.

Multiple DPN probes to increase the throughput of dip-pen nanolithography were made popular by Chad A. Mirkin and coworkers.[225, 226, 229] They used parallel SFM cantilevers for parallel deposition of an alkanethiol on a Au substrate. Linear arrays of cantilevers were also developed by Liu and coworkers.[227, 228] Very impressive is the 55,000-pen two-dimensional array of SFM cantilevers developed by Mirkin and coworkers.[225, 229, 230] The tips were separated by 90 µm and 20 µm in the *x*- and *y*-directions, respectively, and patterned for example 55,000 identical replica of the face of a five-cent coin. Afterwards, the tips performed SFM imaging of their individually patterned structures. The multiple SFM and DPN probes can be used for high-throughput patterning of parallel identical structures with very high resolution. But only minor attempts were made to take advantage of the multitips to form one large merged image frame. In addition, *in situ* modification of surface films in electrolyte solution has not been reported to the author's knowledge.

Various reports can be found about the parallelization of UMEs. Many multi-probes were fabricated very close to the design of the classical UME. They were often made for purposes other than time reduction. Dual UMEs for example consist of a pair of closely spaced but independent UMEs, which can be of amperometric[231-235] or potentiometric[236] type. Usually, the dual functionality is given by applying different signals in order to detect the working distance at one electrode while the other electrode is used for a chemically selective measurement. One of the electrodes is used to position the entire probe with a defined distance to the sample surface before performing constant height imaging. Ultramicroheptodes consist of one central UME surrounded by six interconnected UMEs and were applied in a ring-disk arrangement to exploit the mutual shielding effects.[237, 238] Alternative ring-disk UMEs were introduced as SECM probes for the so-called disk-generation/ring-collection experiments.[239, 240]

Only occasional efforts were made for parallel SECM operations. A first attempt was the concept developed by Meyer *et al.*[63] They used an array of 400 individually addressable UMEs arranged in 10 mm × 10 mm square matrix (500 µm electrode spacing, 36 µm × 36 µm active electrode area) for the two-dimensional mapping of O_2, H_2O_2 and glucose distributions within 2 min. The electrodes had to be read successively and neither the array nor the sample could be moved. Thus, the distances in-between the electrodes are identical to the distances in-between data points. The substrates were attached directly to the array which was placed face-up in the electrochemical cell. No possibilities were described to scan a sample. In addition, interferences between electrodes caused noisy signals. This concept can determine time-resolved changes in the distribution of an redox-active species but it is not suitable for SECM imaging. Matsue and coworkers[64] proposed an addressable microelectrode array of two parallel band electrodes that are perpendicularly orientated on opposing chips. The analyte solution is placed inside the gap and individual measurement points are addressed by activating one individual band in each of the two arrays by “raw” and “column”.

The concept for parallel SECM imaging closest to the approach in this thesis was demonstrated by Barker *et al.*[65] They fabricated a linear array of 16 independent disk UMEs (10 µm in diameter) on a silicon chip. Due to the applied microfabrication techniques the UMEs were slightly recessed in an insulation layer. The electrodes were spaced 120 µm from each other in order to ensure that diffusion layers of neighboring electrodes do not overlap. The chip was mounted face-up in the bottom of the electrochemical cell and the sample was moved along the *x*- and *y*-axes. Usually, electrodes in arrays give slightly different responses due to minimum differences in electrode size and geometry. For this purpose the authors plotted normalized currents by dividing the original current values by the individual bulk steady-state currents $i_{T,\infty}$. The imaging time using 5 electrodes could be reduced significantly by a factor equal to the number of used electrodes. However, this system was without probe-sample alignment control and mechanical polishing of the probe array as a reactivation step for the electrodes would remove the insulating nitride layer. This limits the life time and no further publications including the UME array indicate that the system was not established for routine SECM applications.

Deiss *et al.* [66] introduced a multiscaled SECM probe for parallel surface modification by chemical etching of an optical fiber bundle. Six thousands nanotips were constructed on a disk-shaped area of 300 µm diameter. The probe was used to create patterns into a Teflon substrate. However, the probes were not individually addressable and lateral translation for patterning was not demonstrated.

Our new concept. Our idea was to fabricate linear arrays of microelectrodes for parallel imaging and modification to reduce the experimental time significantly and to allow working on big samples approaching square centimeter. Details about concept (Sections 6.1-6.2), fabrication and characterization (Section 6.3), and experiments (Chapters 6-8) will be discussed in this thesis.

5 Experimental Details

5.1 Chemicals

Aqueous solutions were prepared using deionized water produced by a Milli-Q plus 185 model (Millipore, Zug, Switzerland) or by Purelab® Classic (Elga LabWater, United Kingdom). Chemicals for electrolyte solutions used generally in the experiments of this thesis are listed in Table 4. All chemicals were of analytical grade and were used as received. Polymer films used as supports for soft probe preparation are listed in Table 5.

Table 4. General chemicals for electrochemical experiments.

Product	Formula	Supplier	Grade
(1-mercapto-undec-11-yl)hexa (ethylene glycol)	$HS(CH_2)_{11}(OCH_2CH_2)_6OH$	[a]	-
acetonitrile	CH_3CN	VWR	>99 %
disodium hydrogen phosphate dihydrate	$Na_2HPO_4\ 2{\cdot}H_2O$	Fluka	99 %
ethanol	C_2H_5OH	VWR	>99.8 %
ferrocenyl methanol	FcMeOH	Sigma-Aldrich Alfa Aesar	≥97 % 97 %
hexaammineruthenium(III) chloride	$[Ru(NH_3)_6]Cl_3$	Sigma Aldrich	98 %
hexadecanethiol (HDT)	$C_{16}H_{33}SH$	Alfa Aesar	>95 %
hydrogen peroxide 30 % (w/w)	H_2O_2	Fluka	-
potassium bromide	KBr	Fluka	≥99.5 %
potassium chloride	KCl	Roth Sigma-Aldrich	≥99.5 % ≥97 %
potassium nitrate	KNO_3	Roth Sigma-Aldrich	≥99 % ≥99 %
sodium dihydrogen phosphate	NaH_2PO_4	Fluka	99 %
sodium sulfate	Na_2SO_4	Merck	99 %
sulfuric acid	H_2SO_4	Merck	suprapure
tetrabutylammonium trifluoromethanesulfonate	$(CH_3CH_2CH_2CH_2)_4N(CF_3SO_3)$	Sigma-Aldrich	≥99 %

[a] synthesized by Jan Ross (group of Prof. Dr. Jens Christoffers, Carl von Ossietzky University of Oldenburg).

Table 5. Polymer films applied as supports for soft SECM probes.

Product	Manufacturer/Supplier	Section
polyethylene terephthalate (PET), Melinex®	DuPont (Wilmington, DE, USA)	6.3.1
polyimide (PI), Kapton HN®	Goodfellow (Huntingdon, England)	6.3.2
PI, Kapton HN®	Dr. D. Müller Ahlhorn GmbH (Ahlhorn, Germany)	6.3.3

Ink used for carbon microelectrodes:

The carbon electrodes and connection pads were fabricated by Electrador carbon ink (Electra Polymer & Chemicals Ltd., Roughway Mill, Dunk Green, England).

Ink used for Aerosol Jet® printing:

A water-based gold nanodispersion (Nanocolltech Ltd., Hungary) was used as received. The gold nanoparticle content was 15 wt.%. The average particle size was 10 nm. Data were specified by the manufacturer.

Ink used for inkjet printing:

For inkjet printing, the silver nano-ink SunTronic® Silver EMD5603 (Sun Chemical Corp., Parsippany, USA) was used as received. Silver content was 20 %, viscosity 0.01 - 0.013 Pa s (25 °C), surface tension 0.027 - 0.031 N m^{-1}, and average particle diameter 150 nm. Data were specified by the manufacturer.

Chemicals used for the Pt plating mixtures:

Table 6 contains the chemicals used for Pt plating mixtures.

Table 6. Chemicals for Pt plating mixtures.

Product	Formula	Supplier	Grade
hexachloroplatinic acid hydrate (HCPA)	$H_2PtCl_6 \cdot x\ H_2O$	Sigma-Aldrich	99.9 %
hexachloroplatinic acid solution 5 % (w/w)	H_2PtCl_6	Fluka	p.a.
octaethylene glycol monohexadecyl ether	$C_{32}H_{66}O_9$	Sigma-Aldrich	98 %

5.2 Sample Preparations

Preparation of gold surfaces. Gold substrates were prepared on cleaned microscope slides. The glass slides (2.5 cm × 2.5 cm) were cleaned subsequently for several minutes in ultrasonic baths (at room temperature) containing water and isopropanol, respectively. An evaporation chamber (minicoater, Tectra GmbH, Frankfurt, Germany) was used to deposit a thin layer of chromium (0.5 nm) followed by a gold film (100 nm). The amount of deposited material was monitored via a quartz crystal microbalance (Tectra GmbH, Frankfurt, Germany). The gold substrates were always freshly prepared prior to use.

Microcontact printing. For µCP a polydimethylsiloxane (PDMS) stamp was casted from a silicon master obtained by photolithography using the Sylgard® 184 Elastomer Kit (Dow Corning, Wiesbaden, Germany). The stamp was inked in a 1 mM ethanolic solution of HDT and dried afterwards for 2 min under a stream of nitrogen or argon. The stamp covered with HDT was then pressed gently on the Au surface for 1 min. After removal of the stamp, the Au surface was rinsed with pure ethanol followed by drying under a stream of nitrogen or argon.

Self-assembly for the formation of OEG SAM. In order to form a homogenous monolayer, the Au samples were immersed in a 3 mM ethanolic solution of OEG-terminated thiol ($HS(CH_2)_{11}(OCH_2CH_2)_6OH$) for 12 h. After removal from the thiol-containing solution the sample was rinsed with pure ethanol and dried under a stream of argon.

Site-selective protein adsorption. The samples covered with locally modified OEG SAM were immersed for 4 h in 100 µg mL^{-1} fibrinogen-Alexa Fluor 488® conjugate in phosphate buffered saline (0.1 M phosphate, 0.15 M NaCl, pH = 7.4) for site-selective adsorption of the extracellular matrix protein.

Au band electrodes. Glass slides were treated with piranha solution and cleaned by sequential sonication in ethanol, acetone, and purified water followed by drying under a stream of argon. Gold films of 100 nm thickness were prepared in an Edwards Auto 306 evaporator. A metallic mask defined the microstructure shape. After the deposition of a 1 nm thick Cr layer, a 100 nm thick Au layer was subsequently deposited.

Pt band electrodes. Pt band electrodes on glass slides were prepared by standard photolithographic processes and employed as test samples for surface reactivity imaging. The width, pitch and thickness of the Pt bands were 100 µm, 100 µm and 100 nm, respectively.

Combinatorial library of C/Pt catalysts. A materials library was provided by G. Denuault (University of Southampton, UK). This library consists of 100 individually addressable C/Pt spots of different composition on a silicon nitride chip. The spots are 1 mm × 1 mm gold squares coated with carbon and then with Pt particles. The carbon layer is circa 200 nm thick and the Pt particles have a diameter ranging between 1 nm and 8 nm. They were prepared by coalescence of Pt clusters during physical vapor deposition of Pt.

5.3 Deposition of mesoporous Pt on the carbon microelectrodes

A detailed description of the electrodeposition of Pt on the carbon microelectrodes can be found in the BSc. thesis of Julian Behnken.[220] The MultiWE32 was used and controlled by IviumSoft. All deposition processes described here took place under potentiostatic control in a three electrode arrangement. First, a thin Pt layer was deposited electrochemically onto the carbon microelectrodes in 1.2 mM H_2PtCl_6 and 0.1 M HCl. The deposition was controlled by applying simultaneously a potential of E_T = -0.05 V *vs.* Ag/AgCl/3 M KCl to all carbon microelectrodes. The procedure was stopped until a charge of approximately -15 µC (negative value because of cathodic currents) was transferred through each carbon microelectrode. Small variations of flowed charge were due to differences in the sizes of the active electrode areas (Section 6.3.1). Subsequently, the deposition was tested by cyclic voltammetry in dilute sulfuric acid.

The electrodeposition of mesoporous Pt on the carbon electrodes was adopted from literature.[68, 241-243] The procedure is based on a molecular template, which is formed by a hexagonal (H_I) lyotropic liquid crystalline phase.[242] This was realized by a ternary mixture of 42 % (w/w) nonionic surfactant octaethylene glycol monohexadecyl ether ($C_{16}EO_8$), 29 % (w/w) hexachloroplatinic acid hydrate (HCPA) and 29 % (w/w) water.[68] The components were put together in a glass vial. The vial was sealed and stored at 40 °C for 40 minutes. Then the mixture was stirred manually with a glass rod and heated a second time under the same conditions as before. Afterwards, the mixture was relaxed for 12 h at room temperature. The surfactant molecules aggregate into rods which orientate in a three-dimensional template.[241] The hydrophobic alkyl chain of $C_{16}EO_8$ is arranged towards the inside of these rods. HCPA is dissolved in the surrounding aqueous phase. The electrodeposition of the mesoporous Pt film also was realized in a three electrode arrangement. The highly viscous Pt plating mixture was manually coated onto a Pt plate which served as auxiliary electrode (Aux). The microelectrode array and a Ag/AgCl/3 M KCl-reference electrode (RE) were stuck into the solution and the electrodeposition was started after 30 min relaxation time. A potential of E_T = -0.05 V *vs.* Ag/AgCl/3 M KCl was applied simultaneously to all microelectrodes until electrode-dependent charges between -16 µC and -30 µC were transferred. The variations were caused by differences in the sizes of the active electrode areas (Section 6.3.1). It was assumed that a Pt nanostructure with cylindrical pores on a hexagonal lattice was achieved by the native hexagonal phase H_I of the template mixture as described in literature.[68, 241-243] This structure is denoted as H_I-

ePt.[242] After the deposition, the arrays were stored in pure water for 12 h in order to dissolve residues of the plating mixture in the nanotubes. The deposition was tested by cyclic voltammetry in dilute sulfuric acid.

5.4 Instrumentation

SECM. Electrochemical experiments were performed using two identical custom-built SECM instruments which were located in the electrochemistry labs of the Wittstock group (Oldenburg) and of the Girault group (Lausanne). The workstation consists of a Märzhäuser three-axes positioning system (Märzhäuser Wetzlar, Wetzlar, Germany), a tilt table for mounting the electrochemical cell and for tilt elimination (Zaber Technologies, Vancouver, Canada) and an Ivium CompactStat Potentiostat (Ivium Technologies, Eindhoven, The Netherlands) connected to an Ivium MultiWE32 unit allowing the operation of up to 32 individually addressable working electrodes. The potential of the working electrodes was controlled using one auxiliary electrode (Aux) and one reference electrode (RE). The Ivium CompactStat without the module MultiWE32 was also used as a (bi)potentiostat with two individual working electrodes. In all measurements a Pt wire served as Aux. A Ag wire acted in almost all cases as quasi-reference electrode (QRE). A7lternatively, a Hg/Hg_2SO_4/sat. K_2SO_4 electrode was used in chloride-free solutions. All potentials in this thesis were referred to the used reference electrodes. The in-house made SECMx software was used to control the experiments, to acquire the data and to plot results. Cyclic voltammetry was controlled with the Ivium software Iviumsoft. Offline data handling (calibration) and plotting was performed with the in-house made software MIRA.

Shear force based SECM. One shear force SECM image of the sintered gold tracks on PI was recorded together with Ushula Mengesha Tefashe from the Wittstock group. In order to control the working distance a modified SECM setup was used consisting of a DS4L controller under SXM software (version 0.19f, Anfatec Instruments AG, Oelsnitz, Germany) running on an independent personal computer. The piezo controller and amplifier E-662 (Physik Instrumente, Karlsruhe, Germany) was operated in open loop and fed with the control signal for vertical positioning. This controller drove a linear piezo stage with a translation range of 80 μm and an internal position sensor (type P-780.20, Physik Instrumente, Karlsruhe, Germany). A custom-made analog bipotentiostat (M. Schramm, University of Düsseldorf, Germany) was interfaced to the PC via an AD/DA board (PCI-DAS 1602/16, Plug-In Electronic GmbH, Eichenau, Germany). The signal from the position sensor of the linear piezo stage was also read by the AD board in order to construct a topographical image. A 700 nm diameter platinum nanoelectrode (with a quartz glass sheath of 18 µm) was fabricated by Ushula Mengesha Tefashe and used in this thesis. Details are described in his PhD thesis.[244] The nanoelectrode was excited with a sine wave (395 kHz frequency and 579 mV amplitude) generated by the DS4L controller. This excitation signal was directed to a piezo plate whereas the vibration was detected with a second piezo plate as reported by Ballesteros Katemann *et al.*[56] and briefly described in Section 4.2. A three electrode configuration was used with a Pt wire as Aux and a Ag wire is QRE. The sample was unbiased during the measurements.

Confocal Laser Scanning Microscopy. A confocal laser scanning microscope (CLSM, TCS SP2 AOBS, Leica Microsystems GmbH, Wetzlar, Germany) running under Leica Control Software (version 2.61) was used in reflection mode with an Ar laser (488 nm) in order to investigate the cross-section of the active electrode areas of the soft SECM probes. After adsorption of fibrinogen-Alexa Fluor 488® on the modified OEG SAM regions, the dye was excited at a wavelength of 488 nm and the fluorescence was detected with a spectral range of 500-535 nm.

Scanning Force Microscopy. SFM and Pulsed Force Mode (PFM) SFM were performed in close collaboration with Frank Meiners from the Wittstock group.

SFM in the Tapping Mode™ was used to obtain the topographic information of the sintered gold tracks on polyimide films in air and at room temperature. A Nanoscope IIIA controller, a Dimension 3100 sample stage, a Dimension SPM head scanner and a RTESP tip (all Veeco Instruments Inc., Plainview, NY, USA) running under the Nanoscope Software (V5.30r3sr3) were used.

SFM was used in the PFM to characterize the OEG SAM after the electrochemical modification by the soft array probes (Section 7.1.3). The measurement was performed under ambient conditions with the modified SFM setup. The Nanoscope IIIA controller, the Dimension 3100 sample stage and a Dimension "G" scanning head (all Veeco Instruments Inc., Santa Barbara, CA, USA) operated in PFM (WITec, Ulm, Germany).[245, 246] Topography, stiffness, and adhesion were recorded. The Au-coated SFM tip (Olympus OMCL-RC800PB, 0.82 N/m) was modified in 1 mM 11-mercaptoundecanoic acid to form a COOH-terminated SAM as described previously in order to detect the hydrophilic and hydrophobic properties of the non-modified and modified OEG SAM as demonstrated by Zhao *et al.*[164]

SFM and PFM SFM were used to record 256 × 256 pixel images of 100 µm × 100 µm areas and were recorded with a scan rate of 0.1 Hz and 0.5 Hz, respectively. Image flattening was performed by subtracting a background from the raw data in order to eliminate the vertical offset between line scans and the tilt in each line scan. The background was constructed by finding a least-squares fit to first-order (for adhesion and stiffness) and third-order (for topography) polynomials for the selected image region using the Nanoscope software.

Scanning Electron Microscopy. Scanning Electron Microscopy was performed with a Hitachi S-3200N (Scientific Instruments, Nissei Sangyo GmbH, Ratingen, Germany) in order to image the active electrode areas of the soft probes. The used polymeric materials are pure insulators and charging effects prevent SEM imaging of good quality. Usually, these kinds of probes are sputtered with a thin Au layer to make the sample conductive. However, the probes are not usable for further experiments and initially conductive parts are hardly to be distinguished from initially insulating materials. Alternatively, the probe was covered with a thin conductive film of the room temperature ionic liquid 1-ethyl-3-methylimidazolium bis(trifluoromethyl) imide as adopted from Arimoto *et al.*[247] The Au microelectrode was measured with the lowest available acceleration voltage of 5 kV. However, charging effects reduced the quality of the image.

Estimation of the force exerted of soft probes. Two approaches were followed in order to estimate the force exerted by soft probes on the sample surface: direct force measurement and the resonance frequency of the free vibration.

i) Measurement of the force. An array was mounted on the custom-built SECM holder with an inclination angle of 20° (Section 6.4) with respect to the surface normal and was approached from air to an analytical balance plate with the z motor of the used SPI positioning system. The force was measured by reading the mass from the display of the analytical balance Sartorius CP 124 S for four vertical displacements and multiplying each value with the gravity constant ($g = 9.81\ \mathrm{m\ s^{-2}}$).

ii) Determination of the resonance frequency of the soft probes. The resonance frequency of vibrating soft probes was measured. A soft probe was mounted and suspended freely in air. A HeNe Laser (632.8 nm, Thorlabs) was directed on the transparent probe. The vibration was manually stimulated and the free vibration was monitored by the deflection of the reflected beam detected by a photodiode. An oscilloscope was used to record the signal and a resonance frequency was read from the display.

Determination of the specific resistance. The resistance of the gold structures was measured using a four point probe measurement which is unaffected by contact resistances.

Four linearly arranged contact pins were separated by a distance of 2 mm and brought in mechanical contact with the gold or silver tracks. A known current is applied between the outer pins and the voltage is measured between the two inner pins. An ohmic resistance can be measured.

6 Soft Linear Arrays of Microelectrodes as New Probe Type for SECM

In order to overcome the typical SECM limitations for large sample areas, such as long imaging times and the difficulty to keep a constant working distance (Chapter 4), a new type of SECM probes is introduced in this chapter. This chapter explains the concept, fabrication and characterization of new probe types, and developments in the SECM setup and software.

6.1 Concept

Our approach was to fabricate microelectrodes in flexible polymeric materials that can scan in a brushing-like way on flat, tilted and corrugated surfaces. Microelectrodes of similar dimensions as conventional UMEs are enclosed in-between two thin polymeric layers. These flexible materials provide a bending of the probe when it gets in mechanical contact with the sample and an almost constant working distance can be achieved during sliding on the substrate as shown schematically in Figure 20a.

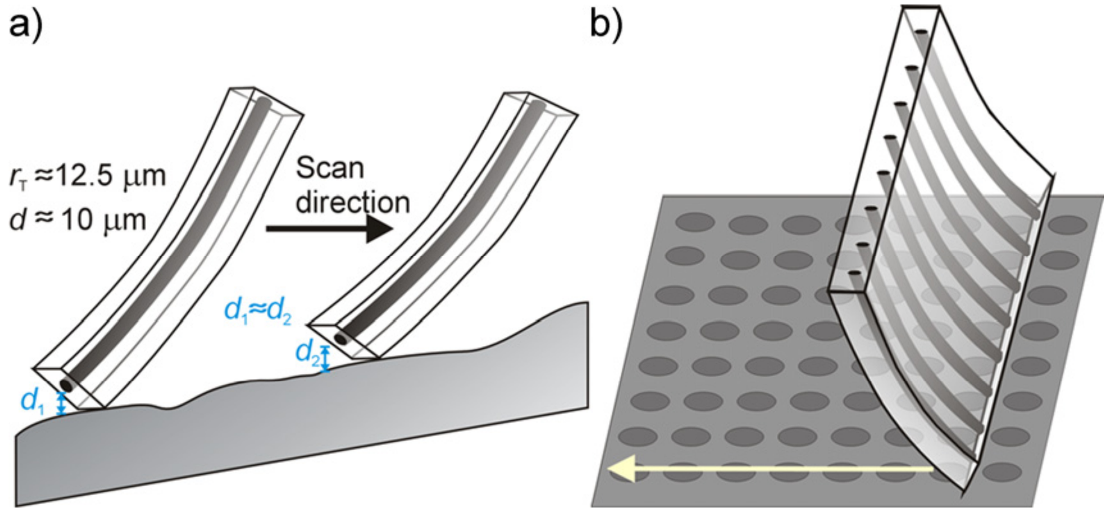

Figure 20. Our concept to keep a constant working distance and to reduce the imaging time. a) Soft base materials like thin polymeric layers allow scanning in contact mode. The probe follows the topography and a constant working distance is obtained. b) Parallel operation of the microelectrodes in a soft array allows high-throughput imaging and surface modification.

The soft probe can be seen as a giant SFM cantilever with integrated microelectrodes. Therefore, the concept is comparable to the SFM-SECM hybrid technique (compare Figure 16c), but with larger dimensions. The soft probe can follow the main topography of the sample, *e.g.* if the substrate is curved. Limitations will arise with 3D structures that are smaller than the width of the probe. The probe will not slide down into little holes and, contrary, small obstacles will lift off the entire array. In this way, the electrochemical reactivity can be measured independently from the topography of the substrate. Additionally, a tip crash with the surface, which can destroy the probe or the sample, will be avoided when using appropriate parameters. Experiments can be started without prior sample tilt elimination. Moreover, the soft probes are compatible with standard SECM setups, since no additional instrumentation is required. Despite of this, topographic information is not recorded. If needed, it can be obtained by other techniques such as SFM or CLSM.

High-throughput SECM imaging and modification can be achieved by extending the number of microelectrode inside one probe to an array of individually addressable electrodes, as shown schematically in Figure 20b. The distances between the microelectrodes will be large enough to keep interferences by diffusion layer overlapping between adjacent electrodes negligibly small.

6.2 Further Development of Instrumentation and Software

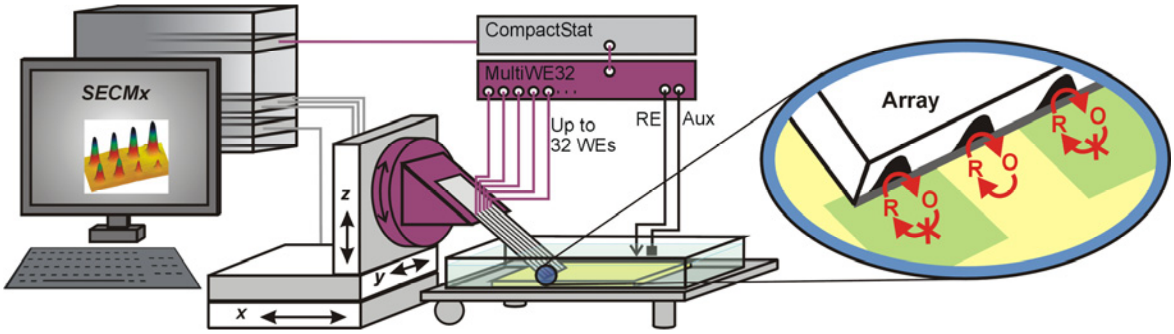

Figure 21. Schematic representation of the modified SECM setup. In comparison to the standard SECM setup (Figure 1) a module MultiWE32 for the potentiostat was implemented to address up to 32 working electrodes individually. A custom-made holder was developed to preset an inclination angle of the soft probe and to adjust the alignment of the probe and the sample. Both new components are colored in purple for an easier differentiation.

In order to control experiments using soft linear microelectrode arrays the basic SECM setup of the Wittstock group had to be expanded. In a schematic representation of the in-house made instrumentation, the new parts are colored in purple (Figure 21). New hardware was required to address individually the microelectrodes of an array. A new multi potentiostat module, namely MultiWE32, was purchased Ivium Technologies

(Eindhoven, The Netherlands). This device is an extension to the bipotentiostat CompactStat which was already used in the Wittstock group for several years. The MultiWE32 can operate with up to 32 WEs via one Aux *vs.* one RE and is controlled via the CompactStat. Details about the device are given in Section 6.2.1. The soft microelectrode array is mounted in a custom-made holder providing the electronic connection and allowing the alignment of the eight probe channels with respect to the sample by taking advantage of a worm drive. The holder was constructed to set an inclination angle of the probe of 20° with respect to the surface normal. Details will be discussed in Section 6.4.

6.2.1 Integration of a Multipotentiostat Module

The MultiWE32 is connected via an M/F HD15 cable to the CompactStat that contains an AD/DA converter for data acquisition and its own microprocessor. This enables the communication between CompactStat and personal computer (PC) via the USB interface. The system can be fully controlled by the Ivium software IviumSoft or by custom-made software. IviumSoft has always to be launched during runtime also when using user-designed software to control the Ivium devices. The CompactStat was already integrated in the SECM system of the Wittstock group and the bipotentiostat can be controlled in the software SECMx via the DLL `drv_ivium_bipot.dll`. A new DLL for the MultiWE32 was created by the author. Basic functions and commands like “Connect device and PC” were adopted from the DLL for the CompactStat, but the control of up to 32 WEs required new algorithms and routines. A new setup window was created in order to allow the experimenter to initialize the MultiWE32 and to enter hardware settings such as the current range, filter and so on. The DLL `IVIUM_remdriver.dll` was provided by Ivium and was integrated by the author into the DLL `drv_ivium_we32.dll` after transformation into a static library (LIB). Then the LIB `IVIUM_remdriver.lib` communicates via IviumSoft with the hardware. On the one hand this system is convenient because commands such as “Apply a potential” and “Read a current” are sent and everything is controlled by IviumSoft. On the other hand this can cause critical situations as described in the following. The data handling such as filtering cannot be influenced. Filters provided by Ivium have to be used. Furthermore, the processing time inside the digital device can take some milliseconds which limits the frequency of the communication between the PC and the device. In comparison, up to 100,000 values per second can be recorded if channels of an analog device are read with commercial AD/DA boards. If software is not well programmed, the interplay between two running programs can become problematic. Especially when these programs and/or drivers were created in different programming languages, the implementation has to be done with care. In the course of this thesis several bugs were uncovered in the third party software tools and diagnosed/corrected in cooperation with the manufacturer. One example illustrates the type of problems that can occur in such situation. While running SECMx and sending commands like “Read value”, an error message occurred in IviumSoft that stopped IviumSoft and also the SECMx software in inregular intervals. The author quickly figured out that the bug did not originate in our SECMx software but in IviumSoft. However, the problem could only be solved during a two day visit to the company. The staff from the company and the author discovered that IviumSoft issued timer events and communicating with the hardware simultaneously to the commands sent by our SECMx hardware abstraction layer. This caused randomly a crash in the Ivium Software. The bug was fixed by implementing a new routine that disables Ivium function calls if the communication between MultiWE32 and SECMx is desired.

Besides the programming of the DLL, essential changes had to be made in the main SECMx application with respect to data acquisition, storage and plotting. New class structures were implemented. Program code is not given in this thesis, but basic conceptual ideas are described in the following sections.

6.2.2 Array Concept in SECMx

In order to control arrays of electrodes the program structure was modified. Electrodes of one array are handled as a collection of identical channels. In the software SECMx this is called a “bundle”. This concerns for example the channel (Figure 22) and data structure (Figure 23). Figure 22 shows the channel structure with derived classes for data recording using the Ivium CompactStat and MultiWE32. Both devices are digital and thus their channels are derived from the class `InChannel` which is derived itself from the generic class `Generic Channel`. The CompactStat is representative for other bipotentiostats implemented in SECMx. For each working electrode a class `CustomInUSBChannelWE` derived from `InChannel` exists in the DLL `drv_ivium_bipot.dll`. In these classes, the functions to read a current value of the corresponding working electrode are called and then controlled by Ivium via the `IVIUM_remdriver.lib`. For the MultiWE32, two new classes were added in the main program in order to address the 32 working electrodes individually or simultaneously. These are the classes

`InChannelOfBundle` and `InChannelBundle`, respectively, which are both derived from `InChannel` and located in the DLL `drv_ivium_we32.dll`. The difference between both classes is that 32 custom channels are derived for the individual working electrodes from the former class whereas only one class to control the 32 working electrodes simultaneously is derived from the latter.

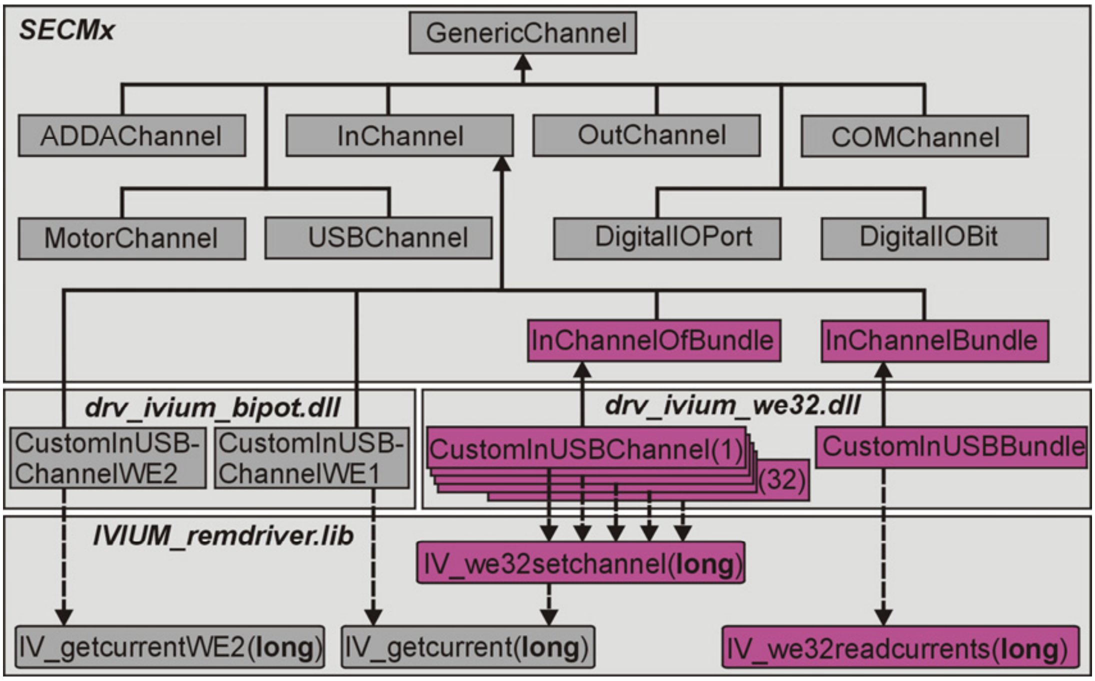

Figure 22. Combined schematic representation of channel class structure and function call in SECMx using digital channels to read current values. New digital channels for reading 32 current values are colored in purple.

This means for data recording that in a simultaneous mode all 32 channels are read simultaneously within 100 ms (value specified by Ivium). This is controlled in the class `CustomInUSBBundle` and the function call `IV_we32readcurrents(long)` (long is the data type). Alternatively, the individual channels are activated and read sequentially. This is organized in the classes `CustomInUSBChannel` in which the functions `IV_we32setchannel(long)` and `IV_getcurrent(long)` are called. The acquisition of an individual channel requires 20 ms (value specified from Ivium). Therefore, all 32 channels will be read theoretically within 640 ms. The simultaneous mode is faster, but, due to instrumental limitations when addressing 32 channels at the same time, the measured signals are less tolerant to noise. In sequential mode, the signal from one electrode is actively recorded at a time and the noise level is lower. For each experiment the experimenter can decide whether to measure all channels sequentially (“sequential”) or simultaneously (“multiplex”). SECMx was programmed in the way that a user-defined number of channels is used. These channels are called “active lines” in SECMx. In simultaneous mode, all 32 channels are read by IviumSoft, but only the values of the active channels are transferred to SECMx. In sequential mode, only the active lines are addressed and read. The active lines also play an important role in the new data structure as described in the following.

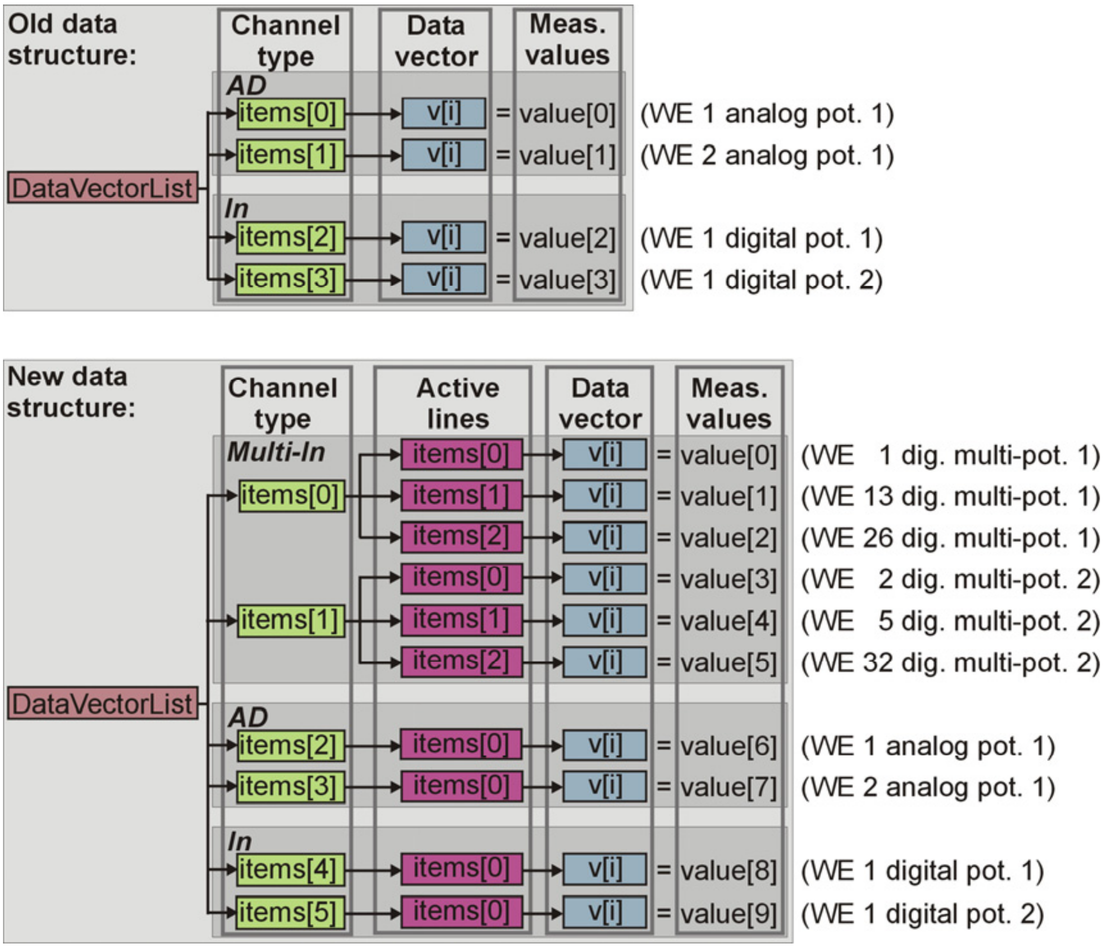

Figure 23. Schematic representation of the old and new SECMx data structure. The “Active Lines” structure was inserted (colored in purple) in order to provide multichannel data storage.

The measured data are stored in a new data structure (Figure 23). In the old structure, each input channel type had one data vector (Figure 23, upper panel). A new level was required to store the measured values from the MultiWE32. This new level represents the active lines of an input channel type (Figure 23, lower panel). Therefore, the current values of several active working electrodes are stored in separated data vectors that belong to one channel type. For the classical channel types including AD and digital input channels, there is always one active line for the single working electrodes.

6.2.3 New Experiments with Array Probes

New generic experiments were integrated into SECMx for using arrays of microelectrodes. These include “Cyclic voltammetry bundle”, *x*,*y* and *z* “Line scan bundle”, “x-t chart recorder bundle”, and “2D image bundle”. The program code is based on the established corresponding experiments for single electrodes with the addition to control the multipotentiostat channels as well as to read, store and plot the array of data.

6.2.4 New Lift-Off Mode for Imaging

For recording an image with soft probes, the probe will be brought into mechanical contact with the sample. A special holder with a preset angle provides suitable bending of the probe (Section 6.4). Afterwards, the probe starts a horizontal forward line scan in the so-called “high frequency” (HF) direction as shown schematically in Figure 24a and 25.

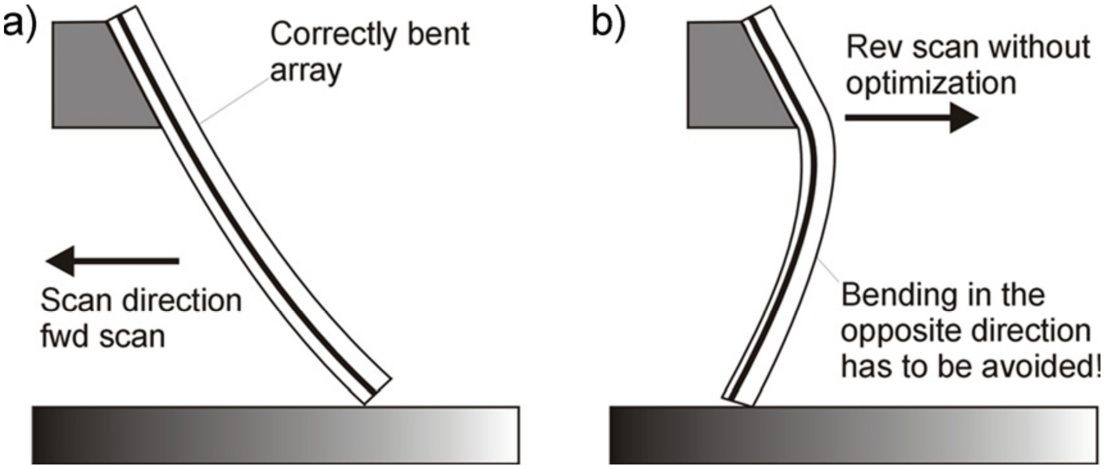

Figure 24. Schematic representation of contact mode SECM using soft probes. a) Forward line scan. b) A probe movement in the reverse direction without retracting the probe would cause a bending of the soft probe in the opposite direction.

The term HF indicates the probe’s coordinate change with a higher frequency than in the perpendicular horizontal direction. The latter one is named “low frequency” (LF) axis. Due to the construction of the probe holder, the HF direction is set to the *x* and the LF direction to the *y* axis, because the HF direction must be in the direction of the probe inclination. During the line scan, currents are measured at the end of each programmed step. After the end of the line scan, the probe has to be repositioned to the starting position. The probe is moved back the HF scan length and after a small step into the LF direction, the next HF forward line scan can be started. With conventional UMEs this is carried out in constant height mode. This would damage the soft probes due to mechanical pressure that is exerted by bending in the opposite direction (Figure 24b). Delamination of the polymer films could occur and abrasion of the soft materials could decrease the quality of the measured signals. Additionally, a continuous re-bending could shift the exact *x*- and *y*-positions of the microelectrode. This problem was solved by a new lift-off (LO) mode which is shown schematically in Figure 25. After completion of a HF forward line scan, the probe is retracted from the sample surface by a defined stroke height so that the probe is freely suspended in the solution. Then the probe is horizontally moved back the HF scan length with fast translation rates (up to 1000 µm s^{-1}) without current recording until the starting position is reached. Although the measurement of currents is possible, the electrodes are too far away from the sample to detect any sample properties. After an incremental step in the LF direction, the probe re-approached by the negative value of the stroke height in order to bring it again into mechanical contact with the sample. Then the next HF forward line scan in contact mode is started. The stroke height, retraction speed and re-approach speed can be selected.

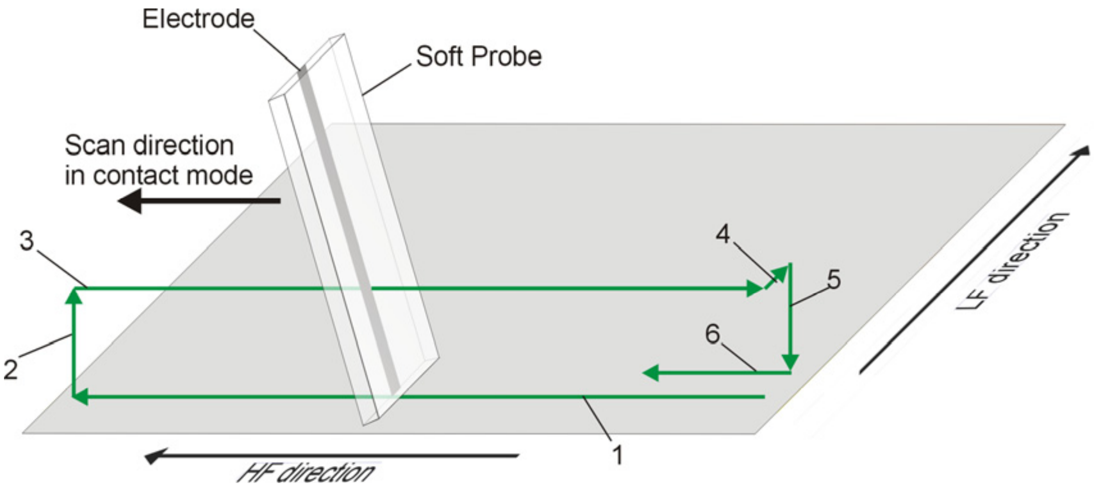

Figure 25. Schematic representation of SECM imaging with new lift-off mode using a soft probe. 1, fwd line scan of HF axis; 2, lift-off; 3, reverse scan; 4, step of LF axis; 5, re-approach.

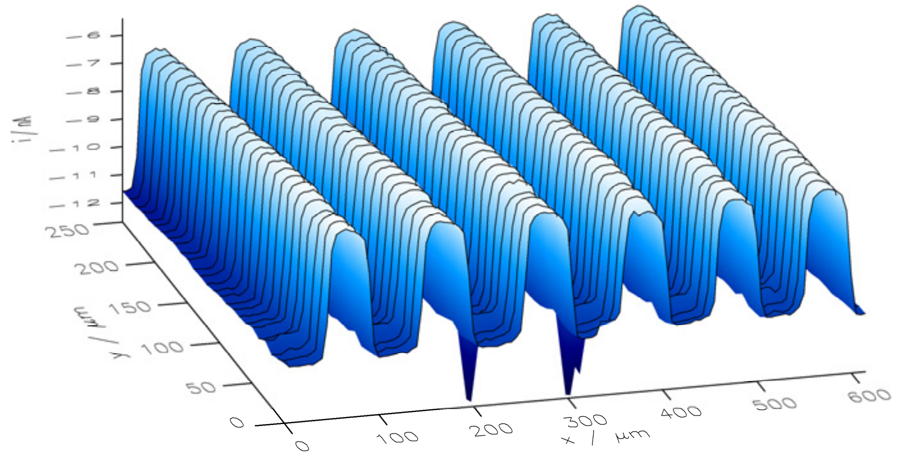

Figure 26: SECM feedback mode image of a gold band structure on glass with lift-off mode using a soft probe with one silver microelectrode. The stroke height was 300 µm with respect to the *z*-position during contact mode. The probe was retracted with 100 µm s^{-1} and re-approached with a speed of 20 µm s^{-1}. Electrolyte solution 2 mM $[Ru(NH_3)_6]Cl_3$ and 0.1 M Na_2SO_4. E_T = -0.6 V *vs.* Ag-QRE, step size 5 µm, translation rate 50 µm s^{-1}.

Figure 26 shows one exemplary image of a gold band structure on glass scanned by a soft probe with a silver microelectrode (preparation in section 6.3.3). In this example, the stroke height was 300 µm which was applied with a retraction speed of 100 µm s^{-1}. Re-approaching is usually performed with a slower translation rate (here 20 µm s^{-1}) in order to avoid possible delamination of the polymeric films or abrasion of the probe materials due to a high pressure released at high speeds. The measurement itself showed a nice current contrast for the gold ($i_T \approx$ -12 nA, positive feedback) structure on glass ($i_T \approx$ -7 nA, negative feedback) using $[Ru(NH_3)_6]^{3+}$ as redox mediator.

The LO mode was programmed very flexibly. It can be applied to the three axes in space meaning also scanning of vertically oriented substrates. The user can decide if to retract the probe during the imaging experiments or not. A very interesting option is the point-to-point LO routine which was also included in SECMx. This option retracts a microelectrode or tip in-between the lateral steps. Thus the probe is retracted during lateral translations and it is in contact for the measurement. In this way, a UME could scan highly viscous polymeric substrates such as cathodic materials for Li-ion batteries.[248] The UME is brought into mechanical contact with the delicate substrate and *e.g.* local impedance measurements could be performed with a UME in direct contact with the substrate. Without the point-to-point LO the UME would scratch on the surface while scanning. The scanning mode including LO opened the way for SECM applications using the soft carbon microelectrode array (Sections 6.3.1, 6.5, and Chapter 7),[A2,A3,A8] gold microelectrode array (Sections 6.3.2 and 6.5)[A6] and silver microelectrode array (Figure 26 and Section 6.3.3), Fountain Pen[A1] and Push-Pull.[A4,A7] Fountain Pen and Push–Pull are described briefly in Section 6.2.5.

6.2.5 Application of Cooperation Partners Enabled by Hardware and Software Development

The software and hardware development allowed the application of other new soft SECM probe types by our cooperation partners in Lausanne. Microfluidic systems were integrated into the soft probe design to image in contact regime the local surface reactivity of initially dry substrates.[A1,A4,A7] First, the Fountain Pen was introduced which contained one carbon microelectrode channel, a Aux/RE, and one open microchannel in order to deliver nanodroplets of electrolyte solution.[A1] The amperometric measurements were enabled at the probe tip where the sample surface area, the WE, and the Aux/RE were in contact with the minimum electrolyte solution droplet. Imaging in contact mode was enabled by the LO mode (Section 6.2.4). A disadvantage was that a wet track of electrolyte solution r on the substrate contaminating the sample and causing precipitation due to solvent evaporation. Therefore, the further development of microfluidic soft probes, namely the Push–Pull, included a second open microchannel for continuous aspiration of the electrolyte solution (Figure 27).[A4,A7] The soft probes with microfluidics allow scanning of delicate samples that cannot stay over long periods inside electrolyte solutions. The microfluidic probes also circumvent solvent evaporation by continuously renewing the electrolyte solution droplet at the probe tip. Metal band structures on horizontally and vertically oriented substrates were scanned.[A4] The fast translation rate of 1000 µm s^{-1} during reverse scans with retracted probe (Section 6.2.4) was required since the delivery and aspiration of the nanodroplet volume at the freely suspending probe was less stable. If the stationary condition is lost, it will not automatically be regenerated in contact mode. Therefore, this situation has to be avoided.

Very attractive is the option to combine SECM with other analytical techniques such as mass-spectrometry (Figure 27) which was introduced for the first time thanks also to the LO mode.[A7] The aspirated solution of the Push–Pull can be analyzed and provides additional information about the substrate which are not achievable by amperometric detection. For example, the reactivity of a latent human fingerprint contaminated with the explosive picric acid was scanned by SECM and the explosive was detected by matrix-assisted laser desorption/ionization mass spectrometry (MALDI-MS).[A7] The activity of immobilized enzymes was investigated by combining SECM with electrospray ionization mass spectrometry (ESI-MS).[A7]

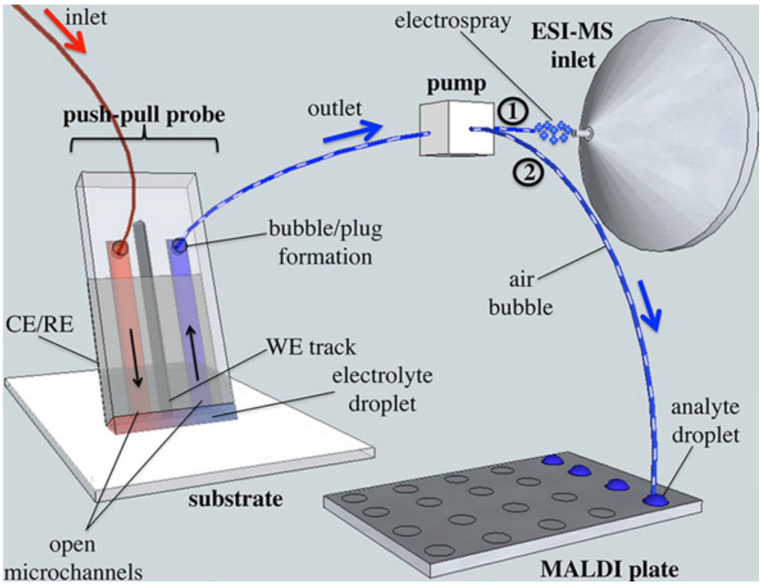

Figure 27: Schematic representation of the general operation principle of the Push–Pull combined with ESI-MS (1) or MALDI-MS (2) tools. (Figure as published in [**A7**].)

6.3 Fabrication and Characterization of Soft Microelectrode Arrays

In the course of this PhD research project, three types of soft microelectrode arrays were developed taking advantage of various microfabrication techniques suitable for batch production, such as UV laser ablation, Aerosol-Jet® printing and inkjet printing. These tools led to the successful application of carbon, gold and silver microelectrode arrays. The soft arrays are all based on the same basic design principle. Conductive tracks are deposited on thin polymeric sheets and an even thinner insulating layer is coated on top. The active electrode areas are achieved by exposing the cross-section of the conductive tracks using mechanical or laser-assisted cutting. Currently an 8 channel design is used as shown schematically in Figure 28a. The practical realization as carbon microelectrode array is depicted in Figure 28b.

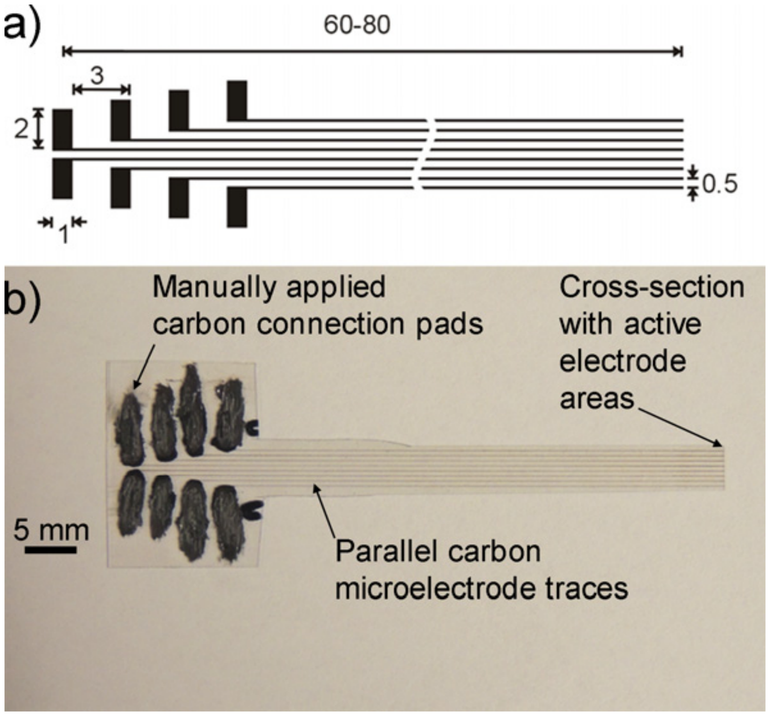

Figure 28. Basic design of linear arrays consisting of 8 microelectrodes. a) General dimensions applied for all used microfabrication tools. All specified dimensions are given in mm. b) Optical photograph of a carbon microelectrode array.

A midpoint-to-midpoint distance between electrodes of 500 µm was selected in most cases in order to minimize the overlap of the diffusion layers between adjacent individual electrodes. Barker *et al.*[65] proposed an electrode distance of 120 µm for 10 µm diameter electrode in order to have a smaller diffusion layer thickness than half of the distance between two neighboring electrodes. FEM simulations by the cooperation partner showed that diffusional overlap between neighboring electrodes (*i.e.* 500 µm midpoint–midpoint distance and 40 µm electrode width) produced a current difference of 2.1% in comparison to a single electrode during an approach curve. No differences among inner and outer electrodes were obtained.**[A2]** Therefore, the used design made a good compromise between parallelization and cross-talk. In order to connect the microelectrodes to the multi-potentiostat 1 mm × 2 mm patterns are created at the end of the tracks as shown on the left side of Figure 28a. The predefined pads are enlarged by manually applying carbon ink to produce contact areas as shown in Figure 28b. The 8 channel design made a good compromise between the evaluation of the experimental performance and the inception of high-throughput scanning. In parallel to the fabrication of linear arrays the development of another kind of soft probes was started at the EPFL within our joint project. The UV laser ablation allowed integrating empty channels inside the soft probes for delivery and aspiration of electrolyte solutions for various applications as described in Section 6.2.5.

6.3.1 Soft Carbon Microelectrode Arrays

Soft linear microelectrode arrays consisting of carbon microelectrodes were used most frequently in this thesis. The design and the fabrication process was adopted from the Soft Stylus Probes developed by our cooperation partners at the EPFL.[249] The Soft Stylus Probe consisted of one carbon microelectrode. Thus, a linear array is the extension from a single electrode channel to 8 parallel lines and required modified electronic connections. The concept was developed at the EPFL within the joint project due to the availability of a UV laser ablation system. The author prepared probes by himself during the stays in Lausanne. The basic steps of the fabrication protocol are shown in Figure 29.

Firstly, microchannels with 10 – 30 µm depth, 15 – 50 µm width and 7 cm length were engraved by UV photoablation with a 193 nm ArF excimer laser beam (Lambda Physik, Göttingen, Germany, fluence = 0.25 J, frequency = 50 Hz) into 100 µm thick polyethylene terephthalate (PET) films. The pulsed beam was directed to a fixed metallic mask including a small gap. During pulsing the substrate was moved with continuous velocity in order to achieve uniform channel dimensions (*i.e.* width and depth). The channels were uniformly separated either by 250 µm or 500 µm (midpoint-to-midpoint distance). Afterwards, the channels were filled manually with carbon ink and cured at 80°C for one hour. The sintered carbon tracks were then covered and sealed with an insulating Parylene C layer. Parylene C is a polymer (poly-monochoro-*p*-xylylene) which is formed on a substrate at ambient conditions by a pyrolyzed dimer. The thickness can be defined with high precision at the used automatic Parylene deposition system. The Center of MicroNanoTechnology (CMi) at the EPFL used different thicknesses of the Parylene C coating on a weekly basis and the author selected one of these when a deposition was required. Therefore, the applied varying thicknesses usually did not have a specific reason. They did not influence significantly the result of experiments. In this thesis, carbon arrays with Parylene C layers between 1 µm and 10 µm were used. Electronic connection pads for the individual electrodes were prepared by manually applying carbon ink with a spatula followed by a curing process.

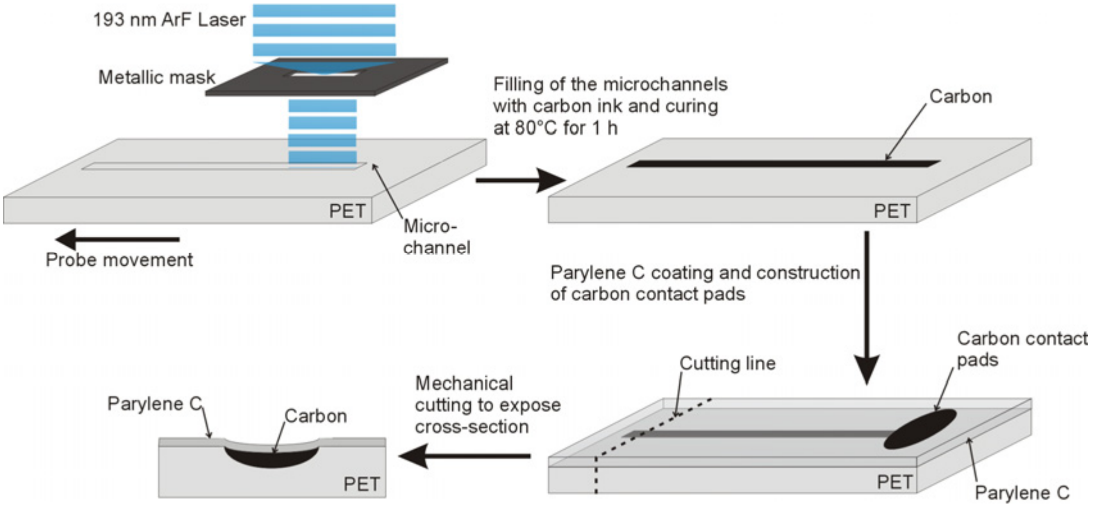

Figure 29. Representation of the protocol to fabricate soft carbon microelectrodes. (Figure as published in SI of Ref. [**A8**].)

The cross-section and therefore the active electrode areas were exposed by mechanical cutting with a razor blade mounted in a custom-made cutting device or by laser ablation. A refresh of the active electrode areas was required after each SECM image. This was also performed by cutting, since mechanical polishing for reactivation cannot be performed for soft electrode arrays for the following reasons. In our group, flat polishing pads are used which are mounted at discarded computer hard disks that can be rotated with a motor. The soft probes are very flexible and therefore it is difficult to preserve the exact geometry while polishing on a rotating disk. On the other hand it was impossible to place all the individual electrodes aligned with the polishing disk surface because no positioning control is currently available. Optical inspection was not possible in the micrometer scale. In addition the hard disks rotate sometimes in a wobbling way. Furthermore, the rotation rate at the outer part of the disk was faster than inside. Therefore, more material was removed at the outer part of the array when it was fixed perpendicular to the rotation direction. When placing the array parallel to the rotation direction, the removal of material was also inhomogeneous over the length of the cross-section. During polishing the rotating disk was wetted with deionized water in order to remove the particles. However, an accumulation of material at the probe could be observed which could cause delamination of the Parylene C layer. This problem became worse when embedding the probe in a resine intended to increase the stiffness and to be removed by acetone after the polishing. Therefore, cutting with a laser or a razor blade was much faster and more effective. Many tries were made to find the best and fastest way of cutting. Better results were obtained when the electrode site of the soft probe was facing the blade or laser. Blade cutting with electrode structures down snapped off the Parylene C coating. Currently, no suitable laser is available in Oldenburg for laser ablation. Therefore, cutting was performed with a razor blade. However, it is not trivial and influences the result of experiments. The cut has to be very straight. Otherwise the working distances of the individual channels will vary. This was observed when using a manually operated scalpel blade. To overcome this limitation a guillotine-like cutting device was developed in which the blade could be fixed straight (Figure 30).

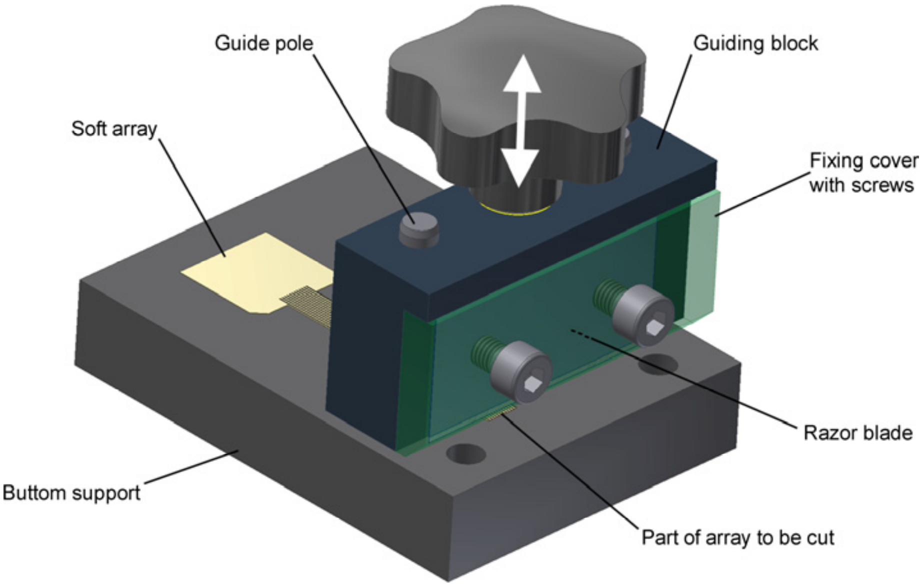

Figure 30. Schematic of the custom-made cutting device to cut the soft microelectrode arrays. (Schematic was kindly provided by F. Roelfs, workshop of the University of Oldenburg.)

For each cut, a fresh blade was used and cleaned in isopropanol in an ultrasonic bath to remove the oily film usually present on commercial razor blades. When cutting soft materials there is always a deformation of material especially when entering. Therefore, a second thin polymeric film (100 µm PET or 125 µm PI) was placed on top. The array and the film were fixed with an adhesive tape. Cut arrays could be used several times for many hours until electrochemical signals significantly lost quality. If the deactivation of the microelectrode or abrasion of the polymeric materials occurred, fresh electrode surfaces were simply created by a new razor blade cut.

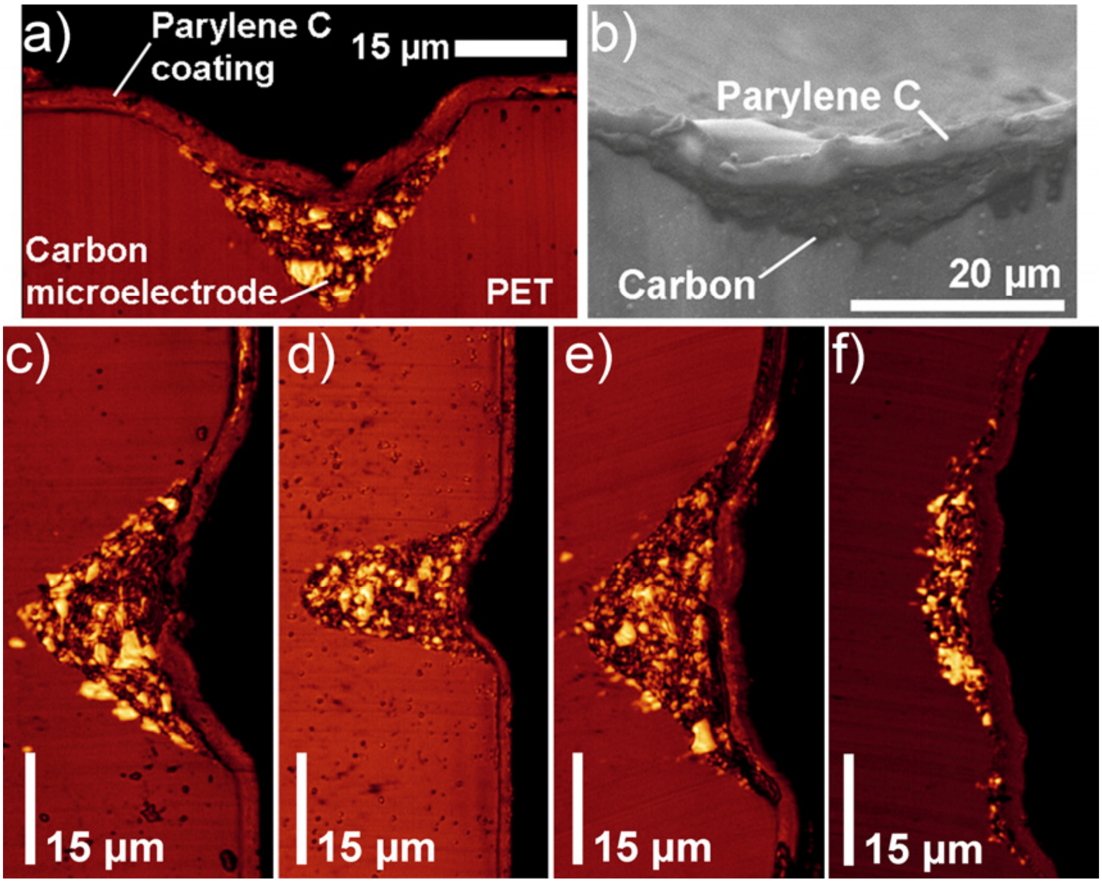

Figure 31. Six carbon microelectrodes of different arrays cut with a fresh and cleaned razor blade were measured by CLSM (a,c-f) and SEM (b). For the SEM image the probe was wetted with an ionic liquid in order to provide electronic conductivity. (a) and (c) as well as (b) and (f) are electrodes from the same array.

The cross-section of the active carbon electrode areas was investigated by CLSM and SEM. Figure 31 shows six microelectrodes from four different arrays of four different batches. All cross-sections were exposed by cutting with a razor blade. The structure of the microelectrode in Figure 31a shows that, in contrast to standard UMEs consisting of a flat polished Pt disk electrode, sintered particles constitute the active electrode area. The exact composition of the ink is not known and was not investigated. Therefore, no assumptions about residues from the solvent or other compounds can be made. The PET film as support and the Parylene C coating are easily identifiable. In SECM experiments in contact mode the Parylene C layer will face the sample. From all images in Figure 31, it can be seen clearly that the carbon electrodes are recessed. The carbon tracks shrink during the sintering process reducing the thickness of the electrode. But also the geometries vary. This is due to the quality of the laser ablation process, which was not stable during this PhD research project. It changed from batch to batch which can be explained by the overall runtime of the system (more than one decade) and by the slight variations of the setup due to different operators with different applications. In Figure 31, the electrode shapes appear as triangles with one curved site (a,c,e), and as distorted sickle with different aspect ratios (b,d,f). The variations of eight electrodes within one linear array are of much higher importance. Table 7 shows exemplarily the active areas *A* of the individual microelectrodes *k* in one array investigated by CLSM.

Table 7: Active areas of eight individual microelectrodes in one exemplary array. Measured with CLSM.

k	1	2	3	4	5	6	7	8
A (µm^2)	263.50	254.96	240.41	256.53	178.42	243.31	272.92	220.48

A mean value of 241.32 µm^2 with a standard deviation of 30 µm^2 (12 %) can be calculated. UMEs with a microelectrode radius of r_T = 12.5 µm have an area of 490.87 µm^2. Therefore, the carbon microelectrodes are about the same dimensions. The overall shape of the carbon electrodes is identical, but the slight variations in their sizes in one array are given by the fabrication process and not negligible. The pulsed laser beam in combination with the continuous movement of the substrate during the ablation process can vary the depth and width of the fabricated microchannels. In addition, the manual filling with carbon ink leads to minor variations in the thickness. Furthermore, each cut of the polymeric materials to expose a fresh cross-section is different resulting in different areas. Therefore, the areas vary depending on the batch and on the cut for each individual electrode. These limitations in the fabrication process were known from the beginning but did not represent a road block for the main goal of this thesis, *i.e.* reactivity imaging and modification of large samples. The variation of the responses between individual electrodes can be leveled by calibration routines (Section 6.5.4). Experiments like approach curves to extract quantitative data such as reaction rates constants at the substrate require well-defined electrode shapes and were never intended to be performed with the soft electrode arrays described here. Therefore, the electrode areas of all used arrays are not given in this thesis. Cyclic voltammograms in 2 mM FcMeOH were recorded to characterize the electrochemical behavior of the microelectrodes (Figure 32). A sigmoidal response was obtained as expected for a microelectrode. This indicated hemispherical diffusion together with low charging currents as a consequence of a good sealing between the carbon track and the covering Parylene C coating. The differences in the steady-state currents were due to the slightly varying electrode geometries and sizes. The average of the absolute steady-state current was equal to 5.35 nA with a standard deviation of 0.5 nA (9 %). No attempts were made to calculate the exact active electrode area of the electrodes, which consisted of a sintered composite material. Also the roughness after cutting was unknown. Due to the arbitrary shape in contrast to the well-defined disk-shaped UMEs the standard equations for the diffusion-limited currents could not be applied. However, these information are of minor importance for qualitative reactivity imaging.

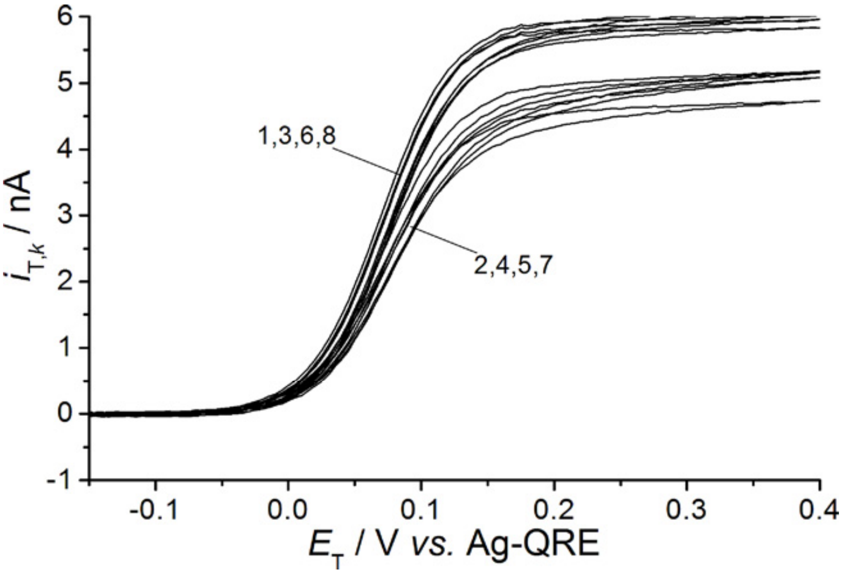

Figure 32. CVs of one array with eight carbon microelectrodes exposed by blade cutting in 2 mM FcMeOH and 0.1 M KNO_3. Potential scan rate 20 mV s^{-1}. All electrodes were measured simultaneously.

In order to investigate the quality of the active microelectrode areas, a wave-slope analysis of the CVs was performed by plotting the applied potential E as a function of $\log[(i_{T,\infty,k}-i_{T,k})/i_{T,k}]$ where $i_{T,\infty,k}$ are the diffusion-limited currents of the individual electrodes and $i_{T,k}$ is the current measured at the corresponding E (Figure 33). The calculated slopes are -62.2 mV, -64.9 mV, -61.0 mV, -69.5 mV, -65.0 mV, -60.8 mV, -74.3 mV and -60.2 mV. The differences to the theoretical value of -59.1 mV[81] for a reversible system are most likely due the internal resistance of the carbon tracks and limitations of the electron transfer rate at the active electrode area. For the Soft Stylus Probe a sheet resistance of 12.8 kΩ could be estimated by the cooperation partners for a carbon track of 5 cm length and a width of 30 µm.[249] For a current of 5 nA this would result in an iR drop of 0.064 mV. The carbon microelectrodes yielded good electrochemical responses. The variations of geometries and current responses of the individual electrodes were around 10 %, which represents a good value with respect to the used preparation protocol.

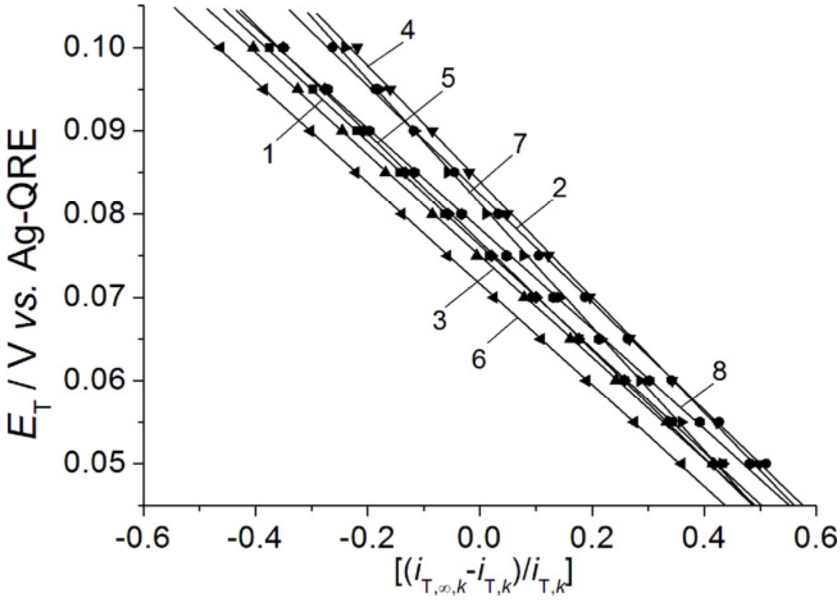

Figure 33. Wave-slope analysis for a reversible system of the eight microelectrodes. Symbols represent measured values and the lines the individual linear fits.

6.3.2 Soft Gold Microelectrode Arrays

The gold microelectrode arrays were fabricated using the Aerosol Jet® printer work station (Optomec Inc., Singer, Albuquerque, USA) installed at the Fraunhofer Institute for Manufacturing Technology and Applied Materials Research (IFAM) in Bremen. Aerosol Jet® printing was used to save the preparation steps of microchannel fabrication and filling (Section 6.3.1), and to deposit the electrode material directly onto the substrate with high reproducibility. The substrate (125 µm thick Kapton HN® film from Goodfellow) was cleaned with isopropanol and dried under a stream of nitrogen. The basic design in Figure 28a with 8 lines of about 6 cm length, a midpoint-to-midpoint distance of 500 µm using and contact areas was transferred into CAD-format and was loaded in the Optomec software. During printing the substrate was constantly heated up to 55°C. The translation rate of the substrate was 3 mm s^{-1}. It can happen that the flow of aerosol towards the sample interrupts during printing for a microsecond. This effect occurs when the ink is accumulated at the nozzle which can happen in particular when printing over longer periods. Therefore, the lines of some arrays were printed two times. In order to remove the solvent and to achieve electrical conductivity between the gold nanoparticles of the ink, the substrate was sintered at ambient conditions for 2 h at 400 °C. The substrate was placed in the oven at room temperature. The temperature was ramped up with a rate of 1 K min^{-1} until 400 °C and hold there for 2 h. Afterwards, the sample was cooled down to room temperature with 1 K min^{-1}. This slow heating and cooling rate is important, since a not negligible amount of organic additives (sodium citrate or polyvinyl pyrrolidone; ink description in Section 5.1) is used for stabilization of Au nanoparticles in the ink, and a complete removal of these compounds is required. Otherwise, the electronic conductivity is restricted and the structure tends to form cracks, which completely interrupts the conductivity of the tracks. Depending on the printing parameters, the obtained line widths were either 40 µm (one time printing) or 50 µm (two times printing) for all tracks in one array. The probes were then coated by a 200 nm thick Parylene C coating in Lausanne. This thickness is quite small and was chosen to achieve a small working distance because the height of the active gold electrode areas was only around 1 µm (*vide infra*). The electronic connection pads for the individual gold tracks were made in the same way as for the carbon microelectrodes. A cross-section of the gold array structure was exposed by UV laser ablation or by cutting with a razor blade as described in Section 6.3.1 for the carbon electrodes.

A top view of one array with eight sintered gold tracks is shown in Figure 34a. The array was cut out from the film along the dashed line. Scratching with a surgical scalpel cannot demolish the gold tracks from the PI film due to an excellent adhesion (result not shown). The midpoint-to-midpoint distance between two adjacent electrode tracks was 500 µm and the width of an individual track in this array was approximately 50 µm (Figure 34b), *i.e.* the inter electrode spacing was 450 µm. A line width of about 40 µm was also used which was achieved by a change of the printing parameters. During the sintering process at 400 °C the PI film underwent relaxation.[250] The thickness of the film increased except for the areas covered with gold. As a consequence, the gold tracks appeared to be slightly recessed from the surrounding polymer sheet as can be seen in the topographic SFM image (Figure 35a-b). This made it difficult to investigate the height of the Au gold tracks by SFM. Two horizontal line scans along the black and gray line were extracted from the SFM image and plotted in a two-dimensional graph (Figure 35b).

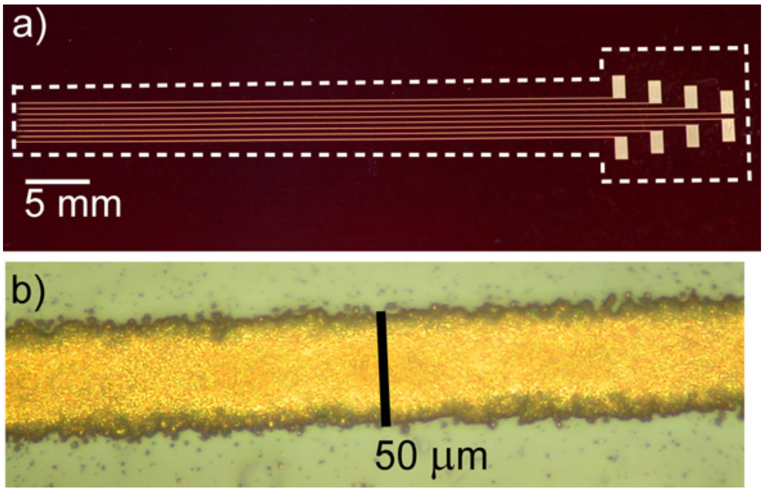

Figure 34. a) Optical photograph of printed gold structure on polyimide film after sintering. The dashed line indicates the shape of the array after fabrication. Midpoint-to-midpoint distance was 500 µm. b) Optical micrograph of a single sintered gold track with a width of 50 µm. (Images slightly modified from Ref. [**A6**].)

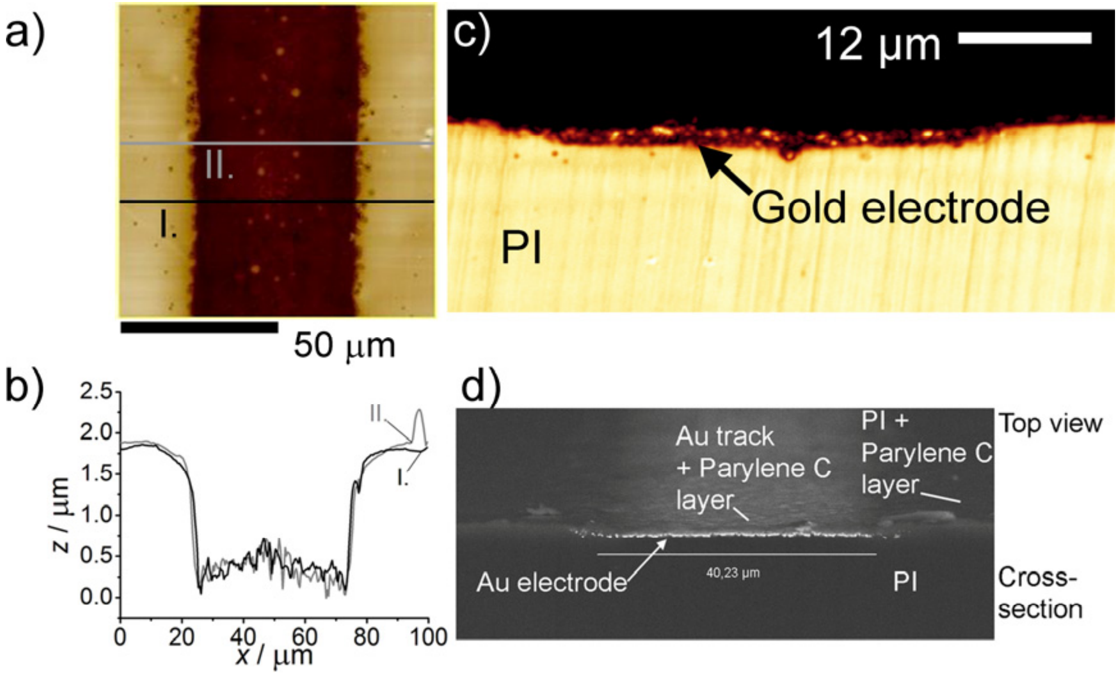

Figure 35. a) Topographic SFM image of one sintered gold track with a width of 50 µm. Two extracted topographic line scans demonstrated that the gold electrode sunk into the PI film (b). c) CLSM reflection image of one cross-section covered with Parylene C coating. Cutting was performed with a razor blade. d) SEM image of a different electrode of the same array with a tilted view on the cross-section. (Images slightly modified from Ref. [**A6**].)

The PI film swelled next to the gold track, which was nearly 1.3 µm recessed from the polymer film surface. The gold structure consisting of sintered nanoparticles is readily identifiable. Alternatively, the height of the gold microelectrode could be obtained from the CLSM image of the cross-section after Parylene C coating (Figure 35c). The Parylene C layer of 100 nm was too thin to be identifiable in the CLSM image. The gold microelectrodes had a shape of a band electrode with a width of 40 µm and a height of 1.67 µm giving an area of approximately 67 µm^2. The SEM image also shows the recess of the gold electrode (Figure 35d). A spike on pure Kapton HN® can be obtained in the grey colored topographic line scan in Figure 35b. These features are observed all over the polymer sheet after sintering at 400 °C and are considered as real. The described relaxing process during sintering may cause this change. This could be proven in an SFM topographic image of pure Kapton HN® after sintering and is shown in Figure 36.

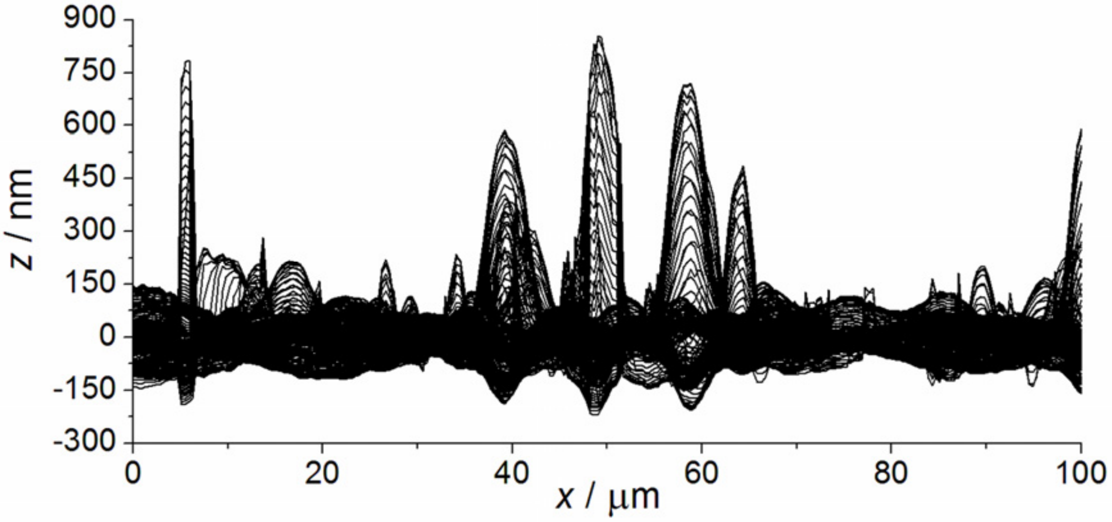

Figure 36. Multiple 2D plot of a topographic SFM image of a pure Kapton HN® area of 100 µm × 100 µm after the sintering process. (Figure slightly modified from SI of Ref. [**A6**].)

The heights of the spikes can reach 1 µm. Therefore, they are much higher than the thickness of the Parylene coating and the thickness of the active electrode area. As will be discussed in Section 6.4, this can significantly influence the working distance and the SECM feedback current. The electrochemical reactivity of the sintered gold tracks before the Parylene C coating was checked with shear force-based SECM in feedback mode. During scanning of an area of 700 µm × 500 µm including two unbiased Au tracks the nanoelectrode was kept at a constant working distance. The electrochemical reactivity as well as the topographic information of the sample were recorded simultaneously by reading the nanoelectrode current and the position signal of the piezo actuator applied to retain a constant *d*, respectively. Figure 37a shows a stacked 3D plot of the measured SECM current and topographic signal. A line scan is shown in Figure 37b.

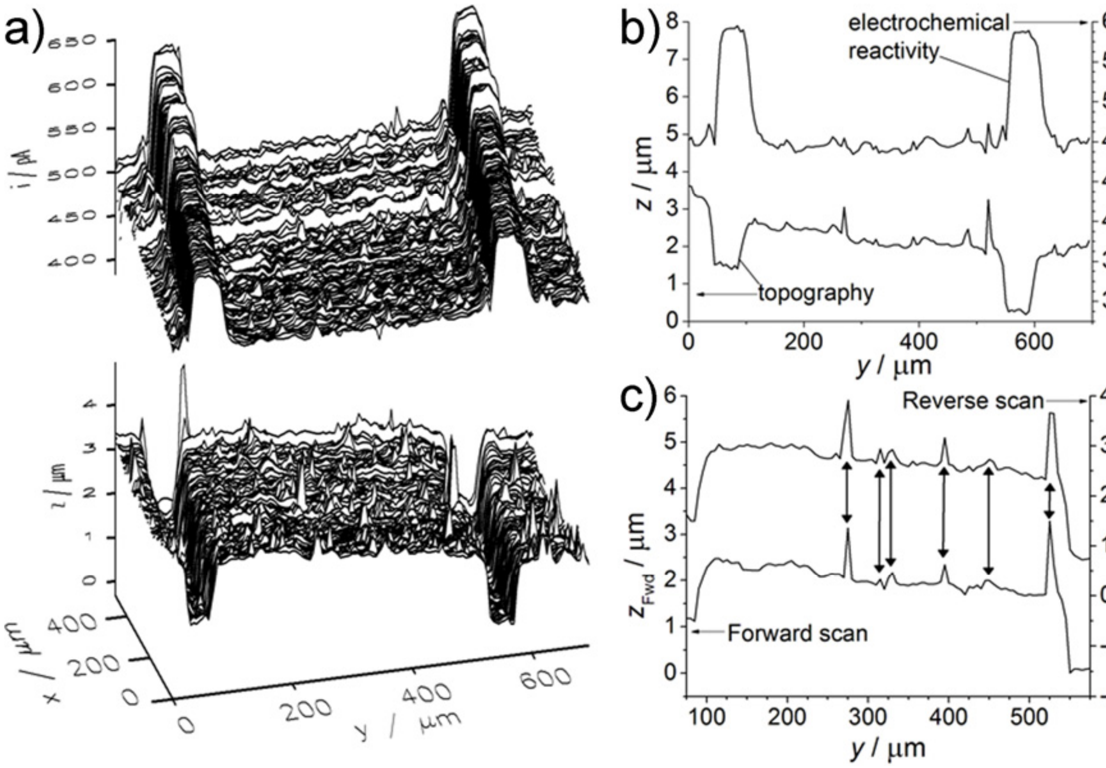

Figure 37. Shear force based SECM image (a) and line scan (b) of two sintered Au tracks with simultaneously measured surface reactivity (top) and topographic information (bottom) in aqueous 2 mM FcMeOH and 0.1 M KNO_3; E_T = 0.3 V *vs.* Ag-QRE, translation rate 25 µm s^{-1}, step size 5 µm. c) Topographic forward and reverse line scan of the same area. Significant spikes located at the same *y*-positions are indicated by vertical arrows. (Results published in Ref. [**A6**].)

The measured currents over the gold tracks are significantly larger than over the PI film due to positive feedback and the homogenous electrochemical reactivity indicated the successful sintering process. The nanoelectrode moved down over the gold area following its recess, but the sintered nanoparticle structure could not be detected due to the dimensions of the used shear force nanoelectrode. Suspicious in the topographic image are the spikes over pure PI as observed and discussed in the SFM image (Figure 36). They were obtained in the forward and in the corresponding reverse scans in the topographic image as exemplarily shown for one forward and reverse scan in Figure 37c. The six double arrows point to identical spikes at the same lateral positions. In addition to the SFM data, the shear force experiments proved that the measured heights can be considered as real features rather than noise or artifacts from the electronic feedback. The gold microelectrode arrays were electrochemically characterized after Parylene C coating and razor blade cutting by cyclic voltammetry in 2 mM FcMeOH solution at 10 mV s^{-1}. Figure

38a shows a CV of an array with six connected microelectrodes. Capacitive currents are higher than expected from the geometric area. This is caused by the preparation from a nanoparticle aerosol and from the laser cutting process. A local melting of the probe materials caused by the laser beam may change the sintered Au nanoparticle structure.

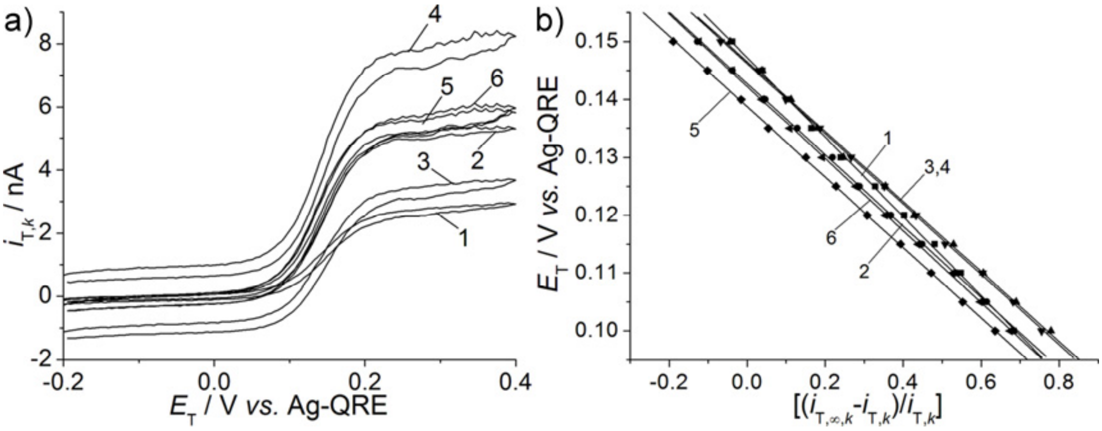

Figure 38. a) CVs of one array with eight gold microelectrodes exposed by laser cutting in 2 mM FcMeOH and 0.1 M KNO_3. Potential scan rate 10 mV s^{-1}. All electrodes were measured simultaneously. b) Wave-slope analysis for a reversible system of the six microelectrodes. Symbols represent measured values and the lines the individual linear fits. (Figures slightly modified from Ref. [**A6**].)

Sigmoidal responses were obtained for all electrodes demonstrating steady-state behavior. The shift of two CVs along the current axis was probably caused by a cross-talk between these two electrodes. This happened when two or more tracks were electrically short-circuited by an overlapping of the carbon pads. It was obtained rarely. The manually applied connection pads represent a weakness of the fabrication process. Some investigations were made in this direction, but are not presented in this thesis. The carbon pads can be separated by scratching with a scalpel blade. However, if they remain short-circuited, also with a resistance of some MΩs, the Ivium device shifts the CVs in positive and negative direction. When using all channels simultaneously it did not influence the reactivity imaging, because the internal resistance of the tracks is some orders of magnitude lower. The shift can be corrected afterwards (Section6.5.4). The slopes -68.6 mV, -61.5 mV, -60.5 mV, -60.8 mV, -60.8 mV, and -62.3 mV were calculated for the individual electrodes in Figure 38b for the wave-slope analysis for a reversible system. The slopes are slightly larger than the theoretical value of -59.1 mV. This can be explained similarly as for the carbon electrodes with limitations due to the internal resistance of the gold tracks. A resistance of $R = 8.13\ \Omega$ was measured using the four point method. The specific resistance ρ was calculated by

$$\rho = R \cdot \frac{A}{l} \tag{18}$$

where $l = 2$ mm is the length and $A = 83.63\ \mu\text{m}^2$ is the area of the cross-section of the measured gold track. This yielded a specific resistance of $\rho = 3.4 \times 10^{-7}\ \Omega$ m and hence a measured conductivity of $\sigma = 2.94 \times 10^6$ S m^{-1} which is 6.5 % of the value for bulk gold material. The large difference is due to the nature of sintered nanoparticles providing a resistance for the electron transfer. However, the measurements proved the electrical connection between the Au nanoparticles and a homogenous removal of the organic additives in the gold containing ink during sintering.

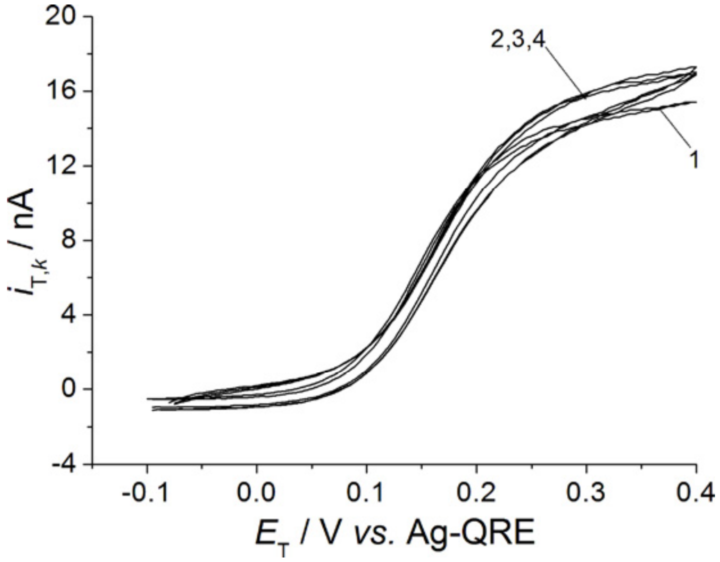

Figure 39. CVs of one Au microelectrode after blade cutting in 2 mM FcMeOH and 0.1 M tetra-butylammonium trifluoromethane sulfonate dissolved in acetonitrile. Each of the individual cycles was performed directly after renewal of the solution. CVs were taken after 0 min (curve 1), 30 min (2), 60 min (3) and 90 min (4). Potential scan rate was 20 mV s^{-1}. (Figure slightly modified from [**A6**].)

One advantage of the Au microelectrodes over carbon as electrode material is their tolerance to organic solvents such as acetonitrile. The used polymeric materials PET, PI and Parylene C resist most organic solvents, but the carbon ink can be dissolved. Figure 39 shows several CVs of one single Au microelectrode in 2 mM FcMeOH in acetonitrile with a potential scan rate of 20 mV s^{-1}. The first CV was taken directly after immersing the probe in solution. A steady-state behavior can be seen. Within 30 min, the response of the electrode changed slightly, but was then stable also after 60 min and 90 min. Before recording each of the CVs in Figure 39, the electrolyte solution was renewed in order to provide comparable conditions without influences by evaporated acetonitrile. The arising capacitive currents can be explained by residues from not completely removed organic additives that were stabilizing the Au nanoparticles in the ink and that were dissolved in acetonitrile. However, the structure is stable as can be seen from the CVs. The gold microelectrodes may also be used with a more diverse range of redox mediators and compounds which are difficult to convert at carbon electrodes (O_2, H_2O, H_2/H^+).

6.3.3 Soft Silver Microelectrode Arrays

The characterization and use of silver microelectrode arrays was performed in collaboration with Daniel Witte during the preparation of his MEd thesis for which the author provided practical guidance. Inkjet printing is an established technique to produce patterns with high accuracy and is suitable for batch production. It is easily operable and represents an example of simple array probe fabrication. The printing process itself was the core part of the MEd thesis of D. Witte which contains specific details.[181] Briefly, the Dimatix Materials Printer (DMP) 2831 (Fujifilm Dimatix, Inc., Santa Clara, USA) was used to print the silver lines (ink description in Section 5.1) on 125 µm thick Kapton HN® films. A 30 µm drop-spacing was chosen in order to assure good overlapping and track conductivity. A standard waveform provided by the printer's manufacturer was used. The cartridge was heated up to 35 °C whereas the substrate was left at room temperature during printing. Afterwards, the ink was sintered for 20 minutes at 200 °C. For this purpose, the sample was placed in a pre-heated oven.

A typical example of sintered silver lines is shown in Figure 40a with a midpoint-to-midpoint distance of 100 µm. The lines were printed as a test sample for SECM reactivity imaging and had a width of 51.66 (± 0.81) µm. Due to a much lower temperature required for sintering the Ag ink (200 °C) compared to the used Au ink (400 °C), the PI film did not undergo relaxation. Therefore, the Ag tracks did not "sink" into the Kapton HN® film and the height of the tracks was measured by SFM.[181] With 200 nm height the cross-section of the band-like shaped silver microelectrodes after sealing have a calculated area of approximately 10 μm^2. Using the four point method and Eq. (18) yielded a specific resistance of $2.4 \times 10^{-7}\ \Omega$ m and a conductivity of 4.1×10^{6} S m^{-1} which is 6.7 % of the value for bulk silver.[181] This result is very close to the results for sintered Au microelectrodes. The standard design for an array of eight microelectrodes was printed with a midpoint-to-midpoint distance of 500 µm between silver lines and a Parylene C coating of 3 µm was deposited. During a one week stay of the author at the EPFL, no other thickness was provided by the clean room facilities. Compared to the height of the silver lines this thickness was too much as discussed in Section 6.4.

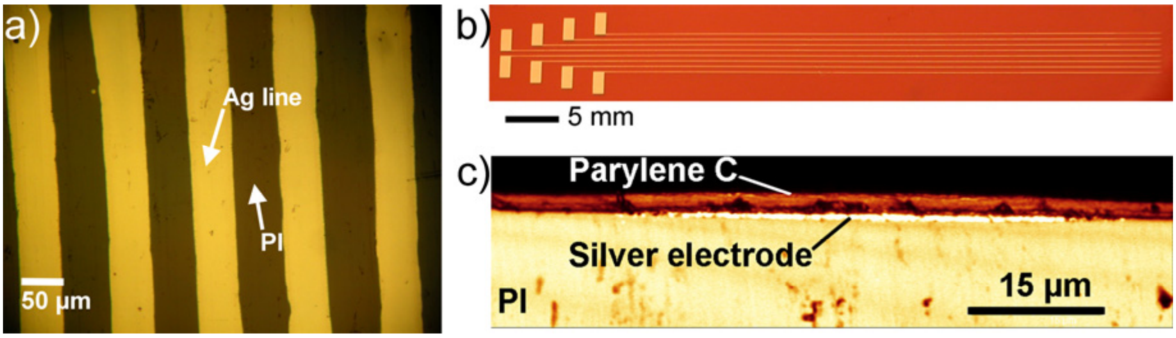

Figure 40. a) Optical micrograph of sintered Ag lines with a midpoint-to-midpoint distance of 100 µm as a test sample. b) Optical micrograph of the printed structure for usage as soft linear microelectrode array. c) CLSM reflexion image of the cross-section of one Ag microelectrode after deposition of a 3 µm Parylene C coating and cutting with a razor blade.

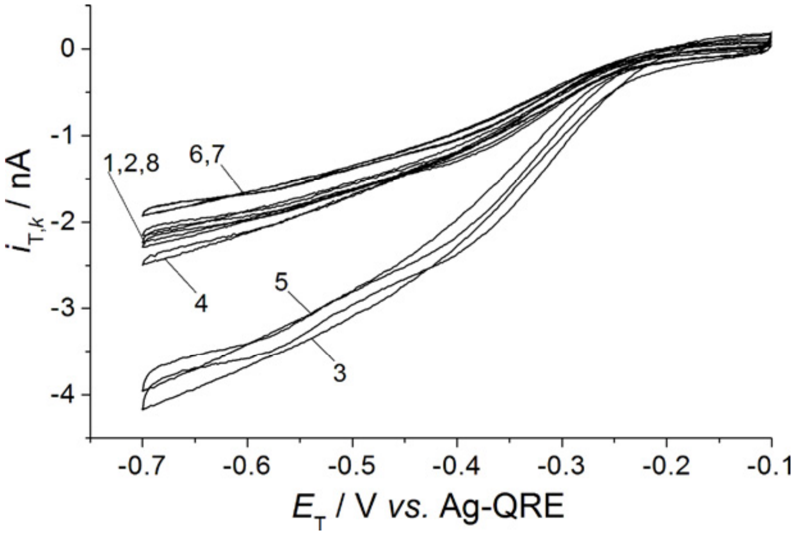

Figure 41. CVs of one Ag microelectrode array after blade cutting in 2 mM $[Ru(NH_3)_6]Cl_3$ and 0.1 M Na_2SO_4. Potential scan rate was 1 mV s^{-1}.

Silver has a low redox potential and started to dissolve anodically already at potentials around 0.5 V *vs.* Ag-QRE which overlays with the oxidation of FcMeOH. Therefore, the redox mediator $[Ru(NH_3)_6]^{3+}$ was used that is reduced at -0.3 V *vs.* Ag-QRE. The CVs in Figure 41 show that no steady-state behavior exists for the reduction of the redox mediator at the silver microelectrodes. The influence of oxygen reduction was not determined and will contribute to the overall current.

6.4 Vertical Positioning of the Soft Probes

The arrays were mounted in a custom made holder with a preset inclination angle γ of 20° with respect to the surface normal and the Parylene C coated carbon, gold or silver tracks were facing the sample as shown schematically in Figure 42a. Two exemplary approach curves to gold and to glass were recorded with one soft carbon microelectrode (Figure 42b). The currents increased or decreased until the probe reached mechanical contact with the sample. Approaching was continued and the probe started to bend slightly. In this situation the distance between sample and active electrode area of the probe remains almost constant (Figure 20a) and causes constant currents (Figure 42b). In order to assess the influence of the bending soft probe on the working distance, some geometric considerations were developed. The array has a vertical length l_{T} (in unbent state) and a height of the attachment point above the sample h_{A} as shown in Figure 42a, left panel. The vertical difference between these two points defines the important quantity h_{P}.

$$h_{\mathrm{P}} = h_{\mathrm{A}} - l_T \tag{19}$$

h_{P} becomes negative when the probe continues approaching after mechanical contact between probe and sample. α represents the angle between the sample surface and the probe surface including the active electrode areas. Depending on the cutting angle used to expose the cross-section of the probe, α is smaller or equal γ when the array is placed in solution bulk. After mechanical contact, α increases with decreasing h_{P}, so that it may exceed γ. t_{L} represents the thickness of the thin insulating Parylene C layer and considers also the recess of the individual electrodes. All these quantities are required for calculation of the effective working distances in contact and contactless modes (c or cl, Eqs. (20) and (21)).

$$\text{cl: } d_{\mathrm{cl}} = h_{\mathrm{P}} + t_{\mathrm{L}} \cdot \sin(\alpha);\, h_{\mathrm{P}} \geq 0 \quad \text{(contact - less regime)} \tag{20}$$

The working distance after contact with the sample is calculated by

$$\text{c: } d_{\mathrm{c}} = t_{\mathrm{L}} \cdot \sin(\alpha);\, h_{\mathrm{P}} < 0 \quad \text{(contact regime)} \tag{21}$$

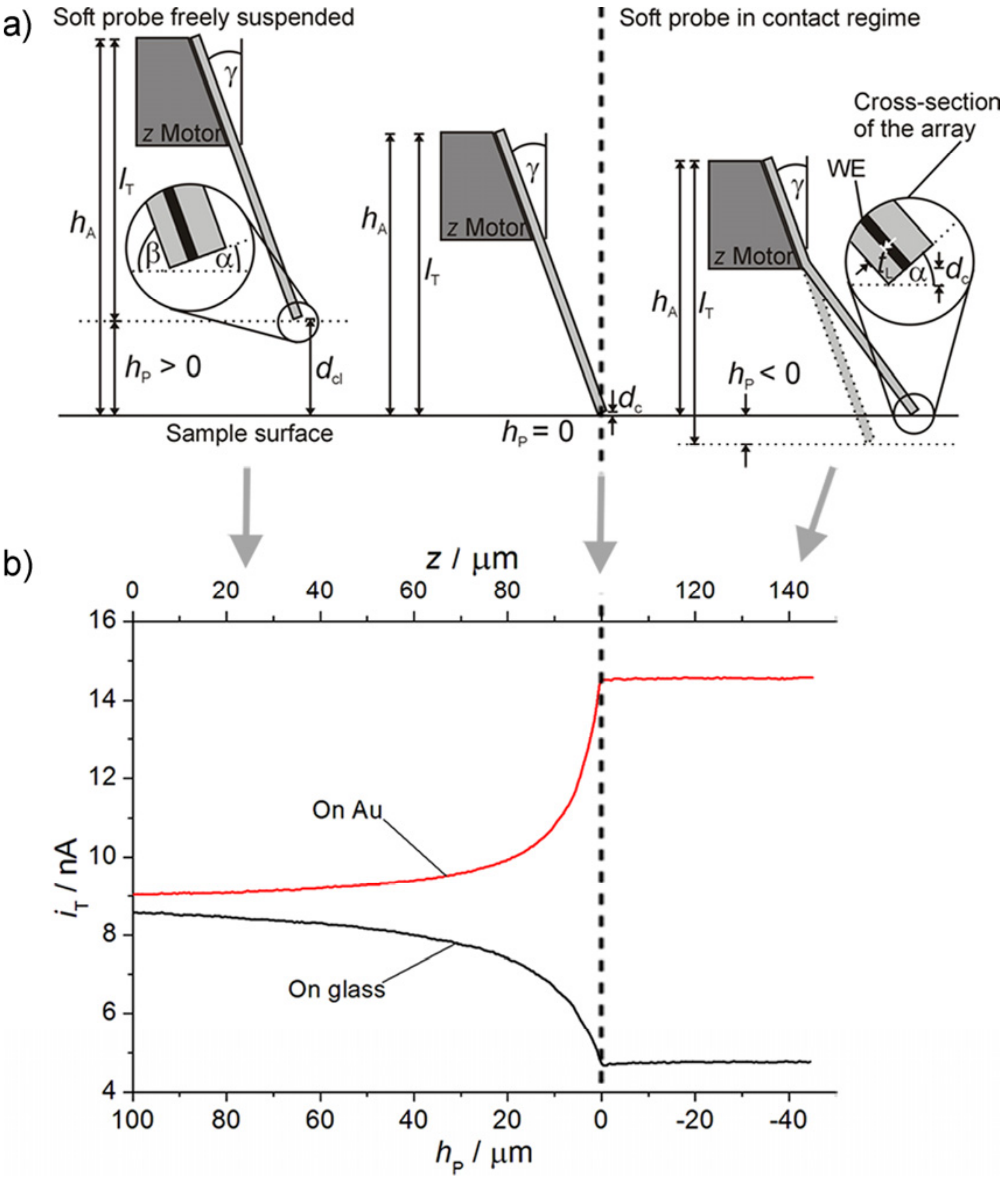

Figure 42. a) Schematic representation of the soft probes mounted in the custom made SECM and performing an approach curve. b) Two experimental approach curves to glass and to gold using one soft carbon microelectrode in 2 mM FcMeOH and 0.1 M KNO_3 are shown. Step size 0.5 µm. After contact with the sample the currents stay almost constant due to the sliding probe. The top *x* axis shows original *z* values and the buttom *x* axis shows the h_P values.

Taking into account the geometries and inclination angle the working distances *d* do not approach 0 µm. In addition, the recess of the electrodes avoids mechanical contact with the substrates. To conclude, it can be stated that if the probe is in contact with the sample ($h_p \leq 0$ µm), *d* is almost always larger than 0 µm and represents a constant value.

When using an array of eight microelectrodes, the alignment of the probe with respect to the LF axis of the substrate surface can be of importance. Figure 43 shows three approach curves to glass with a soft carbon microelectrode array consisting of eight microelectrodes in feedback mode. In comparison to Figure 42 where the x axis represents the z values, in Figure 43 and in all following Figures containing approach curves, the x axis represents the h_P values. The currents are original values and were not normalized.

The cross-section of the array including the active electrodes was approached under various tilt angles φ that describe the misalignment in the LF direction of the sample surface. These angles are approximated values and were calculated by information extracted from the approach curves. The distances between channels are known and the protrusion of the array whose edge makes the contact with the sample was about the same size (500 µm) as shown schematically in the inset in Figure 43a. The working distances of tilted probes where assumed by comparison with the approach curve without tilt (Figure 43c). With φ = 4.6° the measured feedback current did not decrease significantly. In particular for electrode no. 8 the blocking effect caused by the insulating surface did not appear. Further approaching did not decrease d. This is a very important information. The probes are flexible and they bend in the HF direction, but they are stiff enough to keep d constant. In order to assess the result, the currents when the probe touches the sample ($h_p = 0$ µm) were normalized by Eq. (22) and the values of Figure 43a-c are listed in the Table 8.

$$I' = \frac{i_{T,k}\left(h_P = 0\,\mu\mathrm{m}\right)}{i_{T,\infty,k}} \tag{22}$$

Table 8. Calculated normalized currents I' at h_p = 0 µm.

K	1	2	3	4	5	6	7	8
I' (φ = 4.6°)	0.92	0.93	0.94	0.95	0.97	0.97	0.98	0.99
I' (φ = 1°)	0.74	0.76	0.80	0.82	0.86	0.85	0.88	0.90
I' (φ = 0°)	0.52	0.48	0.43	0.47	0.58	0.45	0.50	0.51

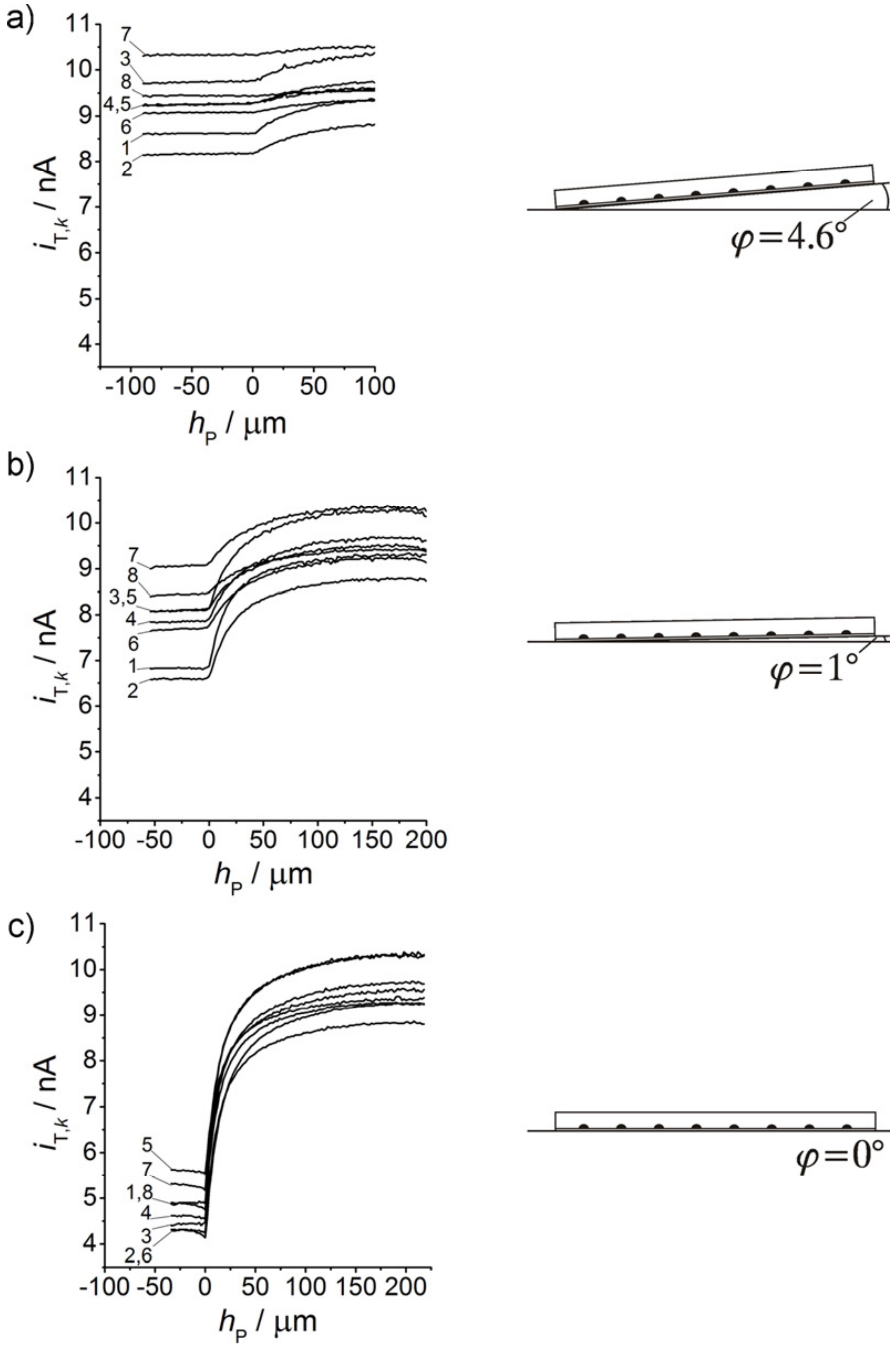

Figure 43. Feedback mode approach curves to glass with a carbon microelectrode array of eight electrodes demonstrating the influence of probe-to-sample alignment. Electrolyte solution 2 mM FcMeOH and 0.1 M KNO_3. Step size 2 µm and translation rate 5 µm s^{-1}. Estimated tilt angles φ are 4.6° (a), 1° (b) and 0° (c).

The tendencies are clear. With 4.6° the values for I' are close to $i_{T,\infty,k}$ in the solution bulk. This angle is quite big and can be identified by eye. Therefore it represents an extreme value for demonstration. More realistic is a value around 1° where a much better hindered diffusion was realized. A probe aligned to the surface (φ = 0°) reaches values for I' of about 50% of $i_{T,\infty,k}$. These can be reached in general with the holder system and blade cutting. With UMEs a much smaller working distance can be achieved indicated by the I_T values in the experimental approach curve to glass in Figure 5. This has to be considered when such small working distances are required for specific tasks. In general, a probe-sample-alignment is not required. Scanning is quickly possible with good results. However, for optimum resolution, alignment of the probe in the LF direction is recommended as described below. In addition, the working distance cannot be normalized by the radius as done for UMEs (Figure 6). The geometries are completely different and vary from array to array. However, for high-throughput imaging it is not required, whereas it must be re-emphasized that soft microelectrode arrays are not suitable for quantitative kinetic studies in which knowledge of exact working distances, electrode shapes and bulk currents is indispensible.

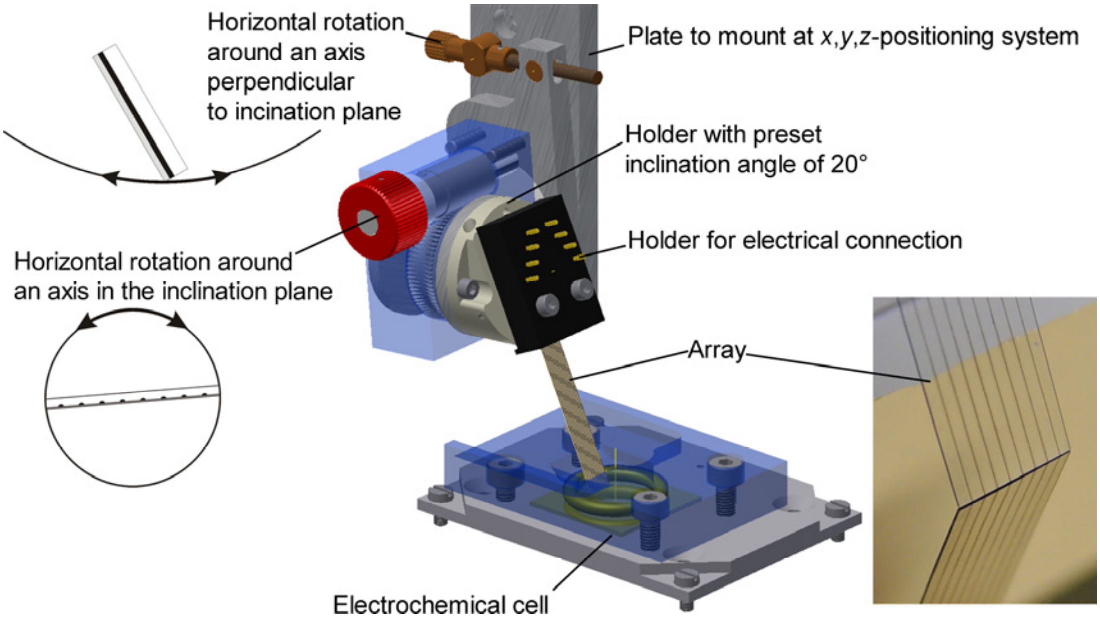

Figure 44. SECM holder system for soft linear arrays of eight microelectrodes. The array is placed in a holder component with a preset inclination angle of 20°. This angle can be modified as shown in the upper left part. Probe-to-sample alignment can be achieved by a worm drive. (Schematic of holder and cell was kindly provided by F. Roelfs, workshop of the University of Oldenburg, optical photograph kindly provided by C. Dosche, University of Oldenburg.)

In order to align the array and sample surface, a new holder system was developed (Figure 44). The probe was mounted to a component with a preset inclination angle of 20° with respect to the surface normal. This inclination angle could be varied by an additional screw that rotated horizontally the main holder. This was one of the last developments in the author's PhD project and was not extensively used. The influence on the current contrast was not significant in first tests. In all measurements in the thesis, the inclination angle was 20°. However, a small negligible variation can be caused when the soft array itself is slightly pre-bent. A worm drive allowed horizontal rotation of the array for the probe-sample-alignment. Therefore, approach curves were performed before imaging in order to determine h_p and to align probe and sample. The smaller the active microelectrode areas of soft probes are the more important becomes the closest achievable working distance. Figure 45a and b show approach curves to gold and glass using one gold microelectrode array.

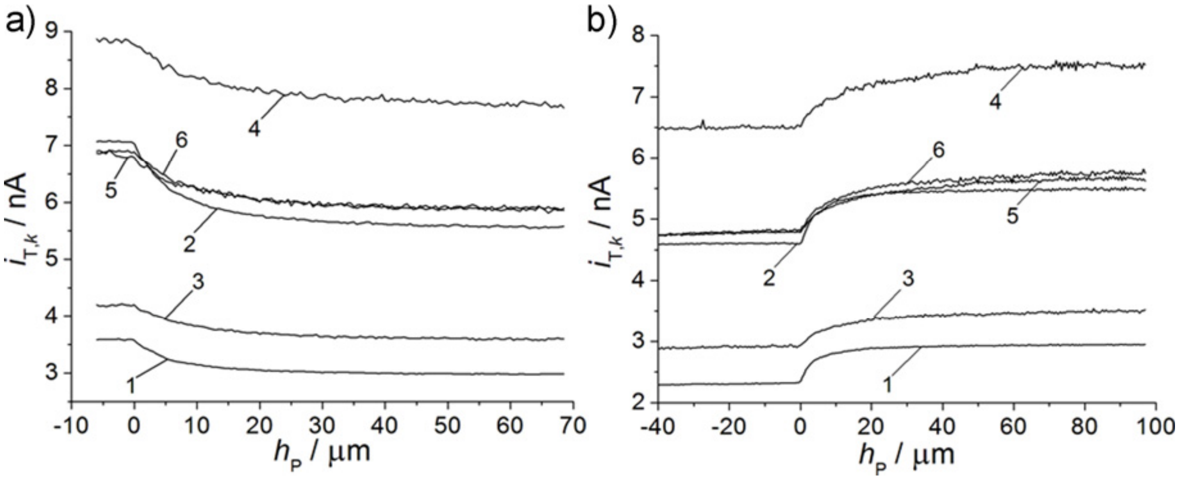

Figure 45. Feedback mode approach curves to gold (a) and to glass (b) of a gold microelectrode array with six electrodes after laser cutting. 2 mM FcMeOH and 0.1 M KNO_3. Translation rate 2 µm s^{-1}; E_T = 0.35 V *vs.* Ag-QRE. (Images slightly modified from Ref. [**A6**].)

It can be seen clearly, that the current increase or decrease is much less than for the carbon microelectrode arrays. A cross-section of a gold electrode is shown in Figure 35. Although the thickness of the Parylene C layer was only 100 nm, the working distance could not be decreased significantly. This can be explained by the topographic features in the PI film. They were measured in the range of up to 900 nm preventing a closer approach of the microelectrodes to the substrate. In addition, cutting procedures by blade cutting and laser cutting can lead to a deformation of the materials increasing the working distance. Electrodes are also recessed and their shapes vary slightly.

Even more difficult was the operation of silver microelectrode arrays. These band-like microelectrodes were much smaller in one direction than the gold microelectrode. The height of the silver tracks was just 0.2 µm. In addition, the Parylene C coating thickness was 5 µm, which was a too high value for this electrode thickness. Figure 46 shows one exemplary approach curve of a Ag microelectrode array towards glass in 2 mM $[Ru(NH_3)_6]Cl_3$ and 0.1 M Na_2SO_4. Some electrodes did not detect the influence of the sample at all. This cannot be explained by a probe-sample misalignment as indicated by the relative position of the microelectrodes. Microelectrode no. 2 showed the highest effect of hindered diffusion in contrast to no. 1 and no. 3 that showed less and no negative feedback behaviour at all. Some electrodes in this array did not work due to insufficient adhesion of the carbon connection contact pads to the Ag lines. Alternatively, the deformation or delamination due to razor blade cutting may change the electrode geometry or block the active electrode areas.

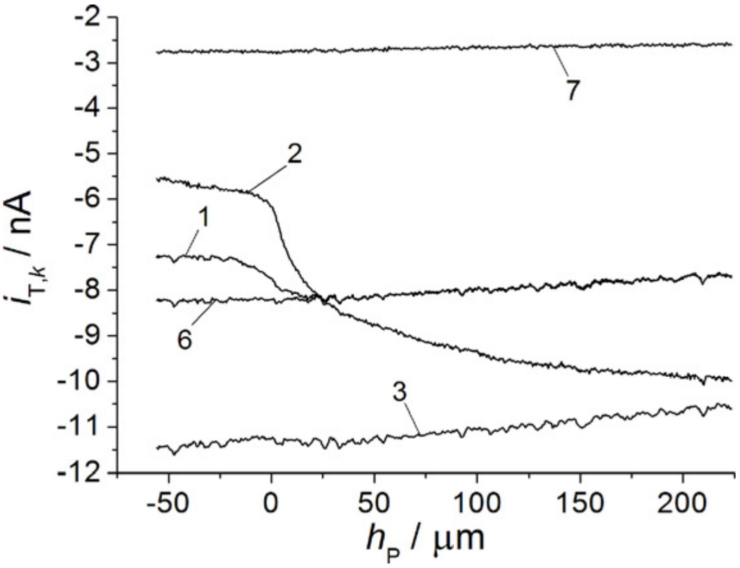

Figure 46. Approach curves to glass of one silver array with five Ag microelectrodes (out of eight) in 2 mM $[Ru(NH_3)_6]Cl_3$ and 0.1 M Na_2SO_4. E_T = -0.6 V *vs.* Ag-QRE, step size 0.5 µm, translation rate 1 µm s^{-1}.

In the following, approach curves were used to detect the sample surface and to determine and control the h_p value. They were also applied for the probe-sample alignment. However, imaging is also possible with a tilted probe as long as the surface features cause a change of the probe signal.

6.5 High-Throughput Surface Reactivity Imaging Using Soft SECM Probes

For high-throughput imaging soft linear arrays of microelectrodes are used. In order to scan areas of square centimeter size the imaging routine as described in Section 6.2.4 had to be further modified in SECMx.

6.5.1 Multiple Imaging

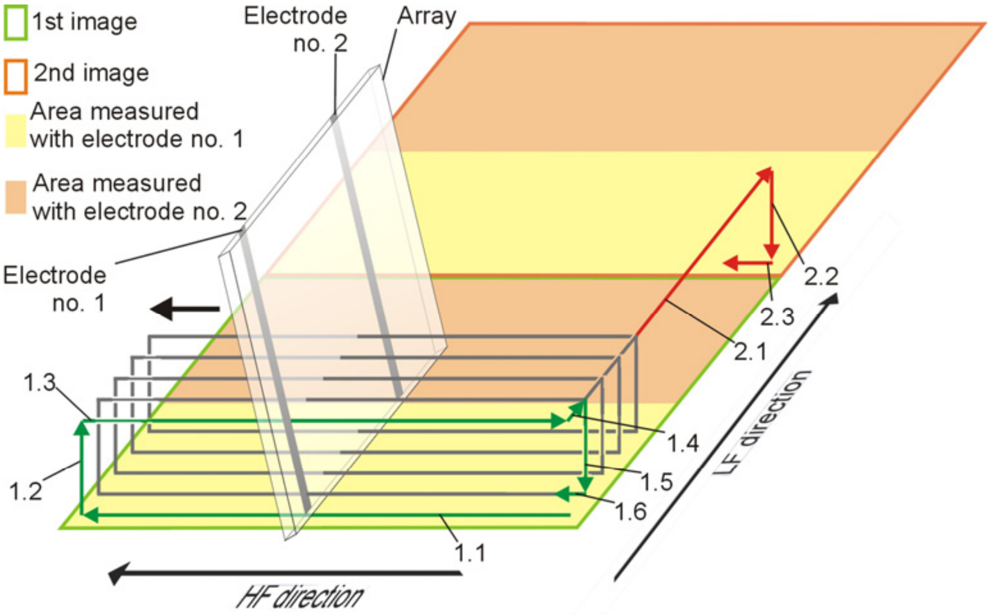

Figure 47. Schematic of the soft microelectrode array movement (linear multiprobe with two electrodes); 1, line scan of the first sensor; 1.1, starting point; 1.2, HF fwd scan; 1.3, lift-off; 1.4, HF rev scan; 1.5, standard step in LF direction; 1.6, re-approach; 2, large step of LF axis. For simplicity an array with only 2 electrodes is shown. (Image slightly modified from SI of Ref. [**A8**].)

The scanning mode of a microelectrode array uses the basic movements explained in Section 6.2.4 where the lift-off mode was introduced for the utilization of soft probes in contact mode. The basic movements are equal as can be seen in the schematic representation in Figure 47. During SECM imaging with the microelectrode array, the individual electrodes will eventually scan over areas that were already scanned by the adjacent electrodes. For this purpose, a new imaging routine was implemented in SECMx allowing to tile image frames in an automated procedure. When the situation of double scanning occurs, the retracted array is translated a large step in the LF direction (red line in Figure 47) and is placed besides the last scan of the *k*-th electrode, *i.e.* on previously not investigated regions. The next HF line scan is started and the same probe movements are performed as in the first image. In this way, several adjacent image frames can be scanned in just one experiment providing a single data set. This can be processed as one experiment offline in MIRA to construct a complete image. A high-throughput image of an interdigitated gold band structure on glass is shown in Figure 48.

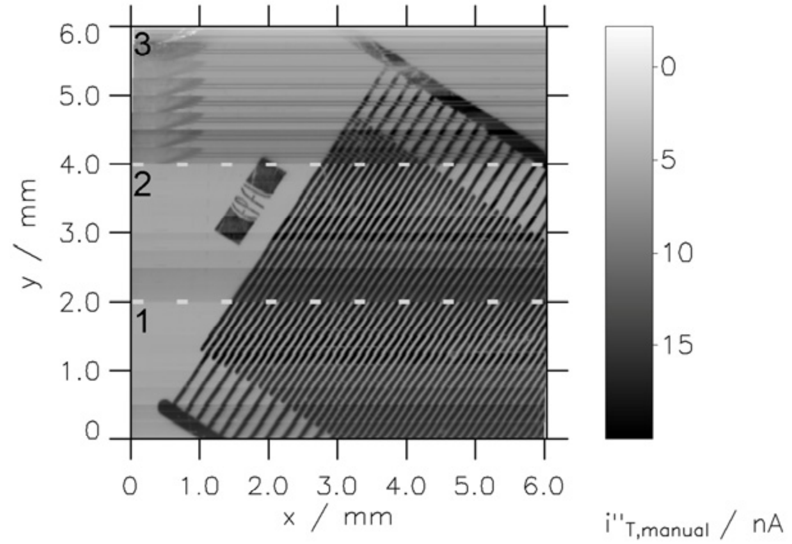

Figure 48. SECM feedback multiple image with three large steps of an interdigitated gold band structure on glass scanned with an array of eight microelectrodes and a midpoint-to-midpoint electrode spacing of 250 µm. Scanning parameters for high-throughput imaging: h_P = -60 µm, LO stroke height 200 µm, LO retract speed 100 µm s^{-1}, LO approach speed 10 µm s^{-1}, HF fwd step size 10 µm, HF $v_{T,fwd}$ = 25 µm s^{-1}, HF fwd delay before data acquisition 0.1 s, HF rev step size 10 µm, HF $v_{T,rev}$ = 1000 µm s^{-1}, LF fwd step size 25 µm, LF $v_{T,fwd}$ = 25 µm s^{-1}, LF large step 2000 µm, total imaging time required was 5 h 18 min.

The currents and positions were corrected. The protocol for this calibration is described in Section 6.5.4. The midpoint-to-midpoint distance of the individual electrodes was 250 µm. A step size of 25 µm in the LF direction was set. This means that 10 line scans can be performed without double scanning (1st line scan at y = 0 µm, 10th line scan at y = 225 µm). With eight electrodes in one array a scan length of 7 × 250 µm + 225 µm = 1975 µm was achieved in the LF direction of this first image. A large step of 2000 µm was performed to investigate the adjacent area. In a second image with equal movements like in the first image, the area between y = 2000 µm and y = 3975 µm was measured. Finally, two large steps were performed to scan an area of overall 6000 µm × 5975 µm. The HF scan length was chosen in the way that a squared image was recorded. In this thesis, the area of such an image will be denoted for simplicity as 6 mm × 6 mm. The number of experimentally measured data points of the image in Figure 48 can be calculated as follows: 601 steps in HF direction × 10 line scans per image × 3 images × 8 electrodes = 144,240 data points. The time required to measure the image was only 5 h 18 min.

6.5.2 Reduction of Imaging Time

The factor of time saving of high-throughput imaging using soft microelectrode arrays is less than the number of integrated microelectrodes. Table 9 shows experimental values applied in two imaging experiments to a single conventional UME and to an array of eight microelectrodes. The same positioning system was used and the conventional UME was controlled with the Ivium CompactStat while the microelectrodes of the array were addressed by the CompactStat connected to the MultiWE32 in simultaneous mode. Typical imaging parameters were set to scan an area of 4 mm (*x*-direction) × 3.99 mm (*y*) with an equal number of data points (160,400).

Table 9. Measurement time and parameters of the experimental investigation of the real time reduction in SECM imaging of an area of 4 mm × 3.99 mm by using a soft array of eight microelectrodes compared to a single conventional UME. Values in bold indicate differences in parameters between both probe types. Data acquisition was carried out during fwd line scans. Reverse movements were only applied for repositioning

Probe	Conventional UME	Soft array of eight electrodes (midpoint-to-midpoint distance 250 µm)	
Number of microelectrodes	**1**	**8**	
Step size	10 µm	10 µm	
Translation rate fwd	25 µm s^{-1}	25 µm s^{-1}	
Translation rate rev	1000 µm s^{-1}	1000 µm s^{-1}	
Lift-off height	-	**200 µm**	
Lift-off speed	-	**200 µm s^{-1}**	
Re-approach speed	-	**20 µm s^{-1}**	
Steps per line scan	401	401	
Performed line scans	**400**	**50**	
Delay before data acquisition	0.1 s	0.1 s	
Data points	160,400	160,400	
Data acquisition	(sequential)	**simultaneous**[a]	**sequential**[b]
Measured time	**28 h 50 min 24 s**	**5 h 10 min 55 s**	**5 h 22 min 54 s**

[a] in the simultaneous mode all 32 channels have to recorded (see Section 6.2.1)

[b] in the sequential mode 8 channels are recorded consecutively

The measured factor of time saving using an array of eight microelectrodes in this example is only **5.6** in simultaneous and **5.4** in sequential mode instead of **8**. One reason is the lift-off mode representing additional motor movements. In this example, the measured time due to LO is **570 s** (50 times 1 s for lift-off and 10 s for re-approach plus time for sending the "move" commands to the controller of the positioning system). This alone cannot explain the experimentally observed decrease of the time saving factor. The other reason is quite obvious and refers to the data acquisition. More time is needed at each step to read 32 current values in simultaneous mode and 8 electrodes in sequential mode. Due to noise in electrochemical systems a signal averaging or filtering, typically of 20 ms is required. In this image, it was **1 h 34 min 37 s** and **1 h 56 min 6 s**, respectively. It has to be stated that in simultaneous mode the same imaging time would be required if the array would consist of 32 electrodes measuring an area of 4 mm × 15.99 mm whereas **10 h 58 min 52 s** are needed for 32 electrodes in sequential mode. Sequential reading increases the time significantly and it becomes more important with an increasing number of used electrodes. It also has to be taken into consideration that the estimation of time reduction in the described example was based on typical soft array probe movements. The reverse scan with a translation rate of 1000 μm s^{-1} is practically never used for a conventional UME in constant height mode. The UME and the sample would be damaged in case the probe would get in mechanical contact with sample at such high speeds. Therefore, the reduction of time is efficiently larger than by the values of Table 9.

6.5.3 Correction of Positional Offsets

A Pt band structure on glass was imaged (3 mm × 3 mm) in feedback mode by a gold microelectrode array consisting of six microelectrodes with a midpoint-to-midpoint distance of 500 µm. The positions of the positioning system were stored. Therefore, eight images with identical *x*- and *y*-positions were constructed as shown as a stacked plot in Figure 49. The positional offsets between the individual electrodes *k* in LF direction (called $y_{\mathrm{offs},k}$) were well defined by the fabrication process. Therefore, each *y*-position of an individual electrode y_k was corrected by a shift of $(k - 1) \cdot 500$ µm to give y'_k.

$$y'_k = y_k + y_{\mathrm{offs},k} \tag{23}$$

The image after correction of the *y*-positions is shown in Figure 50a. Original currents and *x*-positions are plotted. The correction was carried out using the software MIRA. MIRA was expanded in order to perform these offline corrections for data measured with arrays of electrodes.

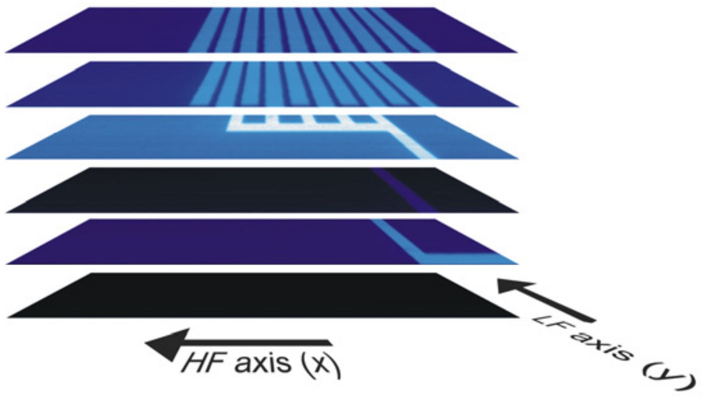

Figure 49. Feedback mode image in 2 mM FcMeOH and 0.1 M KNO_3 with original current values of a Pt band structure on glass imaged by an array of six gold microelectrodes (midpoint-to-midpoint distance 500 μm) after laser cutting. The *x*- and *y*-positions are original and represent the movement of the positioning system. Imaging conditions: h_P = -42.5 μm, LO stroke height 300 μm, LO retract speed 250 μm s^{-1}, LO approach speed 10 μm s^{-1}, HF fwd step size 10 μm, HF $v_{T,fwd}$ = 25 μm s^{-1}, HF fwd delay before data acquisition 0.1 s, HF rev step size 10 μm, HF $v_{T,rev}$ = 250 μm s^{-1}, LF fwd step size 10 μm, LF $v_{T,fwd}$ = 25 μm s^{-1}.

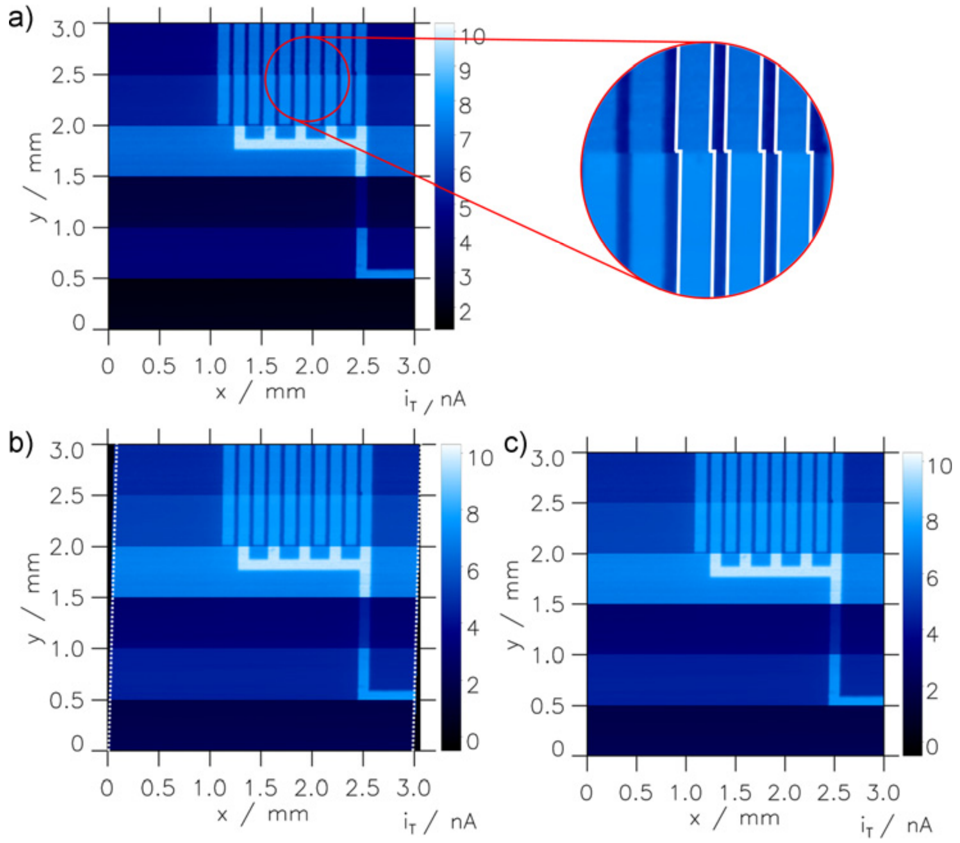

Figure 50. Correction of the positional offsets in the feedback image shown in Figure 49. a) Corrected *y*-positions; extraction shows the positional shift in *x*-direction. Three exemplary bands of the sample are highlighted as guides to the eye. b) Corrected *x*-positions. c) Subsets were cut in order to provide a rectangular image frame. (Images slightly modified from Ref. [**A6**].)

Positional offsets along the HF direction $x_{\text{offs},k}$ were caused by the manual cutting procedure or a misalignment due to the manual placement in the holder. They are corrected similar to the y-positions using Eq. (24). The correction values are listed in Table 10.

$$x'_k = x_k + x_{\text{offs},k} \tag{24}$$

Table 10. Positional offsets applied to correct Figure 49. The result is demonstrated in Figure 50c.

k	1	2	3	4	5	6
$y_{\text{offs},k}$ (μm)	0	500	1000	1500	2000	2500
$x_{\text{offs},k}$ (μm)	0	20	30	40	50	55

Positional offsets in x-direction could be determined from well-defined surface structures like sharp lines perpendicular to the scan direction or by imaging rectangular shapes. Alternatively, one could scratch the sample with a scalpel blade to create a line at which $x_{\text{offs},k}$ can experimentally be determined.

The image with corrected x values is shown in Figure 50a. Close inspection show that the vertical structures appear rugged and the angles of the structure are not exactly reproduced. Shifting the x values by $x_{\text{offs},k}$ (Table 10) reproduces the right angles of the sample in the image (Figure 50b). The edges of the image are clipped by 60 μm at each side of the x axis to yield again to a rectangular image frame (Figure 50c). The original currents of the six sensors vary slightly which is clearly observed in Figure 50a-c. The correction of this effect is discussed in Section 6.5.4.

6.5.4 Current Calibration Routines

Figure 51 shows the same CVs as in Figure 38 with the additional description of individual current offsets. These current offsets $i_{\text{T,off},k}$ of the electrodes k shift the individual CVs to larger or smaller currents and can either be caused by instrumental limitations using a multipotentiostat or by interferences between adjacent electrodes. The gold microelectrodes $k = 3$ and 4 were short-circuited, most likely at the carbon connection pads. This is one disadvantage of the manual pad fabrication. However, in case electrodes are connected, imaging can be performed in simultaneous mode without noticeable influences of the interferences, *e.g.* detecting also the surface reactivity of the substrate area beneath the neighboring electrode. This advantage is due to the fact that the currents flow predominantly through the tracks of the lowest resistance, *i.e.* the gold tracks.

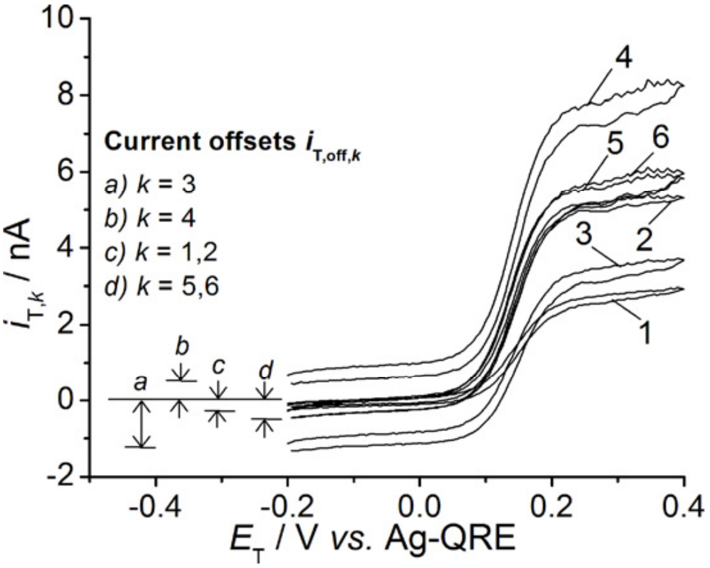

Figure 51. CVs from Figure 38a of an array with six gold microelectrodes in 2 mM FcMeOH and 0.1 M KNO_3. Due to differences in the sizes of the active electrode areas and geometries various steady-state currents can be observed. Additionally, current offsets of individual electrodes can be obtained.

A calibration routine was developed in order to level the current responses. Electrode-depended current offsets $i_{T,offs,k}$ are extracted from the CVs and subtracted from the original currents $i_{T,k}$ of the individual electrodes using Eq. (25).

$$i'_{T,k} = i_{T,k} - i_{T,offs,k} \tag{25}$$

The CVs after applying this correction are shown in Figure 52 and the calibration values $i_{T,offs,k}$ are listed in Table 11.

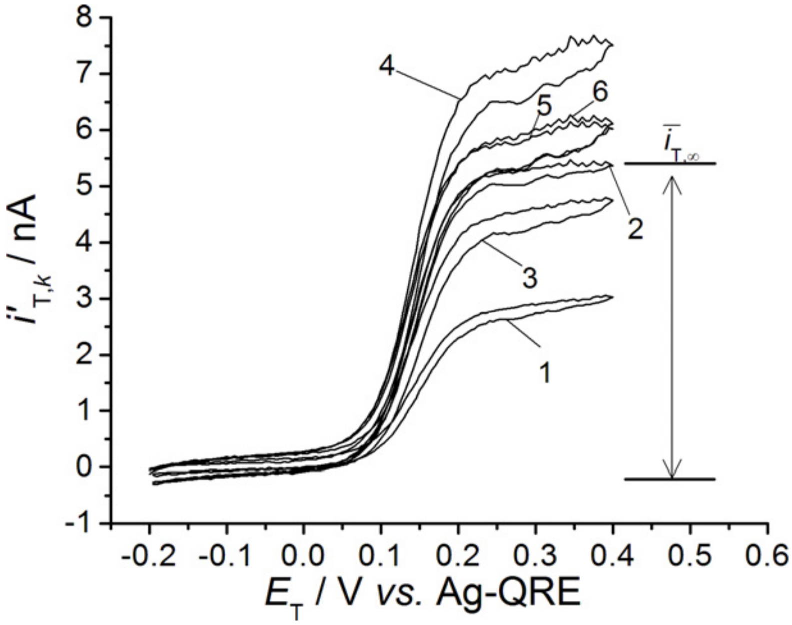

Figure 52. CVs from Figure 38 and 51 corrected by $i_{T,offs,k}$ with Eq. (25).

Table 11. Current offsets of the CVs shown in Figure 52.

k	1	2	3	4	5	6
$i_{\mathrm{T,offs},k}$ (nA)	-0.091	-0.059	-1.070	0.725	-0.200	-0.161

The current offsets are corrected which can be seen in the overlaying CVs at potentials smaller than 0.05 V. The next step is the calibration with respect to different electrode sizes and geometries. This is performed with an electrode-dependent scale factor s_k. For this purpose, an average steady-state current ($\bar{i}_{\mathrm{T},\infty}$ = 5.46 nA) is calculated at the vertex potential of the CVs ($E_{\mathrm{T,vertex}}$ = 0.4 V *vs.* Ag-QRE). s_k is then given by the quotient of $i_{\mathrm{T},\infty,\mathrm{k}}$ and $\bar{i}_{\mathrm{T},\infty}$. The final calibrated currents $i''_{\mathrm{T},k}$ are then calculated by multiplying $i'_{\mathrm{T},k}$ by s_{k}.

$$i''_{\mathrm{T},k} = i'_{\mathrm{T},k} \cdot \frac{i_{\mathrm{T},\infty,k}}{\bar{i}_{\mathrm{T},\infty}} = \left(i_{\mathrm{T},k} - i_{\mathrm{T,offs},k}\right) \cdot s_k \tag{26}$$

The CV after this calibration is plotted in Figure 53 and the scale factors are listed in Table 12. It can be seen clearly, that the initially different CVs appear almost equal after leveling by the Eqs. (25) and (26).

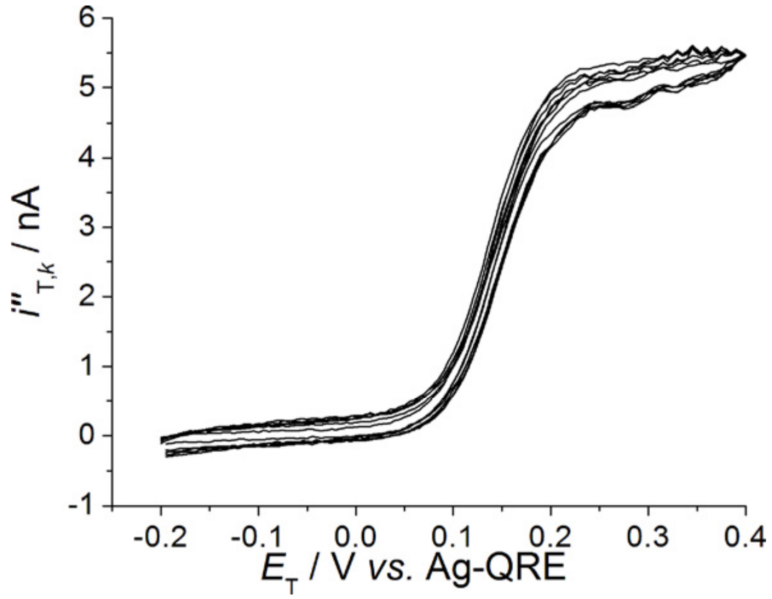

Figure 53. CVs from Figure 38 and 51 corrected by $i_{\mathrm{T,offs},k}$ and s_k.

Table 12. Scale factors of the CVs shown in Figure 53.

k	1	2	3	4	5	6
s_k (nA^{-1})	1.806	1.018	1.151	0.727	0.908	0.894

The correction values from Tables 11 and 12 were then transferred to the feedback image of the Pt band structure in Figure 50c in order to correct this image. The result is shown in Figure 54. After the calibration, there are still significant variations in the current values for negative as well as for positive feedback. Manual correction of the values could be performed in principle until a leveled image is achieved. However, this would be a time-consuming procedure and, in case values are modified noticeably, it would not represent a valid procedure.

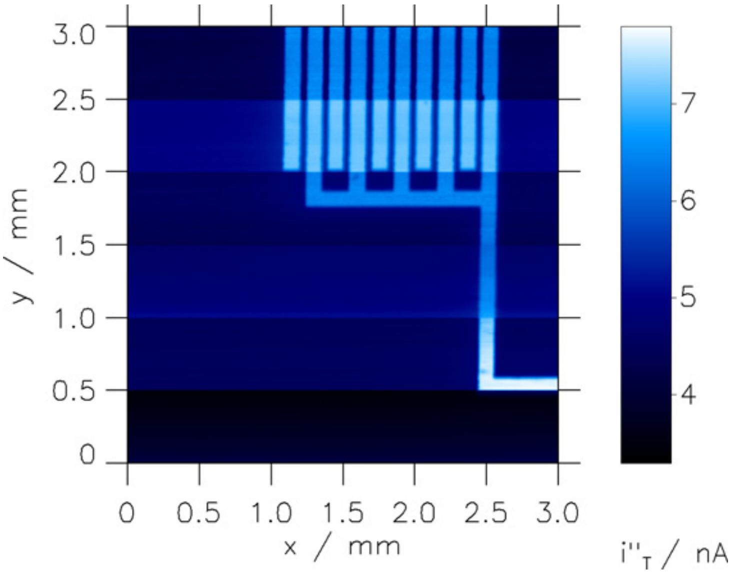

Figure 54. Feedback image of the Pt band structure on glass (original values in Figure 49) with applied current offsets (Table 11) and scale factors (Table 12) from the CV analysis. It can be seen clearly that the currents vary significantly demonstrating that an improvement of calibration is required.

Therefore, an optimized calibration routine was developed which is based on the treatment of the original current data set of the image to correct. The first modification was the interpretation of the current offset (Eq. (25)). $i_{\mathrm{T,offs},k}$ is now the negative feedback current extracted from line scans of the image.

$$i_{\mathrm{T,offs},k} = i_{\mathrm{T,min},k} \tag{27}$$

This procedure sets the negative feedback currents to zero (Figure 55a). Table 13 shows the correction values. The electrode-dependent scale factor s_k to compensate for size and distance variations was now applied to set the maximum corrected currents of each individual electrode to 1. For this purpose, s_k was the reciprocal of the offset-corrected maximum current $i'_{\mathrm{T,max},k}$ (Eq. (28)).

$$s_k = \frac{1}{i'_{\mathrm{T,max},k}} = \frac{1}{i_{\mathrm{T,max},k} - i_{\mathrm{T,offs},k}} \tag{28}$$

Applying these current values in Eq. (29) leads to relative current values and to the corrected image in Figure 55b.

$$\frac{i'_{\mathrm{T},k}}{i'_{\mathrm{T,max},k}} = \left(i_{\mathrm{T},k} - i_{\mathrm{T,offs},k}\right) \cdot s_k \tag{29}$$

The current values are not perfectly leveled. This is due to the fact that the soft probes can change during an image, which influences the current signal (discussion *vide infra*). A minor manual correction of $i_{\mathrm{T,offs},k}$ was carried out for sensors 1, 2 and 3 (values in brackets in Table 13). Figure 55c shows the result after all performed corrections.

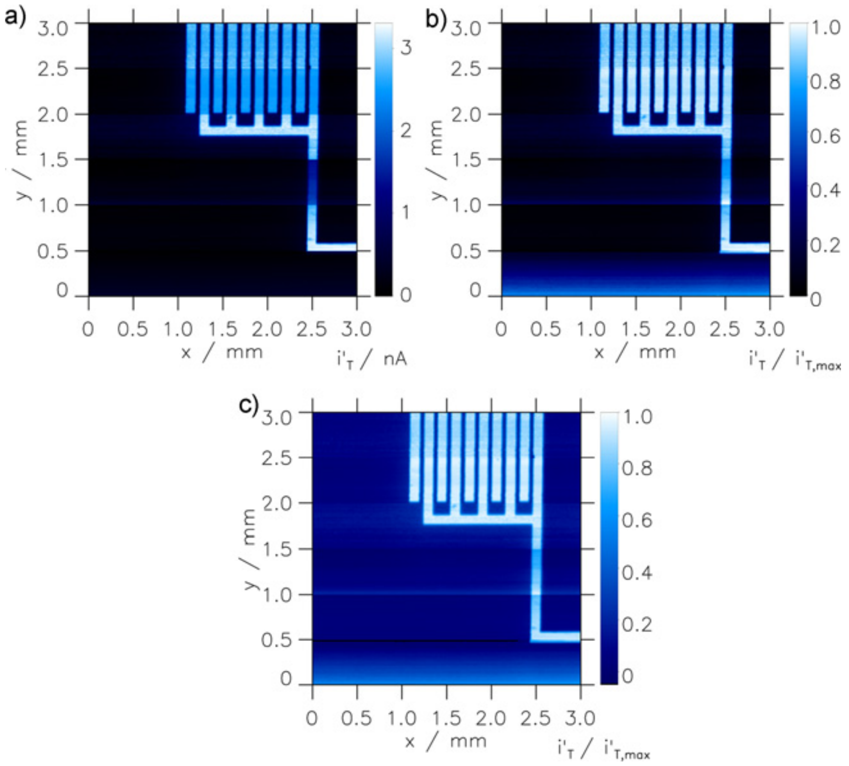

Figure 55. Correction of the measured current values in feedback image shown in Figure 49. a) Image after applying $i_{\mathrm{T,offs},k}$. b) Image after application of s_k. c) Image after minor manual adjustments to $i_{\mathrm{T,offs},k}$ and s_k. (Images slightly modified from Ref. [**A6**].)

Table 13. Current offsets and scale factors applied to calibrate the original current values of Figure 49. The final result is shown in Figure 55c.

k	1	2	3	4	5	6
$i_{\mathrm{T,off},k}$ (nA)[a]	1.76 (1.85)	4.26	2.91 (3.0)	6.53	5.16	4.36
s_k (nA^{-1})[a]	1.60	0.30 (0.28)	0.52	0.30	0.37	0.32

[a] values in brackets represent manually adjusted values.

This change of the response of some electrodes became obvious in a larger image of 6 mm × 6 mm which was scanned immediately after the image shown in Figures 49-55 without sample cleaning, array cutting or renewing of the solution (Figure 56). The calibration parameters were not modified and thus the values from Table 13 were used.

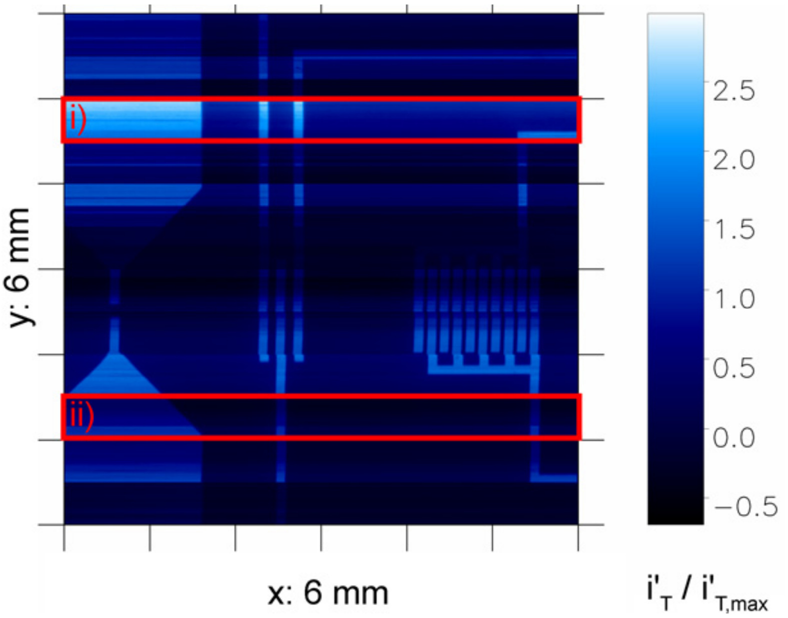

Figure 56. Transformed multiple SECM feedback image of an area of 6 mm × 6 mm of the platinum band structure on glass with the array of six microelectrodes performed in 2 mM FcMeOH and 0.1 M KNO_3 solution. Calibration values from the previous measurement were used (Figure 55). The response of some microelectrodes changed during the image. Either continuously increasing (i, sensor 4) or decreasing currents (ii, sensor 3) were obtained and are shown as 2D plots in Figure 57. Imaging conditions: h_P = -42.5 µm, LO stroke height 300 µm, LO retract speed 250 µm s^{-1}, LO approach speed 10 µm s^{-1}, HF fwd step size 10 µm, HF $v_{T,fwd}$ = 25 µm s^{-1}, HF fwd delay before data acquisition 0.1 s, HF rev step size 10 µm, HF $v_{T,rev}$ 250 µm s^{-1}, LF fwd step size 10 µm, LF $v_{T,fwd}$ = 25 µm s^{-1}, LF large step 3000 µm, total imaging time required was 18 h 30 min for 360,000 grid points. (Figure slightly modified from [**A6**].)

Using the corrections values from Table 13 could not provide convincing results because the response of some individual electrodes changed over time. For instance, the currents from sensor no. 4 increased progressively during the experiment (see consecutive line scans of sensor 4, Figure 56(i), 57a), while for sensor no. 3 the current decreased (see consecutive line scans of sensor 3, Figure 56(ii), 57b). The current increase with time can be explained by the increase of the redox mediator concentration as a consequence of solvent evaporation during the experiment over the prolonged imaging time. A current decrease could be a result of the deactivation of individual electrodes by adsorption of impurities present in the electrolyte solution or by precipitation over the electrode areas of the highly concentrated supporting electrolyte or redox mediator. The gold inks contain organic components that may not be removed completely by sintering and may contaminate the working solution as well. The Parylene C coating is subjected to abrasion when sliding over the sample for prolonged time. Abraded parts of the Parylene C coating may mechanical obstruct the small working area of the probe. Despite these unfavorable circumstances, the surface reactivity is clearly resolved and the electrochemical response of all channels is clearly detectable even after nearly 24 h of continuous imaging without renewal of the solution or of the active electrode area. A fresh cut of the array or a renewal of the electrolyte solution could help.

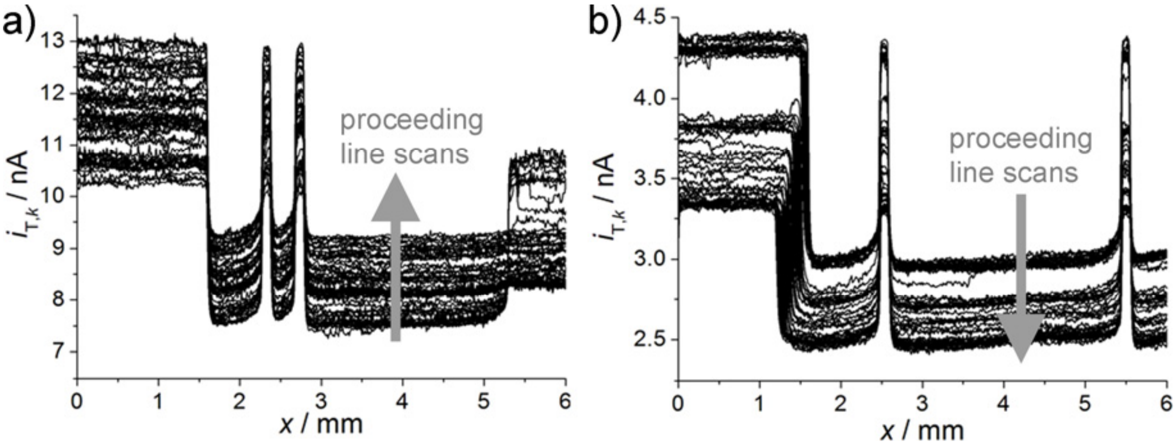

Figure 57. Two-dimensional plots of the images (i) and (ii) in Figure 56. Original current values are shown. Increasing and decreasing can be obtained due to a probe altering. (Figure slightly modified from [**A6**].)

6.5.5 Tilted, Rough, Curved and Corrugated Substrates

Curved substrates. In order to demonstrate that large curved substrates on centimeter-scale can be scanned on a short time scale, an area of 1.5 cm × 0.8 cm of a pin from the University of Oldenburg (Figure 58a) was scanned with a soft array of eight carbon microelectrodes in SECM feedback mode using FcMeOH as redox mediator. The imaging time for recording 192,320 data points was just 7 h and is shown in Figure 58b. Table 14 lists the calibration values. One large step was performed and the relative large step sizes of 25 µm were chosen to give a good resolution in an appropriate imaging time. The pin is made of a metal and the letters are engraved with various depths. Additionally, they are painted with an unknown paint. The current responses rely on the positive feedback over the metallic surface.

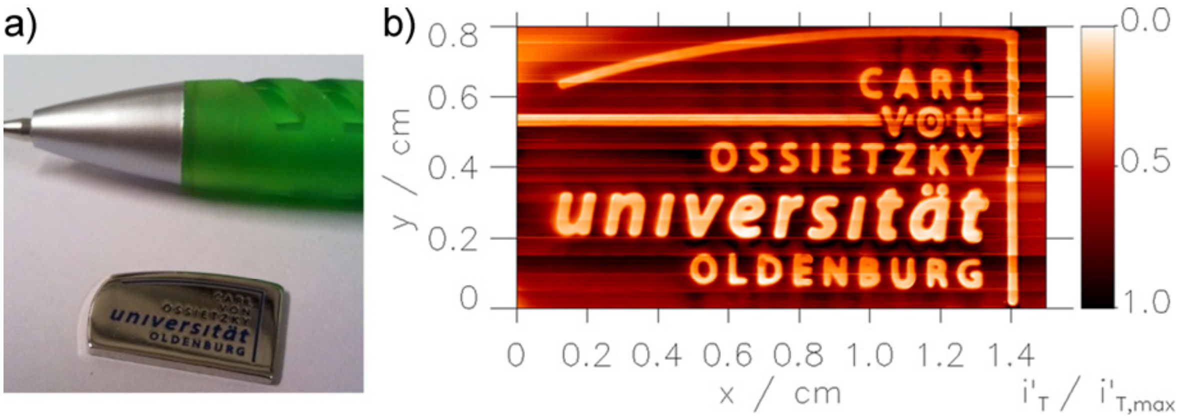

Figure 58. SECM feedback mode imaging of a large curved pin from the University of Oldenburg (kindly provided by Prof. Dr. Katharina Al-Shamery) using a linear array of eight carbon microelectrodes. a) Optical photograph of the pin. b) SECM image in 2 mM FcMeOH + 0.1 M Na_2SO_4. Imaging conditions: h_P = -100 µm, LO stroke height 500 µm, LO retract speed 200 µm s^{-1}, LO approach speed 20 µm s^{-1}, HF fwd step size 25 µm, HF $v_{T,fwd}$ = 50 µm s^{-1}, HF fwd delay before data acquisition 0.1 s, HF rev step size 25 µm, HF $v_{T,rev}$ = 1000 µm s^{-1}, LF fwd step size 25 µm, LF $v_{T,fwd}$ = 100 µm s^{-1}, LF large step 4000 µm, total imaging time required was 7 h 8 min for 192,320 grid points.

Table 14. Current offsets and scale factors applied to calibrate Figure 58.

k	1	2	3	4	5	6	7	8
$x_{\mathrm{off},k}$ (µm)	0	0	0	0	0	0	0	0
$y_{\mathrm{off},k}$ (µm)	0	500	1000	1500	2000	2500	3000	3500
$i_{\mathrm{T,off},k}$ (nA)^a	5.91	5.90	4.17	6.31	5.72	6.23	6.95	6.71
s_k (nA^{-1})^a	0.16	0.15	0.28	0.12	0.16	0.17	0.12	0.27

The soft array follows the curved topography of the pin but it cannot enter into the graves because they have much smaller dimensions than the width of the array. The current in the feedback image decreases due to the increasing working distance over the graves to reach the steady-state current in solution bulk which was normalized to zero and provided the current contrast. The imaging time of 7 hours is about 4.5 times less than the calculated time for a conventional image using one UME. In addition, a conventional SECM setup using a single classical UME cannot scan such a large curved area without additional instrumentation to control the working distance. As a result, d would enlarge too much or the UME would easily get in contact with the substrate. Furthermore, the applied reverse translation rate of 1000 µm s^{-1} (included in the calculation for the UME) is not applicable for a classical UME. It would increase the danger of breaking the UME when touching the surface. Moreover, the feedback loops as applied in shear force SECM for a distance control are time-dependent and limit the scan rate. This image demonstrates in a very convincing way the opportunities of high-throughput imaging with soft linear microelectrode arrays.

Tilt in *y*-direction. The custom-made holder allows aligning the eight electrodes of one array to the sample surface by using the experimental information extracted from approach curves.

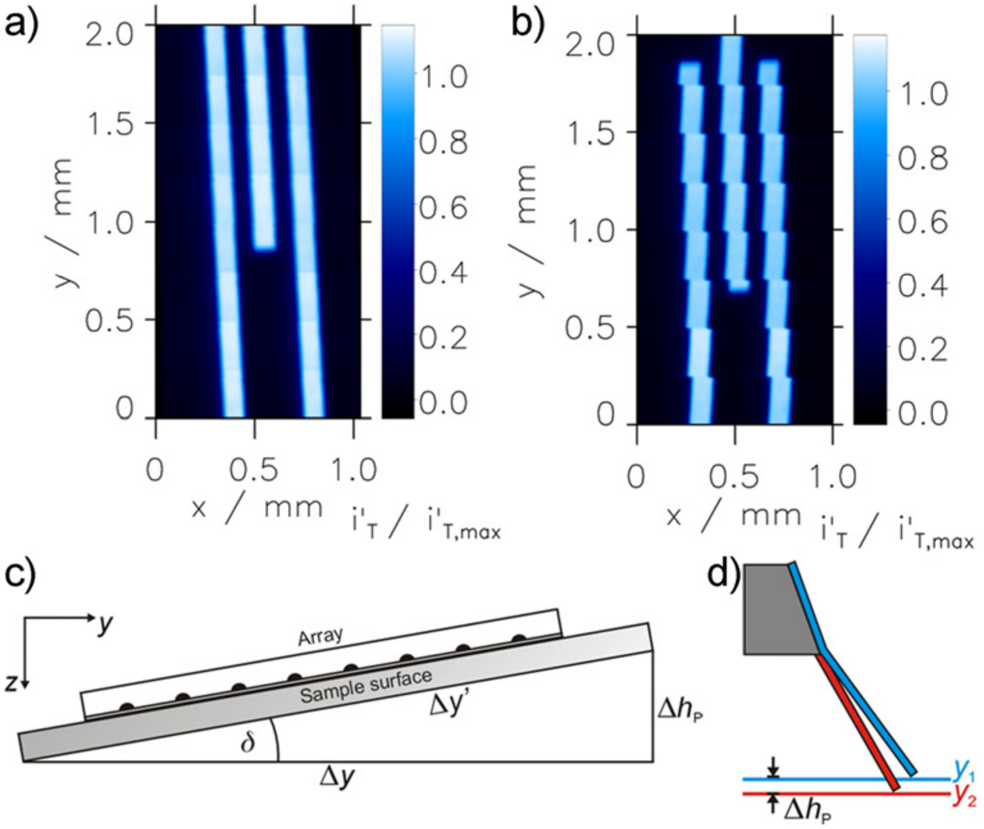

Figure 59. Influence of sample tilt in *y*-direction. Sample is with aligned probe. a) SECM feedback mode image of a sample without tilt. b) SECM feedback mode image of a sample with a tilt of 2° in *y*-direction. c) Schematic representation of the tilt angle δ, real step size Δy and Δh_P. d) Schematic representation of shift in *x*-direction due to Δh_P.

Figure 59a shows a feedback image of a Pt band structure on glass without any sample tilt. The tilt was eliminated before by using the three point approach curve method with conventional UME. The currents were calibrated and the image shows very well the Pt lines. Figure 59b was measured with the sample tilted by 2 degrees in *y*-direction. The array was made align as shown schematically in Figure 59c and an image was recorded. Clearly a continuous shift of the x values is obtained for the individual electrodes. This is due to a change in the h_p value. The translation axes of the positioning system are not parallel (x,y) and perpendicular (z) to the substrate surface. Since the absolute z-position at each data point is fixed the point of attachment of the probe with the sample is shifted if the sample is tilted in y-direction as demonstrated in Figure 59d. It is also possible that the probe can lose contact to the sample, *e.g.* if it makes a large step with large negative sample tilt. Then the measurement cannot be continued.

With the known geometries and dimensions the measured data can be corrected. First, the influence of the tilt angle δ on the applied LF step size Δy is calculated for two exemplary δ values (2° and 4°) by using Eqs. (30)-(31).

$$\Delta y'_{2^\circ} = \frac{\Delta y}{\cos\delta} = \frac{20\,\mu\mathrm{m}}{\cos 2^\circ} = 20.01\,\mu\mathrm{m} \tag{30}$$

$$\Delta y'_{4^\circ} = \frac{\Delta y}{\cos\delta} = \frac{20\,\mu\mathrm{m}}{\cos 4^\circ} = 20.05\,\mu\mathrm{m} \tag{31}$$

The real step sizes $\Delta y'$ are increased to 20.01 µm ($\delta = 2^\circ$) and 20.05 µm ($\delta = 4^\circ$), respectively. These enhancements of 0.05 % and 0.25 % are negligible and were not taken into consideration. Relevant are changes in the h_P value which can be calculated with Eq. (32).

$$\Delta h_\mathrm{p} = \Delta y \cdot \tan\delta \tag{32}$$

A step of 20 µm in LF direction changes the h_P value already about 3.5 % and 7 %.

$$\Delta h_{\mathrm{p},2^\circ} = 20\,\mu\mathrm{m} \cdot \tan 2^\circ = 0.7\,\mu\mathrm{m} \tag{33}$$

$$\Delta h_{\mathrm{p},4^\circ} = 20\,\mu\mathrm{m} \cdot \tan 4^\circ = 1.4\,\mu\mathrm{m} \tag{34}$$

These values cannot be neglected. The change of h_P can be used to correct the x-positions. Three situations are calculated and shown schematically in Figure 60: a) h_P = 0 µm, b) h_P = -40 µm and c) $h_\mathrm{P} + \Delta h_\mathrm{P}$.

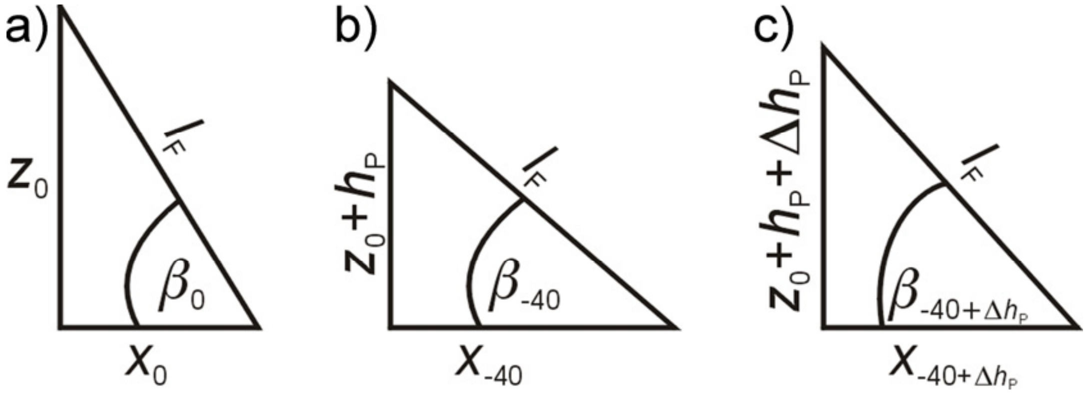

Figure 60. Schematic representation of the geometric arrangements with h_P = 0 µm (a), h_P = -40 µm (b) and $h_P = h_P + \Delta h_P$ (c).

The length l_F represents the freely suspended part of the probe. It can be measured with a caliper. If the probe is in contact with the sample with h_P = 0 um, the vertical length z_0 can be calculated with knowledge of the inclination angle γ.

$$z_0 = l_F \cdot \sin\beta_0, \quad \beta_0 = 90° - \gamma \tag{35}$$

If the probe is approached further the distance x_{-40} is given by Eq. (36) taking into consideration the value h_P = -40 µm value.

$$x_{-40} = \frac{z_0 + h_p}{\tan\beta_{-40}} \tag{36}$$

This equation requires β_{-40} which can be calculated with Eqs. (37)-(38).

$$\sin\beta_{-40} = \frac{z_0 + h_p}{l_F} = \frac{l_F \cdot \sin\beta_0 + h_p}{l_F} \tag{37}$$

$$\beta_{-40} = \arcsin\left(\frac{l_F \cdot \sin\beta_0 + h_p}{l_F}\right) \tag{38}$$

Eq. (36) then gives a modified expression for x_{-40}.

$$x_{-40} = \frac{l_F \cdot \sin\beta_0 + h_p}{\tan\beta_{-40}} = \frac{l_F \cdot \sin\beta_0 + h_p}{\tan\left[\arcsin\left(\frac{l_F \cdot \sin\beta_0 + h_p}{l_F}\right)\right]} \tag{39}$$

This value represents the x value at the starting position of the first HF line scan within an image. Following x-positions in this line scan are calculated by $x + \Delta x$ and overlay with the stored positions applied by the positioning system. The real x-positions of an array will change in LF direction proportional to the change in Δh_P and can be calculated by

$$x_{-40+\Delta h_p} = l_F \cdot \cos\beta_{-40+\Delta h_p} \tag{40}$$

where the angle β is calculated by Eqs. (41)-(42).

$$\sin\beta_{-40+\Delta h_\mathrm{p}} = \frac{z_0 + h_\mathrm{p} + \Delta h_\mathrm{p}}{l_\mathrm{F}} = \frac{l_\mathrm{F}\cdot\sin\beta_0 + h_\mathrm{p} + \Delta h_\mathrm{p}}{l_\mathrm{F}} \tag{41}$$

$$\beta_{-40+\Delta h_\mathrm{p}} = \arcsin\left(\frac{l_\mathrm{F}\cdot\sin\beta_0 + h_\mathrm{p} + \Delta h_\mathrm{p}}{l_\mathrm{F}}\right) \tag{42}$$

For n steps in y-direction, β_n is

$$\beta_n = \arcsin\left(\frac{l_\mathrm{F}\cdot\sin\beta_0 + h_\mathrm{p} + n\Delta h_\mathrm{p}}{l_\mathrm{F}}\right) \tag{43}$$

This is used to give a modified expression for the real x-position (Eq. (44)).

$$x_{-40+h_\mathrm{p}} = \frac{l_\mathrm{F}\cdot\sin\beta_0 + h_\mathrm{P}}{\tan\beta_{-40+h_\mathrm{P}}} \tag{44}$$

For the case of the n-th steps in LF direction, the positional shift in x-direction compared to the initial point is given by

$$x_n - x_{-40+h_\mathrm{p}} = \frac{l_\mathrm{F}\cdot\sin\beta_0 + h_\mathrm{P} + n\Delta h_\mathrm{p}}{\tan\beta_n} - \frac{l_\mathrm{F}\cdot\sin\beta_0 + h_\mathrm{P}}{\tan\beta_{-40+h_\mathrm{P}}} \tag{45}$$

This was performed for the tilt angles 2° and 4° and is shown in Figure 61. Figures 61a,c show the images with calibrated currents and original x-positions. The plots in Figures 61b,d were constructed with corrected positions x'. The x values were calculated using the software Wolfram Mathematica 8.

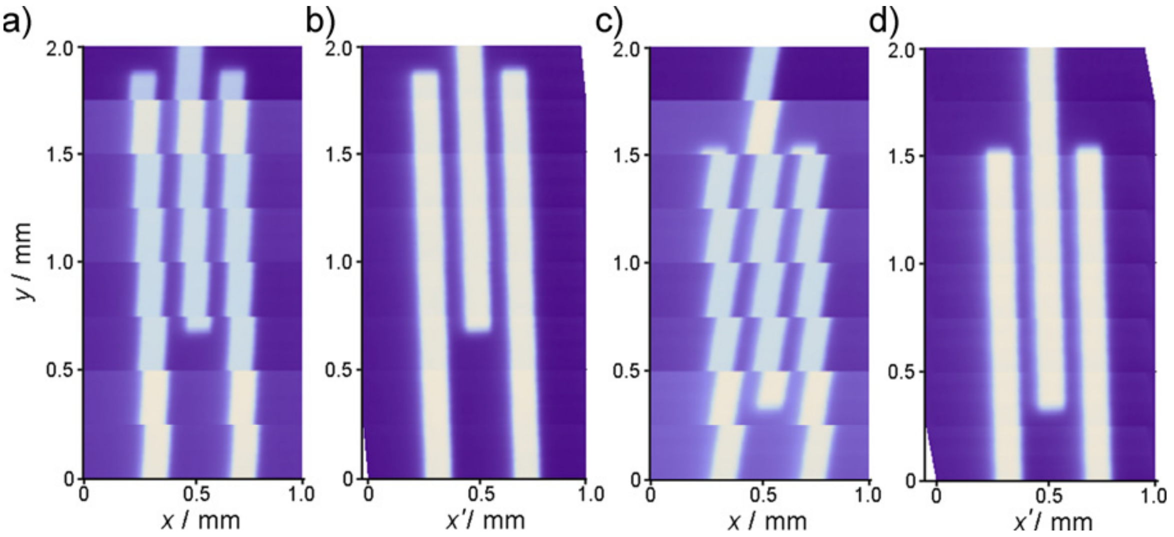

Figure 61. Feedback mode images of a Pt band structure on glass with tilt in *y*-direction. *δ* = 2° (a,b) and 4° (c,d). Original *x* values (a,c) and corrected positions (b,d).

Tilt in *x*-direction. A sample tilt in *x*-direction changes the real *x* step size significantly as shown in Figure 62. 13 gold tracks of an interdigitated array (midpoint-to-midpoint distance of 100 µm) on glass were scanned with several sample tilts. An average distance of the gold bands was calculated as a mean value of the 13 maximum currents. The measured value of 100 µm for the aligned sample matches to the real value. But a variation of the tilt angle ω of ±1° changes the measured distance about ±5 µm (5%) and is not negligible. If ω is positive the distance slid by the probe on the surface is larger than the performed step from the positioning system as shown schematically in Figure 62b. Therefore, the 13 gold bands are scanned apparently on a shorter scan length and the measured gold line separation is only 95 µm. For a negative sample tilt in x-direction the effect is *vise versa*. A longer scan length is required to scan the 13 gold tracks because the real step size $\Delta x'$ on the sample is shorter than Δx (Figure 62c).

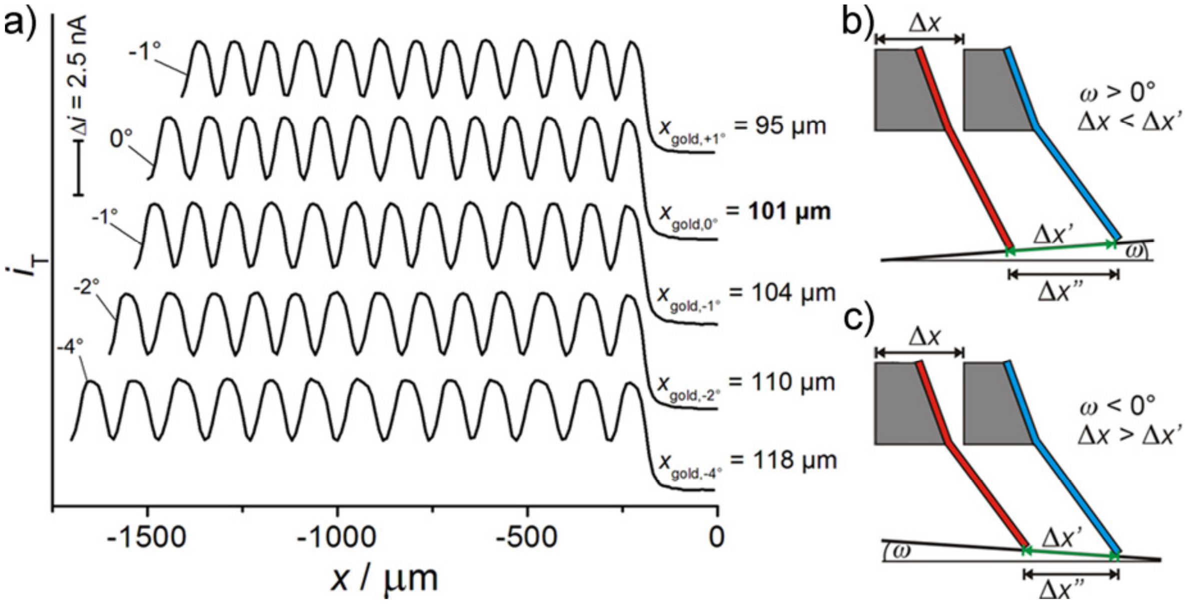

Figure 62. Feedback mode line scans of 13 gold bands on glass using one carbon microelectrode in a soft array. The sample was tilted -1°, 0°, +1°, +2°, +4° which affects the real step size $\Delta x'$. The gold bands appear compressed or stretched.

Similar to the tilt in y-direction geometric arrangements can be made to calculate the effect of ω on the performed step size Δx. The configuration is more complex than with a tilt in y-direction and is plotted schematically in Figure 63.

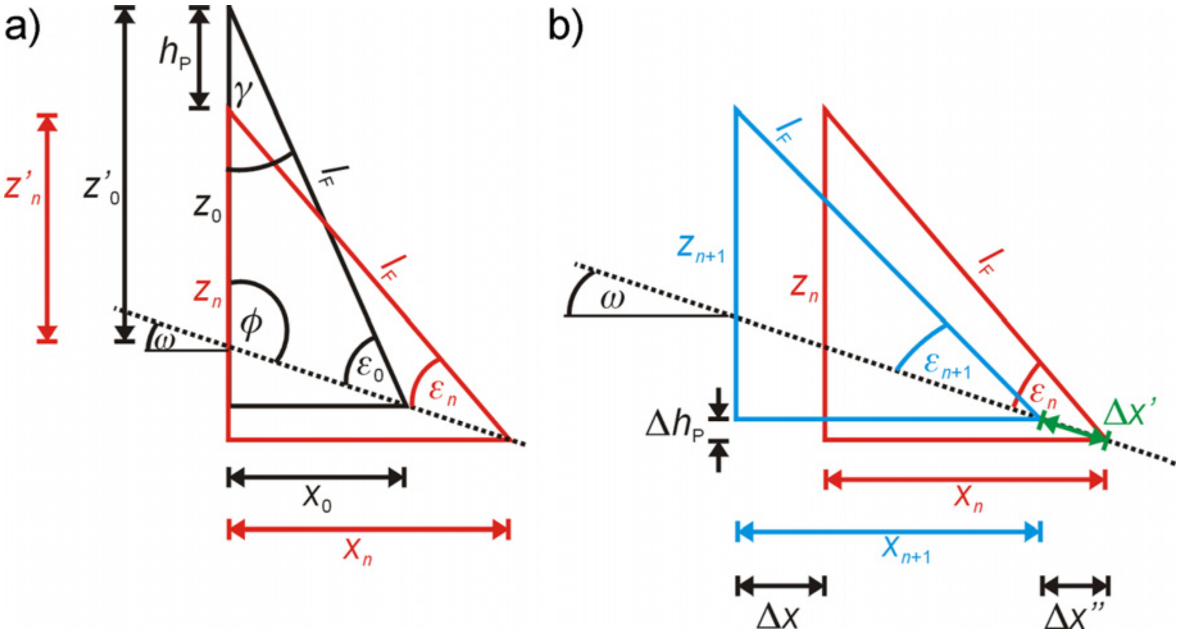

Figure 63. Schematic representation of the geometric arrangements with a sample tilt ω in *y*-direction. a) h_P = 0 µm (black) and h_P < 0 µm (red). b) Situation after the probe performed a step Δx (blue). The real step size $\Delta x'$ differs from the step size Δx which is applied by the positioning system.

The black triangle in Figure 63a represents the situation with h_P = 0 µm. The probe is brought to mechanical contact with the sample surface but does not start to bend and slide. The vertical length x_0 can be calculated with knowledge of l_F and the inclination angle γ.

$$x_0 = l_F \cdot \sin\gamma \tag{46}$$

ϕ represents the angle between surface normal and tilted substrate surface and be calculated by using Eq. (47).

$$\phi = 90° + \omega \tag{47}$$

z'_0 can be calculated with ε_0 which is the angle between the probe and the tilted surface with h_P = 0 µm.

$$z'_0 = \frac{l_F}{\sin\phi} \cdot \sin\varepsilon_0 = \frac{l_F}{\sin\phi} \cdot \sin(180° - \phi - \gamma) \tag{48}$$

The red triangle shows the situation when the probe was approached further and starts to slide. Hence z'_0 changes by h_P to give z'_n.

$$z'_n = z'_0 + h_P \tag{49}$$

This changes ε_0 to ε_n.

$$\varepsilon_n = \arcsin\left(\frac{z'_n \cdot \sin\phi}{l_F}\right) \tag{50}$$

For following calculations z_n and x_n have to be known and are given by Eqs. (51) and (52).

$$z_n = \frac{l_\mathrm{F}}{\sin\phi}\sin\varepsilon_n \tag{51}$$

$$x_n = \sqrt{l_\mathrm{F}^2 - z_n^2} \tag{52}$$

If the probe is laterally translated, z_n and x_n change. Only l_F is constant. For one exemplary step this is shown as the blue triangle in Figure 63b. The real step size $\Delta x'$ differs from Δx. The absolute x value after the first step (index n+1) can be calculated by Eq. (53).

$$x_{n+1} = l_\mathrm{F} \cdot \cos\left[\arcsin\left(\frac{z_n + (n+1)\Delta h_\mathrm{P}}{l_\mathrm{F}}\right)\right] \tag{53}$$

A lateral quantity $\Delta x''$ is given by

$$\Delta x'' = \Delta x + x_n - x_{n+1}\,. \tag{54}$$

Therefore, the real step size $\Delta x'$ is

$$\Delta x' = \frac{\Delta x''}{\cos\omega} = \frac{\Delta x + x_n - x_{n+1}}{\cos\omega}\,. \tag{55}$$

The discussed investigations with known angles δ in y- and ω in x-direction demonstrate the behavior of the sliding bent soft probes on tilted substrates. It is not intended to do these calibrations for each measurement. Soft probes are made for fast experiments on curved and tilted substrates. But the results illustrate how to interpret images if a sample tilt cannot be neglected because it shifts positions or stretches/compresses distances. The problem becomes more problematic for samples tilted both in x- and y-direction. Even more complex is the variation of the real step size in x-direction on curved substrates where $\Delta x'$ can increase and decrease during one line scan. Real dimensions cannot be extracted from measurements with soft probes if no tilt calibration was performed. The tilt should be eliminated or different techniques such as SFM or CLSM have to be used to detect the sample dimensions.

7 Parallel Imaging and Template-Free Chemical Patterning of Self-Assembled Monolayers

In this chapter, high-throughput patterning and scanning of self-assembled monolayers, used as a model system for delicate samples, are reported. Notably, these systems are easily damaged when other scanning probe techniques, such as SFM, are used in contact mode. The localized modification of OEG SAM by bromine generation followed by site-selective protein adsorption was performed by the soft carbon microelectrode arrays. Furthermore, the capability to create complex patterns on a large scale will be demonstrated.

7.1 Investigation of Force and Pressure Exerted by the Soft Probe on the Sample

Before performing experiments on delicate samples using the soft arrays in contact mode, the magnitude of the pressure exerted by the soft probes on the sample surface should be determined. In order to assess this pressure, the force was estimated independently by a direct force measurement and by determination of the resonance frequency of the free vibration. For the first approach a gold microelectrode array was mounted to the custom-built holder with an inclination angle of 20° (as typically used in this thesis) and was approached slowly from air to an analytical balance plate which served as the substrate surface. The mass was recorded for four vertical displacements h_P. The force was calculated by multiplying each value with the gravity constant (g = 9.81 m s^{-2}) and plotted versus h_P (Figure 64). Linear regression of the measured points through zero gives

$$F = -k \cdot h_\mathrm{P} = -29.7\ \mu\mathrm{N}\ \mu\mathrm{m}^{-1} \cdot h_\mathrm{P} \tag{56}$$

where k is the slope and represents the spring constant of the soft probe. Note, that a representative displacement during SECM experiments is an h_P value of -42.5 µm. The estimated force is then 126.2 µN.

The second approach used for the estimation of the force was the determination of the resonance frequency of a freely vibrating soft gold microelectrode array. By means of a laser, photodiode and an oscilloscope a resonance frequency of f = 18.25 Hz was measured. The spring constant was then calculated with the measured mass (m = 0.075 · 10^{-3} kg) of the vibrating part of the soft probe using Eq. (57).

$$F = 4 \cdot \pi^2 \cdot f^2 \cdot m = 1.04\ \mathrm{kg\ s}^{-2} \tag{57}$$

Therefore, with a displacement of h_P = -42.5 μm the calculated force F gave 44.2 μN which is about the same magnitude from the value estimated from the mass (126.2 μN).

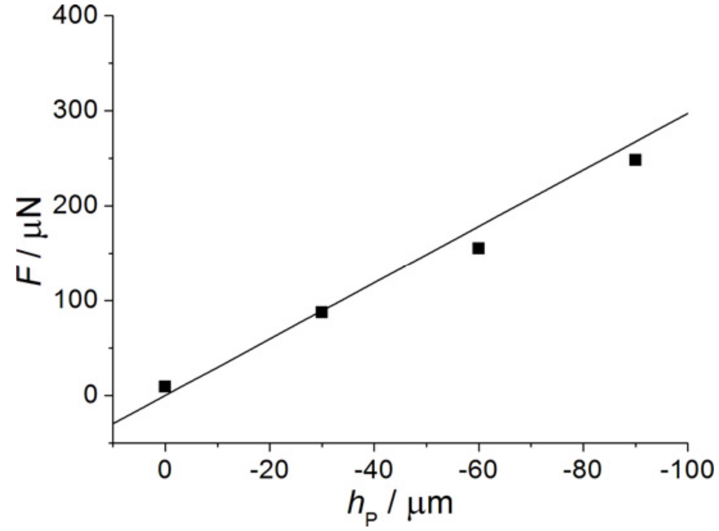

Figure 64. F plotted *vs.* h_P for four displacements. Linear regression gives a linear equation with a slope k which is the spring constant of soft probe. (Figure as published in SI of Ref. [**A6**].)

The pressure was calculated as $p = F\,A_{\mathrm{cont}}^{-1}$ where A_{cont} is the contact area of the soft probe with the sample surface. This contact area was difficult to determine. SEM images of laser-ablated probes before and after scanning showed some abrasion and deformation of the polymeric materials which were sliding on the substrate. These images (not shown in this thesis; the reader is directed to the SI of Ref. [**A6**]) were used to estimate a contact area of A_{cont} = 1840 μm^2 with an array of eight microelectrodes (midpoint-to-midpoint distance 500 μm and taking into consideration the whole length of the cross-section). This results in a vertical pressure of $p = 68.6 \cdot 10^3$ N m^{-2} and $24.0 \cdot 10^3$ N m^{-2} for the direct force measurement and the resonance experiment, respectively. In comparison, conventional SFM tips apply forces in the range of 1 nN < F < 100 nN in contact mode on a contact area with a diameter of 2 - 10 nm.[251] The calculated pressure exerted by SFM tips, taking the smaller limit of the force F = 1 nN and the upper limit of the contact area A_{cont} = 78 nm^2, gives $p = 1.3 \cdot 10^7$ Nm^{-2} which corresponds to a value that is three orders of magnitude larger than those of the soft probes.

7.2 Contact Mode Scanning of Delicate Thin Organic Films

Imaging of delicate samples without damaging the sample surface and the probe was verified by imaging a SAM of hexadecanethiol (HDT). Square-shaped patterns of HDT

SAM were formed by µCP on Au (Section 5.2) and imaging was performed in SECM feedback mode with a linear array of eight carbon microelectrodes (250 µm midpoint-to-midpoint distances of the individual electrodes) in 2 mM FcMeOH. Figure 65a shows a 2 mm × 2 mm region of this pattern. Table 65 shows the correction values for the performed calibration. The stamped squares of 50 µm × 50 µm (periodicity was 70 µm) and also imperfections in the pattern are clearly resolved. The experiment was repeated with a four times larger image frame (4 mm × 4 mm, Figure 65b, correction values in Table 16), including in the center the previously imaged region. The highly resolved SAM pattern proves that no removal or damages were introduced into the SAM by the mechanical sliding of the soft probe.

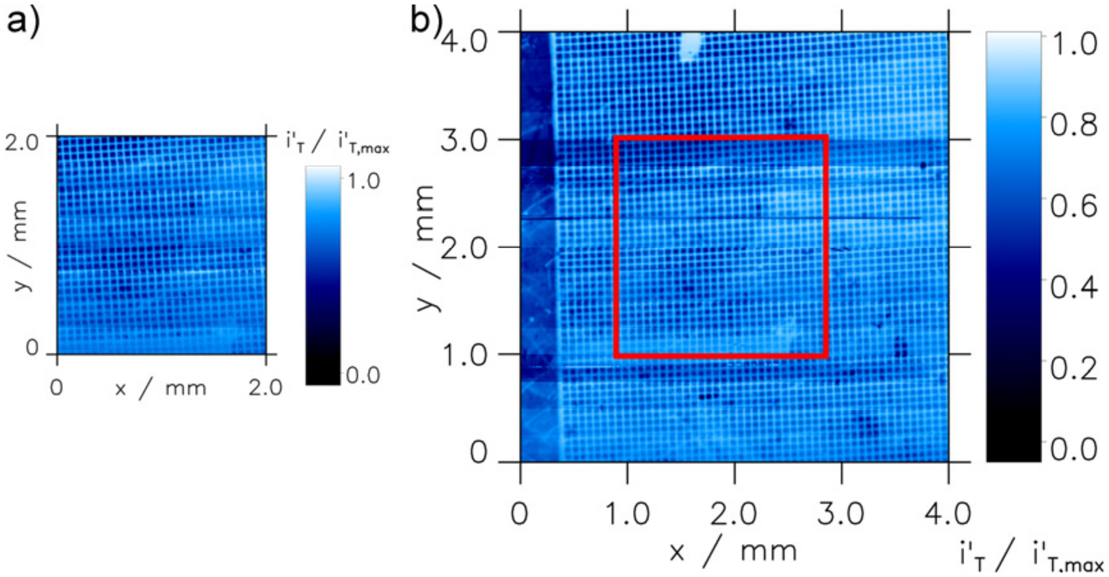

Figure 65. Calibrated SECM feedback mode images in 2 mM FcMeOH and 0.1 M KNO_3 over µCP-SAM on Au using an array of eight carbon microelectrodes. E_T = 0.4 V *vs.* Ag-QRE. a) An area of 2 mm × 2 mm was scanned. b) Subsequently, a second image (4 mm × 4 mm) was recorded that included the frame of Figure 2b (red square). Experimental conditions of (a): h_P = -46 µm, LO stroke height 300 µm, LO retract speed 250 µm s^{-1}, LO approach speed 10 µm s^{-1}, HF fwd step size 5 µm, HF $v_{T,fwd}$ = 25 µm s^{-1}, HF fwd delay before data acquisition 0.1 s, HF rev step size 5 µm, HF $v_{T,rev}$ = 250 µm s^{-1}, LF fwd step size 5 µm, LF $v_{T,fwd}$ = 25 µm s^{-1}, total imaging time required was 5.5 h. Experimental conditions of (b): h_P = -46 µm, LO stroke height 300 µm, LO retract speed 250 µm s^{-1}, LO approach speed 10 µm s^{-1}, HF fwd step size 10 µm, HF $v_{T,fwd}$ = 25 µm s^{-1}, HF fwd delay before data acquisition 0.1 s, HF rev step size 10 µm, HF $v_{T,rev}$ = 250 µm s^{-1}, LF fwd step size 10 µm, LF $v_{T,fwd}$ = 25 µm s^{-1}, LF large step 2000 µm, total imaging time required was 7 h. (Figures as published in [**A8**].)

Table 15. Current offsets and scale factors applied to calibrate Figure 65a.

k	1	2	3	4	5	6	7	8
$x_{\mathrm{off},k}$ (µm)	0	15	30	45	60	75	90	110
$y_{\mathrm{off},k}$ (µm)	0	250	500	750	1000	1250	1500	1750
$i_{\mathrm{T,off},k}$ (nA)[a]	7.78	7.15	6.43	6.23 (4.50)	6.57	6.13	6.76	4.76
s_k (nA^{-1})	0.076	0.066	0.057	0.034	0.064	0.05	0.062	0.111

[a] value in brackets represents manually adjusted value.

Table 16. Current offsets and scale factors applied to calibrate Figure 65b.

k	1	2	3	4	5	6	7	8
$x_{\mathrm{off},k}$ (µm)	0	-4.5	-9	-13.5	-18	-22.5	-27	-31.5
$y_{\mathrm{off},k}$ (µm)	0	250	500	750	1000	1250	1500	1750
$i_{\mathrm{T,off},k}$ (nA)	9.83	8.93	8.11	7.71	8.03	7.43	8.03	4.98
s_k (nA^{-1})	0.075	0.065	0.055	0.036	0.061	0.048	0.058	0.110

Furthermore, this image is a good example for demonstrating the expected resolution of the soft carbon microelectrodes. The shape of the individual carbon electrodes appears asymmetric due their slightly different dimensions in x (≈ 10 µm) and y (≈ 30-50 µm) direction. As a consequence, the resolution in y–direction is more limited than in x-direction. However, features of the printed SAM which are much smaller than the printed squares can be well identified (Figure 65, left) indicating a resolution comparable to conventional UMEs. The principle of SECM feedback imaging of the SAM pattern is based on the fact that the HDT SAM shows less permeability for the redox mediator FcMeOH which resulted in smaller currents over HDT-covered regions than over bare Au where direct redox mediator regeneration takes place (positive feedback).

In order to demonstrate the vulnerability of SAMs to mechanical stresses, the HDT squares were gently scratched by a plastic Eppendorf pipette tip and SECM imaging afterwards detected the mechanical removal of the SAM (Figure 66). Summarizing, the soft array probes can be used to image delicate samples, which are proved to be very delicate, without inducing any detectable damage.

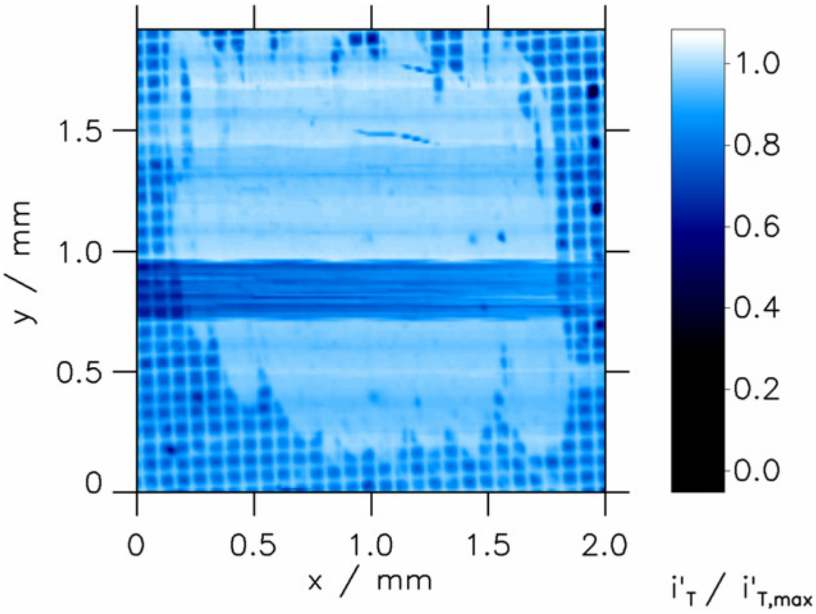

Figure 66. Calibrated feedback image in 2 mM FcMeOH and 0.1 M KNO_3 of the µCP SAM structure after gently scratching with a plastic Eppendorf pipette tip. E_T = 0.4 V *vs.* Ag-QRE. Experimental conditions of (b): h_P = -46 µm, LO stroke height 300 µm, LO retract speed 250 µm s^{-1}, LO approach speed 10 µm s^{-1}, HF fwd step size 10 µm, HF $v_{T,fwd}$ = 25 µm s^{-1}, HF fwd delay before data acquisition 0.1 s, HF rev step size 10 µm, HF $v_{T,rev}$ = 250 µm s^{-1}, LF fwd step size 10 µm, LF $v_{T,fwd}$ = 25 µm s^{-1}, total imaging time required was 2 h. (Figure as published in SI of [**A8**].)

Table 17. Current offsets and scale factors applied to calibrate Figure 66.

k	1	2	3	4	5	6	7	8
$x_{\text{off},k}$ (µm)	0	-6	-12	-18	-24	-30	-36	-42
$y_{\text{off},k}$ (µm)	0	250	500	750	1000	1250	1500	1750
$i_{\text{T,off},k}$ (nA)	5.48	5.28	4.69	4.44	4.63	4.32	4.67	3.02
s_k (nA^{-1})	0.146	0.113	0.101	0.055	0.114	0.081	0.108	0.157

7.3 Modification of Oligo(Ethylene Glycol)-Terminated Self-Assembled Monolayers

The modification of surfaces on a microscale is very attractive in order to direct the adhesion of living cells on the modified substrate. In fact, controlling the location and the size of the areas that promote cell adhesion is crucial to manage the survival, growth, differentiation and migration of the cells.[252] The size of cell adhesive regions does also influence the number of cells that can be attached in each modified spot. One approach - to achieve the localized control of cell adhesion - employs the formation of micropatterned areas with a sufficient degree of cell adhesiveness surrounded by cell repellent regions. Commonly, photolithography and microcontact printing techniques are used to pattern microstructures of cytophobic and cytophilic materials. However, advantages and disadvantages of these techniques were already discussed in Chapter 3. Generally, cells bind to proteins and hence surface patterns have to be suitable for the adsorption of proteins of the extra cellular matrix (ECM) like fibronectin to enable cell attachment. Another methodology uses the local creation of static or even dynamic stimuli for cell adhesion and was popularized by the work of Mrksich and Yousaf.[253, 254] Dynamic substrates can be modulated in real time providing pathways to study cell responses including migration and differentiation phenomena which were provoked by changes in the cells' environment. In their works, Mrkisch and coworkers[253], and Yousaf and coworkers[255, 256] took advantage of the possibility to electrochemically oxidize and reduce SAMs by the polarization of the sample.[163, 257] *In situ* patterning of proteins inside microfluidic devices integrated with microelectrodes was presented by Kaji *et al.*[257] The same group also introduced SECM for a probe induced manipulation of bovine serum albumin (BSA)-coated glass substrates to direct cell adhesion as mentioned in Section 3.1.[163]

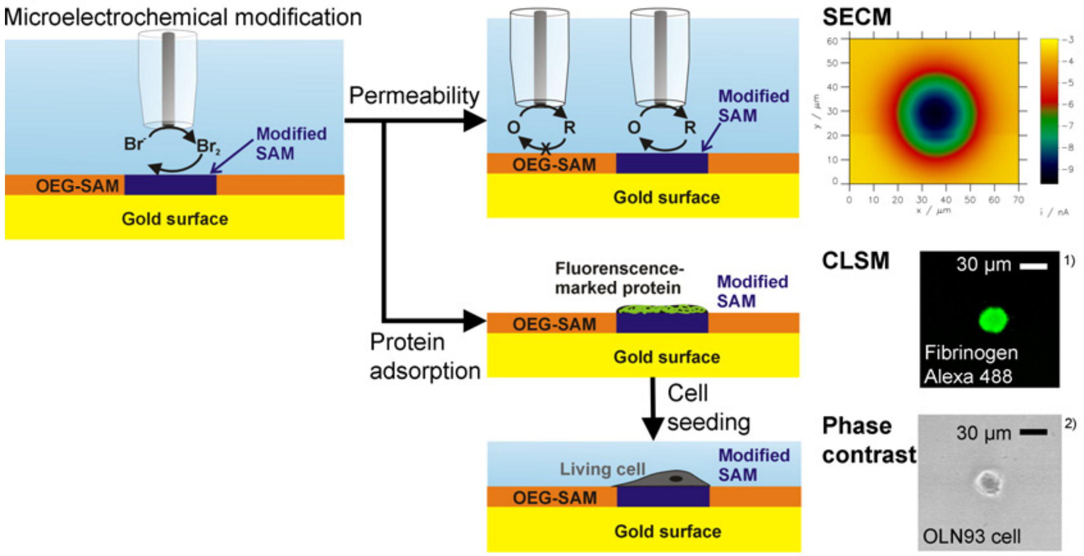

Figure 67. Overview of SECM induced localized modification of OEG SAM by electrogeneration of Br_2/HOBr followed by inspection by SECM or by successive adsorption of proteins and OLN93 cells. Adopted and modified from Ref. [94]. The SECM image was recorded with a conventional Pt-UME (r_T = 12.5 µm, *RG* = 10) after tilt correction. Pulse duration for modification was 5 s. Electrolyte solution 1 mM $[Ru(NH_3)_6]Cl_3$ and 50 mM KBr in 0.1 M phosphate buffered solution (pH 7). Step size 2 µm, translation rate v_T = 25 µm s^{-1}, E_T = -0.35 V *vs.* Ag-QRE. 1) Image modified from Zhao *et al.*[67, 94] 2) Image modified from Diploma thesis of B. Vaske.[258]

Among these methods, SAMs prepared with OEG terminal units ($Au\text{-}S(CH_2)_{11}(OCH_2CH_2)_nOH$; $n = 3–7$) are currently seen as one of the best cell adhesion resistant systems whereas alkyl chains can be used for protein adsorption.[254, 259, 260] The idea of removing the OEG units from the OEG SAM by an electrochemically induced chemical reaction was followed by Wittstock and coworkers. This method was mentioned in Section 3.1 and is summarized in Figure 67. Wittstock and coworkers used the molecule $HS(CH_2)_{11}(OCH_2CH_2)_6OH$ (Figure 68, Section 5.1) to form the SAM on a thin gold film. The patterning of the cell-repellent OEG SAM was then based on the electrogeneration of bromine at a UME which was positioned close to the OEG SAM. The Br_2/HOBr (Section 3.1) diffused to the surface and reacted with the OEG units. The OEG units were removed and it was proven that the degradation of the OEG units takes place at a much higher rate compared to the removal of the alkyl chains.[261]

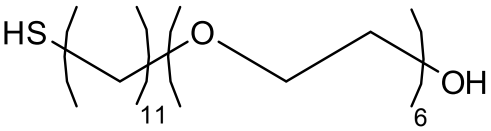

Figure 68. Structural formula of the ($HS(CH_2)_{11}(OCH_2CH_2)_6OH$) molecule which forms the OEG SAM on gold surface.

In buffered electrolyte solutions containing both KBr (source for Br_2) and $Ru[(NH_3)_6]Cl_3$ (redox mediator for SECM feedback mode), the modification was performed by the oxidation of Br^- at the UME whereas reactivity imaging was achieved by changing the applied potential at the UME in order to reduce the ruthenium complex. Alternatively, the electrolyte solution could be changed after modification in order to use FcMeOH as redox mediator for reactivity imaging. Approach curves in 0.5 mM FcMeOH and 0.2 M Na_2SO_4 showed an almost negative feedback for pristine OEG SAMs due to the impermeability for the redox mediator ($k_{\mathrm{eff}} \approx 0$ for FcMeOH). In a custom-made galvanic cell a macroscopic area covered with OEG SAM was homogenously modified by exposure to a 5 µM Br_2 and 0.1 M Na_2SO_4 solution for 300 s. From an approach curve an effective first order rate constant $k_{\mathrm{eff}} = 0.036$ cm s^{-1} was obtained which represents a value close to the diffusion-limited reaction rate a sample. This experiment demonstrates the permeability for the redox mediator after OEG SAM modification by Br_2. In order to locally modify the OEG SAM by SECM, an electrolysis with a typical pulse duration of 5 s was applied to produce Br_2 at the UME and the modified spot, generated with this procedure, was imaged by SECM in feedback mode (Figure 67). The higher absolute currents in the SECM image over the modified regions indicate the higher permeability for the redox mediator.

After the localized modification of the OEG SAM by SECM, the site-selective adsorption of fluorescence labeled proteins was demonstrated by Wittstock and coworkers and investigated by CLSM.[67] The protein adsorbed only on the modified regions. Furthermore, the proteins could successfully promote the formation of micropatterns of cells such as OLN93 cells or human fibroblasts on the sample (Figure 67).[67, 258] In order to attach cells dynamically, the UME was used to modify already pre-patterned cellular substrates to create a second cell population on an adjacent area.[67, 94] The first steps of this multipatterning was either µCP[94] or microelectrochemical modification.[67]

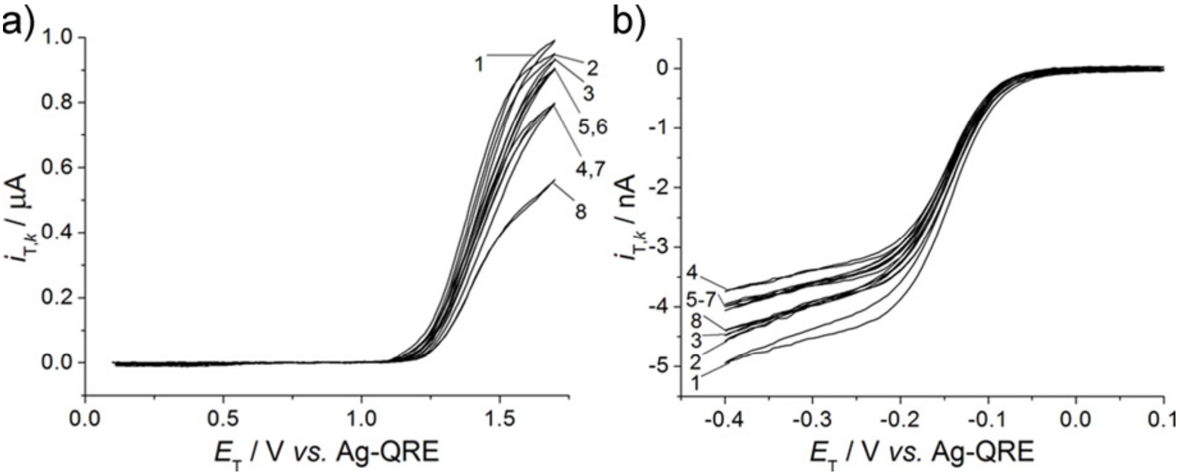

Figure 69. CVs of a linear array of eight carbon microelectrodes in 1 mM $[Ru(NH_3)_6]Cl_3$ and 50 mM KBr in 0.1 M phosphate buffered solution (pH 7). The generation of bromine by oxidation of Br^- for modification (a) and the steady-state reduction current of $[Ru(NH_3)_6]^{3+}$ for SECM imaging (b). Potential scan rates were 50 mV s^{-1} (a) and 10 mV s^{-1} (b).

In this thesis, the afore mentioned system was adopted for the parallelized surface modification using soft microelectrode arrays on a larger scale as a proof of principle test for biochemical applications. Figure 69 shows CVs of one carbon microelectrode array in 1 mM $[Ru(NH_3)_6]Cl_3$ and 50 mM KBr in 0.1 M phosphate buffered solution (pH 7). The oxidation of bromide to bromine for surface modification and the reduction of $[Ru(NH_3)_6]^{3+}$ for SECM feedback mode imaging yielded well defined CVs allowing the use of these probes for the designated surface modification and successive characterization experiments.

Figure 70 shows exemplary approach curves towards the OEG SAM. A negative feedback is obtained indicating the passivation of the gold substrate.

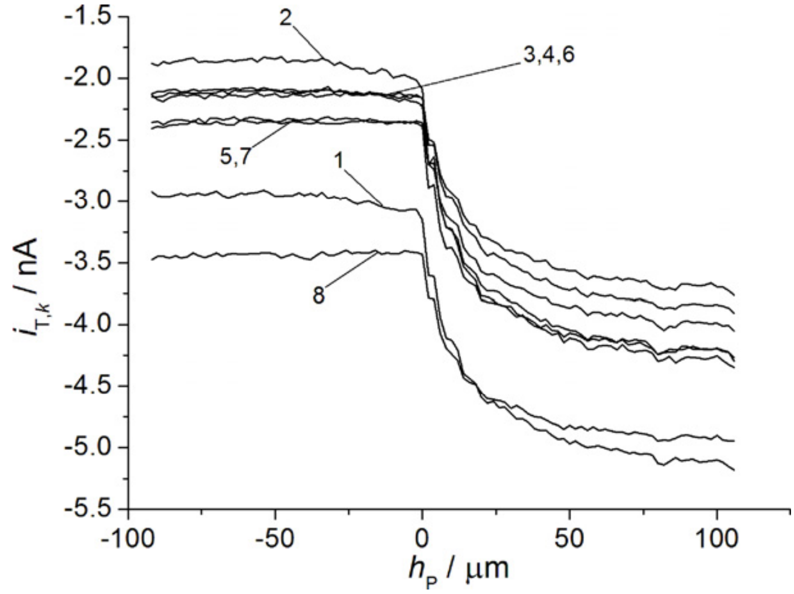

Figure 70. Approach curve with a probe array towards OEG SAM in 1 mM $[Ru(NH_3)_6]Cl_3$ and 50 mM KBr in 0.1 M phosphate buffer solution (pH = 7). Numbers indicate the number of the array elements. E_T = -0.35 V *vs.* Ag-QRE, step size 2 µm, translation rate 10 µm s^{-1}. (Figure modified from SI of Ref. [**A8**].)

Before modification, the soft linear array was approached until a defined h_P value of -43.5 µm was reached. No correction of the sample tilt was performed. The array was translated 500 µm with 50 µm s^{-1} in *x*-direction and at each step the array rested while a potential pulse (E_{puls} = 1.8 V *vs.* Ag-QRE) of 5 s was applied. The pulse duration was adopted from experiments with conventional Pt-UMEs since electrode area and working distance were comparable. During the movement of the probe a potential was applied without causing a reaction at the carbon electrode (E_T = 0.1 V *vs.* Ag-QRE). After this procedure, the same carbon microelectrode was used to image the modified regions in feedback mode (Figure 71a). The spots can be clearly identified by the increased permeability for the redox mediator through the monolayer (increase in current) and the image shows inclined D-shaped modified regions. The distorted shapes can be explained by an array that was not placed perpendicular to the direction of the inclination. The D-shape of the spot was certainly caused by the diffusion layer of Br_2 resulting from the sickle-like active carbon microelectrode areas. A conventional UME (r_T = 12.5 µm, *RG* = 10, *d* = 3 µm) was used to scan the same six regions after sample tilt correction in order to image the modified spots with higher resolution (Figure 71b). The D-shapes were smaller and appear much clearer as a result of the higher image resolution. The distance between the spots is increased with respect to the expected one (110 μm instead of 100 μm). This feature is caused by a sample tilt in *x*-direction during the modification with the array (Section 6.5.5).

a) Investigation by one array electrode:

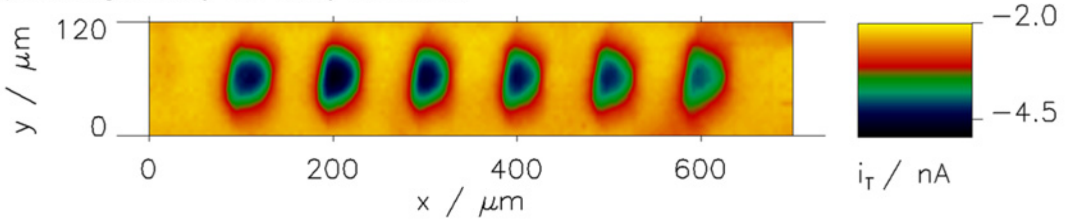

b) Investigation by conventional UME:

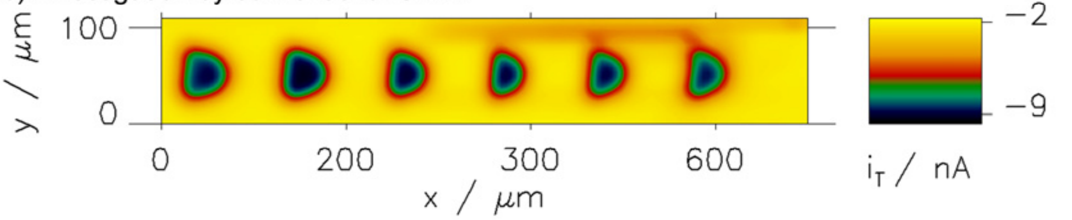

Figure 71. SECM feedback mode images of the same six spots created by a 5 s pulse at a soft carbon microelectrode. No tilt correction. Modification details in the text, E_{puls} = 1.8 V *vs.* Ag-QRE. The modified regions were scanned with the single soft carbon microelectrode (a) which also had performed the modification and with a conventional Pt UME (b, r_T = 12.5 μm, *RG* = 10, *d* = 3 μm) after tilt correction. Electrolyte solution 1 mM $[Ru(NH_3)_6]Cl_3$ and 50 mM KBr in 0.1 M phosphate buffered solution (pH 7). a) Step size 5 μm, translation rate v_T = 50 μm s^{-1}, E_T = -0.35 V *vs.* Ag-QRE. b) Step size 2 μm, translation rate v_T = 25 μm s^{-1}, E_T = -0.35 V *vs.* Ag-QRE.

The modifications in Figure 71 were performed from right to left. Although the same conditions were applied at each step, two effects can be identified: i) the shapes of the spots vary slightly and ii) the sizes of the modified regions increase in the direction of modification. One explanation of this outcome could be that the highly reactive, probe-generated Br_2/HOBr also reacts with the carbon composite material itself modifying its shape or reactivity: the carbon could be made more active and/or the active electrode area may increase as well. Both effects would lead to a higher rate of bromine generation during a constant pulse of 5 s and consequently to a broadening of the modified regions. Note, that in general, the size of the modified areas is influenced by the pulse duration and the working distance.

The obtained modified area was further characterized by means of Pulsed Force Mode (PFM) SFM as already demonstrated by Wittstock and coworkers for μCP SAMs.[164] In this thesis, the SFM tip was prior modified with a SAM containing a hydrophilic functional group as described in literature.[164] This allowed the differentiation between OEG SAM and modified SAM due to their hydrophilic and hydrophobic properties. PFM SFM is a non-resonant, intermediate-contact technique that gives information about surface properties such as topography, stiffness, and adhesion. These three surface properties were measured simultaneously and are plotted in Figure 72a-c.

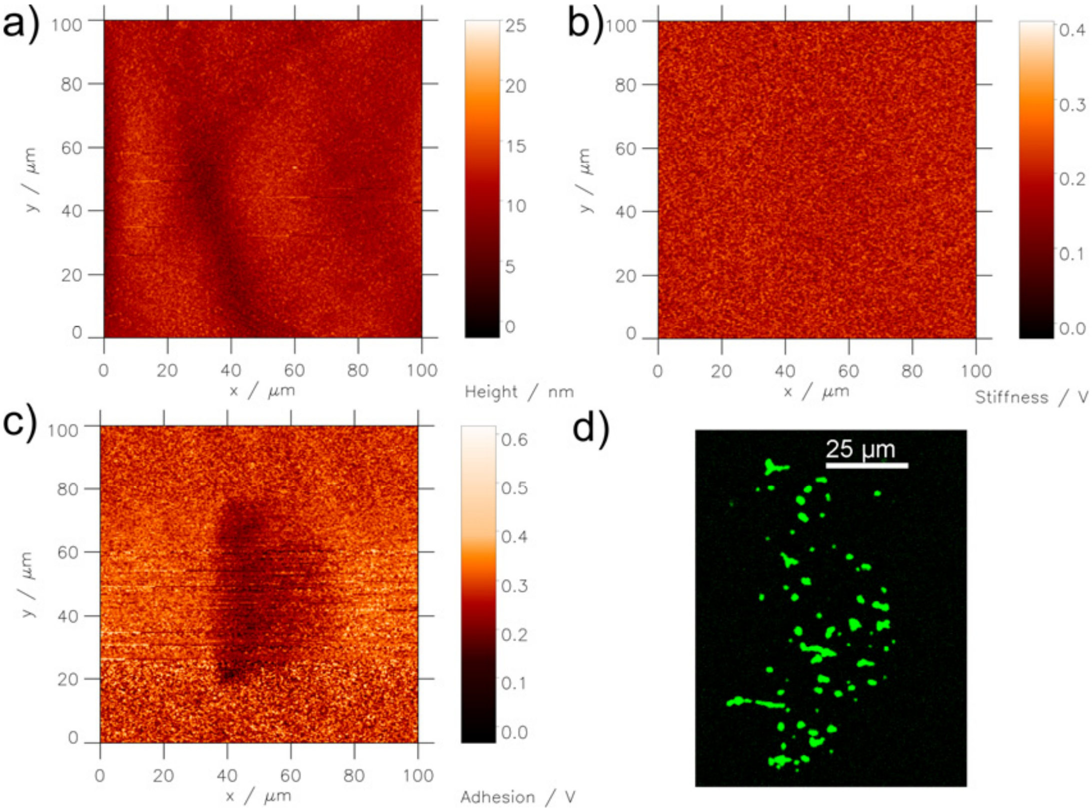

Figure 72. a-c) PFM SFM images of the modified OEG SAM region, created by a 5 s pulse with a soft carbon microelectrode. a) Topography, b) stiffness, c) adhesion. d) CLSM image of selectively-adsorbed fibrinogen-Alexa Fluor® 488 on a different modified region. (Figure a-c as published in SI of Ref. [**A8**].)

By means of an SFM tip, the technique provides a much higher lateral resolution than SECM. A clear contrast is only identifiable in the adhesion image (Figure 72c). The horizontal stripes are caused by the measurement and do not represent real surface features. The SFM tip was modified with a hydrophilic SAM. Therefore, the measured adhesion (values are given in volts) is based on the interaction between the hydrophilic tip with the hydrophobic (modified OEG SAM) and hydrophilic regions (untreated OEG SAM), respectively. Natural water condensation on the surface under ambient conditions enhances this effect. A D-like shape was detected as in the SECM image, but with a smaller and more accurate dimension representing the real shape of the modified spot. In fact, the SECM image relies on the diffusion of the redox mediator and, due to the larger working distance and the much larger microelectrode area compared to the SFM tip, the shape inspected by SECM appears larger. A higher resolution would be reached with a nanoelectrode operated in shear force mode. In the PFM SFM adhesion image it can be seen clearly that the shape of the modified spot is much sharper on the left side. This can be explained by the probe-sample arrangement during the modification. The probe with an inclination angle of 20° was in contact with the sample at the left side of the spot. Here, the diffusion of Br_2/HOBr was affected by the Parylene C layer thickness and by the recess of the electrode. On the left side the sample-electrode distance was smallest leading to a sharp transition between modified and unmodified regions whereas d increased to the right due to the angle α (Figure 42). To the right the Br_2/HOBr diffusion was less efficient which is evident in the adhesion image: i) the measured signal within the modified spot increased from left to right demonstrating slightly hydrophilic properties caused probably by some residual OEG units on the surface at the right and ii) the border between the modified and unmodified OEG SAM at the right is less sharp than the border at the left. However, this trend could not be observed in the SECM image demonstrating that the permeability is not influenced by residual OEG-terminated molecules in the transformed region. In earlier publications of the Wittstock group it had been noted that the permeability for a redox mediator in SECM imaging and the protein adsorption behavior do not show necessarily the same trend.[94] Recently, Nunige *et al.*[18] made theoretical and experimental investigations about the surface coverage $\Theta_{\text{C-Br}}$ of a bromo-terminated SAM after probe induced modification. They illustrated the time dependence and the local change of $\Theta_{\text{C-Br}}$ from modified to non-modified regions. Furthermore, it is important to notice that no shape related to the modification can be recognized in the stiffness image (Figure 72b) and in the topographic image (Figure 72a) indicating that the gold layer was not etched.

The site-selective adsorption of the fluorescence labeled protein fibrinogen-Alexa Fluor® 488 on the OEG-free SAM was performed and gave similar results as expected from reports in literature.[67] One example is shown in Figure 72d. The proteins were attached in a D-like arrangement whose dimensions match with the PFM SFM adhesion image (Figure 72c). However, the proteins do not completely cover the modified spot. One explanation could be that the OEG units are not completely removed. But adversatively, the OEG SAM could also be partly removed completely exposing locally bare gold areas. Both effects would obstruct the protein adsorption, but are unlikely. More probably, the protein adsorption did not work reliably with the used solution causing the incomplete coverage to the modified spot.

In order to modify larger areas than a spot, the array can be laterally translated in *x*-direction while a constant potential is applied to generate bromine. This was performed manually by using the MultiWE32 to apply a potential of E_T = +1.8 V *vs.* Ag-QRE and the Märzhäuser positioning system to control the movement of the probe. The potential was switched off directly after the movement of the probe had been stopped. Parallel lines of various lengths were drawn into the OEG SAM and investigated afterwards in SECM feedback mode. The carbon microelectrodes in one array imaged the areas they modified themselves (Figure 73a-c).

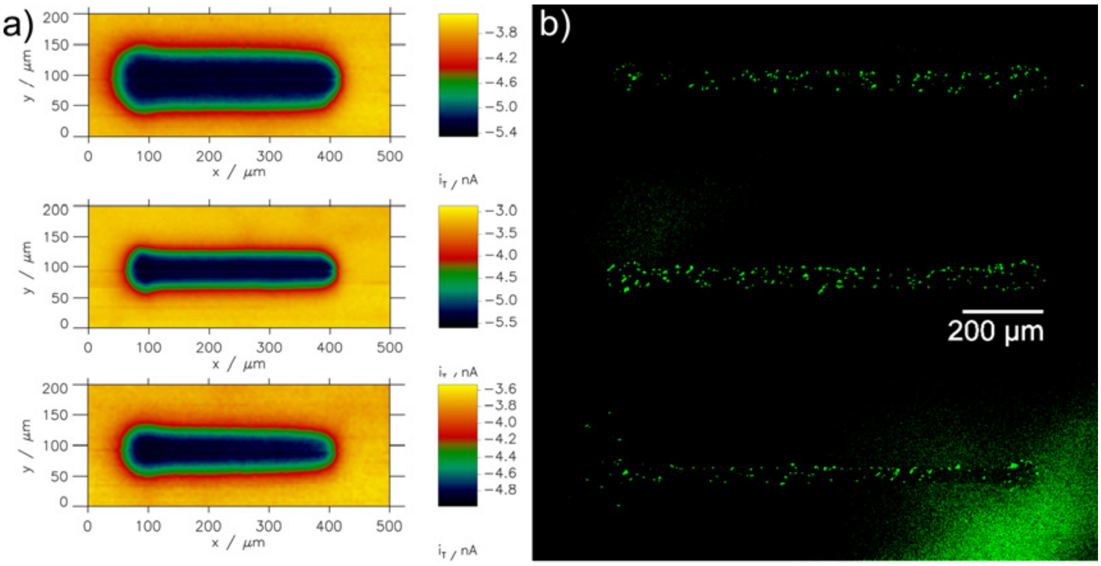

Figure 73. a-c) SECM feedback mode images of three modified lines in the OEG SAM by using three electrodes in one soft carbon microelectrode array. Images were recorded by the array electrodes itself. The potential was switched on for modification (E_T = +1.8 V *vs.* Ag-QRE), the probe was translated in contact mode with v_T = 25 µm s^{-1} and the potential was switched off after the movement had been stopped. Electrolyte solution 1 mM $[Ru(NH_3)_6]Cl_3$ and 50 mM KBr in 0.1 M phosphate buffered solution (pH 7). d) Three 1 mm long modified lines allowed adhesion of fibrinogen-Alexa Fluor 488® in phosphate buffered saline and investigation by (CLSM). Experimental conditions of (a): E_T = -0.35 V *vs.* Ag-QRE. h_P = -40 µm, LO stroke height 200 µm, LO retract speed 100 µm s^{-1}, LO approach speed 10 µm s^{-1}, HF fwd step size 5 µm, HF $v_{T,fwd}$ = 25 µm s^{-1}, HF fwd delay before data acquisition 0.1 s, HF rev step size 5 µm, HF $v_{T,rev}$ = 1000 µm s^{-1}, LF fwd step size 5 µm, LF $v_{T,fwd}$ = 50 µm s^{-1}.

The direction of the probe movement during modification was from right to left. A broader shape at the end of the lines was caused by the manual modification procedure and an operational delay between stopping the probe translation and switching off the potential for modification. The shape of the modification is controlled besides the size of the microelectrode by the amount of generated bromine, the working distance and the translation rate. A slower speed of the probe and a larger working distance broaden the line due to the expansion of the diffusion layer of bromine whereas the length of the modified line is basically influenced by the performed probe translation. In addition, the effect of an increased activity of the carbon microelectrodes during modification as described in Figure 71 is confirmed in Figure 73c where the width of the modified region became clearly broader in the direction of the performed probe movement. Proteins were adsorbed subsequently as demonstrated for three parallel lines generated by using three neighbored carbon electrodes in one array with a midpoint-to-midpoint distance of 500 µm (Figure 73d). The probe was moved 1 mm for modification showing the possibility of high-throughput modification.

7.4 Software-Assisted Parallel Patterning and Imaging

The utilization of microelectrode arrays in combination with self-made software offers the possibility to perform automated micropatterning. As demonstrated in the previous section, manually controlled parallel surface modification was performed with soft linear microelectrode arrays. For an automated routine we took advantage of some technical options provided by the Ivium devices for multi-electrode control. A base potential can be applied to all electrodes by the MultiWE32 module. For individual electrodes an offset potential (±2 V with respect to the base potential) can be applied. This feature allows applying of one potential to one or more electrodes of the array at which no electrochemically induced reactions and thus no modification occur (Off-potential). The offset potential is instead set to generate bromine in order to induce surface modification (On-potential). Using these options, high-throughput patterning can be performed in two ways. The first possibility is that the electrodes pattern individual structures which are separated by the distance of the electrodes. The constructed shapes can be identical or different from each other. The second strategy is to pattern also the areas in-between electrodes in order to construct one large merged image.

The patterning can be accomplished with our new *x* modification line scans, included in SECMx, in which On-potential pulses are applied to the individual electrodes at defined translation steps in order to draw a designed structure. The scan length, translation rate and step size are defined in the SECMx software interface like for the standard SECM line scan procedures. The shape of the pattern is extracted from an ASCII file which can be created with a text editor. These files contain the pulse durations in seconds for several successive steps (in lines) for each individual electrode (in rows) as shown exemplary in Figure 74 for the capital letter "A". Zero pulse duration stands for no modification.

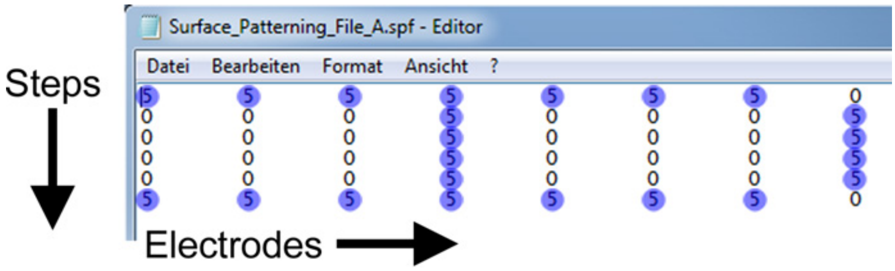

```
5       5       5       5       5       5       5       0
0       0       0       5       0       0       0       5
0       0       0       5       0       0       0       5
0       0       0       5       0       0       0       5
0       0       0       5       0       0       0       5
5       5       5       5       5       5       5       0
```

Figure 74. Surface patterning ASCII file to write the capital letter "A" with an array of 8 microelectrodes. The values represent pulse durations in seconds for 6 steps (6 lines) and for 8 electrodes (8 columns).

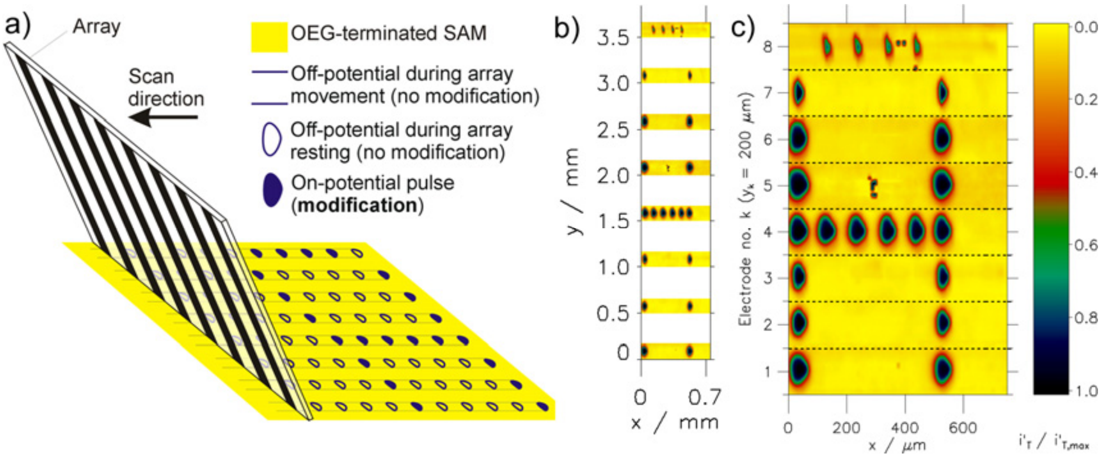

Figure 75. a) Schematic representation of surface modification line scan to write the capital letter "A" into the OEG SAM. For modification an On-potential is applied with a defined pulse duration whereas an Off-potential is applied for no reaction at the microelectrode. Parameters for writing with a carbon microelectrode array (midpoint-to-midpoint distance 500 μm): $E_{T,On}$ = +1.9 V, $E_{T,Off}$ = +0.1 V *vs.* Ag-QRE, v_T = 25 μm s^{-1}, delay before pulse 0.5 s, step size 100 μm. The total time for the line scan was 58s. b) The "A" was scanned afterwards in SECM feedback mode using the same array and electrolyte solution (1 mM $[Ru(NH_3)_6]Cl_3$ and 50 mM KBr in 0.1 M phosphate buffered solution (pH 7)). Scanning parameters: h_P = -140 μm, LO stroke height 200 μm, LO retract speed 100 μm s^{-1}, LO approach speed 10 μm s^{-1}, HF fwd step size 10 μm, HF $v_{T,fwd}$ = 25 μm s^{-1}, HF fwd delay before data acquisition 0.1 s, HF $v_{T,rev}$ = 1000 μm s^{-1}, LF fwd step size 10 μm, LF $v_{T,fwd}$ = 25 μm s^{-1}, total imaging time required was 26 min. Only the modified areas were scanned and arranged together excluding the non-scanned areas (c). (Figure as published in Ref. [**A8**].)

The electrode numbers are ordered is in the file from left to right and correspond to the positive *y*-direction in the SECM setup. The scan direction in *x*-direction is always negative for the bent arrays. This characteristic is unimportant for a symmetric shape like the "A", but is more determining for more complex structures like "Uni OL" and has to be taken into consideration that the original ASCII file has to represent the mirrored shape of the desired pattern. Figure 75a shows schematically the writing of the "A". The Off-potential is applied during array movement and when no modification is requested. The On-potential induces modification at each step when it is applied. In the software, a delay before and after the pulse can be set in order to reduce the convective disturbances and to ensure that the generation of the etchant stopped when moving the probe further. In this way, equal conditions for each modification are provided.

The character "A" was written in 58 s. The distances between the generated spots in the perpendicular direction to the scanning one were defined by the distance of the individual electrodes in the array (500 µm in this example). High-throughput feedback mode imaging was carried out within 26 min with the same array providing the shape of each spot (Figure 75b). These experiments demonstrate that the modification and detection performance of the newly developed procedure is really fast. In order to further accelerate the experiment, scanning of non-modified areas was avoided. Arranging the eight image frames into one image resulted in Figure 75c giving a concise overview about the achieved quality for each individual "pixel". It can be seen that despite the electrodes were calibrated, the spots produced by the individual electrodes slightly vary from each other. In fact, the diffusion of generated etchants and hence the shapes of the modified spots are affected by the electrode size, geometry and working distance. The same considerations are valid for the diffusion of the redox mediator in feedback mode imaging.

The newly implemented SECMx surface modification tool is based on modifying individual spots separated by a step size. In order to draw a line the spots must overlap. An alternative would be to switch on the potential at an individual electrode, to move the probe over a defined distance and to switch off the potential similarly to the aforementioned continuous manual procedure (Section 7.1.3)). This option was not used for the following reasons: one advantage of the individual spot performance is a more precise control of the amount of produced bromine (via the pulse duration) and thus of the size of the modified regions. In a continuous movement, the amount of bromine per area would depend strongly on the probe translation rate. A slow translation rate would broaden the line and a fast translation rate could introduce convection reducing the sharpness of the spot. Furthermore, from the programming point of view, the individual electrodes are addressed sequentially. As described in Section 6.2.1, the communication between PC and the microprocessor of the Ivium CompactStat via USB takes approximately 20 ms per command and channel. In the new procedure the time is measured with high accuracy to switch on and off the potential in order to achieve the desired pulse duration for each channel. A continuous movement of the array during the modification experiment would instead cause a lateral shift from channel one to eight due to the delay caused by communication between software and hardware. Additionally, in the spot modification routine, delay times before and after the modification are introduced. In this way, the conditions at each step are equal and the influence of convection is reduced.

The abbreviation "Uni OL" for the University of Oldenburg was written into the OEG SAM within 69 s and read in high-throughput SECM imaging (Figure 76) in 29 min. This example demonstrates that an area of 2900 µm × 200 µm × 8 can be modified and scanned within just half an hour. Afterwards, the protein fibrinogen-Alexa Fluor 488® was adsorbed on the modified regions and imaged by CLSM. Due to a maximum image size of 800 µm × 800 µm with the used objective in the CLSM, 32 image frames were recorded and assembled after cutting to form a continuous image (Figure 77).

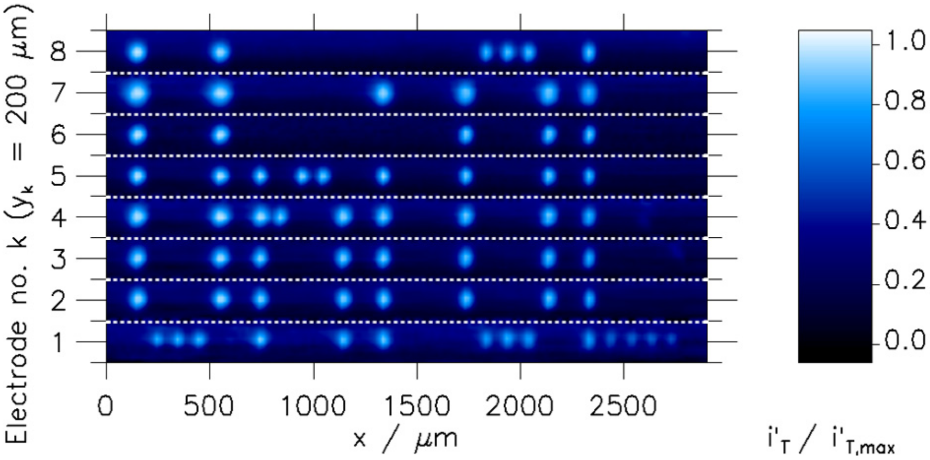

Figure 76. SECM feedback image of "Uni OL" pattern written by an array of eight carbon microelectrodes in 1 mM $Ru[(NH_3)_6]Cl_3$ + 50 mM KBr in 0.1 M phosphate buffered solution (pH 7). Patterning parameters: $E_{T,On}$ = +1.8 V, $E_{T,Off}$ = +0.1 V *vs.* Ag-QRE, delay time before and after pulse 0.5 s, translation rate 50 µm s^{-1}. SECM feedback image parameters: E_T = -0.35 V *vs.* Ag-QRE, h_P = -40 µm, LO stroke height 200 µm, LO retract speed 100 µm s^{-1}, LO approach speed 10 µm s^{-1}, HF fwd step size 20 µm, HF $v_{T,fwd}$ = 50 µm s^{-1}, HF fwd delay before data acquisition 0.1 s, HF rev step size 20 µm, HF $v_{T,rev}$ = 1000 µm s^{-1}, LF fwd step size 20 µm, LF $v_{T,fwd}$ = 25 µm s^{-1}, total imaging time required was 29 min.

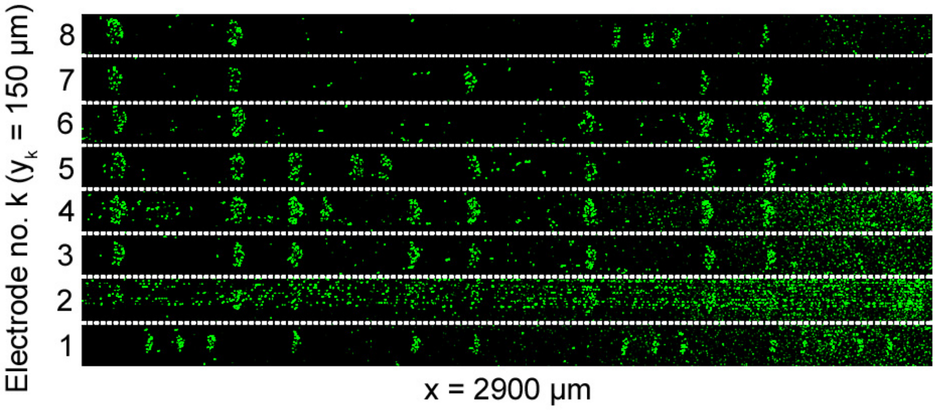

Figure 77. Assembly of 32 confocal laser scanning micrographs of the "Uni OL" pattern after successful site-selective adsorption of fibrinogen-Alexa Fluor® 488.

In this section, it was demonstrated that high-throughput modification can be performed in an easy and efficient way. However, in the course of some modification experiments using a carbon microelectrode array, a positive feedback could be obtained over the whole surface instead of the modified spots. This might be due to a complete removal or an irreversible disorder of the OEG SAM. Approach curves were recorded all over the surface and showed positive feedback indicating a bare gold surface or a SAM surface with high permeability for the redox mediator instead expected non-modified OEG SAM (negative feedback). The reason for this effect is unknown. The Au substrate covered with OEG SAM in all experiments was unbiased. An electrical short circuit due to mechanical contact between the carbon electrode and the Au surface can be excluded. Approach curves using $[Ru(NH_3)_6]^{3+}$ as redox mediator requires a cathodic potential (here E_T = -0.3 V *vs.* Ag-QRE) at the microelectrode. In non-deaerated solutions, oxygen can also be reduced producing reactive species whose influence cannot be predicted for the used systems. Hapiot and coworkers[174] obtained highly reactive hydroxyl radicals by reducing oxygen at a Pt-UME. These radicals removed locally organic thin films. However, in the course of this thesis, the effect was only observed after performed modification. Thus, the chemical reaction of the OEG SAM with Br_2/HOBr during the modification may cause an unknown counter reaction at the substrate whose influence on the OEG SAM cannot be predicted. It was not possible to reproduce this effect. Changing the sample and performing the same protocol for modification using the same array and setup worked without or again with a change of the OEG SAM. A situation in-between was also obtained as described in the following. Figure 78a shows the approach curve on OEG SAM before generating bromine.

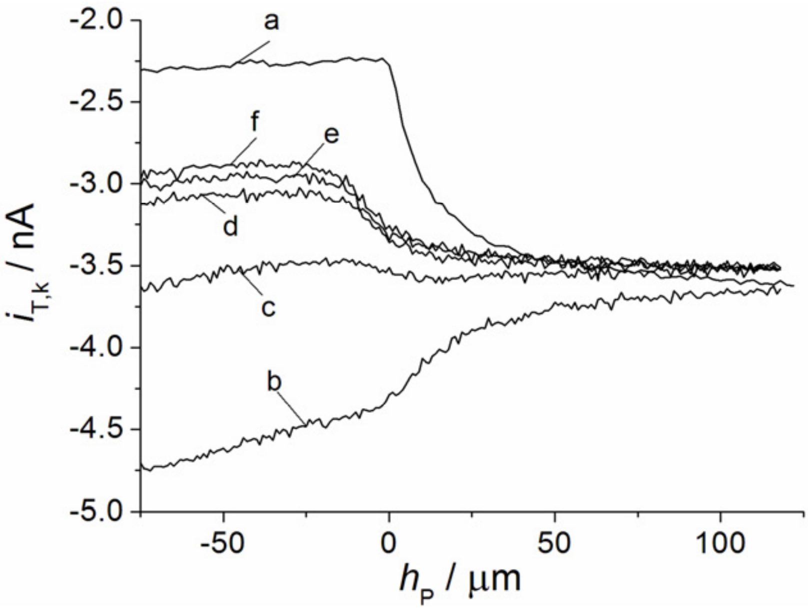

Figure 78. Time-dependent change of approach curves to non-modified OEG SAM from positive to negative feedback before (a) and after localized modification (b-f) by probe-generated bromine in a lateral distance of 100 µm to the performed modification. One exemplary carbon microelectrode within a soft array in 1 mM $[Ru(NH_3)_6]Cl_3$ and 50 mM KBr in 0.1 M phosphate buffer solution (pH 7). E_T = -0.3 V *vs.* Ag-QRE, step size 2 µm (a) and 1 µm (b-f), v_T = 10 µm s^{-1}. Starting times of the approach curves after modification were 10 s (b), 321 s (c), 755 s (d), 1089 s (e) and 1543 s (f).

The curve clearly indicates negative feedback. After a modification line scan, the probe was moved 100 µm further over a non-modified area. The probe was retracted and re-approached (Figure 78b) 10 seconds after the modification was stopped. Positive feedback was observed. Further approach curves at the same position showed that the feedback currents turned to negative feedback again depending on the time (Figure 78c-f). However, also after more than 16 min the currents for negative feedback did not decrease to the one recorded before the performed modification. But this phenomenon could also be caused by a change of the active carbon electrode area due to exposure to the reactive bromine. These results indicate a change of the OEG SAM structure. The monolayer may become disordered allowing in this way the redox mediator to penetrate through the monolayer and to be regenerated at the Au surface causing positive feedback. Over time the OEG SAM can possible reorganize making the monolayer in a certain degree less permeable for the redox mediator, but not able to block it completely. Anyway, the OEG SAM seems to be less compact than before. In the worst cases, the positive feedback remained over time. At this point, it cannot be stated if the monolayer is disordered or completely removed. A short circuit was introduced by connecting a Au wire to the part of the Au surface that is not inside the electrochemical cell and placing this wire also inside the electrolyte solution, but no improvements were obtained. However, this was not further investigated. The applied potentials for bromine generation were in some cases quite large ($E_{\mathrm{T,On}}$ = +1.9 V *vs.* Ag-QRE) which also could oxidize water to O_2. The modification potentials were reduced in the course of this thesis (*e.g.* 1.5 V *vs.* Ag-QRE) as a try to overcome the problem of the structural change or even the removal of the monolayer. However, it has to be stated that this procedure is not based on a known or proposed chemical reaction mechanism.

7.5 From a JPG-File to High-Throughput SECM Surface Modification

The utilization of microelectrode arrays in combination with the automated microstructuring tool is capable of forming even larger and more complex patterns. Displacing the array in the LF direction in-between surface modification line scans enables modification of an area as big as the array covers. In this way, a JPG-file showing *e.g.* the face of a human can be patterned into a surface. In the following, the complete sequence from a graphic file (JPG) to the transfer into an OEG SAM layer by surface modification and its SECM feedback image are described in detail. The following text and the figures are slightly modified from the Supporting Information of Ref. [**A8**]. An optical photograph was taken with a digital camera of a smartphone (2560 × 1920 pixels, Samsung Galaxy S I9000, Samsung Electronics, Republic of Korea) and saved in JPG-format. This file was loaded in Adobe Photoshop CS2 (Version 9.0). First of all, the background was removed (Figure 79a). Then, the picture was converted into a black-white two color scale TIFF-file (Figure 79b). For SECM high-throughput modification a compromise was made between resolution and image size. Finding the appropriate parameters with respect to step sizes and spot shape was crucial for the experimental performance. The sizes of the sickle-shaped modified spots are given by the electrode geometries, working distances and the amount of Br_2/HOBr reaching the OEG SAM. Accordingly to these considerations, an average spot size can be adopted from the PFM SFM image (Figure 72c) of 60 µm (*y*-direction) and 40 µm (*x*-direction). As a consequence and in order to get overlapping modified regions (*i.e.* continuous modified regions), the spot distance was set to 50 µm (*y*) and 37.5 µm (*x*). With these settings the image can be represented by 80 × 69 pixels (LF (*y*) × HF (*x*), Figure 79c, saved as TIFF-file). Such an image can be realized if the 8 individual electrodes of an array with 500 µm electrode separation perform 10 modification line scans (8 × 10 *y*-positions) in *x*-direction each with 69 steps. This will transfer the image on an area of 3950 µm × 2550 µm. The free software tool "ascii-pixelhaufen" was used to transfer the two level TIFF-file into a two character text file in ASCII format (ascii-pixelhaufen 2008.exe, Ruben Demus).

Figure 79. First three steps of the surface modification. a) A photograph was taken with a digital camera (2560 × 1920 pixels). b) The JPG-file was converted into a black-white two color scale TIFF-file (2560 × 1920 pixels). c) The resolution of the black-white TIFF-file was reduced to 80 × 69 pixels with a pixel ratio *x*/*y* = 0.75. (As published in SI of Ref. [**A8**].)

"0" was selected for white and "5" for black. The "table" representing this ASCII file content is shown in Figure 80 (left). Cells of the table that encode surface modifications (meaning a 5 s pulse) are highlighted in blue. Due to the order of electrodes within the array, the first ten columns from right to left refer to the 1st electrode, the next ten to the 2nd and so on. Ten modification line scan files were extracted from the table and arranged each to a line scan modification file as input data for SECMx as shown exemplarily for the first one in Figure 80 (right).

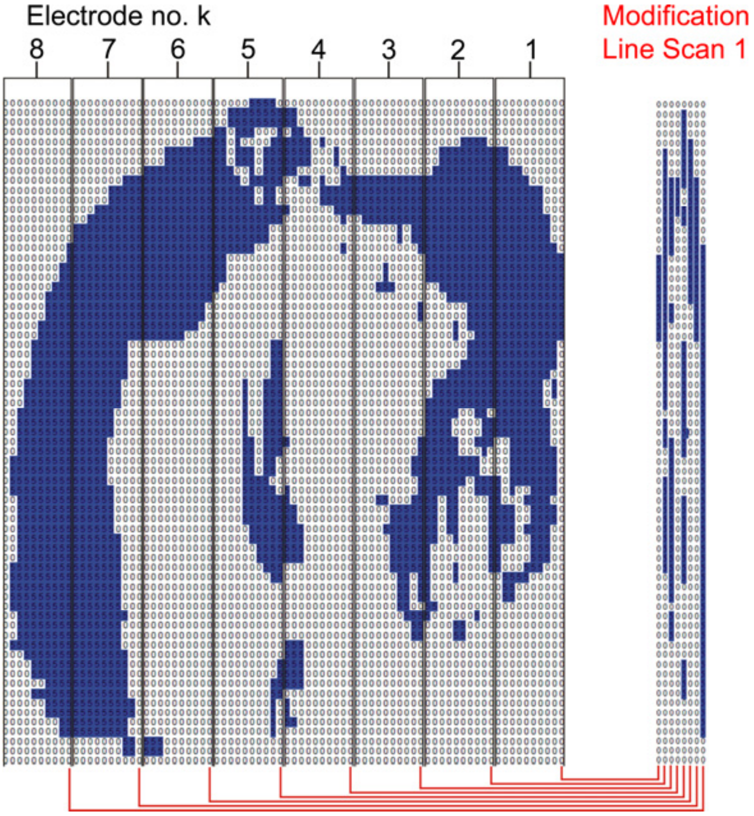

Figure 80. Forth step of surface modification. Left: Into pulse duration converted ASCII file. 5 s pulse is highlighted in blue. Ten line scans per electrode can be extracted for ten modification line scan files applicable in SECMx as shown exemplary for the first line scan (right). The order of electrode and line scans is from left to right as it is the positive *y*-direction. (As published in SI of [**A8**].)

The ten modification line scans were performed with a separation of 50 µm in the LF direction. In this way the eight electrodes modified the eight areas distinguishable by blue lines in Figure 81a. The Off-potential (no modification) of $E_{\mathrm{T,off}}$ = +0.1 V *vs.* Ag-QRE, and the On-potential $E_{\mathrm{T,on}}$ = +1.5 V *vs.* Ag-QRE to generate Br_2/HOBr for modification were set together with the HF step size of 37.5 µm and a delay of 0.5 s before and after applying a pulse. The array electrode itself was moved in contact mode on the surface with a translation rate of 100 µm s^{-1} between modification pulses. The positioning of the array in-between the modification line scans (retraction, lateral reverse movement, lateral step in LF direction and re-approach) was performed manually by the author in SECMx. SECM imaging of the modified regions (read-out) was recorded within 6.5 h by 3 microelectrodes (midpoint-to-midpoint distance 1500 µm) of the same array. A much smaller step size was used compared to the modification for achieving a higher resolution (Figure 81b). The image is composed of 119,160 individual data points (the 3 electrodes recorded overall 120 line scans each having 331 steps within one line scan) to cover an area of

3300 µm × 4487.5 µm. A current calibration was applied with current offsets to give i'_T. A scale factor was not required. The obtained SECM image clearly shows the feature of the human face obtained by patterning of the SAM.

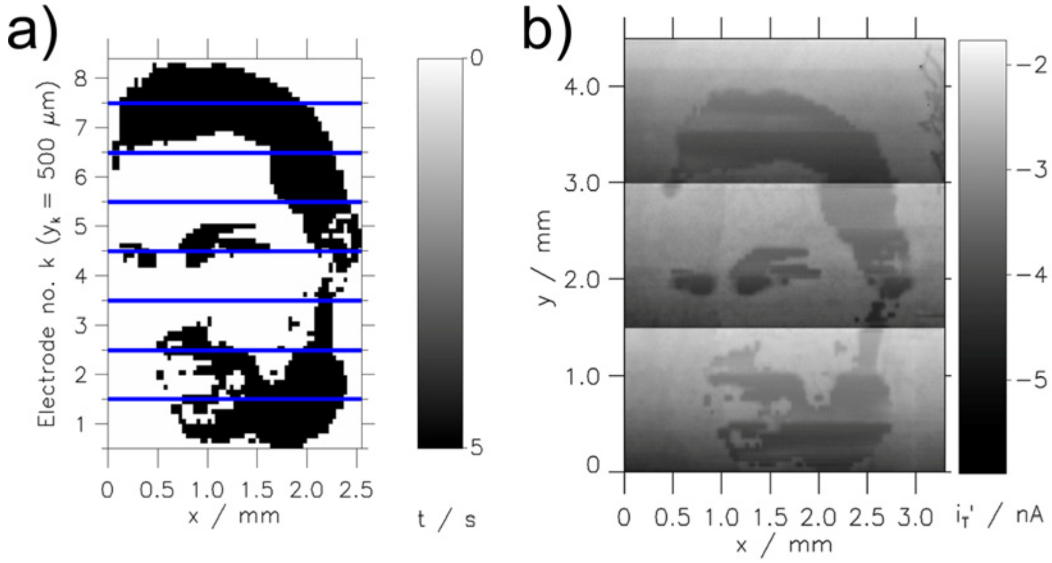

Figure 81. Last two steps of the surface modification. a) Plotted pulse durations after the performed modification of a closed area of 2.5 mm × 4 mm. The individual areas from the individual sensors are marked. f) Read-out image in SECM feedback mode by three microelectrodes of one array (midpoint-to-midpoint distance 1500 µm). Electrolyte solution: 1 mM $[Ru(NH_3)_6]Cl_3$ and 50 mM KBr in 0.1 M phosphate buffer solution (pH 7). Experimental conditions: E_T = -0.3 V *vs.* Ag-QRE, h_P = -40 µm, LO stroke height 500 µm, LO retract speed 100 µm s^{-1}, LO approach speed 20 µm s^{1}, HF fwd step size 10 µm, HF $v_{T,fwd}$ = 100 µm s^{-1}, HF $v_{T,rev}$ = 1000 µm s^{-1}, LF fwd step size 12.5 µm, LF $v_{T,fwd}$ = 50 µm s^{-1}. Total imaging time was 6.5 h. A current calibration was applied with current offsets to give i'_T. A scale factor was not required. (Figure as published in SI of [**A8**].)

Another proof of the achieved surface modification was obtained by cooling down the sample under ambient conditions for water condensation in the hydrophilic parts of the sample using a Peltier element (Figure 82, right). Hydrophilic non-modified and hydrophobic modified regions can be clearly identified. It is also evident that some line scans lead to less effective surface modifications that are also in a less clear way identified at the same location in the SECM image. The eight areas modified by different electrodes can be clearly distinguished because the contrast of modification increased from line scan to line scan likely because of an activation of the carbon electrodes by the reactive bromine species as discussed above. As a result of this electrode activation, more bromine could be produced at identical pulse conditions.

Figure 82: Comparison of the modified OEG SAM by SECM (a) and by optical photography after water condensation on hydrophilic parts (b). (Figure as published in SI of [**A8**].)

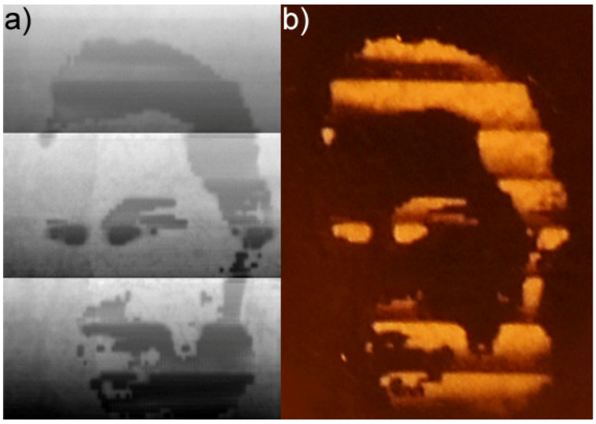

8 Array Probes for Testing Electrocatalysts

The oxygen reduction reaction (ORR) is technologically and biologically very important. With a view on current energy research, the ORR plays a pivotal role in fuel cells, biofuel cells and metal-air batteries in which the ORR takes place at the cathodes. The mechanisms of the ORR are also fundamental for the oxygen depolarized cathodes in the energy saving, large scale alkali-chlorine-electrolysis. The ORR is mechanistically complicated and it is still controversially discussed. Various mechanistic pathways were proposed and are summarized in Figure 83.[174, 262-266] The general scheme suggested by Wroblowa *et al.*[262] gives a simplified picture of the ORR and contains the two-electron and four-electron pathways. The one-electron reduction and recent reports about a three-electron pathway[174] were added. Oxygen diffuses from the solution bulk (*) to the electrode surface (S) where the experimental conditions, such as solvent and pH, and the nature of the electrode material influence the mechanism of the heterogeneous reduction. The possible reactions and their underlying conditions are listed in Table 18.

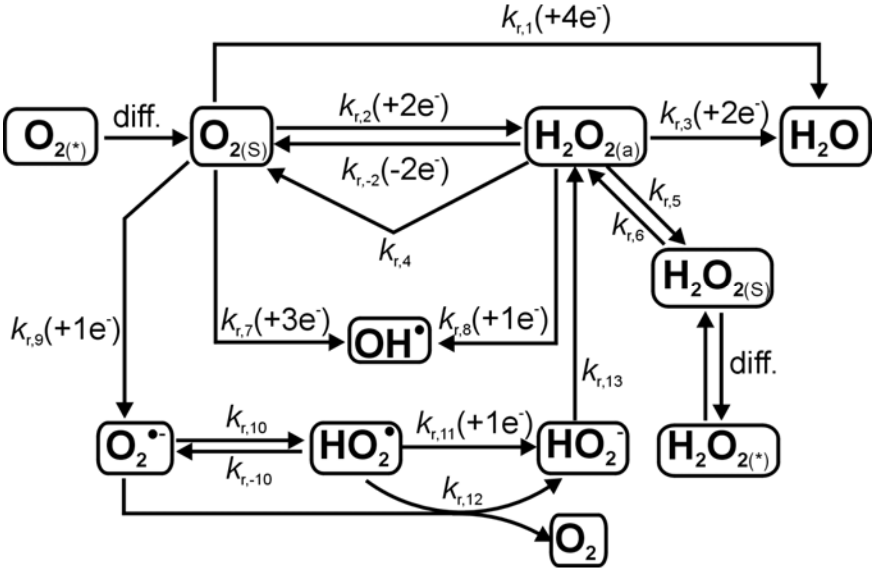

Figure 83. General scheme of the ORR. The rate constants k_r for the reactions are indexed and refer to the reactions listed in Table 18. The species can be in solution bulk (*), in close vicinity to the electrode surface (S) or adsorbed to the surface (a). Adopted and modified from Wroblowa[262] and Bülter.[267]

The most often discussed pathways are the four-electron and the two-electron pathways. The four-electron pathway is the irreversible direct reduction of oxygen to water in acidic solutions ($k_{r,1}$, Eq. (72)) and is desired in polymer electrolyte membrane (PEM) fuel cells. It provides a high efficiency and no stable intermediates or side products are detectable.

Table 18. Mechanistic pathways of the ORR.[174, 262-266, 268, 269] Adopted and modified from Bülter.[267] Indexes *m* are for the rate constants $k_{r,m}$ in Figure 83.

Pathway	Medium	Reaction	*m*	Eq.
1e$^-$	aprotic or strongly alkaline	$O_2 + e^- \rightarrow O_2^{\bullet -}$	9	(58)
	acidic	$O_2^{\bullet -} + AH \rightleftharpoons HO_2^{\bullet} + A^-$	10	(59)
		$HO_2^{\bullet} + e^- \rightarrow HO_2^-$	11	(60)
		$HO_2^{\bullet} + O_2^{\bullet -} \rightarrow HO_2^- + O_2$	12	(61)
		$HO_2^- + AH \rightarrow H_2O_2 + A^-$	13	(62)
2e$^-$	acidic and neutral	$O_2 + 2H^+ + 2e^- \rightarrow H_2O_2$	2	(63)
		$H_2O_2 + 2H^+ + 2e^- \rightarrow 2H_2O$	3	(64)
		$2H_2O_2 \rightarrow 2H_2O + O_2$	4	(65)
	alkaline	$O_2 + H_2O + 2e^- \rightarrow HO_2^- + OH^-$	2	(66)
		$HO_2^- + H_2O + 2e^- \rightarrow 3OH^-$	3	(67)
		$2HO_2^- \rightarrow 2OH^- + O_2$	4	(68)
3e$^-$	neutral and alkaline	$O_2 + 2H^+ + 2e^- \rightarrow H_2O_2$	2	(69)
		$H_2O_2 + e^- \rightarrow OH^- + OH^{\bullet}$	7	(70)
		$O_2 + 2H^+ + 3e^- \rightarrow OH^- + OH^{\bullet}$	8	(71)
4e$^-$	acidic	$O_2 + 4H^+ + 4e^- \rightarrow 2H_2O$	1	(72)
	neutral and alkaline	$O_2 + 2H_2O + 4e^- \rightarrow 4OH^-$	1	(73)

Contrary, the two-electron reduction or "series" pathway leads to the formation of hydrogen peroxide in acidic and neutral media ($k_{r,2}$, Eq. (63)). Electrochemical reduction of H_2O_2 can follow ($k_{r,3}$, Eq. (64)). Therefore, H_2O_2 can be formed as final product or as intermediate depending on the used electrocatalytic material. Hydrogen peroxide can desorb from the electrode surface and diffuse in the solution bulk which makes it potentially harmful for the PEM because it lowers the efficiency, and causes electrode corrosion and cell degradation.[270] The decomposition of hydrogen peroxide leads to the formation of free reactive radicals that can create holes into the PEM. Depending on the conditions H_2O_2 can be produced by ORR at the cathode but also by the oxidation of H_2 at the anodic side of the fuel cell, respectively.[268, 270, 271] The incomplete reduction of O_2

hence reduces the efficiency of PEM fuel cells. However, in a subsequent two-electrode reduction H_2O_2 may be electrochemically transformed into water and OH^-, respectively.

It is very difficult to distinguish between the different mechanisms of the ORR that can occur in parallel or in series although the detection of H_2O_2 is very important in particular for fuel cells. This demonstrates the importance to find easy and cheap possibilities for an efficient *in situ* detection and discrimination of the reaction products of the ORR. The rotating disk and rotating ring-disk electrode (RRDE) techniques are often used on a macroscopic scale. Information can be extracted as a function of the applied potential. Using the RRDE, H_2O_2 generated at the disk can be oxidized at the ring causing an anodic current. This helps to estimate the influence of the peroxide route. However, a large variety of values for n can be found in literature for identical materials and conditions. Probably, the synthesis and pretreatment of the electrocatalytic materials can affect significantly the heterogeneous reaction rates. Besides the electrochemical oxidation at the disk H_2O_2 can disproportionate: thus it is not detectable at the ring.

The determination of hydrogen peroxide is also of great importance in biology.[272] For instance, medical sensing devices such as first generation blood glucose monitors rely on the detection of H_2O_2 that is formed from glucose at immobilized glucose oxidase.[273]

SECM was introduced for analyzing the ORR,[274, 275] but also to investigate the hydrogen oxidation reaction (HOR),[186, 276] and oxygen evolution reaction (OER).[26, 277] The four-electron reduction of O_2 is irreversible which inhibits the use of the FB mode. In the TG/SC mode (Section 2.3), O_2 was constantly electrogenerated in oxygen-free solutions at the UME and reduced at various substrates beneath the microelectrode to map the local ORR activity.[110, 274, 278] The use of the pulsed redox competition (RC) mode[76] and the continuous RC mode[108] for the investigation of the ORR was already described in Section 2.4.

8.1 Deposition of Mesoporous Platinum on the Carbon Microelectrodes

The accurate detection of hydrogen peroxide with amperometric techniques is difficult, because the electrochemical reactions are irreversible and cyclic voltammograms often show irreproducible shapes at the majority of electrode surfaces. Figure 84a show CVs of an untreated carbon microelectrode in 1 mM H_2O_2 and 0.1 M phosphate buffer solution (pH = 7). Very small currents and two weak oxidation peaks in the forward and reverse scan originate from the oxidation of H_2O_2 and indicate a strongly limited reaction rate at the cured carbon electrode material. In order to detect hydrogen peroxide, the carbon surface has to be modified. Evans *et al.*[279] reported the deposition of a mesoporous Pt film on Pt-UMEs allowing hydrogen peroxide detection over long periods due to a steady-state response. A flat polished Pt surface alone does not show a stable response because the oxidation as well as the reduction of H_2O_2 takes place under mixed kinetic and diffusion control.[279]

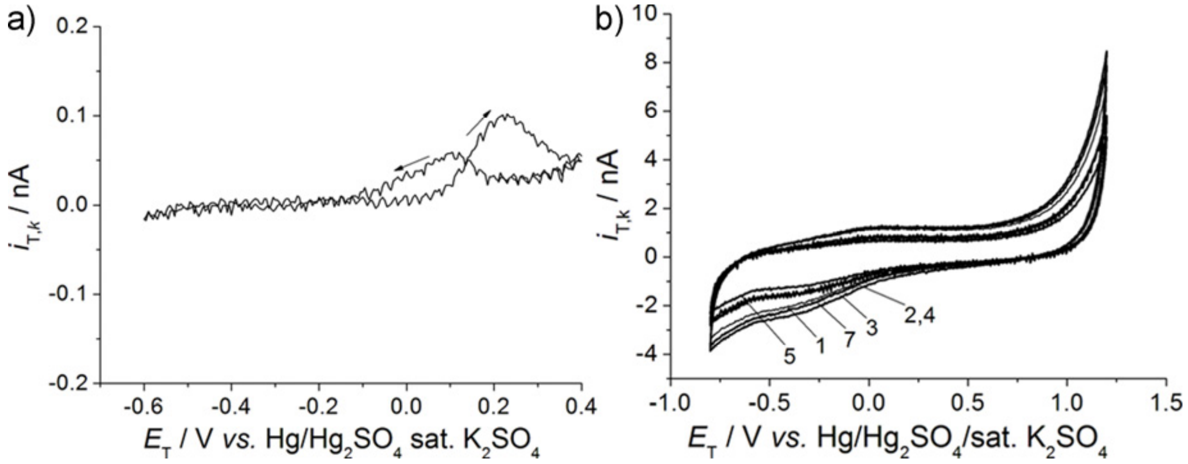

Figure 84. a) CV of one carbon microelectrode within a linear array in 1 mM H_2O_2 + 0.1 M phosphate buffer solution (pH = 7). Potential scan rate 1 mV s^{-1}. b) CVs of an array of carbon microelectrodes in 0.5 M H_2SO_4 (argon-purged). Potential scan rate 200 mV s^{-1}.

Figure 84b shows CVs of the carbon microelectrodes in dilute sulfuric acid before deposition of Pt. After deposition of the Pt films, a deposit on the carbon electrodes can be clearly identified by CLSM (Figure 85a). The shape of the CVs in dilute sulfuric acid (Figure 85b) prove that Pt is effectively on the surface because the well known shapes in the hydrogen region, double layer region and oxygen region are shown. The two oxidative peaks at $E_T < -0.3$ V *vs.* Hg/Hg_2SO_4/sat. KCl indicate the presence of polycrystalline Pt. A quantitative analysis of the increase in roughness was not performed since the results of deposition varied significantly from batch to batch and was not meaningful. However, a factor of 25 for the increase in roughness can be estimated from the measured current values of significant peaks in the CVs of the thin Pt film[220] and of the H_I-ePt. This indicates a nanostructure, but does not represent a proof. In literature, the increase of internal surface area is reported to be about 100 times.[279] The electrodeposition of a thin Pt film was applied prior to the deposition of H_I-ePt because in the course of the performed experiments it appeared to give the most promising results. Direct deposition of the H_I-ePt on carbon in potentiostatic, galvanostatic and pulsed potentiostatic modes gave less reproducible and stable results.

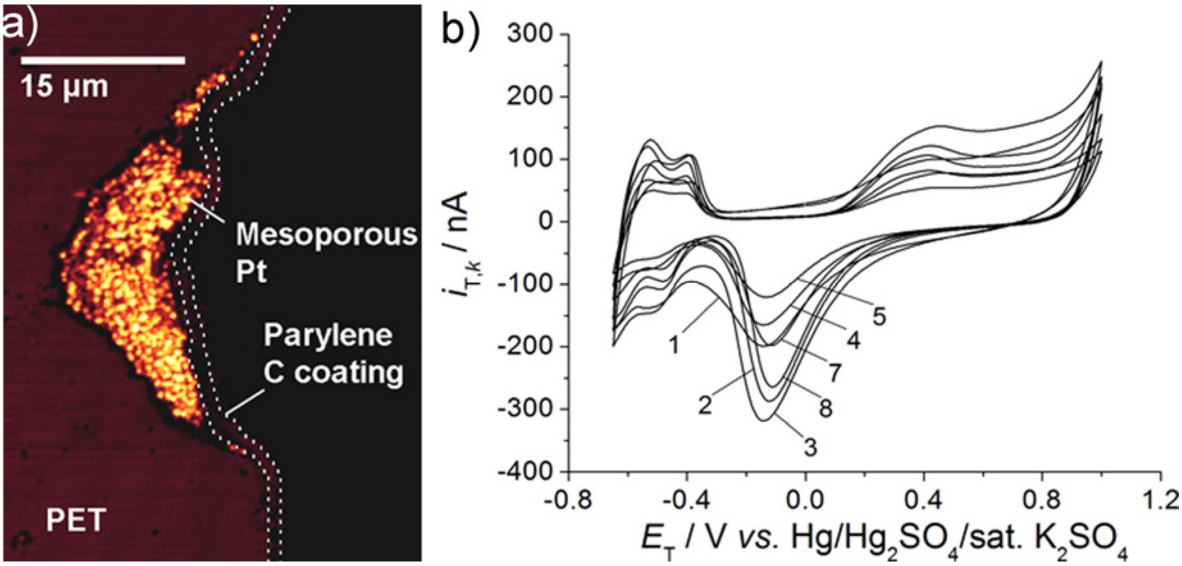

Figure 85. CLSM reflection image of deposited mesoporous Pt on a carbon microelectrode. Dotted lines to b) CVs of an array of carbon microelectrode covered with mesoporous Pt in 0.5 M H_2SO_4 (argon-purged). Potential scan rate 500 mV s^{-1}.

8.2 Detection of Hydrogen Peroxide

CVs in 1 mM H_2O_2 and 0.1 M phosphate buffer solution (pH = 7) were recorded in order to test if a steady-state response for the reduction and oxidation of H_2O_2 can be achieved at the deposited nanostructure (Figure 86). At cathodic potentials, the reduction of H_2O_2 overlapped with the reduction of O_2. No steady-state was obtained. The presence of oxygen could not be avoided in the used cell. However, with respect to the material library (Section 8.3), the author was interested in the oxidation of H_2O_2. The oxidation of H_2O_2 did not show a steady-state response at anodic potentials. This demonstrates that the deposited nanostructure does not achieve the same quality reported in literature for a H_I-ePt structure on Pt-UME.[220, 279]

In chronoamperograms (CAs), this trend was confirmed. A potential of 0.2 V *vs.* Hg/Hg_2SO_4/sat. K_2SO_4 was applied for about 6 h and the current decreased continuously. Exemplarily, it decreased about 25 % ($i_{T,\infty}$(5 min) = 13 nA; $i_{T,\infty}$(360 min) = 9.81 nA). However, it should allow imaging in an appropriate time scale. Anyway, the CAs and CVs in Figure 86 indicate the presence of a nanostructure, in fact, the kinetics are improved compared to bare carbon electrodes, but no steady-state responses can be achieved.

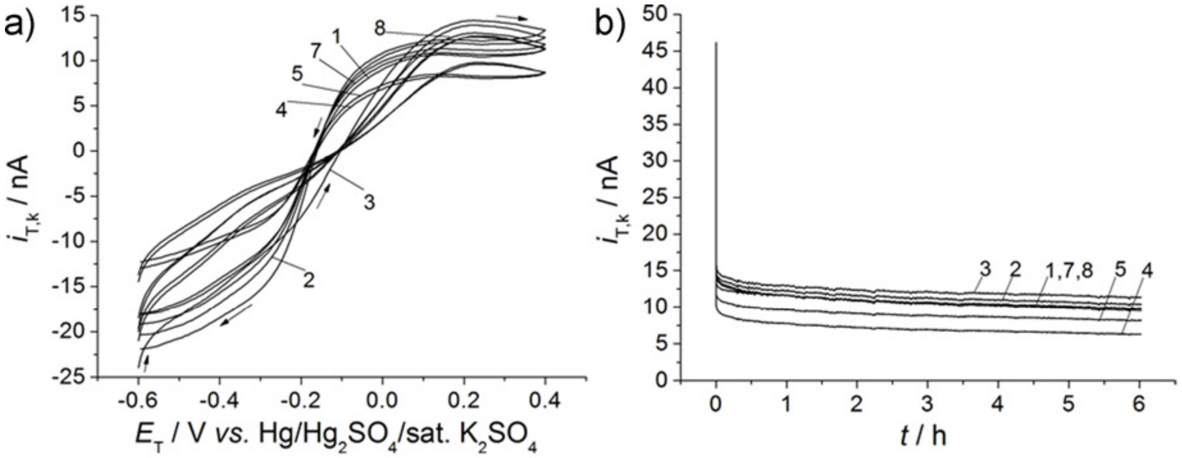

Figure 86: a) CVs of carbon microelectrode array with deposited mesoporous Pt; potential scan rate 1 mV s^{-1}.b) CAs of carbon microelectrode array with deposited mesoporous Pt, E_T = 0.2 V *vs.* Hg/Hg_2SO_4/sat. K_2SO_4. Electrolyte solution for was 1 mM H_2O_2 + 0.1 M phosphate buffer solution (pH = 7). Electrode no. 6 was not connected.

8.3 Testing the Catalytic Activity of a Material Library for H_2O_2 Decomposition

Approach curves towards the insulating material of the material library were performed in 1 mM H_2O_2 and 0.1 M phosphate buffer solution (pH = 7) using an array with two active microelectrodes with deposited H_I-ePt (electrodes no. 7 and no. 8, Figure 87a). Both curves show negative feedback. The current decrease was only 35 % (no. 7) and 21 % (no. 8), respectively. However, for the investigation of the catalytic activity in redox competition mode this is advantageous because a more efficient hindered diffusion on the one hand and the H_2O_2 consumption by the catalyst on the other hand would hardly be distinguishable. The probe was approached further and a line scan using electrode no. 8 was performed with h_P = -110 µm in redox competition mode in which sample and the H_I-ePt-electrode were biased at E_T = E_S = 0.2 V *vs.* Hg/Hg_2SO_4/sat. K_2SO_4 in order to oxidize H_2O_2 (Figure 87b). The catalytically active C/Pt spot can be identified clearly by the decrease of the probe current. The decrease of the current for the insulator-catalyst-border on the right side is sharper than on the other side. Because the scanning direction in Figure 87b was from right to left, the diffusion layer caused by oxidation of H_2O_2 was blocked by the soft array until it reached the catalytically active region. Then the current decreased immediately as soon as the catalytic area is scanned. In contrast to that, the influence of H_2O_2 consumption by the sample influences the current at the H_I-ePt-electrode at the other border. One important result of performed approach curves and line scans was that the deposited H_I-ePt structure stayed on the carbon during and after these measurements. A loss of the structure due to mechanical stress by the probe bending was not observed.

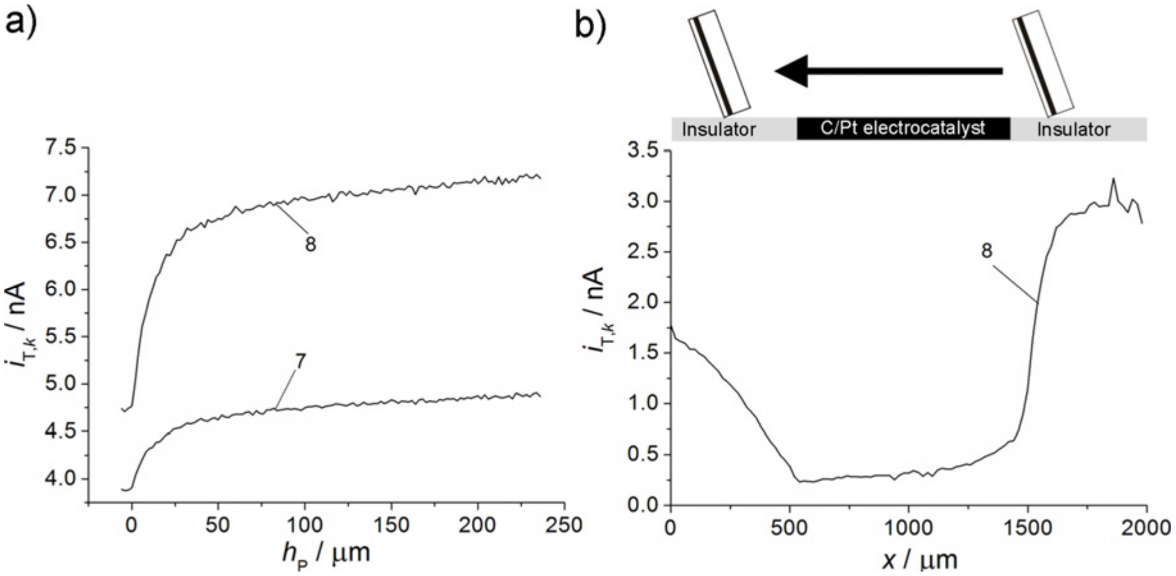

Figure 87. a) Approach curves towards an insulating material using two carbon microelectrodes (no. 7 and no. 8) in one array with deposited H_I-ePt. E_T = 0.2 V *vs.* Hg/Hg_2SO_4/sat. K_2SO_4; step size 2 µm; translation rate 10 µm s^{-1}. b) Line scan in redox competition mode over a C/Pt catalyst spot (width 1 mm) using one carbon microelectrode (no. 8) in one array with deposited H_I-ePt; h_P = -110 µm; E_T = E_S = 0.2 V *vs.* Hg/Hg_2SO_4/sat. K_2SO_4; step size 20 µm; translation rate 100 µm s^{-1}; scan direction was from right to left.

In order to increase the current contrast over insulator and catalyst spot, the probe was retracted until it was freely suspending in bulk solution (h_P = 30 µm). An image in redox competition mode was recorded with the retracted array. Because the macroscopic sample continuously consumed H_2O_2 and a linear diffusion of H_2O_2 towards the nanometer sized Pt particles on the substrate can be expected over time, a fast translation rate (100 µm s^{-1}) and data acquisition (no delay time before recording) was applied to the array. In addition, a LO with very fast reverse translation rate (1000 µm s^{-1}), and fast re-approach were set to provoke some convection in order to stir the solution within the probe-sample-gap. Figure 88 shows the redox competition image which was recorded in only 38 min using two neighbored microelectrodes (2,626 data points per electrode). A manual correction was performed by using Eq. 26 (Section 6.5.4) with $i_{T,\mathrm{off},k}$ / nA= {0.0; 0.0} and s_k / nA^{-1} = {0.9; 1.1}. The catalyst spot is clearly resolved in this measurement. In both images of the individual electrodes, large currents were measured and appear as horizontal stripes in the image which stayed for some line scans, but disappeared after. The effect was reproduced in a second image (not shown) and cannot be explained yet. Figure 89 shows three exemplary adjacent line scans extracted from the image in Figure 88.

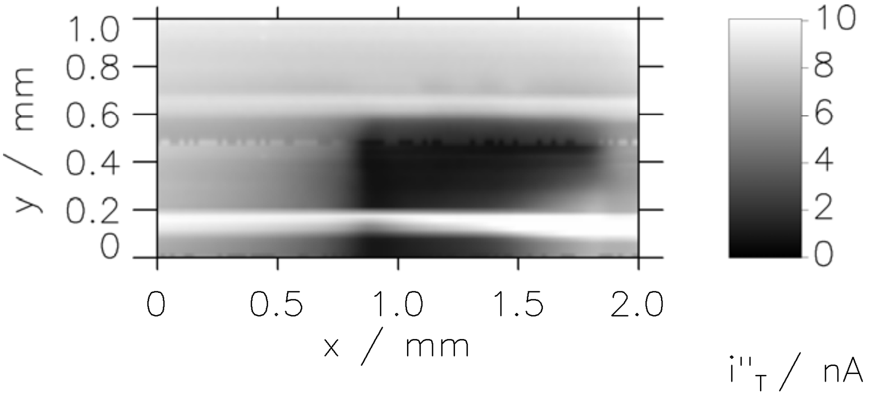

Figure 88. Redox competition image of a C/Pt catalyst using two neighbored carbon microelectrodes in one array with deposited mesoporous Pt (midpoint-to-midpoint electrode distance 500 µm). h_P = 30 µm, HF fwd step size 20 µm, HF $v_{T,fwd}$ = 50 µm s^{-1}, HF fwd delay before data acquisition 0 s, LO stroke height 100 µm, LO retract speed 200 µm s^{-1}, LO approach speed 50 µm s^{-1}, HF rev step size 20 µm, HF $v_{T,rev}$ = 1000 µm s^{-1}, LF fwd step size 20 µm, LF $v_{T,fwd}$ = 50 µm s^{-1}, total imaging time required was 38 min.

In comparison to the line scan in contact mode in Figure 87b, the current values over the catalytically active spot were recorded with a lower resolution, but at the same time a sharper boarder and a larger current contrast between catalyst spot and insulator was obtained keeping the array in bulk solution. With these experiments it could be demonstrated that scanning of a catalyst spot can be performed with modified soft arrays in contact mode and contactless mode. Redox competition along with the utilization of soft probe arrays was shown for the first time. The results presented in this section demonstrate that high-throughput imaging using soft microelectrode arrays are applicable to the screening of combinatorial material libraries of electrocatalysts.

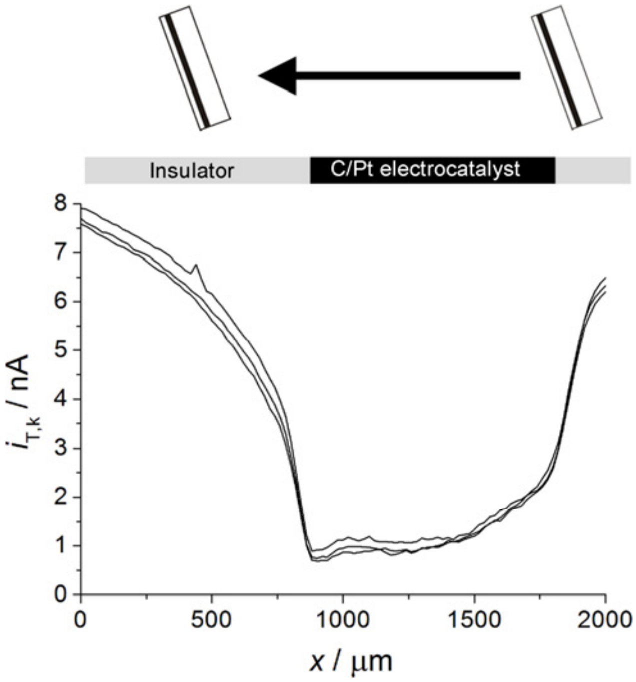

Figure 89. Three adjacent line scans (separated by 20 µm) in redox competition mode over one biased C/Pt catalyst (width 1 mm) using one carbon microelectrode (no. 7) with deposited mesoporous Pt in 1 mM H_2O_2 + 0.1 M phosphate buffer solution (pH = 7). Line scans were extracted from Figure 88 between y = 0.42 mm to 0.46 mm, $E_T = E_S$ = 0.2 V *vs.* Hg/Hg_2SO_4/ sat. K_2SO_4, h_P = 30 µm, step size 20 µm, translation rate 50 µm s^{-1}, scan direction was from right to left.

9 New SECMx Software Features for the Implementation of Digital Potentiostats

The in-house made SECMx software is based on generic programming (see also Section 2.5) which is thus applied to experiments such as “cyclic voltammetry” and “2D imaging”. This means, that in the main application a generic algorithm is used for an experiment independent on the used potentiostat. The device specific function calls are located in the corresponding DLLs in custom classes which were derived from the generic classes. By the usage of pointers, the correct device and channel are addressed by the main application. This generic concept has advantages and disadvantages. Favorable is the flexibility in using and exchanging devices without changing the program code of the software. New potentiostats can be implemented by the creation of a new DLLs. Usually, the main application does not have to be modified since all potentiostats have equal functionalities including “apply a potential” and “read a current” which are required for standard electrochemical as well as for SECM experiments. Experiments are programmed in a custom-made way. For example, if the operator opens the generic experiment “cyclic voltammetry” (centered panel in Figure 90), a user interface is created in which experimental parameters can be entered.

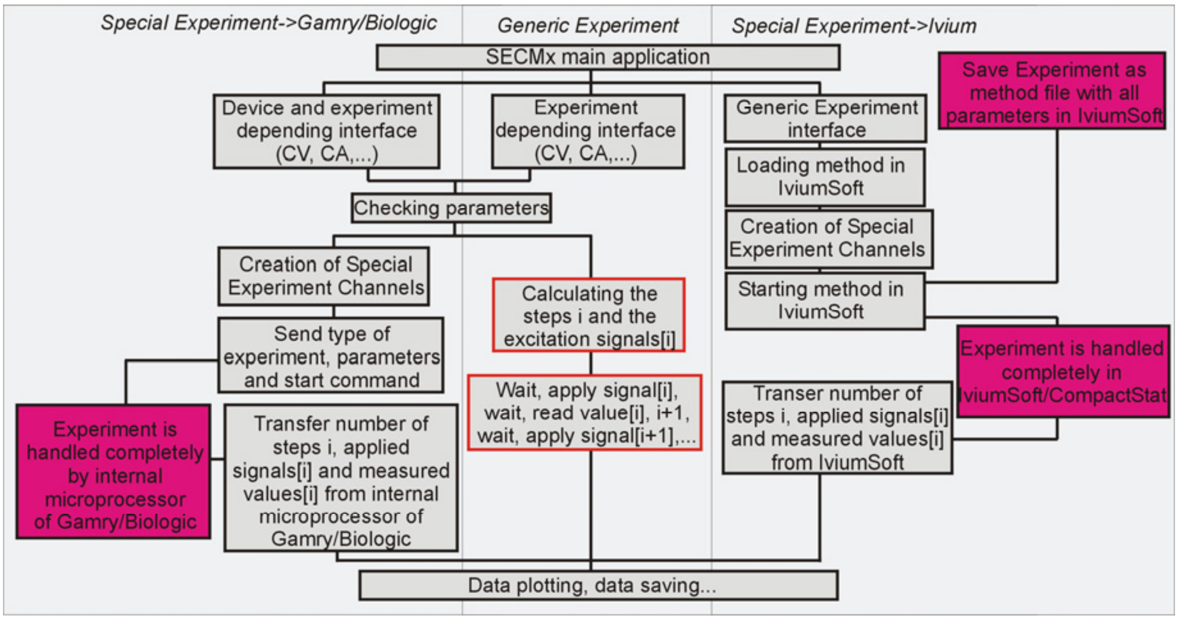

Figure 90. Block diagram of generic (centered panel) and hardware specific experiments (left and right panel) for digital potentiostat of Gamry, Bio-Logic, and Ivium.

After starting the experiment, the program checks if the parameters are reasonable followed by the calculation of all potential steps and the construction of the data structure. Then each step of the experiment is controlled by SECMx. The actual time is measured in order to apply the potential value and to measure the current at the desired times. With commercial AD cards 100,000 values per second can be read, but the smallest increment of time in SECMx has been limited by the participated programmers (*e.g.* 0.1 s in the "x-t chart recorder"). One reason is the required time for filtering which is necessary in electrochemical measurements. Another limitation arises if digital potentiostats are used for the generic experiments. These devices include hardware for data acquisition which is handled by the microprocessor of these devices. The data transfer is then mostly carried out via USB. Due to these processes, the time between sending of a command and receiving of the corresponding value can exceed the calculated time and may not be constant. Both drawbacks inhibit for example very fast CVs (scan rate 1000 V s^{-1}) with appropriate minimum steps by the SECMx routine. But digital potentiostats are able to perform such fast experiments with high temporal resolution by being controlled by their own integrated microprocessors. The device-dependent libraries, which are provided by the manufacturers of the devices and which have been included in the DLLs of SECMx, allow the integration of this option into SECMx. Our idea was to create hardware specific experiments that allow to set experimental parameters in the user interfaces and to start the selected experiment. Then the whole experiment is completely controlled and handled by the device. This includes the calculation of the steps and the times, the application of signals, and the data acquisition. SECMx waits until the data transfer is enabled by the device in order to plot and store the data in SECMx. This can be performed during the running experiment or after the experiment has finished. For these experiments, specific channels are dynamically created and they are deleted when the experiment is closed in SECMx. The size of the data vectors is also changed dynamically since the final number of applied and measured values is only known after the experiment has finished. The implementation of this new kind of experiments depends strongly on the provided device specific library. The author created such "special experiments" (as they are called in SECMx) for bipotentiostats from Ivium, Gamry and Bio-Logic. In general, most bipotentiostats of these companies are very similar and can be used directly for these "special experiments" after minor modifications due to the fact that they normally use the same libraries. For Gamry and Bio-Logic (left panel in Figure 90), individual "special experiments" were created for CV and CA. The user interfaces look like in the generic experiments. Parameters are set and controlled in SECMx. The complete set of parameters and the type of experiment are sent to the device followed by the start of the experiment. The applied values and measured signals are transfered and plotted during runtime, and can be saved after the experiment has finished. It is also possible to abort the experiment. The implementation of the hardware-specific experiments of Ivium is significantly distinguished from the ones of Gamry and Bio-logic (right panel in Figure 90). It is based on the loading of an Ivium method file which has been created and saved before by the operator in the Ivium software. This method file contains the type of experiment and all desired parameters. Therefore, the interface of the experiment does not contain text boxes to enter parameters but a button to load the method (left window in Figure 91). During runtime it is not possible to transfer the data to SECMx. This will be performed after the experiment has finished, followed by data plotting.

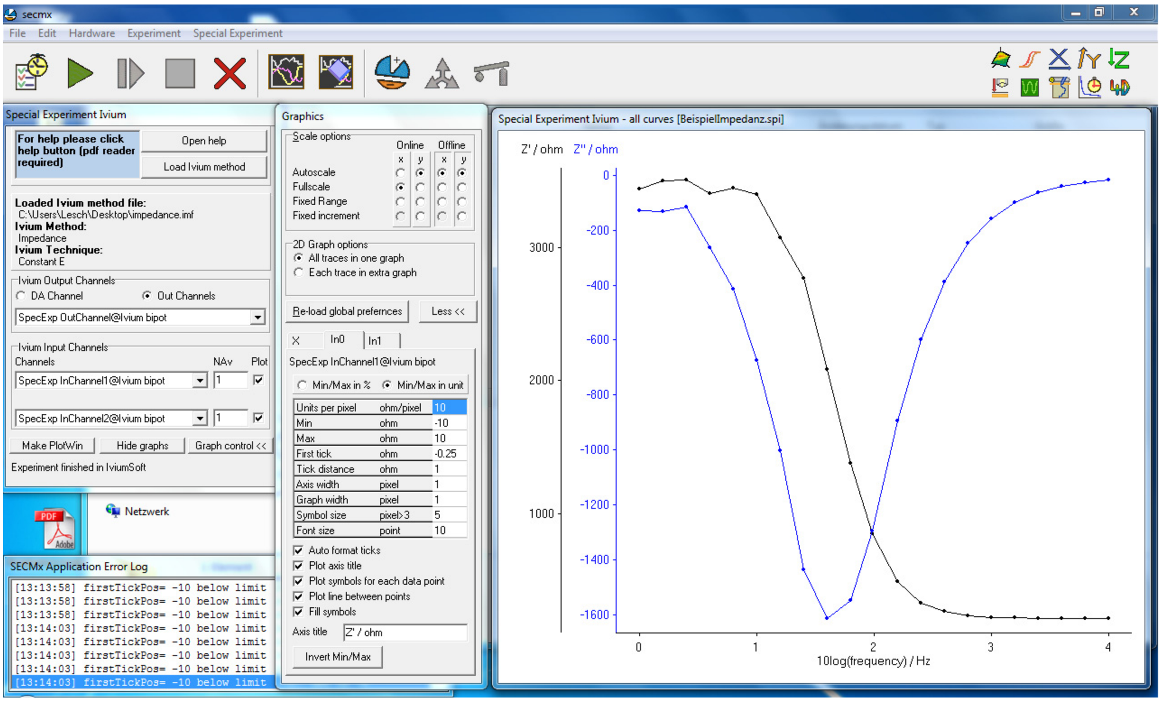

For help please click help button (pdf reader required)

Loaded Ivium method file:
C:\Users\Lesch\Desktop\impedance.imf
Ivium Method:
Impedance
Ivium Technique:
Constant E

Ivium Output Channels
○ DA Channel ● Out Channels
SpecExp OutChannel@Ivium bipot

Ivium Input Channels

Channels	NAv	Plot
SpecExp InChannel1@Ivium bipot	1	☑
SpecExp InChannel2@Ivium bipot	1	☑

Experiment finished in IviumSoft

```
[13:13:58] firstTickPos= -10 below limit
[13:13:58] firstTickPos= -10 below limit
[13:13:58] firstTickPos= -10 below limit
[13:14:03] firstTickPos= -10 below limit
[13:14:03] firstTickPos= -10 below limit
[13:14:03] firstTickPos= -10 below limit
[13:14:03] firstTickPos= -10 below limit
[13:14:03] firstTickPos= -10 below limit
```

Scale options

	Online x	Online y	Offline x	Offline y
Autoscale	○	●	●	●
Fullscale	●	○	○	○
Fixed Range	○	○	○	○
Fixed increment	○	○	○	○

2D Graph options
● All traces in one graph
○ Each trace in extra graph

SpecExp InChannel1@Ivium bipot
○ Min/Max in % ● Min/Max in unit

Units per pixel	ohm/pixel	10
Min	ohm	-10
Max	ohm	10
First tick	ohm	-0.25
Tick distance	ohm	1
Axis width	pixel	1
Graph width	pixel	1
Symbol size	pixel>3	5
Font size	point	10

☑ Auto format ticks
☑ Plot axis title
☑ Plot symbols for each data point
☑ Plot line between points
☑ Fill symbols
Axis title: Z' / ohm

Figure 91. SECMx interface for a hardware specific experiment carried out and controlled by the CompactStat from Ivium. In this example the impedance of an electrical circuit for testing was measured and presented as a Bode plot.

The presented new strategy offers another very big advantage. All available experiments of the used device can be carried out by SECMx. This includes experiments of complex and complicated structure such as impedance spectroscopy which cannot be programmed for SECMx as a generic experiment. Figure 91 shows the SECMx interface after a performed impedance “special experiment” carried out by the CompactStat. The measurement is presented as a Bode plot. In impedance measurements, two input signals are recorded: the real and the imaginary part of the impedance. This requires two input channels which are generated dynamically. This dynamic initiation of a flexible number of input channels offers a new further development in SECMx in combination with digital potentiostats, that is to read all physical quantities the measurement provides, like applied potential, measured potential, measured time, measured current, and other signals such as analog voltages measured at auxiliary channels. This option is also very attractive for the so-called “volume scan” which is an SECM image with performance of an additional experiment at each grid point of the image. This has been used before in the form of pulsed RC mode[76] and was available in SECMx,[280] but this new feature greatly expands the options.

10 Conclusions and Outlook

SECM can image the local electrochemical reactivities of various surfaces, it can measure local analyte concentrations, it can induce localized surface modifications, and homogeneous as well as heterogeneous reaction rates can be determined. This makes SECM attractive for applications such as screening of combinatorial catalyst libraries, imaging of latent human fingerprints, testing the integrity of technical coatings, and parallelized surface modification. These examples are based on large samples. With conventional SECM instrumentation, scanning of large samples approaching square centimeter takes very long time due to the requirement of flat and aligned samples and slow translation rates. Long imaging time causes artifacts in the detected signals due to solvent evaporation, electrode fouling or sample aging. In this thesis, the concept, development and application of high-throughput SECM imaging and modification using soft linear arrays of eight microelectrodes has been reported that can overcome those problems.

The new concept relies on soft probes fabricated in flexible polymeric films that scan in contact mode over surfaces providing an almost constant working distance. Integrating linear arrays of microelectrodes into these soft probes allows a parallel operation and decreases the measurement time significantly. The commercial multipotentiostat module MultiWE32 was integrated in the existing custom-made SECM setup. The in-house made SECM control software SECMx had to be modified and was expanded in order to operate the soft linear microelectrode arrays. This included a redesign of data structures in order to record, plot and store signal values. For this purpose, a new category “bundle” representing a collection of identical channels was defined for input and output channels. Data acquisition of the microelectrodes can be performed simultaneously or sequentially. Simultaneous measuring is faster whereas sequential reading is more stable against noise. During scanning in contact mode, a bending of the probes in the opposite direction by inverting the direction of translation has to be avoided, because it would damage the probe due to mechanical stress. Therefore, a new lift-off routine was integrated into SECMx to retract the probe for repositioning and for the incremental movements in-between the line scans of an image. A retracted probe is freely suspending in electrolyte solution and can be moved with fast translation rates of up to 1000 $\mu m\ s^{-1}$. A slow re-approaching brings the probe again into mechanical contact with the substrate.

Soft linear arrays of carbon, gold, and silver microelectrodes were prepared by taking advantage of several successive fabrication techniques: first UV laser ablation was used followed by Aerosol Jet® and then inkjet printing. For all techniques, a uniform array design with eight parallel microelectrodes was used. The electrode-to-electrode distances were selected in most cases as 500 µm in order to minimize diffusional overlapping of neighboring electrodes.

Carbon microelectrode arrays were fabricated by photoablating microchannels into a thin polyethylene terephthalate (PET) film and filling them manually with a conductive carbon ink. Aerosol Jet® (for gold microelectrodes) and inkjet printing (for silver) enables an easier and more reproducible way of preparing soft probes. The nanoparticle inks are directly printed onto thin polyimide films avoiding the step of microchannel filling. The printing devices, in particular inkjet printers, are established tools for batch fabrication. Different nanoparticulate inks can be used and thus further electrode materials can be foreseen. After the materials deposition, the three probe types were sintered and the conductive tracks were covered and sealed with an insulating Parylene C coating. Mechanical cutting with a razor blade or UV laser-assisted cutting exposed the cross-section of the conductive tracks that become active electrode areas. This procedure can easily be repeated to achieve a fresh electrode surface avoiding mechanical or electrochemical polishing.

The cross-sections of the probes were optically and electrochemically investigated. While the carbon microelectrodes have the shape of a distorted sickle, the gold and silver microelectrodes have a microband-like geometry. Cyclic voltammograms in aqueous solutions containing common redox mediators like ferrocenyl methanol or hexaammineruthenium(III) chloride showed sigmoidal shapes as typical for ultramicroelectrodes. The introduction of gold as electrode material offers the possibility to use a more diverse range of redox mediators and to detect compounds that are difficult to convert at carbon electrodes, such as O_2, H_2O, H_2/H^+. Additionally, they can be used in organic solvents, whereas carbon could be dissolved.

Approach curves in SECM feedback mode were performed towards various surfaces. After getting into mechanical contact with the substrate, the probes start to bend slightly. Then the probes slide on the surface while they are approached further. Constant current values during sliding indicate a constant working distance. The approach curve is stopped and this position is set as the vertical reference position for SECM imaging. SECM imaging is performed in contact regime. Retract scans are performed using the new lift-off mode. The time required for imaging a defined area with an array of eight microelectrodes is reduced by a factor of approximately 6 compared to a single UME in conventional SECM, while the resolution and sensitivity is preserved. A multiple image routine was integrated into SECMx in order to image larger areas than the width of the microelectrode array. This is performed by a software-controlled tiling of individual adjacent image frames.

In order to construct SECM images from experiments with soft microelectrode arrays, the individual microelectrodes must have the same current response characteristics and the exact electrode positions have to be known. The electrode-to-electrode distances of the array probes are well defined by the fabrication processes. The electrochemical responses of the individual active electrode areas vary slightly due to minimum varying electrode sizes caused by the preparation steps and blade cutting. These and differences in the lateral position can be corrected by calibration measurements. For this purpose, a current offset and a scale factor were defined, that set the currents for negative feedback to zero and for positive feedback to 1 in dimensionless form.

Imaging of tilted and curved substrates has been demonstrated in this thesis. The probe follows the topography of the sample but the probe cannot slide down into holes that are smaller than the width of the array. Scanning of tilted substrates shifts the position of the probe slightly which can be corrected as described in this thesis.

The utilization of soft arrays permits SECM imaging of delicate samples such as self-assembled monolayers (SAMs) in mechanical contact without inducing damages to the SAM thanks to very weak pressures that are exerted by the probe on the surface. These pressures are about three orders of magnitude less than the pressures exerted by conventional scanning force microscope tips.

The soft microelectrode arrays can also be used as a simple tool for high-throughput micropatterning. As an example, Br_2/HOBr was electrogenerated at the microelectrodes in phosphate buffered solutions to locally modify oligo(ethylene glycol)(OEG)-terminated SAMs. This system is well established for the dynamic stimulation of surface films to direct protein and cell adhesion. In this thesis, complex patterns, such as letters or a JPG-file, were written into the OEG SAMs by a newly developed software-controlled modification line scan. A patterning file containing pulse durations in seconds in ASCII format is loaded in SECMx and patterning is performed by applying at each translation step different potentials to the individual microelectrodes for modification and non-modification. The modified areas were analyzed by SECM in feedback mode, adsorption of fluorescently labeled proteins, and Pulsed Force Mode scanning force microscopy with surface modified tips. Optical inspection was possible by preferential water condensation. Thanks to the weak forces exerted by the probe on the sample, it might be possible to scan cells or to provide dynamic stimuli to cultured cell networks. The array probes could also be applied to numerous other electrochemical micropatterning procedures. Different electrode materials or the deposition of various noble metals would extend the range of reagents for surface modification. Even more complex potential programs could be created and applied to the individual electrodes.

Soft carbon microelectrode arrays with deposited mesoporus Pt represent a new conceptual extension of soft probes that allowed the detection of hydrogen peroxide by the array electrodes. Depending on the used solution, H_2O_2 can be an intermediate or product in the oxygen reduction reaction (ORR). In technical applications of the ORR, hydrogen peroxide has to be avoided for example in the polymer electrolyte membrane (PEM) of PEM fuel cells since it lowers the cell efficiency and causes cell degradation. In this context, a combinatorial material library consisting of C/Pt electrocatalysts for H_2O_2 decomposition was investigated by an array in contact and contactless regime using the SECM redox competition mode. In this thesis, one spot was scanned, but it should be possible to scan the complete catalyst library in order to detect the most active C/Pt composition for H_2O_2 decomposition. These experiments show that soft microelectrode arrays may contribute to important future challenges concerning renewable energy, energy storage and electromobility. Also combinatorial material libraries of other electrocatalysts such as the hydrogen evolution reaction or the oxygen evolution reaction in the production of solar fuel represent interesting future extensions of this concept.

In this thesis, arrays with only eight microelectrodes have been developed. The used multipotentiostat module allows the parallel operation of up to 32 working electrodes and can be expanded to control simultaneously 256 electrodes. An array of this size would further accelerate imaging and modification procedures of even larger surface areas.

The soft array probes presented in this thesis follow the topography of curved substrates. Thus, all electrodes are lifted when the probe scans over an obstacle, also when its dimension is smaller than the probe width. This should be overcome by using arrays of individually flexibly mounted UMEs (Figure 92). Steel tubes encapsulate the UME bodies. They are placed in separated indentations and a permanent bar magnet under the indentations attached the UMEs at the holder. If the UMEs are not in contact with the substrate, the rods are orientated in parallel to the bar magnet (Figure 92, left panel). If the

UMEs are brought into mechanical contact with the substrate, the tubes are rotated upwards. The magnetic forces ensure that the tubes will rotate downwards, when the UMEs scan about holes. Thanks to this, the UMEs can individually follow the topography of substrates. Sensors could be mounted to the individual UMEs detecting the topographic change. In this way, Pt disk microelectrodes could also be used for quantitative analysis due to their well-defined geometry.

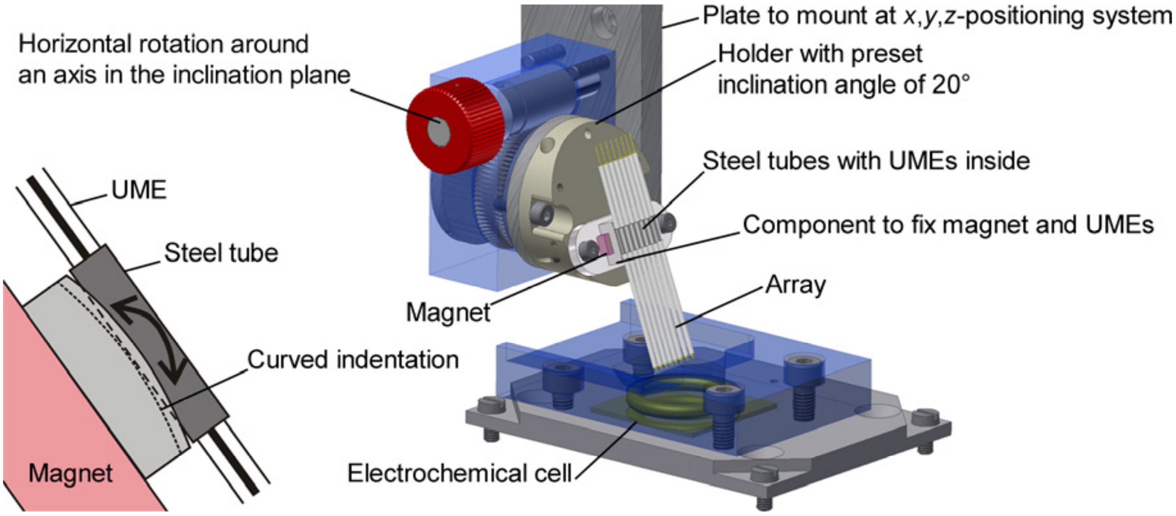

Figure 92. New concept of an array of conventional UMEs. The separated UMEs are mounted in individual curved indentations. The UMEs are flexibly fixed by a permanent magnet (NdFeB) below the indentations and steel tubes (1.2210 115 CrV) encapsulating the UMEs. (Right scheme was kindly provided by F. Roelfs, workshop of the University of Oldenburg)

The implementation of digital bipotentiostats opened a new way of experiments in SECMx. Each of the digital devices has its own microprocessor allowing the control of fast and/or complex experiments such as fast cyclic voltammetry (100 V s^{-1}). These experiments cannot be programmed for custom-made software due to several limitations including time accuracy and fast data transfer. The experiments can be started via SECMx at each grid point of an SECM image which results in a so-called 4D volume scan. After or during the runtime of the experiment, the data are transferred and stored in the SECMx data structures.

In conclusion, the soft linear arrays of eight microelectrodes can be used for high-throughput imaging and local electrochemical modification of surfaces. The fabrication of arrays with a larger number of microelectrodes is feasible and would further speed up SECM experiments. It might be possible to brush cultured living cells and tissue samples using the soft array probes. This could enable the electrochemical analysis of tissues in the square-centimeter range for imaging drug distribution in cancer tissue or screening for disorders in redox metabolism.[281, 282] Soft linear microelectrode arrays containing additional empty microchannels for the delivery and aspiration of electrolyte solutions could open the way towards high-throughput modification of dry surfaces. The release of various reagents to individual electrodes could be used to create different surface functionalities, and allow the combination with analytical methods such as mass spectrometry.**[A7]** It can be expected, that the soft probes will extend the scope of SECM applications in addition to their proven applicability as electrochemical imaging tool.

11 Appendix

11.1 Abbreviations

Abbreviation	**Meaning**
AC	alternating current
AD	analog-to-digital
AFM	atomic force microscopy
Aux	auxiliary electrode
bpy	bipyridine
BSA	bovine serum albumin
C	capacitor
CA	chronoamperometry
CELT	confined etchant layer technique
CIJ	continuous inkjet
CLSM	confocal laser scanning microscopy
CMi	Center of MicroNanoTechnology
CV	cyclic voltammetry
DA	digital-to-analog
DBCNP	double barrel carbon nanoprobe
DFG	Deutsche Forschungsgemeinschaft
DLL	dynamic link library
DMP	Dimatix Materials Printer
DOD	drop-on-demand techniques
DPN	dip-pen nanolithography
DSSC	dye sensitized solar cell
EBL	electron beam lithography
ECM	extracellular matrix
ECSTM	Electrochemical scanning tunneling microscopy
EPFL	École Polytechnique Fédérale de Lausanne
ESI	electrospray ionization
FIB	focused ionic beam
FcMeOH	ferrocenyl methanol

G/C	generation/collection mode
HCPA	hexachloroplatinic acid
HDT	hexadecanethiol
HF	high-frequency
H_I	hexagonal
H_I-ePt	mesoporous platinum
HOR	hydrogen oxidation reaction
IC	intermittent contact
IFAM	Fraunhofer Institute for Manufacturing Technology and Applied Materials Research
In	digital input channel
LED	light emission diode
LEPA	Laboratoire d’Electrochimie Physique et Analytique
LF	low-frequency
LIB	static library
LO	lift-off
LPCVD	low pressure chemical vapor deposition
MALDI	matrix-assisted laser desorption/ionization mass spectrometry
MIRA	software for offline data analysis
MS	mass spectrometry
O	oxidized redox-active species
OEG	oligo(ethylene glycol)
OER	oxygen evolution reaction
ORR	oxygen reduction reaction
Out	digital output channel
PDMS	polydimethylsiloxane
PET	polyethylene terephthalate
PECVD	plasma enhanced chemical vapor deposition
PEM	polymer electrolyte membrane
PFM	Pulsed Force Mode
phen	1,10-phenanthroline
PI	polyimide
PTFE	poly(tetrafluoroethylene)

QRE	quasi-reference electrode
R	reduced redox-active species resistor
RC	redox competition
RE	reference electrode
RRDE	rotating ring-disk electrode
SAM	self-assembled monolayer
SECM	scanning electrochemical microscopy
SECMx	SECM control software
SEM	scanning electron microscopy
SG/TC	sample-generation/tip-collection
SFM	scanning force microscopy
SI	supporting information
SICM	scanning ion conductance microscopy
SNOM	scanning near-field optical microscopy
SPM	scanning probe microscopy
TG/SC	tip-generation/sample-collection
TPM	tip-position modulation
UME	ultramicroelectrode
UV	ultraviolet
VSM	voltage-switching mode
WE	working electrode
µCP	microcontact printing

11.2 Symbols

Symbol	**Quantity**	**Dimension**
A	area	cm^2
A_{cont}	contact area	μm^2
c	concentration	$mol\ cm^{-3}$
c^*	bulk concentration	$mol\ cm^{-3}$
D	diffusion coefficient	$cm^2\ s^{-1}$
d	UME-substrate distance	µm

d_0	positional offset	µm
E_g	band gap energy	eV
E_puls	applied potential during a pulse	V
E_T	UME potential	V
$E_\mathrm{T,On}$	On-potential, applied during a potential pulse	V
$E_\mathrm{T,Off}$	Off-potential	V
F	Faraday constant Force	C µN
f	frequency	Hz
g	geometric-dependent electrode factor	none
h	Planck’s constant	Js
h_A	distance from the sample surface to the probe attachment point	µm
h_P	real probe–substrate distance for plastic microelectrodes	µm
hv	photon energy	eV
$I_\mathrm{S,kin}$	normalized current for finite substrate kinetics	none
i_S	sample current	nA
I_T	normalized UME current	none
$I_\mathrm{T,cond}$	normalized current obtained for a conductive substrate	none
$I_\mathrm{T,ins}$	normalized current obtained for an insulating substrate	none
i_T	UME current	nA
$i'_{\mathrm{T},k}$	current offset corrected current	nA
$i'_{\mathrm{T},k} / i'_{\mathrm{T,max},k}$	calibrated currents	none
$i''_{\mathrm{T},k}$	current offset corrected current and taking into account $\bar{i}_{\mathrm{T},\infty}$	nA
$i'_{\mathrm{T,max},k}$	current offset-corrected maximum current	nA
$i_{\mathrm{T,offs},k}$	current offset	nA
$i_\mathrm{T,ref}$	reference current	nA
$i_{\mathrm{T},\infty}$	steady-state UME current in bulk solution	nA
$\bar{i}_{\mathrm{T},\infty}$	average steady-state current	nA
k	number of electrode in an array	none

	spring constant	μN μm^{-1}
k_{eff}	first order heterogeneous rate constant	cm s^{-1}
k_{r}	heterogeneous rate constant	cm s^{-1}
k_{S}	pseudo first-order reaction rate	cm s^{-1}
L	Normalized distance	none
l	length	cm
l_{F}	length of the freely suspended part of a soft probe	mm
l_{T}	vertical length of the soft probe	μm
	heat diffusion length	μm
l_{α}	optical penetration depth	μm
m	mass	kg
N^{*}_{i}	normalized number densities of states i	none
n	number of transferred electrones	none
p	pressure	N m^{-2}
R	ohmic resistance	Ω
RG	ratio of insulating sheath and electrode	none
r_{glass}	insulating glass sheath radius	μm
r_{T}	active electrode radius of a UME	μm
s_{k}	scale factor for current correction	nA^{-1}
t	time	s
t_{C}	critical time of an experiment	s
t_{L}	thickness of the thin insulating Parylene C layer	μm
v_{T}	UME translation rate	μm s^{-1}
$v_{\mathrm{T,fwd}}$	UME translation rate during forward line scans	μm s^{-1}
$v_{\mathrm{T,rev}}$	UME translation rate during reverse line scans	μm s^{-1}
x'_{k}	corrected *x*-position	μm
$x_{\mathrm{offs},k}$	positional offset in *x*-direction	μm
y'_{k}	corrected *y*-position	μm
$y_{\mathrm{offs},k}$	positional offset in *y*-direction	μm
z_{max}	vertical UME position at which UME made contact with the sample	μm
α	angle	degrees
β	angle	degrees
γ	angle	degrees

Δh	ablated layer thickness	µm
δ	thickness of the diffusion layer	µm
	angle	degrees
ε	angle	degrees
Θ	collection efficiency	none
$\Theta_{\mathrm{C\text{-}Br}}$	surface coverage of a bromo-terminated SAM	none
κ	dimensionless heterogeneous rate constant	none
μ_{D}	thickness of diffusion layer	µm
ν	frequency	s^{-1}
ρ	specific resistance	Ωm
σ	conductivity	$\mathrm{S\,m}^{-1}$
τ	time constant	s
	relaxation time	
τ_{T}	thermal relaxation time	s
υ_{la}	laser ablation velocity	$\mathrm{cm\,s}^{-1}$
φ	angle	degrees
ω	angle	degrees
ϕ	laser fluence	$\mathrm{J\,cm}^{-2}$
	angle	degrees
ϕ_{th}	fluence threshold of a material	$\mathrm{J\,cm}^{-2}$

12 Bibliography

[1] G. Binnig, H. Rohrer, *Helv. Phys. Acta* **1982**, *55*, 726.
[2] G. Binnig, C. F. Quate, *Phys. Rev. Lett.* **1986**, *56*, 930.
[3] S. R. Higgins, R. J. Hamers, *J. Vac. Sci. Technol., B* **1996**, *14*, 1360.
[4] E. Betzig, J. K. Trautman, T. D. Harris, J. S. Weiner, R. L. Kostelak, *Science* **1991**, *251*, 1468.
[5] R. C. Engstrom, *Anal. Chem.* **1984**, *56*, 890.
[6] R. C. Engstrom, M. Weber, D. J. Wunder, R. Burgess, S. Winquist, *Anal. Chem.* **1986**, *58*, 844.
[7] H.-Y. Liu, F.-R. F. Fan, C. W. Lin, A. J. Bard, *J. Am. Chem. Soc.* **1986**, *108*, 3838.
[8] A. J. Bard, F.-R. F. Fan, J. Kwak, O. Lev, *Anal. Chem.* **1989**, *61*, 132.
[9] A. J. Bard, F.-R. F. Fan, D. T. Pierce, P. R. Unwin, D. O. Wipf, F. Zhou, *Science* **1991**, *254*, 68.
[10] J. Kwak, A. J. Bard, *Anal. Chem.* **1989**, *61*, 1794.
[11] Y. Shao, M. V. Mirkin, *J. Phys. Chem. B* **1998**, *102*, 9915.
[12] A. L. Barker, P. R. Unwin, S. Amemiya, J. Zhou, A. J. Bard, *J. Phys. Chem. B* **1999**, *103*, 7260.
[13] A. L. Barker, M. Gonsalves, J. V. Macpherson, C. J. Slevin, P. R. Unwin, *Anal. Chim. Acta* **1999**, *385*, 223.
[14] C. J. Slevin, J. V. Macpherson, P. R. Unwin, *J. Phys. Chem. B* **1997**, *101*, 10851.
[15] D. Mandler, A. J. Bard, *J. Electrochem. Soc.* **1989**, *136*, 3143.
[16] H. Shiku, T. Takeda, H. Yamada, T. Matsue, I. Uchida, *Anal. Chem.* **1995**, *67*, 312.
[17] T. Wilhelm, G. Wittstock, *Electrochim. Acta* **2001**, *47*, 275.
[18] S. Nunige, R. Cornut, H. Hazimeh, F. Hauquier, C. Lefrou, C. Combellas, F. Kanoufi, *Angew. Chem. Int. Ed.* **2012**, *51*, 5208.
[19] C. Cougnon, F. Gohier, D. Belanger, J. Mauzeroll, *Angew. Chem. Int. Ed.* **2009**, *48*, 4006.
[20] P. R. Unwin, A. J. Bard, *Anal. Chem.* **1992**, *64*, 113.
[21] Q. Wang, J. Rodriguez-Lopez, A. J. Bard, *ChemPhysChem* **2010**, *11*, 2969.
[22] M. V. Mirkin, T. C. Richards, A. J. Bard, *J. Phys. Chem.* **1993**, *97*, 7672.
[23] P. R. Unwin, A. J. Bard, *J. Phys. Chem.* **1991**, *95*, 7814.
[24] J. L. Fernandez, D. A. Walsh, A. J. Bard, *J. Am. Chem. Soc.* **2005**, *127*, 357.
[25] M. Black, J. Cooper, P. McGinn, *Meas. Sci. Technol.* **2005**, *16*, 174.
[26] A. Minguzzi, M. A. Alpuche-Aviles, J. R. López, S. Rondinini, A. J. Bard, *Anal. Chem.* **2008**, *80*, 4055.
[27] A. J. Bard, *J. Am. Chem. Soc.* **2010**, *132*, 7559.
[28] H. Ye, H. S. Park, A. J. Bard, *J. Phys. Chem. C* **2011**, *115*, 12464.
[29] K. Fushimi, T. Okawa, K. Azumi, M. Seo, *J. Electrochem. Soc.* **2000**, *147*, 524.
[30] I. Rianasari, L. Walder, M. Burchardt, I. Zawisza, G. Wittstock, *Langmuir* **2008**, *24*, 9110.
[31] A. Maho, J. Denayer, J. Delhalle, Z. Mekhalif, *Electrochim. Acta* **2011**, *56*, 3954.
[32] F. Cortes-Salazar, M. Zhang, A. Becue, J.-M. Busnel, M. Prudent, C. Champod, H. H. Girault, *Chimia* **2009**, *63*, 580.
[33] M. Zhang, H. H. Girault, *Electrochem. Commun.* **2007**, *9*, 1778.
[34] M. Zhang, G. Wittstock, Y. Shao, H. H. Girault, *Anal. Chem.* **2007**, *79*, 4833.
[35] G. Wittstock, *Fresenius J. Anal. Chem.* **2001**, *370*, 303.
[36] C. Nunes Kirchner, M. Träuble, G. Wittstock, *Anal. Chem.* **2010**, *82*, 2626.
[37] A. Anne, A. Chovin, C. Demaille, M. Lafouresse, *Anal. Chem.* **2011**, *83*, 7924.

[38] O. Sklyar, A. Kueng, C. Kranz, B. Mizaikoff, A. Lugstein, E. Bertagnolli, G. Wittstock, *Anal. Chem.* **2005**, *77*, 764.

[39] C. E. Jones, J. V. Macpherson, Z. H. Barber, R. E. Somekh, P. R. Unwin, *Electrochem. Commun.* **1999**, *1*, 55.

[40] A. Kueng, C. Kranz, A. Lugstein, E. Bertagnolli, B. Mizaikoff, *Angew. Chem. Int. Ed.* **2003**, *42*, 3238.

[41] A. Kueng, C. Kranz, A. Lugstein, E. Bertagnolli, B. Mizaikoff, *Angew. Chem. Int. Ed.* **2005**, *44*, 3419.

[42] C. Kranz, G. Friedbacher, B. Mizaikoff, A. Lugstein, J. Smolier, E. Bertagnolli, *Anal. Chem.* **2001**, *73*, 2491.

[43] A. Lugstein, E. Bertagnolli, C. Kranz, A. Kueng, B. Mizaikoff, *Appl. Phys. Lett.* **2002**, *81*, 349.

[44] J. V. Macpherson, P. R. Unwin, *Anal. Chem.* **2000**, *72*, 276.

[45] P. L. T. M. Frederix, P. D. Bosshart, T. Akiyama, M. Chami, M. R. Gullo, J. J. Blackstock, K. Dooleweerdt, N. F. de Rooij, U. Staufer, A. Engel, *Nanotechnology* **2008**, *19*, 384004.

[46] A. Ueda, O. Niwa, K. Maruyama, Y. Shindo, K. Oka, K. Suzuki, *Angew. Chem. Int. Ed.* **2007**, *46*, 8238.

[47] A. Davoodi, A. Farzadi, J. Pan, C. Leygraf, Y. Zhu, *J. Electrochem. Soc.* **2008**, *155*, C474.

[48] P. S. Dobson, J. M. R. Weaver, M. N. Holder, P. R. Unwin, J. V. Macpherson, *Anal. Chem.* **2005**, *77*, 424.

[49] W. Smirnov, A. Kriele, R. Hoffmann, E. Sillero, J. Hees, O. A. Williams, N. Yang, C. Kranz, C. E. Nebel, *Anal. Chem.* **2011**, *83*, 4936.

[50] R. D. Rodriguez, A. Anne, E. Cambril, C. Demaille, *Ultramicroscopy* **2011**, *111*, 973.

[51] A. Davoodi, J. Pan, C. Leygraf, S. Norgren, *Electrochem. Solid State Lett.* **2005**, *8*, B21.

[52] D. P. Burt, N. R. Wilson, J. M. R. Weaver, P. S. Dobson, J. V. Macpherson, *Nano Lett.* **2005**, *5*, 639.

[53] M. A. Derylo, K. C. Morton, L. A. Baker, *Langmuir* **2011**, *27*, 13925.

[54] T. H. Treutler, G. Wittstock, *Electrochim. Acta* **2003**, *48*, 2923.

[55] M. Ludwig, C. Kranz, W. Schuhmann, H. E. Gaub, *Rev. Sci. Instrum.* **1995**, *66*, 2857.

[56] B. Ballesteros Katemann, A. Schulte, W. Schuhmann, *Chem. Eur. J.* **2003**, *9*, 2025.

[57] P. James, L. F. Garfias-Mesias, P. J. Moyer, W. H. Smyrl, *J. Electrochem. Soc.* **1998**, *145*, 64.

[58] D. Oyamatsu, Y. Hirano, N. Kanaya, Y. Mase, M. Nishizawa, T. Matsue, *Bioelectrochemistry* **2003**, *60*, 115.

[59] Y. Lee, Z. Ding, A. J. Bard, *Anal. Chem.* **2002**, *74*, 3634.

[60] M. F. Garay, J. Ufheil, K. Borgwarth, J. Heinze, *Phys. Chem. Chem. Phys.* **2004**, *6*, 4028.

[61] A. Hengstenberg, A. Blöchl, I. D. Dietzel, W. Schuhmann, *Angew. Chem. Int. Ed.* **2001**, *40*, 905.

[62] W. Liu, H. Ye, A. J. Bard, *J. Phys. Chem. C* **2010**, *114*, 1201.

[63] H. Meyer, H. Drewer, B. Gründig, K. Cammann, R. Kakerow, Y. Manioli, W. Mokwa, M. Rospert, *Anal. Chem.* **1995**, *67*, 1164.

[64] Z. Lin, Y. Takahashi, Y. Kitagawa, T. Umemura, H. Shiku, T. Matsue, *Anal. Chem.* **2008**, *80*, 6830.

[65] A. L. Barker, P. R. Unwin, J. W. Gardner, H. Rieley, *Electrochem. Commun.* **2004**, *6*, 91.

[66] F. Deiss, C. Combellas, C. Fretigny, N. Sojic, F. Kanoufi, *Anal. Chem.* **2010**, *82*, 5169.

[67] C. Zhao, I. Witte, G. Wittstock, *Angew. Chem. Int. Ed.* **2006**, *118*, 5595.

[68] G. S. Attard, P. N. Bartlett, N. R. B. Coleman, J. M. Elliott, J. R. Owen, J. H. Wang, *Science* **1997**, *278*, 838.

[69] J. Kwak, A. J. Bard, *Anal. Chem.* **1989**, *61*, 1221.

[70] G. Wittstock, M. Burchardt, S. E. Pust, Y. Shen, C. Zhao, *Angew. Chem. Int. Ed.* **2007**, *46*, 1584.

[71] M. V. Mirkin, W. Nogala, J. Velmurugan, Y. Wang, *Phys. Chem. Chem. Phys.* **2011**, *13*, 21196.

[72] A. J. Bard, M. V. Mirkin, Second ed., CRC Press Taylor & Francis Group, Boca Raton, London, New York, **2012**, p. 660.

[73] C. Lee, J. Kwak, F. C. Anson, *Anal. Chem.* **1991**, *63*, 1501.

[74] R. D. Martin, P. R. Unwin, *Anal. Chem.* **1998**, *70*, 276.

[75] D. H. Craston, C. W. Lin, A. J. Bard, *J. Electrochem. Soc.* **1988**, *135*, 785.

[76] K. Eckhard, X. Chen, F. Turcu, W. Schuhmann, *Phys. Chem. Chem. Phys.* **2006**, *8*, 5359.

[77] J. Heinze, *Angew. Chem. Int. Ed.* **1993**, *32*, 1268.

[78] K. Stulik, C. Amatore, K. Holub, V. Marecek, W. Kutner, *Pure Appl. Chem.* **2000**, *72*, 1483.

[79] M. Fleischmann, S. Pons, D. R. Rolison, P. P. Schmidt, *Ultramicroelectrodes,* Datatech Systems, Inc., Morganton, NC, **1987**.

[80] F.-R. F. Fan, C. Demaille, in *Scanning Electrochemical Microscopy* Eds.: A. J. Bard, M. V. Mirkin), CRC Press Taylor & Francis Group, Boca Raton, London, New York, **2012**, p. 25.

[81] C. G. Zoski, *Electroanalysis* **2002**, *14*, 1041.

[82] Y. Selzer, D. Mandler, *Anal. Chem.* **2000**, *72*, 2383.

[83] Y. Takahashi, A. I. Shevchuk, P. Novak, Y. Zhang, N. Ebejer, J. V. MacPherson, P. R. Unwin, A. J. Pollard, D. Roy, C. A. Clifford, H. Shiku, T. Matsue, D. Klenerman, Y. E. Korchev, *Angew. Chem. Int. Ed.* **2011**, *50*, 9638.

[84] K. B. Holt, J. Hu, J. S. Foord, *Anal. Chem.* **2007**, *79*, 2556.

[85] C. Demaille, M. Brust, M. Tsionsky, A. J. Bard, *Anal. Chem.* **1997**, *69*, 2323.

[86] K. R. Wehmeyer, R. M. Wightman, *Anal. Chem.* **1985**, *57*, 1989.

[87] C. Combellas, A. Fuchs, F. Kanoufi, *Anal. Chem.* **2004**, *76*, 3612.

[88] B. R. Horrocks, M. V. Mirkin, D. T. Pierce, A. J. Bard, G. Nagy, K. Toth, *Anal. Chem.* **1993**, *65*, 1213.

[89] P. Elsamadisi, Y. Wang, J. Velmurugan, M. V. Mirkin, *Anal. Chem.* **2011**, *83*, 671.

[90] G. Wittstock, M. Burchardt, C. Nunes Kirchner, in *Electrochemical Sensor Analysis, Vol. 49* Eds.: S. Alegret, A. Merkoci), Elsevier, Amsterdam, **2007**, p. 907.

[91] Y. Saito, *Rev. Polarogr.* **1968**, *15*, 177.

[92] C. Combellas, M. Fermigier, A. Fuchs, F. Kanoufi, *Anal. Chem.* **2005**, *77*, 7966.

[93] C. G. Zoski, A. M. Bond, T. E. Allinson, K. B. Oldham, *Anal. Chem.* **1990**, *62*, 37.

[94] C. Zhao, I. Zawisza, M. Nullmeier, M. Burchardt, M. Träuble, I. Witte, G. Wittstock, *Langmuir* **2008**, *24*, 7605.

[95] M. V. Mirkin, F.-R. F. Fan, A. J. Bard, *Science* **1992**, *257*, 364.

[96] R. Cornut, C. Lefrou, *J. Electroanal. Chem.* **2008**, *621*, 178.

[97] J. L. Amphlett, G. Denuault, *J. Phys. Chem. B* **1998**, *102*, 9946.

[98] C. Wei, A. J. Bard, M. V. Mirkin, *J. Phys. Chem.* **1995**, *99*, 16033.

[99] D. T. Pierce, P. R. Unwin, A. J. Bard, *Anal. Chem.* **1992**, *64*, 1795.

[100] M. Burchardt, M. Träuble, G. Wittstock, *Anal. Chem.* **2009**, *81*, 4857.

[101] R. Cornut, P. Hapiot, C. Lefrou, *J. Electroanal. Chem.* **2009**, *633*, 221.

[102] J. L. Fernandez, A. J. Bard, *Anal. Chem.* **2003**, *75*, 2967.

[103] M. Sanchez-Sanchez Carlos, J. Solla-Gullon, J. Vidal-Iglesias Francisco, A. Aldaz, V. Montiel, E. Herrero, *J. Am. Chem. Soc.* **2010**, *132*, 5622.

[104] C. M. Sanchez-Sanchez, J. Rodriguez-Lopez, A. J. Bard, *Anal. Chem.* **2008**, *80*, 3254.

[105] Y. Shen, M. Träuble, G. Wittstock, *Anal. Chem.* **2008**, *80*, 750.

[106] F. Zhou, P. R. Unwin, A. J. Bard, *J. Phys. Chem.* **1992**, *96*, 4917.

[107] K. Eckhard, W. Schuhmann, *Electrochim. Acta* **2007**, *53*, 1164.

[108] W. Nogala, M. Burchardt, M. Opallo, J. Rogalski, G. Wittstock, *Bioelectrochemistry* **2008**, *72*, 174.

[109] U. M. Tefashe, T. Loewenstein, H. Miura, D. Schlettwein, G. Wittstock, *J. Electroanal. Chem.* **2010**, *650*, 24.

[110] D. A. Walsh, J. L. Fernandez, A. J. Bard, *J. Electrochem. Soc.* **2006**, *153*, E99.

[111] D. Falconnet, G. Csucs, H. Michelle Grandin, M. Textor, *Biomaterials* **2006**, *27*, 3044.

[112] M. J. Hynes, J. A. Maurer, *Angew. Chem. Int. Ed.* **2012**, *51*, 2151.

[113] Y. Xia, G. M. Whitesides, *Angew. Chem. Int. Ed.* **1998**, *37*, 550.

[114] H. Fan, Y. Lu, A. Stump, S. T. Reed, T. Baer, R. Schunk, V. Perez-Luna, G. P. Lopez, C. J. Brinker, *Nature* **2000**, *405*, 56.

[115] G. J. Marquez, M. J. Renn, W. D. Miller, *Mater. Res. Soc. Symp. Proc.* **2002**, *698*, 343.

[116] V. Zoellmer, M. Mueller, M. Renn, M. Busse, I. Wirth, D. Godlinski, M. Kardos, *European Coatings Journal* **2006**, 46.

[117] M. A. Roberts, J. S. Rossier, P. Bercier, H. H. Girault, *Anal. Chem.* **1997**, *69*, 2035.

[118] K. Callewaert, Y. Martele, L. Breban, K. Naessens, P. Vandaele, R. Baets, G. Geuskens, E. Schacht, *Appl. Surf. Sci.* **2003**, *208-209*, 218.

[119] S. A. Campbell, *The Science and Engineering of Microelectronic Fabrication,* Oxford University Press, New York, **2001**.

[120] D. M. Kolb, R. Ullmann, T. Will, *Science* **1997**, *275*, 1097.

[121] S. E. Pust, S. Szunerits, R. Boukherroub, G. Wittstock, *Nanotechnology* **2009**, *20*, 075302.

[122] Y. H. Tan, M. Liu, B. Nolting, J. G. Go, J. Gervay-Hague, G.-y. Liu, *ACS Nano* **2008**, *2*, 2374.

[123] A.-S. Duwez, S. Cuenot, C. Jerome, S. Gabriel, R. Jerome, S. Rapino, F. Zerbetto, *Nat. Nanotechnol.* **2006**, *1*, 122.

[124] R. D. Piner, J. Zhu, F. Xu, S. Hong, C. A. Mirkin, *Science* **1999**, *283*, 661.

[125] D. Mandler, in *Scanning Electrochemical Microscopy* Eds.: A. J. Bard, M. V. Mirkin), Marcel Dekker, New York, Basel, **2001**, p. 593.

[126] M. Kongsfelt, J. Vinther, K. Malmos, M. Ceccato, K. Torbensen, C. S. Knudsen, K. V. Gothelf, S. U. Pedersen, K. Daasbjerg, *J. Am. Chem. Soc.* **2011**, *133*, 3788.

[127] A. J. Bard, G. Denuault, C. Lee, D. Mandler, D. O. Wipf, *Acc. Chem. Res.* **1990**, *23*, 357.

[128] M. Sheffer, D. Mandler, *J. Electrochem. Soc.* **2008**, *155*, D203.

[129] G. Valenti, L. Bardini, D. Bonazzi, S. Rapino, M. Marcaccio, F. Paolucci, *J. Phys. Chem. C* **2010**, *114*, 22165.

[130] F. Grisotto, A. Ghorbal, C. Goyer, J. Charlier, S. Palacin, *Chem. Mater.* **2011**, *23*, 1396.

[131] C. Marck, K. Borgwarth, J. Heinze, *Chem. Mater.* **2001**, *13*, 747.

[132] J. Zhou, D. O. Wipf, *J. Electrochem. Soc.* **1997**, *144*, 1202.

[133] K. Borgwarth, C. Ricken, D. G. Ebling, J. Heinze, *Ber. Bunsenges. Phys. Chem.* **1995**, *99*, 1421.

[134] E. Malel, J. Colleran, D. Mandler, *Electrochim. Acta* **2011**, *56*, 6954.

[135] E. Malel, R. Ludwig, L. Gorton, D. Mandler, *Chem. Eur. J.* **2010**, *16*, 11697.

[136] T. Wilhelm, G. Wittstock, *Mikrochim. Acta* **2000**, *133*, 1.

[137] I. Shohat, D. Mandler, *J. Electrochem. Soc.* **1994**, *141*, 995.

[138] O. E. Hüsser, D. H. Craston, A. J. Bard, *J. Electrochem. Soc.* **1989**, *136*, 3222.

[139] C. W. Lin, F.-R. F. Fan, A. J. Bard, *J. Electrochem. Soc.* **1987**, *134*, 1038.

[140] F. Forouzan, A. J. Bard, *J. Phys. Chem. B* **1997**, *101*, 10876.

[141] E. M. El-Giar, R. A. Said, G. E. Bridges, D. J. Thomson, *J. Electrochem. Soc.* **2000**, *147*, 586.

[142] W. Schuhmann, C. Kranz, H. Wohlschläger, J. Strohmeier, *Biosens. Bioelectron.* **1997**, *12*, 1157.

[143] C. Kranz, M. Ludwig, H. E. Gaub, W. Schuhmann, *Adv. Mater.* **1995**, *7*, 38.

[144] H. Sugimura, T. Uchida, N. Kitamura, N. Shimo, H. Masuhara, *J. Electroanal. Chem.* **1993**, *361*, 57.

[145] G. Wittstock, R. Hesse, W. Schuhmann, *Electroanalysis* **1997**, *9*, 746.

[146] T. Wilhelm, G. Wittstock, *Angew. Chem. Int. Ed.* **2003**, *42*, 2247.

[147] C. A. Widrig, C. Chung, M. D. Porter, *J. Electroanal. Chem.* **1991**, *310*, 335.

[148] D. Mandler, A. J. Bard, *Langmuir* **1990**, *6*, 1489.

[149] S. Meltzer, D. Mandler, *J. Chem. Soc. Faraday Trans. 1* **1995**, *91*, 1019.

[150] J. Ufheil, F. M. Boldt, M. Börsch, K. Borgwarth, J. Heinze, *Bioelectrochemistry* **2000**, *52*, 103.

[151] C. Cougnon, J. Mauzeroll, D. Belanger, *Angew. Chem. Int. Ed.* **2009**, *48*, 7395.

[152] C. Hess, K. Borgwarth, C. Ricken, D. G. Ebling, J. Heinze, *Electrochim. Acta* **1997**, *42*, 3065.

[153] I. Turyan, T. Matsue, D. Mandler, *Anal. Chem.* **2000**, *72*, 3431.

[154] S. Meltzer, D. Mandler, *J. Electrochem. Soc.* **1995**, *142*, L82.

[155] S. Sauter, G. Wittstock, *J. Solid State Electrochem.* **2001**, *5*, 205.

[156] L. Zhang, X. Z. Ma, M. X. Lin, Y. Lin, G. H. Cao, J. Tang, Z. W. Tian, *J. Phys. Chem. B* **2006**, *110*, 18432.

[157] Y. Zu, L. Xie, B. Mao, Z. Tian, *Electrochim. Acta* **1998**, *43*, 1683.

[158] Y. Zu, L. Xie, Z. Tian, Z. Xie, J. Mu, B. Mao, *Chin. Sci. Bull.* **1997**, *42*, 1318.

[159] J. J. Sun, H. G. Huang, Z. Q. Tian, L. Xie, J. Luo, X. Y. Ye, Z. Y. Zhou, S. H. Xia, Z. W. Tian, *Electrochim. Acta* **2001**, *47*, 95.

[160] L. Zhang, X. Ma, J. Tang, D. Qu, Q. Ding, L. Sun, *Electrochim. Acta* **2006**, *52*, 630.

[161] D. Mandler, A. J. Bard, *J. Electrochem. Soc.* **1990**, *137*, 2468.

[162] E. Ammann, D. Mandler, *J. Electrochem. Soc.* **2001**, *148*, C533.

[163] H. Kaji, K. Tsukidate, T. Matsue, M. Nishizawa, *J. Am. Chem. Soc.* **2004**, *126*, 15026.

[164] C. Zhao, M. Burchardt, T. Brinkhoff, C. Beardsley, M. Simon, G. Wittstock, *Langmuir* **2010**, *26*, 8641.

[165] C. Marck, K. Borgwarth, J. Heinze, *Adv. Mater.* **2001**, *13*, 47.

[166] K. Borgwarth, N. Rohde, C. Ricken, M. L. Hallensleben, D. Mandler, J. Heinze, *Adv. Mater.* **1999**, *11*, 1221.

[167] C. Combellas, F. Kanoufi, D. Mazouzi, A. Thiebault, *J. Electroanal. Chem.* **2003**, *556*, 43.

[168] C. Combellas, J. Ghilane, F. Kanoufi, D. Mazouzi, *J. Phys. Chem. B* **2004**, *108*, 6391.

[169] C. Combellas, A. Fuchs, F. Kanoufi, D. Mazouzi, S. Nunige, *Polymer* **2004**, *45*, 4669.

[170] F. Kanoufi, C. Combellas, M. E. R. Shanahan, *Langmuir* **2003**, *19*, 6711.

[171] N. Ktari, C. Combellas, F. Kanoufi, *J. Phys. Chem. C* **2011**, *115*, 17891.

[172] S.-Y. Ku, K.-T. Wong, A. J. Bard, *J. Am. Chem. Soc.* **2008**, *130*, 2392.

[173] S. Rapino, G. Valenti, R. Marcu, M. Giorgio, M. Marcaccio, F. Paolucci, *J. Mater. Chem.* **2010**, *20*, 7272.

[174] J.-M. Noel, A. Latus, C. Lagrost, E. Volanschi, P. Hapiot, *J. Am. Chem. Soc.* **2012**, *134*, 2835.

[175] S. Lhenry, Y. R. Leroux, P. Hapiot, *Anal. Chem.* **2012**, *84*, 7518.

[176] S. Magdassi, in *The Chemistry of the Inkjet Inks*, World Scientific Publishing Co. Pte. Ltd., New Jersey, **2010**.

[177] D. Huang, F. Liao, S. Molesa, D. Redinger, V. Subramanian, *J. Electrochem. Soc.* **2003**, *150*, G412.

[178] A. Mette, P. L. Richter, M. Hoerteis, S. W. Glunz, *Progress in Photovoltaics* **2007**, *15*, 621.

[179] G. C. Jensen, C. E. Krause, G. A. Sotzing, J. F. Rusling, *Phys. Chem. Chem. Phys.* **2011**, *13*, 4888.

[180] I. Grunwald, E. Groth, I. Wirth, J. Schumacher, M. Maiwald, V. Zoellmer, M. Busse, *Biofabrication* **2010**, *2*, 014106/1.

[181] D. Witte, Master Thesis, Carl von Ossietzky Universität, **2012**.

[182] D. Bäuerle, *Laser processing and chemistry,* Springer, Berlin, **2000**.

[183] R. Srinivasan, B. Braren, *Chem. Rev.* **1989**, *89*, 1303.

[184] B. J. Seddon, Y. Shao, J. Fost, H. H. Girault, *Electrochim. Acta* **1994**, *39*, 783.

[185] C. G. Zoski, N. Simjee, O. Guenat, M. Koudelka-Hep, *Anal. Chem.* **2004**, *76*, 62.

[186] J. Zhou, Y. Zu, A. J. Bard, *J. Electroanal. Chem.* **2000**, *491*, 22.

[187] G. Denuault, M. Sosna, K.-J. Williams, in *Handbook of Electrochemistry* (Ed. C. G. Zoski), Elsevier B.V., Amsterdam, **2007**, p. 432.

[188] M. A. Alpuche-Aviles, D. O. Wipf, *Anal. Chem.* **2001**, *73*, 4873.

[189] R. T. Kurulugama, D. O. Wipf, S. A. Takacs, S. Pongmayteegul, P. A. Garris, J. E. Baur, *Anal. Chem.* **2005**, *77*, 1111.

[190] X. Zhao, P. M. Diakowski, Z. Ding, *Anal. Chem.* **2010**, *82*, 8371.

[191] D. J. Comstock, J. W. Elam, M. J. Pellin, M. C. Hersam, *Anal. Chem.* **2010**, *82*, 1270.

[192] Y. Takahashi, A. I. Shevchuk, P. Novak, Y. Murakami, H. Shiku, Y. E. Korchev, T. Matsue, *J. Am. Chem. Soc.* **2010**, *132*, 10118.

[193] K. McKelvey, M. E. Snowden, M. Peruffo, P. R. Unwin, *Anal. Chem.* **2011**, *83*, 6447.

[194] K. McKelvey, M. A. Edwards, P. R. Unwin, *Anal. Chem.* **2010**, *82*, 6334.

[195] Y. Takahashi, A. I. Shevchuk, P. Novak, B. Babakinejad, J. MacPherson, P. R. Unwin, H. Shiku, J. Gorelik, D. Klenerman, Y. E. Korchev, T. Matsue, *Proc. Natl. Acad. Sci. U. S. A.* **2012**, *109*, 11540.

[196] F. O. Laforge, J. Velmurugan, Y. Wang, M. V. Mirkin, *Anal. Chem.* **2009**, *81*, 3143.

[197] S. E. Pust, M. Salomo, E. Oesterschulze, G. Wittstock, *Nanotechnology* **2010**, *21*, 105709.

[198] H. Shin, P. J. Hesketh, C. Kranz, D. A. Roudolph, B. Mizaikoff, *Micro-Electro-Mechanical Systems* **2005**, *7*, 383.

[199] H. Shin, P. J. Hesketh, B. Mizaikoff, C. Kranz, *Sens. Actuators B* **2008**, *134*, 488.

[200] P. S. Dobson, J. M. R. Weaver, D. P. Burt, M. N. Holder, N. R. Wilson, P. R. Unwin, J. V. Macpherson, *Phys. Chem. Chem. Phys.* **2006**, *8*, 3909.

[201] A. Lugstein, E. Bertagnolli, C. Kranz, B. Mizaikoff, *Surf. Interface Anal.* **2002**, *33*, 146.

[202] A. Kueng, C. Kranz, B. Mizaikoff, A. Lugstein, E. Bertagnolli, *Appl. Phys. Lett.* **2003**, *82*, 1592.

[203] C. Kranz, A. Kueng, A. Lugstein, E. Bertagnolli, B. Mizaikoff, *Ultramicroscopy* **2004**, *100*, 127.

[204] J. Wiedemair, B. Balu, J.-S. Moon, D. W. Hess, B. Mizaikoff, C. Kranz, *Anal. Chem.* **2008**, *80*, 5260.

[205] M. Salomo, S. E. Pust, G. Wittstock, E. Oesterschulze, *Microelectron. Eng.* **2010**, *87*, 1537.

[206] T. Akiyama, M. R. Gullo, N. F. De Rooij, A. Tonin, H.-R. Hidber, P. L. T. M. Frederix, A. Engel, U. Staufer, *Japanese Journal of Applied Physics, Part 1: Regular Papers, Short Notes & Review Papers* **2004**, *43*, 3865.

[207] M. R. Gullo, P. L. T. M. Frederix, T. Akiyama, A. Engel, N. F. de Rooij, U. Staufer, *Anal. Chem.* **2006**, *78*, 5436.

[208] K. Maruyama, H. Ohkawa, S. Ogawa, A. Ueda, O. Niwa, K. Suzuki, *Anal. Chem.* **2006**, *78*, 1904.

[209] B. Ballesteros Katemann, A. Schulte, W. Schuhmann, *Electroanalysis* **2004**, *16*, 60.

[210] M. Etienne, E. C. Anderson, S. R. Evans, W. Schuhmann, I. Fritsch, *Anal. Chem.* **2006**, *78*, 7317.

[211] B. Ballesteros Katemann, W. Schuhmann, *Electroanalysis* **2002**, *14*, 22.

[212] Y. Takahashi, H. Shiku, T. Murata, T. Yasukawa, T. Matsue, *Anal. Chem.* **2009**, *81*, 9674.

[213] M. Nebel, K. Eckhard, T. Erichsen, A. Schulte, W. Schuhmann, *Anal. Chem.* **2010**, *82*, 7842.

[214] M. Etienne, B. Layoussifi, T. Giornelli, D. Jacquet, *Electrochem. Commun.* **2012**, *15*, 70.

[215] D. O. Wipf, A. J. Bard, *Anal. Chem.* **1992**, *64*, 1362.

[216] M. A. Edwards, A. L. Whitworth, P. R. Unwin, *Anal. Chem.* **2011**, *83*, 1977.

[217] D. O. Wipf, A. J. Bard, D. E. Tallman, *Anal. Chem.* **1993**, *65*, 1373.

[218] C. Gabrielli, F. Huet, M. Keddam, P. Rousseau, V. Vivier, *J. Phys. Chem. B* **2004**, *108*, 11620.

[219] K. Eckhard, T. Erichsen, M. Stratmann, W. Schuhmann, *Chem. Eur. J.* **2008**, *14*, 3968.

[220] J. Behnken, bachelor thesis, Carl von Ossietzky University, **2012**.

[221] B. Kovacs, B. Csoka, G. Nagy, I. Kapui, R. E. Gyurcsanyi, K. Toth, *Electroanalysis* **1999**, *11*, 349.

[222] S. C. Minne, G. Yaralioglu, S. R. Manalis, J. D. Adams, J. Zesch, A. Atalar, C. F. Quate, *Appl. Phys. Lett.* **1998**, *72*, 2340.

[223] P. Vettiger, M. Despont, U. Drechsler, U. Durig, W. Haberle, M. I. Lutwyche, H. E. Rothuizen, R. Stutz, R. Widmer, G. K. Binnig, *IBM Journal of Research and Development* **2000**, *44*, 323.

[224] Y. Oh, C. Choi, K. Noh, D. Villwock, S. Jin, *J. Vac. Sci. Technol., B: Nanotechnol. Microelectron.: Mater., Process., Meas., Phenom.* **2011**, *29*, 06FD03.

[225] S. Lenhert, P. Sun, Y. Wang, H. Fuchs, C. A. Mirkin, *Small* **2007**, *3*, 71.

[226] S. Hong, C. A. Mirkin, *Science* **2000**, *288*, 1808.

[227] X. Wang, C. Liu, *Nano Lett.* **2005**, *5*, 1867.

[228] D. Bullen, C. Liu, *Sens. Actuators, A* **2006**, *A125*, 504.

[229] C. A. Mirkin, *ACS Nano* **2007**, *1*, 79.

[230] K. Salaita, Y. Wang, J. Fragala, R. A. Vega, C. Liu, C. A. Mirkin, *Angew. Chem. Int. Ed.* **2006**, *45*, 7220.

[231] J. E. Baur, H. M. Miller, M. A. Ritchason, *Anal. Chim. Acta* **1999**, *397*, 123.

[232] T. Yasukawa, T. Kaya, T. Matsue, *Anal. Chem.* **1999**, *71*, 4637.

[233] A. Kueng, C. Kranz, B. Mizaikoff, *Biosens. Bioelectron.* **2005**, *21*, 346.

[234] S. Borgmann, I. Radtke, T. Erichsen, A. Bloechl, R. Heumann, W. Schuhmann, *ChemBioChem* **2006**, *7*, 662.

[235] S. Isik, M. Etienne, J. Oni, A. Blöchl, S. Reiter, W. Schuhmann, *Anal. Chem.* **2004**, *76*, 6389.

[236] K. Toth, G. Nagy, C. Wei, A. J. Bard, *Electroanalysis* **1995**, *7*, 801.

[237] J. Ufheil, K. Borgwarth, J. Heinze, *Anal. Chem.* **2002**, *74*, 1316.

[238] O. Sklyar, J. Ufheil, J. Heinze, G. Wittstock, *Electrochim. Acta* **2003**, *49*, 117.

[239] P. Liljeroth, C. Johans, C. J. Slevin, B. M. Quinn, K. Kontturi, *Electrochem. Commun.* **2002**, *4*, 67.

[240] P. Liljeroth, C. Johans, C. J. Slevin, B. M. Quinn, A.-K. Kontturi, *Anal. Chem.* **2002**, *74*, 1972.

[241] J. M. Elliott, G. S. Attard, P. N. Bartlett, N. R. B. Coleman, D. A. S. Merckel, J. R. Owen, *Chem. Mater.* **1999**, *11*, 3602.

[242] G. S. Attard, P. N. Bartlett, N. R. B. Coleman, J. M. Elliott, J. R. Owen, *Langmuir* **1998**, *14*, 7340.

[243] J. M. Elliott, P. R. Birkin, P. N. Bartlett, G. S. Attard, *Langmuir* **1999**, *15*, 7411.

[244] U. M. Tefashe, PhD thesis, Carl von Ossietzky Universität Oldenburg, **2012**.

[245] Y. Okabe, U. Akiba, M. Fujihira, *Appl. Surf. Sci.* **2000**, *157*, 398.

[246] T. Miyatani, M. Horii, A. Rosa, M. Fujihira, O. Marti, *Appl. Phys. Lett.* **1997**, *71*, 2632.

[247] S. Arimoto, H. Kageyama, T. Torimoto, S. Kuwabata, *Electrochem. Commun.* **2008**, *10*, 1901.

[248] A. Fedorkova, R. Orinakova, A. Orinak, H.-D. Wiemhoefer, D. Kaniansky, M. Winter, *J. Solid State Electrochem.* **2010**, *14*, 2173.

[249] F. Cortes-Salazar, M. Träuble, F. Li, J.-M. Busnel, A.-L. Gassner, M. Hojeij, G. Wittstock, H. H. Girault, *Anal. Chem.* **2009**, *81*, 6889.

[250] M. L. Williams, R. F. Landel, J. D. Ferry, *J. Am. Chem. Soc.* **1955**, *77*, 3701.

[251] E. Meyer, H. J. Hug, R. Bennewitz, *Scanning probe microscopy: the lab on a tip,* Springer, Berlin [u.a.], **2004**.

[252] C. S. Chen, M. Mrksich, S. Huang, G. M. Whitesides, D. E. Ingber, *Science* **1997**, *276*, 1425.

[253] M. N. Yousaf, B. T. Houseman, M. Mrksich, *Angew. Chem. Int. Ed.* **2001**, *40*, 1093.

[254] M. Mrksich, *Chem. Soc. Rev.* **2000**, *29*, 267.

[255] D. K. Hoover, E.-j. Lee, E. W. L. Chan, M. N. Yousaf, *ChemBioChem* **2007**, *8*, 1920.

[256] E. W. L. Chan, S. Park, M. N. Yousaf, *Angew. Chem. Int. Ed.* **2008**, *47*, 6267.

[257] H. Kaji, M. Hashimoto, M. Nishizawa, *Anal. Chem.* **2006**, *78*, 5469.

[258] B. Vaske, Diploma thesis, Carl von Ossietzky Universität, **2009**.

[259] K. L. Prime, G. M. Whitesides, *Science* **1991**, *252*, 1164.

[260] K. L. Prime, G. M. Whitesides, *J. Am. Chem. Soc.* **1993**, *115*, 10714.

[261] I. Brand, M. Nullmeier, T. Klüner, R. Jogireddy, J. Christoffers, G. Wittstock, *Langmuir* **2010**, *26*, 362.

[262] H. S. Wroblowa, Y.-C. Pan, G. Razumney, *J. Electroanal. Chem. Interfacial Electrochem.* **1976**, *69*, 195.

[263] J. J. Lingane, *J. Electroanal. Chem.* **1961**, *2*, 296.

[264] A. Damjanovic, A. Dey, J. O. M. Bockris, *Electrochim. Acta* **1966**, *11*, 791.

[265] D. S. Gnanamuthu, J. V. Petrocelli, *J. Electrochem. Soc.* **1967**, *114*, 1036.

[266] I. Katsounaros, W. B. Schneider, J. C. Meier, U. Benedikt, P. U. Biedermann, A. A. Auer, K. J. J. Mayrhofer, *Phys. Chem. Chem. Phys.* **2012**, *14*, 7384.

[267] H. Bülter, Master thesis, Carl von Ossietzky University **2012**.

[268] E. Yeager, *Electrochim. Acta* **1984**, *29*, 1527.

[269] C. Zhang, F.-R. F. Fan, A. J. Bard, *J. Am. Chem. Soc.* **2009**, *131*, 177.

[270] R. Borup, J. Meyers, B. Pivovar, Y. S. Kim, R. Mukundan, N. Garland, D. Myers, M. Wilson, F. Garzon, D. Wood, P. Zelenay, K. More, K. Stroh, T. Zawodzinski, J. Boncella, J. E. McGrath, M. Inaba, K. Miyatake, M. Hori, K. Ota, Z. Ogumi, S. Miyata, A. Nishikata, Z. Siroma, Y. Uchimoto, K. Yasuda, K.-i. Kimijima, N. Iwashita, *Chem. Rev.* **2007**, *107*, 3904.

[271] V. A. Sethuraman, J. W. Weidner, A. T. Haug, S. Motupally, L. V. Protsailo, *J. Electrochem. Soc.* **2008**, *155*, B50.

[272] R. Lei, L. Stratmann, D. Schafer, T. Erichsen, S. Neugebauer, N. Li, W. Schuhmann, *Anal. Chem.* **2009**, *81*, 5070.

[273] J. Wang, *Chem. Rev.* **2008**, *108*, 814.

[274] J. L. Fernandez, N. Mano, A. Heller, A. J. Bard, *Angew. Chem. Int. Ed.* **2004**, *43*, 6355.

[275] B. Liu, A. J. Bard, *J. Phys. Chem. B* **2002**, *106*, 12801.

[276] K. Jambunathan, B. C. Shah, J. L. Hudson, A. C. Hillier, *J. Electroanal. Chem.* **2001**, *500*, 279.

[277] F. M. Toma, A. Sartorel, M. Iurlo, M. Carraro, P. Parisse, C. Maccato, S. Rapino, B. R. Gonzalez, H. Amenitsch, T. Da Ros, L. Casalis, A. Goldoni, M. Marcaccio, G. Scorrano, G. Scoles, F. Paolucci, M. Prato, M. Bonchio, *Nature Chemistry* **2010**, *2*, 826.

[278] J. L. Fernandez, A. J. Bard, *Anal. Chem.* **2004**, *76*, 2281.

[279] S. A. G. Evans, J. M. Elliott, L. M. Andrews, P. N. Bartlett, P. J. Doyle, G. Denuault, *Anal. Chem.* **2002**, *74*, 1322.

[280] K. Szot, W. Nogala, J. Niedziolka-Jonsson, M. Joensson-Niedziolka, F. Marken, J. Rogalski, C. N. Kirchner, G. Wittstock, M. Opallo, *Electrochim. Acta* **2009**, *54*, 4620.

[281] M. L. Reyzer, Y. Hsieh, K. Ng, W. A. Korfmacher, R. M. Caprioli, *J. Mass Spectrom.* **2003**, *38*, 1081.

[282] U. Karst, *Angew. Chem. Int. Ed.* **2004**, *43*, 2476.

13 Own Publications and Conference Contributions

13.1 Publications

[A1] Fernando Cortés-Salazar, Andreas Lesch, Dmitry Momotenko, Jean-Marc Busnel, Gunther Wittstock, Hubert H. Girault; Fountain Pen for Scanning Electrochemical Microscopy, *Analytical Methods* **2010**, *2*, 817-823.

[A2] Fernando Cortés-Salazar, Dmitry Momotenko, Andreas Lesch, Gunther Wittstock, Hubert H. Girault; Soft Microelectrode Linear Array for Scanning Electrochemical Microscopy, *Analytical Chem*istry **2010**, *82*, 10037-10044.

[A3] Fernando Cortés-Salazar, Dmitry Momotenko, Hubert H. Girault, Andreas Lesch, Gunther Wittstock; Seeing Big with Scanning Electrochemical Microscopy, *Analytical Chemistry* **2011**, *83*, 1493-1499.

[A4] Dmity Momotenko, Fernando Cortés-Salazar, Andreas Lesch, Gunther Wittstock, Hubert H. Girault; Microfluidic Push-Pull Probe for Scanning Electrochemical Microscopy, *Analytical Chem*istry **2011**, *83*, 5275-5282.

[A5] Andreas Lesch, Gunther Wittstock, Chris Burger, Benjamin Walther, Jürgen Hackenberg; External Control of anodic dissolution mechanisms of 100Cr6 in nitrate/chloride mixed electrolytes, *Journal of Electrochemical Science and Engineering* **2011**, *1*, 39-54.

[A6] Andreas Lesch, Dmitry Momotenko, Fernando Cortés-Salazar, Ingo Wirth, Ushula Mengesha Tefashe, Frank Meiners, Britta Vaske, Hubert H. Girault, Gunther Wittstock; Fabrication of Soft Gold Microelectrode Arrays as Probes for Scanning Electrochemical Microscopy, *Journal of Electroanalytical Chemistry* **2012**, *666*, 52-61.

[A7] Dmitry Momotenko, Liang Qiao, Fernando Cortés-Salazar, Andreas Lesch, Gunther Wittstock, Hubert H. Girault; Electrochemical Push-Pull Scanner with Mass Spectrometry Detection, *Analytical Chemistry* **2012**, *84*, 6630-6637.

[A8] Andreas Lesch, Britta Vaske, Frank Meiners, Dmitry Momotenko, Fernando Cortés-Salazar, Hubert H. Girault, Gunther Wittstock; Parallel Imaging and Chemical Template-Free Patterning of Self-Assembled Monolayers with Soft Linear Microelectrode Arrays, *Angewandte Chemie International Edition* **2012**, *51*, 10413-10416; Parallele Abbildung und templatfreie Strukturierung

selbstorganisierter Monoschichten mit weichen linearen Mikroelektrodenarrays, *Angew. Chem.* **2012**, *124*, 10559-10563.

Non-refereed publication:

[A9] Andreas Lesch, Britta Vaske, Frank Meiners, Daniel Witte, Dmitry Momotenko, Fernando Cortés-Salazar, Ingo Wirth, Hubert H. Girault, Gunther Wittstock; Soft microelectrode arrays as SECM probes for surface modification and characterization, *Bunsen-Magazin* **2012**, *14*, 203.

13.2 Oral Presentations in National and International Conferences

[B1] Andreas Lesch, Gunther Wittstock, Chris Burger, Benjamin Walther, Jürgen Hackenberg; Two-way anodic dissolution of low alloyed steel in chloride/nitrate mixed electrolytes, INSECT (International Symposium on Electrochemical Machining Technology) 2009, Fraunhofer IKTS Dresden, Germany, 26.-27. November 2009.

[B2] Andreas Lesch, Fernando Cortés-Salazar, Dmitry Momotenko, Hubert H. Girault, Gunther Wittstock; Development of new concept for high throughput SECM imaging, Electrochemistry 2010, Bochum, Germany, 13.-15. September 2010.

[B3] Andreas Lesch, Fernando Cortés-Salazar, Dmitry Momotenko, Hubert H. Girault, Gunther Wittstock; From soft stylus microelectrode arrays via software development to high throughput SECM imaging, 6th Workshop on Scanning Electrochemical Microscopy, Frejus, France, 3.-6. October 2010.

[B4] Andreas Lesch, Britta Vaske, Frank Meiners, Dmitry Momotenko, Fernando Cortés-Salazar, Ingo Wirth, Hubert H. Girault, Gunther Wittstock; Soft Microelectrode Arrays as SECM Probes for Biological Samples. 221st meeting of the Electrochemical Society, Seattle, Washington, USA, 6.-10. May 2012.

[B5] Andreas Lesch, Britta Vaske, Frank Meiners, Dmitry Momotenko, Fernando Cortés-Salazar, Ingo Wirth, Hubert H. Girault, Gunther Wittstock; SECM imaging with soft microelectrode arrays - achievements and future challenges. 63rd Annual Meeting of the International Society of Electrochemistry, Prague, Czech Republic, 19.-24. August 2012.

13.3 Posters in National and International Conferences

[C1] Andreas Lesch, Britta Vaske, Frank Meiners, Daniel Witte, Dmitry Momotenko, Fernando Cortés-Salazar, Ingo Wirth, Hubert H. Girault, Gunther Wittstock; Soft microelectrode arrays as SECM probes for surface modification and characterization, Bunsentagung 2012, Leipzig, Germany, 17.-19. May 2012.

[C2] Andreas Lesch, Fernando Cortés-Salazar, Dmitry Momotenko, Hubert H. Girault, Gunther Wittstock; High-throughput reactivity imaging of unconventional SECM samples, GDCh-Wissenschaftsforum Chemie 2011, Bremen, Germany, 4.-7. September 2011.

14 Curriculum Vitae

Personal data:

First and last name: Andreas Lesch
Gender: male
Date of birth: 24.08.1983
Place of birth: Oldenburg (Oldb.), Germany
Nationality: German
Languages: German (mother tongue), English

Education:

06/2009 – 09/2012	PhD student, specialization in Electrochemistry, Carl-von-Ossietzky University of Oldenburg, Germany. Joint project with applicants Prof. Dr. Gunther Wittstock and Prof. Hubert H. Girault (Ecole Polytechnique Fédérale de Lausanne (EPFL), Switzerland), total of 7 weeks guest student at the EPFL. Project title: “High throughput SECM imaging“. Graduate School “Science and Technology”, PhD program “Interface Science”, University of Oldenburg, Germany.
10/2004 – 05/2009	Diploma in chemistry, Carl-von-Ossietzky University of Oldenburg, Germany. Diploma thesis: ”Parameter study on electrochemical shaping” at Robert Bosch GmbH in Stuttgart, Germany, in cooperation with the group of Prof. Dr. Gunther Wittstock, University of Oldenburg, Germany. *Graduation of Diploma*: 1.0 (on a scale of 1.0 (best) to 5.0 (failed)).
1996 - 2003	Gymnasium an der Willmsstraße, Delmenhorst, Germany *Graduation*: Abitur
1994 – 1996	Orientierungsstufe Schulzentrum-Süd, Delmenhorst, Germany
1990 - 1994	Grundschule Adelheide, Delmenhorst, Germany

Awards

2012 Arbeitsgemeinschaft Elektrochemischer Forschungsinstitutionen e.V. (*AGEF*) Travel Grant to attend the 63rd Annual Meeting of the International Society of Electrochemistry, Prague, Czech Republic, 19.-24. August 2012.

2012 Physical Chemistry Chemical Physics (*PCCP*) Hot Topic Prize for my poster "Soft microelectrode arrays as SECM probes for surface modification and characterisation" at the Bunsentagung 2012, Leipzig, Germany.

2012 Physical Analytical Division (*PAED*) Travel Grant to attend the 221st meeting of the Electrochemical Society, Seattle, Washington, USA, 6.-10. May 2012.

2009 Price of the Faculty of Mathematics and Natural Sciences, Carl von Ossietzky University of Oldenburg, Germany, for my Diploma thesis.

Other employment relationships:

06/2003 – 03/2004 Civilian service in kindergarten „Rappelkiste" for mentally and physically handicapped children, Lebenshilfe e.V., Delmenhorst, Germany.

04/2004 – 07/2004 Temporary employee in kindergarten „Rappelkiste" for mentally and physically handicapped children, Lebenshilfe e.V., Delmenhorst, Germany.

Ich versichere hiermit, dass ich diese Arbeit selbstständig verfasst und nur die angegebenen Quellen und Hilfsmittel benutzt habe. Während der Dissertation sind die unter „Publications“ aufgelisteten Veröffentlichungen entstanden. Die Dissertation hat weder zu Teilen noch in Gänze einer anderen wissenschaftlichen Hochschule zur Begutachtung in einem Promotionsverfahren vorgelegen.

Oldenburg, den 28.09.2012

Andreas Lesch